MATERIAL AND DEVICE CHARACTERIZATION OF $ZnInSe_2$ AND $Cu_{0.5}Ag_{0.5}InSe_2$ THIN FILMS FOR PHOTOVOLTAIC APPLICATIONS

A THESIS SUBMITTED TO
THE GRADUATE SCHOOL OF NATURAL AND APPLIED SCIENCES
OF
MIDDLE EAST TECHNICAL UNIVERSITY

BY

HASAN HÜSEYİN GÜLLÜ

IN PARTIAL FULFILLMENT OF THE REQUIREMENTS
FOR
THE DEGREE OF DOCTOR OF PHILOSOPHY
IN
PHYSICS

MARCH 2016

Approval of the thesis:

MATERIAL AND DEVICE CHARACTERIZATION OF $ZnInSe_2$ AND $Cu_{0.5}Ag_{0.5}InSe_2$ THIN FILMS FOR PHOTOVOLTAIC APPLICATIONS

submitted by **HASAN HÜSEYİN GÜLLÜ** in partial fulfillment of the requirements for the degree of **Doctor of Philosophy in Physics Department, Middle East Technical University** by,

Prof. Dr. Gülbin Dural Ünver
Dean, Graduate School of **Natural and Applied Sciences** _____

Prof. Dr. Mehmet T. Zeyrek
Head of Department, **Physics** _____

Prof. Dr. Mehmet Parlak
Supervisor, **Physics Dept., METU** _____

Prof. Dr. Çiğdem Erçelebi
Supervisor, **Physics Dept., METU** _____

Examining Committee Members:

Prof. Dr. Bülent Akınoğlu
Physics Dept., METU _____

Prof. Dr. Mehmet Parlak
Physics Dept., METU _____

Prof. Dr. Caner Durucan
Metallurgical and Materials Engineering Dept., METU _____

Prof. Dr. Bahtiyar Salamov
Physics Dept., Gazi University _____

Assoc. Prof. Dr. Nurdan Demirci Sankır
Material Science and Nanotechnology Dept., TOBB ETU _____

Date: *23.03.2016*

I hereby declare that all information in this document has been obtained and presented in accordance with academic rules and ethical conduct. I also declare that, as required by these rules and conduct, I have fully cited and referenced all material and results that are not original to this work.

Name, Last name: Hasan Hüseyin Güllü

Signature:

ABSTRACT

MATERIAL AND DEVICE CHARACTERIZATION OF $ZnInSe_2$ AND $Cu_{0.5}Ag_{0.5}InSe_2$ THIN FILMS FOR PHOTOVOLTAIC APPLICATIONS

Güllü, Hasan Hüseyin

Ph.D., Department of Physics

Supervisor: Prof. Dr. Mehmet Parlak

Co-Supervisor: Prof. Dr. A. Çiğdem Erçelebi

March 2016, 251 pages

In this work, material and device characterization of n-type $ZnInSe_2$ (ZIS) and p-type $Cu_{0.5}Ag_{0.5}InSe_2$ (CAIS) polycrystalline thin films were investigated under the aim of possible photovoltaic applications. ZIS polycrystalline structure is a ternary chalcopyrite semiconductor belongs to the group of II-III-VI compounds with the interest of II-VI binary analog of ZnSe structure. Similar to its binary analogs, it has a high band gap value, however low resistivity values compared to ZnSe structure, so that it can be promising material as a window layer. On the other hand, CAIS polycrystalline thin film structure belongs to quaternary chalcopyrite semiconductor compounds and contains both of the elements in the $CuInSe_2$ (CIS) and $AgInSe_2$ (AIS) ternary chalcopyrite structures. Therefore, it is expected to have a similar characteristics with them, such as direct band gap, and high absorption coefficients. This indicates that it can be suitable to use as an absorber layer in the photovoltaic applications. Under the aim of material characterization of these thin film layers, they were deposited on soda lime glass substrates with the evaporation of pure elemental sources by using physical thermal evaporation technique. During the deposition process, the substrate temperature was kept at about 200 °C. The thin films were characterized firstly in as-grown form, and then annealed under the nitrogen environment to deduce the effects of annealing on the structural, electrical

and optical properties of the deposited thin films. In addition to this, diode behaviors and basic diode parameters of these films were characterized. The heterostructure was produced by depositing the films on the Si-wafer having appropriate conductivity type. After completing all material and device characterization steps, as a final aim, ITO/n-ZIS/p-CAIS/In hetero-structure were fabricated as a solar cell application of the combination of these film structures. Detailed electrical characterization of this hetero-junction was performed by the help of temperature dependent current-voltage (I-V) and frequency dependent capacitance-voltage (C-V) measurements to investigate the device characteristics and to determine dominant conduction mechanism in this sandwich structure. Wavelength dependent I-V measurements were also performed to investigate the photo-transport properties. To determine photo-spectral working range of the junction, the spectral photo-response measurements were carried out in the spectral range of 300-1200 nm. This measurement was also performed in order to see the effects and contributions of the film layers on this device structure. Moreover, at room temperature, the photovoltaic characteristics of the deposited hetero-junction were investigated under different illumination intensities varying in between 20 to 115 mW/cm^2.

Keywords: Physical Vapor Deposition, Chalcopyrite Compound, Thin Film, Heterojunction

ÖZ

$ZnInSe_2$ VE $Cu_{0.5}Ag_{0.5}InSe_2$ İNCE FİLMLERİNİN FOTOVOLTAİK UYGULAMALAR İÇİN MALZEME VE AYGIT KARAKTERİZASYONU

Güllü, Hasan Hüseyin
Doktora, Fizik Bölümü
Tez Yöneticisi: Prof. Dr. Mehmet Parlak
Ortak Tez Yöneticisi: Prof. Dr. A. Çiğdem Erçelebi

Mart 2016, 251 sayfa

Bu çalışmada, fotovoltaik uygulamalarda kullanılmak amacıyla n-tipi $ZnInSe_2$ (ZIS) ve p-tipi $Cu_{0.5}Ag_{0.5}InSe_2$ (CAIS) polikristal ince film yapılarının malzeme ve aygıt karakterizasyonları yapılmıştır. ZIS polikristal yapısı, II-VI grubuna ait ZnSe ikili yapısına benzer II-III-VI bileşik grubuna ait bir üçlü kalkopirit yarıiletkendir. İkili yapıdaki örneklerine benzer olarak, yüksek bant aralığına, buna karşılık ZnSe yapısına göre düşük özdirenç değerine sahiptir, böylece umut verici bir pencere tabakasıdır. Diğer yandan, CAIS polikristal ince film yapısı dörtlü kalkopirit yarıiletken bileşikleri içerisindedir ve $CuInSe_2$ (CIS) ve $AgInSe_2$ (AIS) üçlü kalkopirit yapılarının tüm elementlerine sahiptir. Böylece, CAIS polikristal ince filmlerin, bu üçlü yapıların direk bant aralığı ve yüksek soğurma katsayısı özellikleri gibi benzer özelliklere sahip olduğu önerilmektedir. Bu, fotovoltaik uygulamalarda, soğurucu katman olarak kullanılması için uygun olabileceğini göstermektedir. Bu ince film katmanlarının malzeme karakterizasyonu amacı altında, fiziksel termal buharlaştırma tekniği kullanılarak, cam alttaşlar üzerine saf element kaynaklarının buharlaştırmasıyla üretilmiştir. Üretim işlemi sırasında, alttaş sıcaklığı yaklaşık 200 °C'de tutulmuştur. İnce filmler ilk önce, ısıl işlem görmemişken karakterize

edilmiştir. Daha sonra, örneklerin bazılarına, yapısal, elektriksel ve optik özellikleri üzerindeki tavlama etkisini incelemek için, azot ortamında üretim sonrası ısıl işlem uygulanmıştır. Buna ek olarak, bu filmlerin diyot davranışları ve temel diyot parametreleri karakterize edilmiştir. Bu amaç altında, her heteroeklem, uygun iletkenlik tipine göre Si alttaş üzerine üretilmiştir. Tüm malzeme ve aygıt karakterizasyon basamaklarını tamamladıktan sonra, son olarak, ITO/n-ZIS/p-CAIS/In heteroyapıları güneş gözesi uygulamaları olarak üretilmiştir. Bu heteroeklemlerin detaylı elektriksel karakterizasyonu, aygıt karakteristiklerini incelemek ve sandiviç yapıdaki baskın iletkenlik mekanizmasını belirlemek için sıcaklığa bağlı akım-voltaj (I-V) ve frekansa bağlı kapasitans-voltaj (C-V) ölçümleri yardımıyla yapılmıştır. Ayrıca, ışık altındaki tepkisini incelemek için dalga boyuna bağlı I-V ölçümleri yapılmıştır. Eklemin, ışık spektral çalışma menzilini belirlemek için, spektral ışık tepkime ölçümleri 300-1200 nm dalga boyu aralığında yapılmıştır. Bu ölçüm, ayrıca film katmanlarının aygıt yapısı üzerindeki etkilerini ve katkılarını görmek için yapılmıştır. Ayrıca, oda sıcaklığında üretilen heteroeklemlerin fotovoltaik karakteristikleri 20 ile 115 mW/cm^2 aralığında değişen farklı aydınlatma şiddetlerinde incelenmiştir.

Anahtar Kelimeler: Fiziksel Buharlı Biriktirme, Kalkopirit Bileşik, İnce Film, Heteroeklem

To my wife

ACKNOWLEDGMENTS

I would like to express my deep gratitude and thanks to my supervisor Prof. Dr. Mehmet Parlak for his endless patience, understanding, cooperation and support throughout this study. I would like to thank to Prof. Dr. Çiğdem Erçelebi for her excellent guidance, valuable comments and continuous support during the course of this investigation. Thanks are also to the members of the thesis monitoring committee, Prof. Dr. Bülent Akınoğlu and Prof. Dr. Caner Durucan for their valuable discussions and comments. Appreciation is also extended to the members of this thesis committee, Prof. Dr. Bahtiyar Salamov and Assoc. Prof. Dr. Nurdan Demirci Sankır for their comments during the review of this thesis. The fruitful contributions of Prof. Dr. Raşit Turan is gratefully acknowledged.

I appreciate to Özge Bayraklı for her invaluable help with the experiments and friendship during thesis study. I would also like to present my sincere thanks to Dr. Emre Coşkun for his precious help with the experiments, fruitful discussions and valuable friendship. I also appreciate to Dr. Tahir Çolakoğlu for his stimulating guidance and discussions. I will always be grateful to my lab colleagues Dr. Arezoo Hosseini, Dr. İdris Candan and Makbule Terlemezoğlu. I want to acknowledge Harun Tanık for both friendship and help in my experimental works. The technical assistance and cooperation I received from Yücel Eke, Tayfun Yıldız and Dursun Erdoğan is gratefully acknowledged.

I wish also to thank to Center for Solar Energy Research and Applications (GÜNAM), Yasin Ergunt, Emine Hande Çiftpınar, Olgu Demircioğlu, Fırat Es, Merve Kabukçuoğlu, Mustafa Ünal, Kurtuluş Abak, Dr. Hisham Nasser, Mehmet Karaman, Zeynep Demircioğlu, Ergi Dönerçark, Dr. Engin Özkol, Salar H. Sedani, Mona Zolfaghari Borra, for sharing of knowledge and kind friendship.

I am also grateful to all academic and administrative staff of the Department of Physics, especially Gülşen Özdemir Parlak, Zeynep Eke and Özge Topal.

Special thanks go to all of my family for their continuous support and love at the each stage of my educational life. Very special thanks go to Seda Kayra Güllü whose love, steadfast confidence and constant encouragement. Without them this work would never have come into existence.

I also thank The Scientific and Technological Research Council of Turkey (TÜBİTAK) for the financial support I received for this study.

TABLE OF CONTENTS

LIST OF TABLES

TABLES

LIST OF FIGURES

FIGURES

NOMENCLATURE

ZIS	$ZnInSe_2$
CAIS	$Cu_{0.5}Ag_{0.5}InSe_2$
CIS	$CuInSe_2$
AIS	$AgInSe_2$
I-V	current-voltage
C-V	capacitance-voltage
CdS	cadmium sulfide
CIGS	$CuInGaSe_2$
CdTe	cadmium telluride
XRD	X-ray diffraction
PVD	physical vapor deposition
CVD	chemical vapor deposition
CBD	chemical bath deposition
RMS	root mean square
e-beam	electron-beam
DC	direct current
RF	radio frequency
PLD	pulsed laser deposition
XPS	X-ray photoelectron spectroscopy
ESCA	electron spectroscopy for chemical analysis
STM	scanning tunneling microscope
AFM	atomic force microscope
SEM	scanning electron microscopy
EDS	energy dispersive spectroscopy
WKB	Wentzel-Kramers-Brillouin
VRH	variable range hopping
FF	fill factor
ITO	indium tin oxide
Si	silicon
FWHM	full width at half maximum
LO	longitudinal optical
EM	envelope method
SOM	single-effective-oscillator model
CF	crystal-field splitting
SO	spin-orbit splitting
RF	rectification factor
TE	thermionic emission
TFE	thermionic field emission
FE	field emission
SCLC	space charge limited current
IR	interface recombination
RG	recombination-generation

CHAPTER 1

INTRODUCTION

Following the invention of the first solar cell with 1% efficiency of the junction formed by coating Au in a thin layer on Se [1], nowadays, the solar cell technology has been advanced the researches and applications on both wafer-based and thin film form of semiconducting materials. Then, the first practical solar cell, fabricated by single crystalline Si junction, with a sunlight energy conversion efficiency of around 6% was invented [2]. Moreover, single crystal cadmium sulfide (CdS) solar cell was produced with efficiency of 6% [3]. As a result of this demonstration of energy conversion by using direct sunlight illumination, investigations on solar cells are crucially developed in order to obtain higher efficiencies. In addition to bulk materials, from the early days of works on solar cells, thin films have great attraction on the investigations on competed alternative technology. Although the wafer-based mono-crystalline and multi-crystalline Si solar cells can convert 25.6 and 20.4% of the energy in sunlight into electricity, respectively [4, 5], the thin film applications are promising approach for high efficient solar cells. In addition to indirect band gap characteristic of Si structure and fragile behavior of bulk materials, wafer-based Si solar cells require high bulk material with typical thickness larger than 300 μm and high cost production method [6]. On the other hand, the choice of the usage of the thin film technology can offer less requirement of source material, and also simpler fabrication processes with respect to the traditional solar cell technologies.

Although there are several advantages of Si thin film structures in the solar cell technology, due to its indirect band gap nature with lower energy than the value that

is most efficient in the visible region, Si cannot provide the leading position and become the ideal material for the application in this area [7]. Therefore, as an alternative material instead of Si usage, research are concentrated on thin film applications of appropriate materials on solar cells. Thus, II-VI compound and its variations as chalcopyrite based thin films and III-V compound materials are point of interest in the applications on the photovoltaic device. Polycrystalline thin film solar cells based on cupper indium diselenide ($CuInSe_2$ or CIS) and its alloy cupper indium gallium diselenide ($CuInGaSe_2$ or CIGS) and cadmium telluride (CdTe) are subject of interest to be the most suitable alternatives for large scale application of solar cells. In fact, within Si, thin film solar cells, CIGS and CdTe based researches have a transition from the laboratory to the market place [8]. The crystalline nature of these films provides use of severeal substrates and also low cost material deposition techniques.The other advantage is the possibility to tolerate the band gap by changing the constituent elements in the film structure leads to higher band gap [7].

In fact, there are three most common thin-film technologies, a-Si, CdTe and CIGS applied in the solar cell area in both laboratory and module. At present, instead of Si-based thin films, there are two leading candidates for polycrystalline thin film solar cells, CIGS based devices with 21.7% [9] and CdTe based devices with 21% efficiency [10] and in both cases CdS is the best window partner. In recent years, CIGS based thin film solar cell in laboratory and module scale has initiated this research area with 20.5% efficiency [5]. Since CIGS solar cells have the potential for good efficiencies and could be potentially cheap, they are seen as the major competitor to the Si bulk cell in recent years. On the other hand, with the movement toward new and better technologies and increasing demand for the cheap photovoltaic devices, these structures start to be out of interest. Because of containing rare In and Ga, these types of solar cells cannot fulfill the future demand of solar cells. Therefore, in the case of Zn and Sn usage attracts significant interest as an alternative material for these rare elements in the well-known chalcopyrite structures [11].

In case of polycrystalline materials, the economic considerations are the most important. These viewpoint necessitates the use of inexpensive substrates for the large area depositions where high throughput is required. The compromise requires a balance between the cost and performance. The main research and manufacturing efforts were directed towards achieving new and alternative directions in thin film solar cells. Under the effect of the availability of Te, In and Ga elements has been dictated by demand, In could be replaced by II-IV combinations such as Zn and Sn to form a different quaternary alloy and also Se and S elements in group-VI can be used instead of Te, where they have similar chemical properties.

$ZnInSe_2$ (ZIS) structure is a ternary defect chalcopyrite semiconductor based on the combinations of II-III-VI group of elements [12-14]. The defect in this compound arises from the percentage vacancies of Zn elements in the structure [14] and it is the main factor on the physical characteristics of this film. In fact, it is the ternary analog of ZnSe which is an II-VI semiconductor material with the cubic zinc blende structure. Although ZnSe is a very promising compound for the thin film applications of solar cells [15-18], being a defect structure depending on difficulties to control the compositional stoichiometry and high resistivity problem limits their photovoltaic device performances. There are many research on optimizing this resistivity problem of the polycrystalline thin films with high band gap energies and the common approach is alloying them with the elements in group III [19, 20]. Among these, there are many research on ZIS thin films about their crystal and film characteristics; and also applications in solar cells and optoelectronic devices [12-14, 21-36]. These works demonstrated their applicability of buffer layer as a hetero-junction partner for p-type absorber layers materials. They have an n-type conductivity behavior [12] and can be used as a promising candidate for CdS structure with its environment-friendly characteristics.

In the literature, the works reported on the ZIS structure are related both crystal and thin film applications [12-14, 21-36]. Generally, the ZIS ingot [12-14, 21-23] was prepared to analyze the properties of the ZIS in crystal form [13] and it was also used to deposit ZIS thin films [12, 14, 21-23]. In addition, vapor-phase chemical transport

was used to grow ZIS crystal [25, 26]; and the co-evaporation [27], evaporation of precursors and selenization [24], RF sputtering [30], spray deposition [28, 29] and electrodeposition [33] techniques were used to prepare thin film samples.

In the thin film researches, some works on the crystal growth were reported as the preliminary for the thin film fabrication [12, 14, 21-23]. In these works, the obtained ingot was used as an evaporation source for the thermal evaporation process. $Zn_xIn_{1-x}Se$ thin films were also prepared by co-evaporation of In_2Se_3 and ZnSe evaporation sources [27]. In addition, aqueous solutions of zinc sulphate ($ZnSO_4$), indium trichloride ($InCl_3$), and selenourea (CH_4N_2Se) were used in distilled water to prepare the solution for deposition of the ZIS thin films [28]. As a different technique, $ZnIn_2Se_4$ thin films were produced by electrodeposition method [33] and in this process, the $ZnIn_2Se_4$ solution was prepared by mixing zinc sulphate ($ZnSO_4$), indium trichloride ($InCl_3$) and selenium dioxide (SeO_2) solutions. The ZIS samples were also deposited by the combination of sputtering and selenization methods [30].

In the works on ZIS thin films, the results of structural, optical, electrical and device characterizations were presented dependent on the film thickness, substrate temperature, annealing processes, and also sample temperature. Studies on the crystalline structure of the films showed that when the thermal evaporation by using crystal powder takes place at the room temperature on the glass substrate, the as-grown films are formed in the amorphous [12, 14, 22, 23]. On the other hand, by applying post-annealing process at 373 K for 1 hour, the amorphous behavior can transform to the polycrystalline nature with the main orientation at (112) direction [12]. Hendia et al. also indicated that the polycrystalline structure become more apparent with increasing the annealing temperature up to the 573 K, and the peaks observed in the XRD spectra are reported as to be in (112) and (002) directions. With similar crystal growth and film deposition methods, El-Nahass et al. [23] also presented the corresponding XRD spectra of the films. The data obtained in this work showed that the samples annealed at 523 K has a single diffraction peak in (112) direction at about 27° while samples annealed at 573 K and 623 K have secondary peaks in (220) direction at about 45° and in (103) direction at about 32°,

respectively. H.M. Zeyda et al. also obtained these peaks as a result of the annealing procedure [14]. However, in this case, the films annealed at 573 K and 623 K showed both (103) and (220) crystal orientations. From the sputtered films, the peaks were found at 27°, 44.9° and 53.2° that correspond to the tetragonal ZIS phase with crystalline orientation at (112), (204) and (302) directions [30]. K.W. Cheng also reported that although there is no change in the XRD pattern of the films, the diffraction peaks were slightly shifted to higher angles with increase in Zn/(Zn+In) ratio. Different to this reported values, R. Jeyakumar obtained only ZnSe phase in the (111) main direction from the precursor deposition and selenization process [24]. In this work, they showed that the increase in the substrate temperature from 25 to 125 °C cause increase in In/Zn ratio in the precursors and selenized films. As a detailed structural analysis, XPS spectrum was investigated for the Zn(In)Se films and peak profiles of Se 3d, In $3d_{3/2}$, $3d_{5/2}$, Zn $2p_{1/2}$, Zn $2p_{3/2}$ were analyzed. According to this work, the positions of Zn, In and Se XPS lines were observed at 1021.6, 44.2 and 53.5 eV, respectively.

According to Hendia et al., the absorption coefficient of the films deposited at 300 K and also annealed in the temperature range of 373-523 for 1 hour are about between 10^3 and 10^5 cm^{-1}. On the other hand, absorption values were found to be in the range of 10^4 cm^{-1} for all samples in the form of $Zn_xIn_{1-x}Se$ [27]. The optical band gap analysis in the reported studies [18] showed that the as-grown films where the substrate temperature is 300 K, has both direct and indirect optical transition behaviors with band gaps of 3.38 eV and 2.22 eV, respectively. These values are in decreasing behavior from 3.18 to 3.11 and from 2.03 to 1.92 with increasing temperate between 373 and 573 K, respectively. In addition, refractive index , extinction coefficient and dielectric constants were reported as in the similar behavior in annealing process. With similar ZIS films in as-grown form, Zeyada et al. [37] and El-Nahass et. al. [23] worked on the transmittance and reflectance spectra. The absorption analysis of the as-grown films also showed both direct and indirect transitions with band gaps 2.3 eV and 1.76 eV, respectively [22]. Similar to these analyses, the values for the reported studies [23] are 2.21 eV and 1.71 eV. The analysis of the annealing temperate also in similar behavior as reported in the

literature [12]. From the calculations on the optical spectra of the films, it was found the refractive index values can be explained in two models, multi oscillator at the peak of 659 nm and single oscillator models at the wavelength values are greater than 1000 nm [22, 23]. They also showed that the absorption coefficient decreases linearly with scanning wavelength from 0 to 693 nm; it reaches to 0 value at 700 nm. The dispersion in the *n* values was also analyzed in the work given in [22], and the oscillator energy, dispersion energy, dielectric constant at infinite frequency and lattice dielectric constant were reported as 2.49 eV, 14.36 eV, 6.84 and 8.17, respectively. The detailed analysis was given in [23], where these parameters are in a good agreement in this data set. However, with the effect of annealing temperature, the nonlinear susceptibility, static refractive index and nonlinear refractive index were determined for this structure [23]. For the analysis on variations of In and Zn ratios in the composition, the refractive index values were found in the range from 2.45 to 3 with increasing In and decreasing Zn [27]. Moreover, these refractive index values were analyzed in terms of two-order Cauchy dispersion formula as a function of *x* content.

In the optical analysis, there is no any common behavior on the type of the optical transitions and approximate values on their corresponding band gaps. Although in most of the ZIS films deposited by thermal evaporation method shows both direct and indirect transitions [12, 21-23], S. Gariazzo et al. obtained only direct transition and also they found the optical gap values in between 1.85 and 2.65 eV as a function of *x* [27]. Similarly, R. Jeyakumar et al. [24] reported only the direct band gap in 2.35 eV. From the work reported by K.W. Cheng, the direct energy band gaps of samples varied from 1.68 to 1.81 eV depending on the ratio of the metal alloys. These results also concluded as increase in the Zn/(Zn/In) molar ratio causes increase in the energy band gap of the ZIS samples.

For the electrical analysis, the resistivity values of the ZIS films were reported in between $5x10^2$ and $4x10^4$ Ω.cm depending on the substrate temperature of the precursors and also on the selenization temperature [24]. According to this work, it was found that the resistivity increases with increasing In/Zn ratio in the

composition. This behavior was also obtained from the $Zn_xIn_{1-x}Se$ samples when their In content increases [27]. Different than this result, the DC electrical measurements in the work of H.M. Zeyada et al. [12] showed that there are two temperature regions corresponding to two different conduction mechanisms. At the temperatures higher than 365 K, they reported that the thermionic emission behavior is dominant with activation energy of 0.837 eV. On the other hand, at temperatures between 300 and 365 K, they showed that Mott average hopping mechanism is dominant in the conduction process with activation energy of 0.18 eV.

For the device characteristics of the ZIS films, the dark current-voltage behavior of Au/n-ZIS/p-Si/Al diode was analyzed as a function of ambient temperature in the interval of 293-323 K. [12]. In this work, in forward bias case, at bias voltage lower than 0.2 V, thermionic emission of electrons over a barrier potential of 0.28 eV were observed and at bias voltage higher than 0.2 V, single trap space charge limited current was found to be dominant. At higher bias region, the trap concentration and trap energy level were reported as $3.12x10^{19}$ cm^{-3} and 0.24 eV, respectively. According to the photo-electrochemistry measurements on the ZIS thin films deposited on FTO coated glass substrates, the [30], the flat-band potentials in 0.6 M K_2SO_3 aqueous solution of samples were obtained between -0.41 and -0.95 V with an Ag/AgCl electrode.

Furthermore, the ZIS thin films deposited by thermal evaporation method were analyzed under the effect of ϒ-irradiation [21]. In this work, the optical constants, direct and indirect band gap values, and conductivity behavior of the as-grown samples were compared between the unirradiated and irradiated cases. The spectral behavior of the refractive index and extinction coefficient were reported in increasing behavior with incident photon energy similar to the other works. On the other hand, these curves revealed continuous variation depending on the change in wavelength. The band gap values of the unirradiated and irradiated samples are reported in this work as 3 and 3.2 eV for direct transition, and 1.75 and 1.9 eV for indirect transition, respectively. As a conduction mechanism in the ZIS structures at the temperature

interval higher than room temperature, the thermionic emission model was accepted in both thin films with activation energies of 0.89 and 0.95 eV, respectively.

ZIS thin films were also deposited by chemical methods with an aqueous solution [28, 29, 33]. As a result of the spray-deposited films with a substrate temperature of 325°, the XRD pattern of the as-grown films showed the similar crystalline formation as observed in the films deposited by physical deposition techniques [38, 29]. According to these works, the main orientation is at about 27° at (112) direction. However, the deposited films were reported as to be in nano-crystalline nature with rhombohedral crystal structure and lattice constant a=4.05 Å. Although the films electrodeposited on stainless steel substrate has also the same crystalline phase with a diffraction angle similar to the one reported in other works, the main orientation direction is at about 45° in (301) direction [33]. Moreover, the other minor diffraction peaks were reported as to be at about 44, 55 and 61° in (220), (116) and (400) crystalline orientation. This film is found in a good agreement with the tetragonal crystal structure and lattice parameters of a=5.409 Å and a=11.449 Å. From the compositional and surface analysis of the spray-deposited films, compositional ratio of 1:2.3:3.5 and a compact morphology with large number of single crystals were observed. An observation of SEM micrographs of the electrodeposited films showed that on the surface, there are grains formations compact with tetragonal (rod like) shape. The optical studies of these solution based depositions, the nature of the optical transition was determined on the basis of indirect band gap electronic transition in spray-deposited films, while it was reported as direct transition for electrodeposited films. These band gap values are 1.41 and 2.4 eV, respectively. In these works, the electrical properties of the spray-deposited samples were investigated under the effect of sample temperature from 300 to 420 K. The dark resistivity values were obtained in the order of 10^4-10^5 Ω.cm, and the conduction mechanism were examined at low (< 395 K) and high (> 395 K) temperature regions. The intrinsic mechanism was used to explain the conduction in high temperature region, and hopping conduction mechanism was used for the conduction process in low temperature region. The corresponding activation energies were approximated as 0.38 and 0.54 eV, respectively. Moreover, for these films, the

Seebeck coefficient was calculated as to be 0.0016 mV/K. The device applications were reported from both of these films deposited by using chemical deposition techniques. Measurements of the photo-electrochemical cells prepared on the FTO substrates in the literature [29] showed that the dark junction ideality factor and junction ideality factor under illumination were 5.6 and 1.9, respectively. In addition for these types of films, the fill factor and power efficiency conversion were found to be about 0.435% and 1.47%, respectively. In addition, the photosensitivity of these cells were analyzed photo-electrochemical response under chopped light conditions were reported for the electrodeposited films [33].

On the other hand, polycrystalline thin film photovoltaic devices used CIS and AIS ternary compounds are members of I-III-VI_2 chalcopyrite semiconductors and they are point of interest in solar cell applications [39]. These materials are also popularly used in non-linear optical devices due to their stable natures and high absorption characteristics [40]. Group of these ternary compounds is constructed in an analogy of the II-VI binary (zinc-blende) compounds. By replacing two cation atoms to the place of one in this binary lattice structure, alternate series of bonds can be constructed which causes variations in their structural, electronic and optical behaviors. These chalcopyrite semiconductors shows direct band gap nature and efficient absorption coefficients and therefore, they become commonly used thin film materials in the photovoltaic applications [41].

Studies on the quaternary compound, $Cu_xAg_{1-x}InSe_2$ and similarly $Cu_{1-x}Ag_xInSe_2$ are mainly concentrated on obtaining an effective absorber layer of heterojunction in solar cell applications due to a large degree of variation in ratios of the constituent elements, and so that optimizing of the material properties. As a result, this compound which is a quaternary analog of both CIS and AIS, can offer a possibility to optimize the material characteristics, mostly to reach desired optical band gap, absorption coefficient and lattice parameters, for the photovoltaic device requirements. With changing Cu atoms with Ag, it is expected to increase the optical band gap in the interval of 1.05 eV [42] and 1.24 eV [43].

In the literature, although there are some researches on the Cu-Ag-In-Se (CAIS) structure related to the analysis of both crystal and thin film forms [42-57], they are not covered the all characterizations for this structure. For the fabrication of CAIS crystal, the widely reported technique is Bridgman-Stockbarger crystal growth method [42-44, 48-51, 55, 57] and these crystals were characterized in terms of structural, optical and electrical properties [45, 48, 55, 57]. In addition to these studies, most of the works on the thin film applications are concentrated on the films deposited by using these crystal sources [42-44, 49, 51]. For deposition of the films, there are also specific methods categorized as thermal evaporation [50], pulsed laser deposition [44, 51], flash evaporation [42, 43, 49], and sputtering [52-54, 56]. These works on CAIS thin films are related to structural [43, 49], optical [43, 44, 46, 49, 52-54, 56], electrical [41, 45] and device [47, 50] properties. However, the works on these characteristics were not completely reported, and the research are mainly concentrated on limited on change in crystallinity of the thin films with surface temperature, determining basic optical parameters, analyzing Schottky behavior with Al contact, cathodoluminescence and photoluminescence.

With these works on CAIS thin films, there are a few alternative deposition methods presented for the fabrication of this films. Gremenok et al. [51] reported the growth and characterization of $Cu_xAg_{1-x}InSe_2$ (x=0.0, 0.3, 0.5, 0.7 and 1.0) thin films prepared on the glass substrates by pulsed laser deposition. The films were deposited at the substrate temperature range 450-480 °C with deposition rate of 20-40 μm/s under the pressure of about 10^{-5} Torr. I.V. Bodnar et al. [44] also reported the analysis of the CAIS films deposited by the same technique. Although the most of the deposition parameters were also similar in these two works, I.V. Bodnar et al. preferred the substrate temperature as 750-780 K. Among these chalcopyrite semiconductor compounds, most of the works on $Cu_{0.5}Ag_{0.5}InSe_2$ were reported by G.V. Rao et al. [42, 43, 49, 50]. They deposited this film structure by using flash evaporation technique and worked on the film samples deposited at the substrate temperatures between 363 and 803 K at a system pressure of $2x10^{-6}$ Torr. The evaporation rate in the flash evaporation was about 1 nm/s with a final film thickness was between 100 and 4000 nm [42, 43, 49]. In order to fabricate Al/p-CAIS Schottky

barrier diode, the CAIS films were deposited on Au-coated glass substrate at 693 K [50]. The study of A.A. Lavrentyev et al. [46] is related to the comparison of the structural and optical properties of the ternary AIS and CIS, and quaternary $Cu_xAg_{1-x}InSe_2$ compounds. The films were also fabricated by a hybrid process where Cu, Ag, and In were sputtered and elemental Se was evaporated thermally to reach the final film composition [52, 53]. The elements were evaporated with compositions of x=0.0, 0.6, and 1.0, at a constant rate onto soda lime glass substrates at 550 ºC. The same deposition parameters were also used in the related studies [54, 56] to prepare the CAIS films with the Cu/(Ag+Cu) ratios of 0.0, 0.2, 0.4, 0.6, 0.8 and 1.0. In these works, Si (100) wafer was used as a substrate which was kept at 550 °C during the deposition.

According to the study of Gremenok et al. [51] the films deposited by pulsed laser method were in 500-1000 nm thickness range and XRD spectra of them shows a single phase at (112) crystalline direction. The lattice parameters, positional parameters and interatomic distances of the CAIS films were presented depending on the compositional variations. The data obtained in the study of I.V. Bodnar et al. [44] gave similar results with the study of Gremenok et al. [51] in terms of parameters of the unit cell, tetragonal distortion, positional parameter and the lengths of the atomic bonds. Structural studies of the $Cu_{0.5}Ag_{0.5}InSe_2$ thin film samples were concentrated on the effect of the substrate temperature, and so that, the atomic rations in the composition, grain formations, and also crystalline behaviors were investigated [42, 43, 49]. As a result, the chemical composition, structure and surface morphology of these films were reported in terms of the variations on the substrate temperature. In addition, from these work, they reported that the CAIS thin films deposited by flash evaporation method were in In and Se rich, and Ag and Cu deficient composition when the substrate temperature was kept below 683 K. On the other hand, they also showed that if these films were fabricated at about 683-703 K, they became near stoichiometric structure. These works also presented the effect of the substrate temperature on the crystalline structure as, if it was below 573 K, the films were in amorphous nature; if it was at between 573-673 K, the films were in polycrystalline nature without stoichiometric composition; if it was at 623 K, secondary phase in the

form of InSe was appeared; if it was at 693 K, the films were in polycrystalline with strong preferred orientation along (112) direction; if it was at between 683-703 K, the films was in single phase, and nearly stoichiometric; if it was at 723 K, the additional phases of Cu_2Se and Ag_2Se were observed in the diffraction spectra. As a general result from these works, $Cu_{0.5}Ag_{0.5}InSe_2$ films deposited at a substrate temperature of 693 K were single phase, polycrystalline with a strong (112) preferred orientation and the mean grain size of single phase films were around 500 nm. Moreover, the lattice parameters are a=0.5937 nm, c=1.1633 nm, with (c/a)=1.959. From the theoretical and experimental consideration, XPS spectra of the CAIS films were analyzed and the results were explained by the splitting in the energy bands [46].

The optical characteristics of the $Cu_xAg_{1-x}InSe_2$ thin films where x=0.0, 0.3, 0.5, 0.7 and 1.0 were investigated with transmittance and reflectance measurements [44, 51]. The absorption coefficients of these films were found to be about 10^4 cm^{-1} above the fundamental absorption edge. From the optical spectra of these films, refractive index and band structure analysis were done as a function of x content. In addition, in these two works, three direct band optical transitions and corresponding crystal field and spin orbit splitting parameters were reported. The curves of energy band gaps versus the composition variations depending on x content showed that there is a nonlinear dependence between the direct band gap values and x content as, $E_{g,1}$=0.99+0.10x+0.16x^2, $E_{g,2}$=1.04+0.12x+0.16x^2 and $E_{g,3}$=1.22+0.16x+0.20x^2. From the optical transmittance data obtained from the films deposited by G.V. Rao et al. [64], the band gap values, spin orbit and crystal field splitting parameters were determined and the absorption characteristics on transitions from the valence band edge to the conduction band were studied. The analysis of absorption spectra of $Cu_{0.5}Ag_{0.5}InSe_2$ films for several thickness values in 500, 1000 and 1500 nm indicated that band gap energies can be changed in 1.14, 1.19, 1.45 eV under the effect of valence band splitting [43]. Besides, the fundamental optical band gaps of the films were 1.12, 1.14 and 1.15 eV corresponding to the films deposited at substrate temperatures of 623, 693 and 723 K, respectively [49]. Additionally, the non-linear dependence of the band gap energy were investigated by both theoretical

calculations and different experiments for solid solutions as a function of *x* [46]. Similar to the other works, the nonlinear variation in band gap values depending on the x content was explained by three term polynomial relation. The other optical researches on this structure are in about cryogenic cathodoluminescence and photoluminescence analysis of these films. Aquino et. al [52, 53] presented their works as a conference paper in $Cu_xAg_{1-x}InSe_2$ thin films about the emission spectrum of grains and grain boundaries in CAIS with cathodoluminescence and identification of defect levels with photoluminescence analysis. As a result of these studies, as the Cu content in the films increases, specific defect states also increases (with more local chemical variation) and the relatively uniform luminescence from the CAIS films shows that this material may produce more uniform device performances, because minimized fluctuations in film composition and surface recombination. In the study of T. Begou et al. [54], the dielectric constant and band gap values of the films deposited in the same conditions with the study in [52, 53] were analyzed by using real time spectroscopic ellipsometry. The band gap values of CAIS films as a function of Cu/(Cu+Ag) content (0.0, 0.2, 0.4, 0.6, 0.8, 1.0) were found as 1.15, 1.05, 0.98, 0.91, 0.90 and 0.90 eV, respectively. The similar results also found in the study of S.A. Little et al. [56] by in situ and ex situ characterization methods.

The outcome of the works on the $Cu_{0.5}Ag_{0.5}InSe_2$ films is also about their electrical characteristics. The temperature dependence of the electrical conductivity of the CAIS samples were analyzed in the work [42] and it showed that there was an intrinsic conduction above 455 K with an activation energy of 0.55 eV and impurity conduction below 433 K with an activation energy of 0.15 eV. These films were reported as in p-type by the Hall effect measurements, and their electrical resistivity values were calculated in the interval of 30-300 (Ω.cm), and the thermos-electric power in 10-50 (cm^2/(V.s)) [42].

In addition, the device characteristics of this quaternary chalcopyrite alloy were discussed in some works [50]. In the study of G.V. Rao et al. [50], the current vs. voltage (I-V), capacitance vs. voltage (C-V) and photo-response measurements were

carried out to determine the Schottky diode behavior of Al/p-$Cu_{0.5}Ag_{0.5}InSe_2$/Au junction at 303 K. From these measurements, basic Schottky diode parameters such as barrier height, work function and electron affinity, of CAIS were calculated as about 0.55, 4.72 and 3.75 eV, respectively. The effective carrier concentration and the built-in potential values were also determined by C-V measurements and found as $4.5x10^{15}$ cm^{-3} and 0.38 V, respectively.

Different from these work, D.G. Kilday et al. [58] reported common-anion rule and its limits for $Cu_xAg_{1-x}InSe_2$-Ge interfaces where *x* equals to 0.0, 0.25, 0.50, 0.75, 0.90 and 1.0. Therefore, this work was concentrated on the photoemission studies of the interfaces obtained by depositing Ge on CAIS layer. Then, the discontinuity on valence band of the structure was analyzed. From the data from this work, the discontinuity of valence band in this material was found at about 0.60 eV.

CHAPTER 2

THEORETICAL CONSIDERATIONS

2.1 Introduction

In this chapter, the basic concepts about the thin film deposition techniques, material properties and device analysis are presented. Although the thermal evaporation technique was used to deposit the film layers, the general information about thin films and introduction to most common deposition methods are described. Then, material properties of these two type semiconductors are introduced. Finally, basic information on the structural, optical and electrical properties of the semiconductor materials and diode characteristics of heterojunctions are discussed in detail.

2.2 Thin Film Deposition

As a simple case, a thin film material is an atom/molecule/ion/cluster species on a substrate created by condensation process of atom/molecule/ion/cluster species [59]. In general, thin film is mentioned as a simply layer of material, and the term thin is generally used to describe a layer of thickness less than 1 μm [60]. However, thin materials can also be created by a liquid solution process, and these types of films are usually named as thick film [59]. Therefore, the deposition process and consequential effects on the film properties of the films are crucial than its thickness. In fact, thin film is the technique to minimize the material use without loss the properties of the grown material, and also to tailor its characteristics.

Depending on the condensation process, thin film deposition can be carried out with the order of creation of atomic/molecular/ionic species, transport of these species through a medium, and condensation of these species on a substrate [59]. In addition to this, the deposition techniques can be classified as physical vapor deposition (PVD); chemical vapor deposition (CVD); solution based growth as electrodeposition and chemical bath deposition (CBD) [59].

The PVD is the method of a thin film deposition based on vapor production and condensation using physical methods on a given substrate material. In PVD technique, the deposition of the films can take place by stacked layer deposition technique in which the elements or compounds are deposited on the substrate layer-by-layer and by co-evaporation techniques, in which all evaporation sources were condensed on the substrate simultaneously. The physical correspondence of production of a vapor is based simply on a heating of a source material by the help of a filament or crucible. Moreover, there are a lot of special versions of evaporation sources due to the specific requirements include effusion cell and the electron-beam evaporator. The other widespread PVD techniques are sputtering, laser-induced deposition and flash evaporation. Among them, high vacuum condition in the order of 10^{-6} Torr is the common requirement in the deposition process [61].

However, CVD is based on the chemical reactions that transform gas molecules via precursor gas or gases into a heated solid material on the substrate surface. PVD occur by the physical transfer of the vapor of the heated evaporation source or sputtered atom of the bombarded target by energetic particles to the substrate, whereas CVD principally based on the transportation of volatile precursors in gas phase and gas-solid chemical reactions on a heated substrate to produce thin films. Because of thermodynamic and kinetic limitations, and also constraints depending on flow of gaseous reactants and sources, CVD processes are generally more complex than those involving PVD [62].

As another deposition technique, spray pyrolysis relies on a thermally simulated chemical reaction between clusters of liquid/vapor atoms of different chemical

species. In this technique, a solution involving soluble salts of the constituent atoms in the required thin film composition is deposited onto a heated substrate via spraying process [63]. In fact, the preparation of this solution is a combination of ions of different chemical species. The other solution phase method is CBD technique in which compound semiconductors are prepared from aqueous solutions by electrodeposition process [64-68]. CBD has a two-step formation of a solid phase from a solution as nucleation and particle growth. In the CBD procedure, the substrate is dipped in a solution that involves the desired elemental composition and then the electric current through electrolytes provides the deposition of substance in the case of electrolysis [59, 69].

In vapor deposition, the key point to understand the process carrying out under the effect of behavior of gases and vapors is the kinetic theory of gases. Kinetic picture of a gas is based on several assumptions, due to the concentration of the gas molecules in a given volume, separation between the adjacent molecules, their motions and interactions between each other [70]. This microscopic theory is related to the properties of gases from the characteristics of the individual particles as atoms or molecules. In fact, it is based on the calculation of the conductance of gas flow structures and modeling of vacuum system pumping dynamics, and as a result prediction of product of PVD sources. The starting point of the kinetic theory of gases is the energy of particles that can be obtained by the Boltzmann's distribution law and so that it can be evaluated as an entirely translational kinetic energy. Using this energy estimation, the most probable speed, the average speed and the root mean square (rms) speed of the particles can be obtained with the probability distribution of function of the particle speed. In the case of PVD, among these characteristics, the most crucial concept in the kinetic theory is impingement rate of these particles. This rate is defined as the number of collisions per unit area per second that a gas molecules/particles makes with any surface in the deposition system that it can be a chamber wall or a substrate [61]. In addition, its directional distribution is dependent on the cosine law of impingement and this rate can be found by the velocity of the evaporated particles. The directional motion of these particles is also the important effect on deposition rate and thickness uniformity. In addition to the impingement

rate, this theory assists to estimate the parameters that frequently affect the deposition kinetics and purity of a thin film, such as mean free path, heat capacity, diffusivity, viscosity and thermal conductivity. Among them, the mean free path of the particle is defined as the distance traveling by this particle before making any collision, so that this parameter is related to the probability of collision. Therefore, it is inversely proportional to the number of particles in the system, density. Moreover, since the main aim of PVD is to produce a vapor that can condense on a given substrate, this accumulation process is expressed as adsorption and condensation of the particle. Under evaluation of these parameters, the most important external effect on PVD is high vacuum condition in order to attain a desired level of purity of the film. In order to limit possible level of contamination, in addition to the deposition system cleaning, it is dependent on vapor pressure, substrate temperature, substrate surface cleaning and deposition rate.

In PVD methods, the fundamental process is thermal evaporation or namely vacuum evaporation. This step is generally used in direct deposition of the films from evaporation sources. It is also the most cost-effective deposition technique in the case of limited thin film compounds. In addition to the thin film layer fabrication for a special application, this method is the more preferred method in order to deposit ohmic or Schottky contact layer with metal and metal alloys [71]. This deposition process is basically heating and then evaporating the evaporation sources with applying high current to thermal boat. Then, under high vacuum condition, the vapor produced from the source material accumulates on the substrate surface to produce the thin film. On the other hand, heating the evaporation sources may cause some contamination effect from crucibles, heaters, system equipment [62].

The other commonly used PVD technique is the electron-beam (e-beam) technique. Different from the thermal evaporation method, in this technique, the source material in the crucible is heated by bombarding with high energetic electrons generated by heating of filament of electron gun. After emitting electrons from the filament, they are focused and directed to the source material to be heated by magnetic deflection. Then, by acceleration of electrons with various energies depending on the material

properties, the locally evaporated material produces the thin film on the substrate surface. Apart from the thermal evaporation process, since the source material is heated locally by the focused e-beam, the contamination problem is discarded and highly pure thin films can be obtained. In addition, using energetic e-beams, this technique offers to deposit the materials with high melting point, and by the help of focusing process, it also allows a good control over the growth rate and better uniformity in thickness of the deposited films [72].

In sputtering technique, surface of the target material is ejected by bombarding with high energetic atoms or ions [73]. In this case, the atoms were broken off from the material surface as a result of a momentum transfer from the bombarding particles. Basic sputtering system includes a vacuum chamber, a target (cathode) and substrate holder (anode) [72]. Sputtering in its many forms has become perhaps the physical vapor deposition process of most widespread use. The most common sputtering techniques are direct current (DC) and radio frequency (RF) sputtering. The DC sputter deposition method is mostly preferred for the deposition of conductors. It is a parallel-plate discharge system with a simply high-voltage DC power supply. The plasma is created and sustained by the DC source and argon is the most common sputtering gas, at a pressure on the order 1 Torr [59]. In this system, the sputtering target is the cathode of discharge and the anode is the substrate. Non-magnetron DC discharges are not commonly used for film deposition. On the other hand, by using RF sputtering technique, an electrically insulating target can be sputtered for the film deposition. It offers advantages over DC; for instance, lower voltages and lower sputtering gas pressures may be used, with higher deposition rates obtained. It is a capacitive, parallel-plate discharge system with a high voltage RF power supply. In RF sputtering, there are typically a small area cathode (the target) and a large area anode, in series with a blocking capacitor. The capacitor is actually part of an impedance-matching network that improves the power transfer from the RF source to the plasma discharge. Magnetron RF discharges are used much more widely than non-magnetron arrangements.

Pulsed laser deposition (PLD) [74] is a flash evaporation method. A condensable vapor is produced when a powerful laser beam strikes a target, is absorbed, and vaporizes a thin surface region. The laser pulse strikes the target, a fraction of the energy is reflected and the rest is absorbed. The target can take many forms, such as a powder, a single crystal, sintered pellets, or even a liquid. The atoms deposited on the surface per laser photon are sensitive to the surface morphology of the target. During the pulse, there is heat conduction downward from the surface into the target, to a depth of thermal diffusion length. Then, in the heated volume at the surface of the target, the solid material is raised to the melting point and then melts. If there is any energy remaining, evaporation will commence as a fraction of the atoms within the heated volume receive the heat of evaporation.

2.3 Material Properties

2.3.1 II-VI Compound Semiconductors

With the developments in the research area of thin films, II-VI compound semiconductors have usually attracted considerable interest in the technological and scientific works because of their large range of electronic energy band gaps [75]. Almost all II-VI compound semiconductors crystallize either in the zincblende or wurtzite structures [76]. In general, every single atom of each element is bonded to four atoms of the other atom tetrahedrally in this type of structures and this tetrahedral arrangement occurs in a cubic array for zinc-blende and in a hexagonal array for wurtzite structures [75]. These device properties of these materials are commonly research interests in the application of solar cells and detectors [75].

In photovoltaic applications, the Zn and Cd chalcogenides alloyed with Se, S, and Te can offer a wide range of optical and electrical properties. These compounds can be used in different layer formations with tunable characteristics of various properties, especially their energy band gap. The II-VI compounds are typically in n-type characteristic in as-grown form, except ZnTe, which is naturally in p-type behavior. The most of II-VI compound semiconductors have direct energy band gaps. They can

be emitted and/or absorbed electromagnetic radiation efficiently. Therefore, these semiconductors are widely preferred with their optical properties. In addition to the binary II-VI compounds, materials such as ternary and quaternary alloys with tunable properties are also drawn great interest [75].

CdS and ZnSe are the most popular n-type layer in solar cell applications. However, toxic risks of CdS causes environmental concerns in the large scale solar cell applications due to usage of Cd [24]. In fact, Cd metal is classified as a toxic/carcinogen [77]. Therefore, as a Cd free alternative of CdS layer, ZnSe can be used. It is a compound semiconductor of II-VI type that has a cubic zincblende (sphalerite) cubic structure and a member of space $F\bar{4}3m$ and point T_d groups with a lattice constant of 5.6692 Å and crystal density of 5.2621 g/cm^3 at room temperature [78]. As an optical properties obtained at room temperature, it has a direct band gap of about 2.8 eV [79], static and high frequency dielectric constants of 8.1±0.3 and 8.75±0.1, respectively [80], refractive index between 2.436 and 2.86 in the energy interval of 0.5 and 2.65 eV [81]. In addition, electron affinity of this structure is 4.09 eV [38] and its conductivity behavior is n-type with carrier concentration of 10^{16}–10^{17} cm^{-3} [82, 83]. However, due to the nature of the defects in the structure and high resistivity problem, there are several works about alloying this binary structure with elements in group III to obtain optimize material for photovoltaic device applications. Among these, ZIS ternary semiconductors have been researched in various fields [34, 84-86]. In literature, ZIS structure is defined as a ternary defect chalcopyrite semiconductor compound in II-III-VI group [14]. There are many research on ZIS thin films about their crystal and film characteristics; and also applications in solar cells and optoelectronic devices [12-14, 21, 24, 28-31, 34, 87]. These works demonstrated their applicability of buffer layer as a hetero-junction partner for p-type absorber layers materials. They have an n-type conductivity behavior [34] and can be used as a promising candidate for CdS structure with its environment-friendly characteristics.

2.3.2 I-III-VI Chalcopyrite Compound Semiconductors

The materials in chalcopyrite structure have been the subject of interest with their invention in 1917 [88]. This structure can be derived from the cubic zinc blende structure of II-VI materials by ordering the atoms belongs to non-symmetric space group and as a result, the c-axis is nearly doubled and the unit cell is tetragonal [89, 90]. The obtained chalcopyrite structure is also at the space group D_{2d}^{12}-$I\bar{4}2d$ [91]. As an example (Fig. 2.1), the chalcopyrite CIS structure can be obtained from the well-known disordered blende structure of ZnSe by involving the Zn sites alternatively with Cu and In atoms [92]. In this case, the principle cell of the structure is formed with bonding in I (Cu) and III (In) atom with four VI atoms (Se). In other words, there are two bonds to Cu and two to In with each Se atom. Instead of the basic ternary chalcopyrite structure, $CuFeS_2$ having a tetragonal structure with nearly equal to 2 for *c/a* ratio where *c*=525 nm and *a*=1032 nm [93], because of the difference in the strengths of the I-VI and III-VI bonds, the ratio of the lattice constant, *c/a*, is not exactly equals to 2. Thus, the quantity 2-*c/a* (which is -0.01 in CIS) is a measure of tetragonal distortion in chalcopyrite materials [94]. This deviation cause variation in degree of hybridization between anion and cation orbitals and therefore affects the characteristics of the compounds, such as the band gap properties [72]. In addition, the bonding type is primarily covalent with sp^3 hybrid bonds [95].

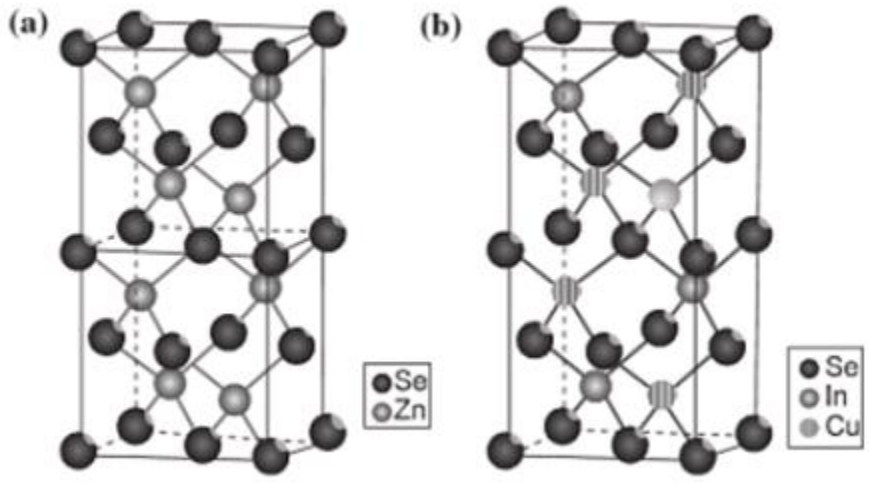

Figure 2.1: Unit cells of the binary (a) and ternary (b) chalcopyrite compounds [96]

I-III-VI_2 compound semiconductors, CIS and AIS, are of interest in various device applications. These ternary compounds have a tetragonal structure and a member of space $I\bar{4}2d$ [94] and point D_{2d}^{12} [97, 98] groups. The lattice constants were reported as a=5.814 Å and c=11.63 Å for CIS [99] and a=6.714 Å and c=10.430 Å for AIS [100]. The crystal densities of them are 5.77 [94] and 5.71 g/cm^3 [100]. As an optical properties, the absorption coefficient of these structures is about 10^4 cm^{-1} at photon energies greater than 1.4 eV [95], they have a direct band gap of about 1.04 and 1.24 eV [95], respectively. Instead of a single fundamental band gap, both of these ternary compounds show a band splitting occurring closely spaced valence bands as a result of p-d hybridization [94, 100, 101]. The spin orbit splitting energy calculated for CIS is 0.04 and for AIS it was reported as 0.12 eV [94]. In addition, the crystal-field splitting energies are 0.17 and 0.30 eV, respectively [94]. Static and high frequency dielectric constants and also refractive indices of them are 9.3 [102], 7.09 [103] and 3.0 [104] for CIS; 12.75 [100], 7.7 [103] and 2.0 [105] for AIS, respectively. In addition, electron affinity of CIS and AIS structures are 4.3 [106] and 4.15 eV [107].The CIS and AIS materials in p-type conductivity behavior have carrier concentrations of 10^{17} cm^{-3} [94].

In the I-III-VI_2 based photovoltaic devices, the larger band gaps can be obtained by Ag and Ga additions in the structure. Therefore, Ag contribution to CIS structure can increase the band gap value to be closer to the ideal value for photovoltaic applications and so that this new structure formation can increase the open circuit voltage which should lead to higher efficiencies. In fact, in thin film research area, the maximum solar cell efficiency was observed by group III isoelectronic substitution of In by Ga with producing the Cu(In,Ga)Se_2 quaternary alloy system. On the other hand, existing Cu atoms in the structure can cause shorting effect due to due to its high diffusivity characteristic [108], and it can be eliminated by Ag substitution with Cu atoms in the structure [56].

2.4 Structural Properties of Semiconductors

2.4.1 X-ray Diffraction

X-ray diffraction (XRD) method is one of the most essential tools used in the investigation of the structural properties of materials. In fact, this characterization technique is based on the phenomena that each solid material in the crystalline structure shows a unique characteristic X-ray pattern and this behavior can be used as a distinguishing property to define the structure of the material. Their penetrating ability and also interaction with materials as being absorbed, emitted, reflected or transmitted are widely used for the identification of the structure of the materials. In a view of the whole spectra, these electromagnetic radiations are defined in a wavelength region between gamma and ultraviolet rays in the electromagnetic spectrum. In addition, the corresponding energy of them is about 100 eV to 10 MeV. In the application of the XRD method, X-ray spectra is commonly chosen as being close to order of magnitude of the shortest interatomic distances in solid materials. Therefore, these regions are confined with the wavelengths range about 0.5 and 2.5 Å [109].

In the XRD systems, in order to produce X-rays, and X-ray tube having an electron source and also two metal electrodes, that are anode and cathode, is used. In this system, electrons radiated from the source are accelerated to give a sufficient kinetic energy by maintaining high voltage difference across the electrodes. Then, these electrons strike to the anode target and as a result of this collision between the electrons with high kinetic energy and the target, X-rays are produced at the point of collision and they can radiate in all directions after the collision. As a matter of fact, the X-ray radiation cannot be obtained in a single wavelength and a specific direction. It includes a mixture of various wavelengths with different intensities. The X-ray spectra obtained from the X-ray tube is illustrated in Fig. 2.2. and the curve observed in this radiation depends on the tube voltage and the characteristics of the anode target. Although, there are some characteristic peaks created in the spectra, in

general, only the *K* lines in which mostly strong sharp $K\alpha$ lines are used in the XRD system since it provides approximately monochromatic radiation.

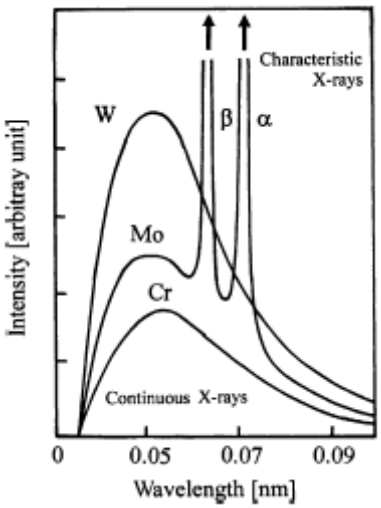

Figure 2.2: Schematic representation of X-ray spectrum [110]

After obtaining a monochromatic X-ray radiation, it directs to the sample surface and then the resultant reflected X-ray beams are evaluated in the XRD analysis. When the X-ray beams come incident on sample, it hits the atom and then this causes an oscillation in the electrons the electrons around the atom with the same frequency as the incoming beam. Although the interaction between the X-ray and the material can be resulted in destructive and constructive types of interferences, the constructive interference of the incident beam on a crystalline substance in specific orientations can generate characteristics X-ray diffraction patterns. It is related to the structure of the material if it is in crystal structure, the atoms are arranged in a regular pattern in the material that allows the beams in a constructive interference. Furthermore, the order of the periodic arrangement in the structure observed as an intensity of the leaving the sample in the same direction that reinforce mutually each other [134]. When X-rays interact with a solid material, the obtained XRD pattern is analyzed as a fingerprint about its crystalline properties. Under the information or predictions on composition of the material, XRD can be used an effective technique to determine its crystalline structure, interatomic distance and angle.

In this method the inter-planar spacing, d, of a crystal is used for the analysis procedures with the case of knowing the wavelength of the incident X-ray, λ, with its incident angle, θ, at which constructive interference occurs. The general relationship between these parameters is known as Bragg's Law, expressed as:

$$n\lambda = 2dsin\Theta \tag{2.1}$$

where an integer n is the order of reflection.

2.4.2 X-Ray Photoelectron Spectroscopy

The other area of X-ray use is X-ray photoelectron spectroscopy (XPS), named also as electron spectroscopy for chemical analysis (ESCA) which is preferred to estimate the chemical state of the compounds located in the surface or near surface of the material. Different than the XRD technique, it is based on the X-ray interaction with the sample surface for the excitation of the material and energy analyzing of emitted photoelectrons [111].

Mainly, when the X-ray with energy of $h\nu$ is incident on the surface of the solid sample, it causes emission of photoelectrons (with the kinetic energy of E_K) from the core levels (containing binding energy of E_b) of constituent atoms at the surface and near-surface region. Then, from the photo-electronic relation, $E_K=h\nu-E_b$ and by measuring E_K, the characteristic E_b of an core electron associated with specific atomic orbital (s, p, d, f, etc.) can be evaluated [112]. As a result of this identification, the characteristic XPS spectrum for the material including all the elements present in the material can be obtained. With this measurement, the concentration of the constituent elements in the near surface structure can also be determined since the intensity of the photoelectron lines is taken as the measure of this quantity. Since, generally, XPS utilizes the incident X-ray beam in the energy not exceed 1 keV, the resulted photoelectrons can be emitted from the material with a depth of 20 Å below the surface [111]. Due to the possible effect of the surrounding atomic environment on the binding energy of the electron, energy shifts can be

observed in the corresponding XPS spectra with respect to the standards. Then, it can be used to identify the chemical bonds of the electron pointed of interest constructing surrounding atoms [111]. Therefore, it is widely used to get reliable chemical and compositional analysis from the surface and near-surface region of the materials [113].

In analytical quantification of XPS spectrum for each of the constituent element, it is mainly related to the XPS peak intensity, peak shape and the peak positions. In the measurements of non-conducting materials, due to the electron ejection from the sample radiated by X-rays, the charging effect can be observed on the surface of the material. This may cause the energy shifts in the photoelectrons that changes the corresponding XPS spectra. Therefore, in order to eliminate this possible effect, the resulting XPS data are generally calibrated in terms of the known reference binding energy of photoelectron line [114].

2.4.3 Surface Analysis

The surface imaging and measuring its properties on a fine scale was developed with the specific microscopy technique that covers the basic principle of related technologies on scanning a surface with a very sharp probe [115]. This scanning probe microscopy method is primarily named according to the interaction between the tip and the sample material, as scanning tunneling microscope (STM) where it is based on the strong distance dependent interaction [116], and atomic force microscope (AFM) where it uses the interaction force existing between them [117, 118].

One of the main limitations of STM is the requirement of sample conductivity since this technique is based on the detection of the weak electrical current flowing between tip and the sample [119]. Then, AFM is one of the most essential microscopy techniques to identify the surface conditions on the various semiconducting sample. The basic principle of AFM is scanning the surface by the tip which is in close contact with the surface to obtain topographic imaging. The tip

is integrated on the edge of the cantilever having very low spring constant which allows it to deflect or bend for the forces existing while scanning the surface by the tip [120]. Both of them are usually fabricated by silicon (Si) or silicon nitride (Si_3N_4) and the tip can be shaped as being very sharp that offers high sensitivity in measurements. During the scanning process, the deflection of the cantilever is detected by the help of the laser beam focused on it. The reflection is maintained by Au coating on the cantilever and this beam is recorded by the detector and mapped by the computer controlled programs as a surface topography of the material. This system is used to magnify the bending of the cantilever and allow detecting the changes on the surface with sensitivity in the order of Å-level.

Moreover, there are three modes of measurement based on force affecting on the tip and therefore, imaging type, that are contact, non-contact and trapping modes [113]. In contact mode, the force on the tip is less than the surface and therefore it experiences repulsive Van der Waals force from the surface. This mode provides fast scanning whereas interaction with tip, soft samples can be deformed. For the trapping mode, the imaging process is again in contact with the surface; however this mode provides oscillation of the cantilever at its resonant frequency. With this mode, AFM measurements allow high resolution on the easily damaged surfaces with slower scan speeds comparing to the contact mode. In the other mode, non-contact mode, tip is very close to the surface but moves without touching it. The interaction force in this case is attractive Van der Waals force and the tip oscillates above the surface during the scanning under the effect of this force.

On the other hand, scanning electron microscopy (SEM) is an imaging tool based on scanning the surface of the material by an electron beam. This technique permits the observation and determination of the surface characteristics of a very wide range of materials on a nanometer to micrometer scale [121]. In fact, it is a type of microscope that uses electrons instead of light beam to form an image and to examine objects on a very fine scale. The key components of the SEM system are; electron gun that is the source of the electron beam; electron lenses used to focus and control the produced electron beam; sample chamber where the materials is placed

and also it provides the interaction between electron beam and sample, and resulted signals and the detectors; various detectors for detecting specific signals coming from the material, and monitoring system to display the image analyzed from the detectors.

The main applications of the SEM are topography and morphology of the surface features, composition analysis with determining the relative amount of the constituent elements in the material, and also crystallographic information that presents how the atoms are arranged in the material. It provides better resolution and depth of field than light microscopes, high resolution of bulk materials with simple sample preparation, and also three dimensional appearance of the materials image as a result of the large depth of field [122].

When the electron beam hits the material, the collision results in various interactions between the electrons and the material. Since the accelerating voltage that gives the kinetic energy to the electrons is applied under the research of interest, the penetration depth of incident electrons can be controlled to get the specific signals and so that specific information from the material. In general, these signals are secondary electrons for SEM images, backscattered electrons and characteristic X-rays for compositional analysis, diffracted backscattered electrons to determine crystal structures and orientations of minerals) [111].

2.4.4 Compositional Analysis

The most common technique in the compositional analysis of the materials is energy dispersive spectroscopy (EDS). This system is operated with the SEM, and use the X-ray spectrum emitted from the material during the bombardment of the material with the energetic electrons. The analysis of the constituent elements is done by the sensitive X-ray detector integrated in EDS system. Commonly, Si (Li) and Si drift detectors are used to resolve the X-rays having different energy coming from different element. Energy resolution is defined as the full width of the peak at half maximum height. The qualitative analysis involves the identification of the peak

energy that gives qualitative information about the constituent elements, and in the quantitative analysis, peak intensity of each element is measured to get information about the element composition relative to each other in the material. However, the limitations of this technique are based on the resolution of the crystal in the detector where Si (Li) crystal can distinguish the X-rays in about 132 eV differences [123].

2.4.5 Raman Analysis

Raman scattering spectroscopy is widely used in structural analysis of the materials for the investigation on chemical structures and physical forms, and identification of the materials from their characteristic spectral patterns. It is based on irradiating the material with a single frequency of radiation, in other words monochromatic light is usually produced by a laser source, and detecting the scattered radiation from the material [124]. The scattered light can be in the same frequency as the incident light, called as Rayleigh scattering. On the other hand, Raman scattering is resulted in an inelastic scattering which means that the frequency of the coming photons changes due to the interaction between incident light and the material. As a matter of fact, incident radiation is absorbed by the material and then reemitted. The change in the frequency of the re-emitted photons is either in shifting up or down with respect to the frequency of the incident photons. These are defined as Stokes and anti-Stokes frequency lines, respectively, characterized by the effect of the vibrational frequency of a molecule in the material [125].

2.5 Optical Properties of Semiconductors

Optical characterization techniques are based on non-contact and non-destructive measurements with minimal sample preparation. In addition, many optical measurement devices are commercially available and automated and/or computer controlled. The main and simple instrument for optical measurements for thin film characterization is UV/Vis/IR spectrometer with a high sensitivity. It provides absorption, reflectance and absorption spectra over a certain wavelength region in order to investigate the optical properties of solid films.

When a beam of light is incident on a thin film, the character of the reflected and transmitted lights by the film differs from that for the uncoated reference substrate. Measurement of certain quantities which characterize the refracted and transmitted beams yield values of optical parameters. In general, a beam of light coming on a semiconducting material can propagate in the incident direction, can be absorbed into the material or reflects from the surface in the same or a different from the incident direction which result in transmission, absorption, reflection or scattering processes, respectively.

2.5.1 Transmission

During transmission measurements, light is incident on the sample and transmitted light is measured as a function of wavelength under the effect of nature of the sample, such as sample thickness, refractive index, extinction coefficient and absorption characteristics. Therefore, the analysis of optical spectra is one of the most useful tools for investigating the electronic structure of the semiconductors. The basic definition of the transmittance of the sample is the ratio between incident and transmitted light intensities [113].

Transmittance of a sample under a light incident normally on the surface, with the possible light interactions on the surface and into the sample, can be expressed as,

$$T = \frac{(1-R)^2 e^{-\alpha d}}{1 + R^2 e^{-2\alpha d} - 2Re^{-\alpha d} cos\varphi} \tag{2.2}$$

where the cosine term is used to take into consideration of spatial frequency discrimination and detection characteristics of the measurements as,

$$\varphi = \frac{4\pi n d}{\lambda} \tag{2.3}$$

and *R* is the reflectance of the sample as,

$$R = \frac{(n_0 - n_s)^2 + k^2}{(n_0 + n_s)^2 + k^2} \tag{2.4}$$

with refractive indices of the substrate, n_0, and the sample, n_s, and extinction coefficient of the sample, k. In this relation, the absorption coefficient is related to the extinction coefficient as,

$$\alpha = \frac{4\pi k}{\lambda} \tag{2.5}$$

Since, semiconductor materials are generally assumed to be transparent for photon energies less than the band gap energy, the transmittance of them becomes,

$$T = \frac{(1 - R)^2}{1 + R^2 - 2R cos\emptyset} \tag{2.6}$$

In general, the variation of transmittance line oscillations are neglected because of the resolution of the measurements, then the transmittance values for the pure semiconductors can be written as,

$$T = \frac{1 - R}{1 + R} \tag{2.7}$$

However, with possible impurities, in the real case, this expression is used in the following form,

$$T = \frac{(1 - R)^2 e^{-\alpha d}}{1 + R^2 e^{-2\alpha d}} \tag{2.8}$$

Then, absorption coefficient of the sample can be obtained from the transmission and reflection measurements as,

$$\alpha = -\frac{1}{d}\left(\frac{\sqrt{(1-R)^4 + 4T^2R^2} - (1-R)^2}{2TR^2}\right) \tag{2.9}$$

In the simplest case where reflection or interference effect is neglected, the Beer-Lambert law [126] gives a description to the fundamental absorption which is the band to band transition, the electron excitation from the valence band to the conduction band. Then, the expression given in Eq. 2.9 can be used as,

$$\alpha = \frac{1}{d}\ln(T) \tag{2.10}$$

where transmittance of the sample is simply calculated from the ratio between the transmitted light intensity detected from the sample and reference substrate as $T=I(\lambda)/I_0(\lambda)$.

There are two types of absorption processes in the band-to-band transition between the conduction and valence bands that are classified as direct and indirect absorption process, or namely optical transitions. In a direct absorption process, a photon is absorbed by the material with the creation of an electron and a hole, and an electron is photo-excited from the maximum of valence band to minimum of conduction band at the same value of momentum vector $\vec{k}$, ($k=0$). For direct transitions between parabolic valence and conduction bands, the absorption coefficient is,

$$\alpha h\nu = A(h\nu - E_g)^{1/2} \tag{2.11}$$

where A is a constant depending on the effective mass of electrons and holes in the sample [127], and E_g is the energy band gap of the sample. However, in indirect band gap semiconductors, the maximum energy of the valence band occurs at a different value of $\vec{k}$ to the minimum in the conduction band energy. During this process, electron phonon scattering required for momentum conservation. For indirect transitions, quadratic dependence on the photon energy is observed and it is evaluated in the following form,

$$\alpha h\nu = B(h\nu - E_g)^2 \tag{2.12}$$

where *B* is a constant depending on the structure of the material.

In addition to the band-to-band transition, a semiconducting material may exhibit impurity effects in the absorption spectrum. These effects can be due to the structural disorders [128]. In a wide variety of materials having disorder of several origins, the absorption coefficient may show an exponential tail called as Urbach tail near the fundamental absorption edge denoted as Urbach region. This simple exponential energy dependence can be written in the form,

$$\alpha \sim e^{E/E_U} \tag{2.13}$$

where E_U is the width of the tail related to absorption with additional broadening expected from any potential fluctuations arising from charged defect states and lattice vibrations [81, 129]. In general, the tail is resulted from the disorder in the material that corresponds to a tail in the valence and conduction bands. Then, the absorption coefficient dependence on the photon energy is determined by,

$$\alpha = \frac{\alpha_0 (h\nu - E_g)^2}{E_U} \tag{2.14}$$

where α_0 is the characteristic parameter of the material. In this relation, E_U can be investigated as an inverse logarithmic slope of absorption coefficient.

2.6 Electrical Properties of Semiconductors

The analysis of electrical properties expresses some of the theoretical concepts and formulas that are appropriate to investigate the electrical conduction process in polycrystalline materials. The simplest evaluation on the lateral and also vertical electronic characteristics on a material is measuring its resistivity. For the

semiconducting materials, the resistivity is expected to be in between 10^{9} and 10^{-3} Ω.cm whereas insulators have resistivity values above 10^{9} Ω.cm and doped semiconductors and metals with resistivity below 10^{-3} Ω.cm [130]. As a matter of fact, it is depend on the measurements technique whether it is due to the surface or bulk of the material. In the ideal case, the distinction in the resistivity value between semiconductors and the other materials, metals and insulators, is mainly based on concept of the fundamental band gap. In other words, the wide range of resistivity of crystalline solids can be explained using electronic band theory. Semiconductors are assumed to have band gaps between 0 and 4 eV, whereas it is higher than 4 eV for insulators and below 0 eV for metals.

Although, ideally the current flow process in a semiconducting material involves the sum of the contributions from all charge carriers, holes and electrons, in the real case, conductivity of the semiconductors is strongly dependent on both the ambient temperature and the purity of the semiconductor [131]. In fact, the concepts in the band theory are derived for the single crystal materials in order to describe conduction and valence energy bands in a semiconductor material. However, there exist several effects on conduction theories of the carrier transport in semiconductors due to the limited degree of electronic conduction that is between metallic conduction and insulating behavior, band gap characteristics and number of carriers depends on temperature and impurity level in the structure. Whereas a band conduction model predicts an Arrhenius temperature dependence of the conductivity where this equation is commonly given in the form of exponential function, the deviating temperature dependence and disordered/impurity atoms in the structure observed in most of the experimental data clearly reveals the existence of the different carrier transport mechanisms. As a result, even the same material is considered, the conductivity values of the single crystal and polycrystalline form of this material may completely differ from each other in terms of the conductivity values. The behavior of the transport parameters in the polycrystalline material is complicated, compared to that of the single crystal; thus, the interpretation of the experimental data can be done with taking into account all factors that differ the structure from the ideal case [132].

Basically, a single crystal material is assumed to consist of a single grain without any grain boundary in the structure. On the other hand, a polycrystalline material can be composed of small crystallites randomly connected by grain boundaries. In fact, it is formed with aggregation of small single crystals, namely crystallites or grains, having sizes in the order between nm to μm. Since they are contact each other and they can have different sizes, the contact points, namely grain boundaries, are assumed to be misaligned with respect to each other [100]. Inside each crystallite, the atoms are arranged in a periodic manner and therefore it can be considered as a small single crystal. Between these crystals, the grain boundary is a complex structure, usually consisting of a few atomic layers of atoms in different orientations. The grain boundaries are formed by impurity segregation at these regions and atoms positioned in these boundary regions are points of transitions between the different orientations of neighboring crystallites [133]. The alignment in the contact points between of the adjoining crystallites is often took place with a high deviation in terms of their orientations. Because of these misaligned crystallites and their grain boundary regions with high densities of dislocation defects, the polycrystalline materials can show higher resistances than the single crystal forms [134]. The resistance of polycrystalline material is generated by the contributions of the grain boundary region and the bulk of the material. If the conduction in the material is much higher than that through the grain boundary, using only the resistance effect of the grain boundary region can be a good assumption in the electrical analysis.

The polycrystalline structure can be occurred depending on the material characteristics, crystal growth and film deposition techniques, the conditions in the fabrication of these materials. The characteristic of the polycrystalline semiconductors with small single crystal regions and their grain boundaries are the main factor on the carrier conduction in the whole material. In other words, the difference in the carrier transport between the single crystal and polycrystalline materials are related to boundary effects on the flow direction, change in the carrier density and decrease in mobility of the carriers when the carriers come across the grains in different orientations. In these regions, there are high densities of states due to the defect and/or impurity atoms, which can trap the carriers. These interface

regions can cause a bending in energy bands within the grains [134, 135]. As a result of this, carrier conduction in polycrystalline materials occur under the effect of grain boundaries of the grains whereas since the grains are formed in periodic array of atoms, the grains themselves cannot be considered as a strong effect on the electronic transport processes [136].

The electrical conduction processes in polycrystalline semiconductor structure can be explained by several theoretical models proposed by considering the band-bending and potential barrier formation under the effects of defects in the grain boundary regions. In general, there are several types of conduction mechanisms, which are dominant in different temperature regions and also adapted for the experimental results. In fact, there is always a possibility on the contributions of the different transport mechanisms, even if they are not observed in the dominant current flow behavior.

2.6.1 Thermionic Emission

The basic model in the conduction process is thermionic emission of energetic carriers over the top of a potential barrier of the grain boundaries. In general, in the high temperature regions, the carriers can gain enough energy to surmount the potential barrier at the grain boundaries and therefore, it is most dominant process in this region above the room temperature [137]. The first concept in this model was proposed by Petritz [137] based on the thermionic emission of carriers from grain to grain. In addition, the generalized model consistent with both theoretical and experimental results was developed by Seto [133]. In the analytical discussion of this model, grains are assumed to be identical with the size of L in cm. It is also assumed that there is only one type of impurity atoms that are totally ionized and that are uniformly distributed with a volume concentration $N\ (cm^{-3})$ concentration exist in the structure. Furthermore, the thickness of the grain boundary can be neglected when compared to the size of the grains and there are $N_t\ (cm^{-3})$ of traps having energy E_t with respect to the Fermi energy E_F located at the boundary of the grains. Another assumption to simplify these models is the trap neutrality in the initial case and then

charging by trapping free charge carriers in the distance of *l* from the each side of the grains [133]. Therefore, the mobile carriers are assumed to be trapped in a region of *(L/2-l)* cm from the grain boundary where the spatial dependence of the potential can be written by the one dimensional Poisson's equation as

$$V(x) = \left(\frac{qN}{2\varepsilon}\right)(x-l)^2 - V_{C0} \tag{2.15}$$

where ε is the dielectric permittivity of the polycrystalline material and V_{CO} is the potential of the conduction band edge of the center of grain [138]. For a given *L* and the trap densities relative to the doping concentration *N*, the dependence of potential barrier height on doping concentration can be evaluated in terms of two possible conditions as, the grain is completely depleted of carriers and the traps are partially filled, $NL<N_t$ and only part of the grain is depleted of carriers, $NL>N_t$ [137]. Under the first case where *l=0*, the potential barrier height, V_B between the region of *L/2*, is

$$V_B = \frac{qL^2N}{8\varepsilon} \tag{2.16}$$

and for the second case where *l>0*, it becomes

$$V_B = \frac{qN_t^2}{8N\varepsilon} \tag{2.17}$$

Then, the average carrier concentration n_a for the grain region can be defined by the spatial dependence of the mobile carrier concentration relation,

$$n_a(x) = N_t exp[(-qV(x) - E_F)/kT] \tag{2.18}$$

where k is the Boltzmann constant.

Then, in the depletion region defined as the region between the boundaries of the crystallite, it can be calculated, for $NL<N_t$ case as,

$$n_a = \frac{n_i}{Lq}\left(\frac{2\pi\varepsilon kT}{N}\right)^{1/2} exp\left(\frac{E_B + E_F}{kT}\right) erf\left(\frac{qL}{2}\left(\frac{N}{2kT\varepsilon}\right)^{1/2}\right) \tag{2.19}$$

and for $NL>N_t$ and case as,

$$n_a = n_b\left[\left(1 - \frac{N_t}{NL}\right) + \frac{1}{qL}\left(\frac{2\pi\varepsilon kT}{N}\right)^{1/2} erf\left(\frac{qN_t}{2}\left(\frac{1}{2}\varepsilon kTN\right)^{1/2}\right)\right] \tag{2.20}$$

where $E_B=qV_B$ is the potential barrier energy, n_i is the intrinsic concentration of single crystallite and n_b is the carrier concentration of the undoped region [133].

When taking the dominant mechanism in the carrier conduction process as thermionic emission in the polycrystalline structure and neglecting the other contributions by the different mechanisms, the relation between the thermionic emission current density at the grain boundary, J_{th}, and an applied voltage V_a across a grain boundary can be defined as,

$$J_{th} = qn_a\left(\frac{kT}{2m^*\pi}\right)^{1/2} exp\left(\frac{-qV_B}{kT}\right)\left[exp\left(\frac{qV_A}{kT}\right) - 1\right] \tag{2.21}$$

where m^* is the effective mass of the carrier. In addition, for a small applied bias, $qV_A<<kT$, it becomes,

$$J_{th} = q^2 n_a\left(\frac{1}{2m^*\pi kT}\right)^{1/2} exp\left(\frac{-qV_B}{kT}\right)V_A \tag{2.22}$$

which is a linear current voltage relationship. Thus, the conductivity of a polycrystalline film [137] is,

$$\sigma_{th} = \sigma_0 exp\left(\frac{-qV_B}{kT}\right) \tag{2.23}$$

where σ_0 is the pre-exponential factor,

$$\sigma_0 = Lq^2 n_a (2m^* \pi kT)^{-1/2} \tag{2.24}$$

Then, the thermally activated effective mobility at the grain boundary can be expressed as

$$\mu_{eff} = \mu_0 exp\left(\frac{-qV_B}{kT}\right) \tag{2.25}$$

where μ_0 is the pre-exponential factor,

$$\mu_0 = Lq(2m^* \pi kT)^{-\frac{1}{2}} \tag{2.26}$$

By inserting the expressions derived for the average concentration n_a, for the two possible doping concentration cases, the corresponding conductivity relations are found as [133], for $NL<N_t$,

$$\sigma_{th} \propto epc\left(-\left(\frac{1}{2}E_g - E_F\right)/kT\right) \tag{2.27}$$

and for $NL>N_t$,

$$\sigma_{th} \propto T^{-1/2} exp\left(-{}^{E_B}/_{kT}\right) \tag{2.28}$$

The expression given in Eq. 2.28 is the well-known Petritz relation [139] where high activation energy of the conductivity is discussed in the Arrhenius behavior of conductivity.

As a result, when the temperature dependence of this conductivity is evaluated with using $ln(\sigma_{th})$ vs $1/kT$ plot, it gives a slope of $E_B/2$- E_F for $NL<N_t$ and E_B for $NL>N_t$. Moreover, this interpretation is not in a good agreement with highly doped materials, where $E_B<<kT$ [133].

2.6.2 Tunneling

Thermionic emission model generally explains electronic carrier transport in polycrystalline semiconductors at high temperatures and the Petritz model is based on the Arrhenius behavior in temperature dependence of the electrical conductivity [140]. On the other hand, in most of the experimental works on the various polycrystalline semiconductors, deviation from the straight lines in the Arrhenius plots has been observed and this occurs mostly with the saturation tendency appearing at low temperature region [141]. Therefore, in order to investigate the electrical conductivity behaviors of these materials at these temperatures, tunneling across the potential barriers and hopping mechanism in the forbidden band have been taken into consideration.

In fact, the crystalline structure of the material does not affect the impurity surrounding, that is, in all cases, the impurity atoms are distributed randomly. Therefore, impurity based conduction process can be expressed as an example of the movement of an electron in a non-periodic field of force. In semiconductors, impurity-conduction movement of an electron takes place directly by tunneling from one impurity atom or point effect to another [142]. Quantum mechanical tunneling of carriers through high, but narrow potential barriers at grain boundaries may become applicable on the mechanisms limiting the resistivity of polycrystalline thin films. It may be pre-dominant at low temperatures when the carriers do not have enough energy to surmount the potential barrier. Tunneling in the conduction process was developed firstly in polycrystalline Si [143] and then, the tunneling mechanism through the grain boundary was offered in addition to the grain boundary trapping model [144, 145]. According to this mechanism, the tunneling density J_{tu} was expressed by WKB (Wentzel-Kramers-Brillouin) approximation as [146],

$$J_{tu} = J_0 \left(\frac{FT}{\sin(FT)} \right) \tag{2.29}$$

where J_0 is the tunneling current density at 0 K, T is the transmission coefficient for tunneling through a barrier, or in other words, the probability that an electron with an energy E can penetrate a potential barrier of height V_0, given by an approximate expression as [131, 146],

$$T \sim exp\left[-\frac{4\pi}{h}\int_0^d \left(2m(V_0 - E)\right)^{1/2} dx\right] \tag{2.30}$$

where (V_0-E), is the effective barrier height, and d is the barrier width, and

$$F = \frac{2\pi^2 (2m^*)^{1/2} kd}{b\bar{\Phi}^{1/2}} \tag{2.31}$$

where $\bar{\Phi}$ is the mean barrier height of the grain boundary potential. Therefore, the conductivity associated with the tunneling current can be written as

$$\sigma_{tu} = LJ_{tu}/V \tag{2.32}$$

which can be evaluated in the similar expression with J_{tu} as

$$\sigma_{tu} = \sigma_0 \frac{FT}{\sin(FT)} \tag{2.33}$$

where σ_0 is the limit of conductivity at 0 K given by

$$\sigma_0 = LJ_0/V \tag{2.34}$$

If FT is sufficiently small, then the equation can be re-written in terms of first two terms in mathematical approximation as

$$\sigma_{tu} = \sigma_0 \left(1 + \left(\frac{F^2}{6}\right) T^2\right) \tag{2.35}$$

2.6.3 Hopping

In addition to these mechanisms discussed above, below the room temperature, weaker temperature dependence can be taken into consideration as an indication of a different conductivity-limiting mechanism. In fact, at lower temperatures, the carriers having low energy can hop between the localized states and conduct the current as a dominant contribution to the charge transport [142]. Whether a material involves impurities is in amorphous or crystalline structure, the impurity atoms that cause disordered arrangements of the atoms, affects the conduction process in the material. When the impurity density is sufficiently low, the impurity states will represent widely spaced atomic like states and can be treated in a tight binding approximation, are not conducting. In general, in the amorphous semiconductor structures, there are sufficiently large defect densities. Thus, they provide the conduction assisted with direct motion between defect states that dominates the transport over significant temperature ranges below room temperature [128]. This can be evaluated as being similar to impurity conduction in polycrystalline semiconductors within the higher impurity concentrations since trap states at the grain boundaries act as localized states [142]. Moreover, there are two types of hopping mechanism that is possible to be observed in the semiconductor materials; variable range hopping (VRH) in which the hopping of the carriers to another empty state away from the nearest one, and the constant range hopping in which the carriers hop to nearest states so that range is constant.

The conduction may arise from hopping between localized states within the grain boundaries as a temperature dependence behavior of the conductivity. At low temperatures, the impurity conduction with the hopping process was established by Conwell [147] and by Mott [148], and the same transportation mechanism was independently developed by Pines [149] with relating to the study of electron relaxation processes in Si. Following the conduction due to electrons with energies near the Fermi energy developed by Mott [142, 150], the probability for an electron can hop between the two localized states with considering a highly disordered semiconductor containing an density of localized states in the order of $10^{18} – 10^{20}$

cm^{-3} [151] depends on the energy difference between the initial and final states, W, expressed as the Boltzmann factor, $exp(-W/kT)$; a factor, υ_{ph}, depending on the phonon spectrum which is taken as in the range of 10^{12} – 10^{13} s^{-1} [152] when approximated to the maximum phonon frequency, w_{max} if $W/\hbar$ is larger than w_{max}; and also a factor depending on the overlap of the wave functions in which it is in the order of unity if there is a considerable overlap of the wave function and it is related to impurity conduction if the overlap is small due to the strong localization with the approximation of being $exp(-2\alpha R)$ where α is the coefficient of exponential decay of the localized states involved in the hopping process, and R is the hopping distance between these two localized states [142].

According the model introduced by Mott [153], hopping conduction can be resulted from states whose energies are concentrated in a narrow band near the Fermi level at low temperatures. By this model, charge carriers cannot pass over the grain boundary potential barrier because of insufficient thermal activation energy; hopping can take place between the localized states near the Fermi level [142, 154]. When only electrons with energy within a range of order kT at the Fermi energy hops between the pairs of localized states, the conductivity can be expressed as,

$$\sigma \cong \left(\frac{e^2}{kT}\right) D \tag{2.36}$$

where D is the diffusion coefficient

$$D = pR^2 N(E_F) kT \tag{2.37}$$

and p is the transition probability,

$$p = \upsilon_{ph} e^{-2\alpha R - W/kT} \tag{2.38}$$

with the number of such electrons, $N(E_F)/kT$ and the distance between each hopping process, R. In addition, the mean activation energy for this hopping process, W, is

inversely proportional to the density of states. For a strong localization, the hopping is only taken place to the nearest neighbor state which indicates

$$W \sim 1/R^3 N(E) \tag{2.39}$$

and for a weak localization where the hopping distance is greater than the distance R and so that the value of localization length, α', gives

$$W \sim \alpha'^3 / N(E) \tag{2.40}$$

In the case of weak localization, since there is a wide choice of states that an electron can hop, the transition probability should be multiplied by a factor $\alpha'^3 R^3$ which is greater than 1. If E_F lies at an interval of ΔE from E_C, α' can be hypothesized as

$$\alpha' \sim \sqrt{((2m\Delta E)/\hbar^2)} \tag{2.41}$$

and therefore,

$$W \sim \left(\frac{2m\Delta E}{\hbar^2}\right)^{\frac{3}{2}} / N(E) \tag{2.42}$$

At low temperatures W cannot remain constant. It is constant if the factor $exp(-2\alpha' R)$ is sufficiently small to ensure that an electron always jump to the nearest state. At low temperatures, the electron can have a higher probability of jumping to a more distant state, because with more states from which to choose the energy difference can be smaller. In other words, in all cases at sufficiently low temperatures, the VRH takes place with the temperature dependent hopping distance which increases with decreasing temperature [138]. At distances less than R from a given atom, the number of states with energies between W and ΔW is given by

$$\left(\frac{4\pi}{3}\right) R^3 N(W) dW \tag{2.43}$$

If R is large, the average spacing ΔW between the energies of the localized energy near the Fermi energy is given by

$$\Delta W = \frac{3}{4\pi R^3 N(E_F)} \tag{2.44}$$

and the hopping probability per unit time is given by

$$v_{ph} = \exp\left(-2\alpha R - \frac{\Delta W}{kT}\right) \tag{2.45}$$

The most probable jumps come from a value of R such that

$$2\alpha = \frac{9}{4\pi R^4 N(E_F) kT} \tag{2.46}$$

which gives a jump frequency of the form

$$v_{ph} = \exp\left(-\frac{B}{T^{1/4}}\right) \tag{2.47}$$

with $B \cong 2.1(\alpha^3/kN(E_F))^{1/4}$. Then, the temperature dependence of the conductivity in the Mott VRH model exhibits the $T^{1/4}$ behavior.

Although, Mott's model for the conductivity is based on the assumption that the density of states near the Fermi level is constant, in actual case, electron-electron Coulomb interaction was proposed by Pollak [155] and Ambegaokar [151]. Coulomb effect was pointed out as an important in the conduction mechanism at low temperatures where it reduces the density of states near the Fermi level. Then, by analogy by Mott law [148], in Efros-Shklovskii VRH model, Coulomb effect serves as a barrier to the conduction process, and the conductivity values can be expressed as $T^{1/2}$ behavior [156, 157].

2.6.4 Hall Effect

In a semiconductor structure, the characteristics of the charge carriers are the main point of interest to analyze the electrical conduction. Although the electrical conduction is assumed to be maintained by the continuing carrier motion in an ideal case without the requirement of external electric field, in a real case, without external field effect, a current density decays exponentially depending on the various collision or scattering processes. Therefore, in describing the typical conduction behavior of the semiconductors, type of charge carriers, concentration of these free carriers and velocity of them are the important concepts. Moreover, in these analyses, instead of dealing with the random motion of the carriers in the structure, as an average drift velocity of them under an electric field, the mobility concept is taken into the consideration.

Related with the electrical conductivity researches, these concepts were evaluated by Hall [158] while working on the features of the force effective on a conductor carrying a current in a magnetic field region. In this work, the direction of the electric field was found in the direction perpendicular both to the direction of the current flow and the magnetic field where the magnetic field is at right angles to the direction of the current flow. In this argument, the current is expressed as a directional motion of the charge carriers. Therefore, if the current is assumed to flow in the positive x-direction, in the case of electrons, the direction of the drift velocity $\vec{v}$ of them will be in the negative x-direction where it will be in the same direction for the holes. With this approach, when there is an external magnetic field affecting on these carriers, they will experience the Lorentz force formulated as $(\vec{v} \times \vec{B})q$ where q is the magnitude of the electronic charge. In other words, they will be deflected in a direction perpendicular to the plane of $\vec{B}$ and $\vec{v}$ and also depends on their charge type. On the other hand, considering a material case instead of the free space, the bounds of the material will be effective on the motion of the charge carriers. Therefore, there will be an electric field generated by these carries that can compensate the Lorentz force, so that a few carriers will be deflected under the effect of $\vec{B}$. Moreover, this field effect will allow the current to continue flowing in a given

direction. In fact, semiconducting material has both electrons and holes as a charge carriers whether being a majority or minority in the structure. So that, depending on their type, they can accumulate on the directions with lower and higher magnetic field.

In the equilibrium condition, the Hall force generated by this accumulation process completely cancels the Lorentz force as,

$$\left(\vec{v} \times \vec{B}\right)q = q\vec{E} \tag{2.48}$$

Then, if the direction of the current flow is assumed to be in the *x*-direction and the magnetic field affects in the *z*-direction, then the Hall field can be re-written as,

$$E_y = -\frac{1}{nq} B_z J_x \tag{2.49}$$

where $\vec{J}$ is the current density generated by the drift velocity $\vec{v}$,

$$\vec{J} = nq\vec{v} \tag{2.50}$$

In addition, the relation between the E_y and $B_z J_x$ is called as Hall coefficient as

$$R_H = -\frac{1}{nq} \tag{2.51}$$

in which it is evaluated as inversely proportional to the concentration of the conduction carriers. In fact, this coefficient is used to determine the type of the semiconductor material whether it is in n-type or p-type conduction behavior with having negative or positive sign, respectively.

In order to express the mobility of the carriers, the electrical conductivity can be defined as with the validity of the Ohm's law as,

$$J_x = \sigma E_x \tag{2.52}$$

and therefore, from Eq. 2.48 it can be related to the drift velocity as,

$$\sigma = nq\, {}^{v_x}/_{E_x} \tag{2.53}$$

Since mobility μ is defined as the carrier drift velocity per unit electric field, then σ can be re-written in terms of this quantity as,

$$\sigma = nq\mu \tag{2.54}$$

When considering the interpretation of the Hall coefficient in Eq. 2.50, this conductivity relation can be expressed as Hall conductivity as [182],

$$\mu_H = \sigma |R_H| \tag{2.55}$$

where μ_H can be considered as a positive quantity regardless of the sign of R_H.

2.7 Photo-conductivity of Semiconductors

Photo-conductivity is a response of the semiconductor material defined as a change in the bulk conductivity of the material under illumination where the energy of the photons incident on the material is greater than the energy band gap and so that the absorption process can cause photo-generated electron-hole pairs [111]. Since it is defined as the variation in the number of charge carriers, this process is considered under the concept of creation of the free carriers by optical absorption, contribution of these carriers to the electrical conductivity, electrical transport mechanisms of them, and also, at last, the recombination or trapping process of the carriers [126].

In the photo-conductivity measurements, an external bias voltage is applied across the contacts of the semiconducting material, and resulting current is measured under dark and illuminated cases. In fact, it is expected that above the absolute zero, there

are some free charge carriers in the conduction and valence bands of the semiconductor. Then, during the dark condition, the conductivity of the semiconductor is expressed by the contribution of both electrons and holes as in the form,

$$\sigma_{dark} = qn_{dark}\mu_e + qp_{dark}\mu_p \tag{2.56}$$

where n_{dark} and p_{dark} are the concentration of the free electrons and holes in the bulk of the material, and also μ_e and μ_p are the mobility of these carriers without any radiance effect, respectively. Then, when the material is illuminated with the photons whose energy exceeds its band gap energy, the conductivity of the material measured in the dark case changes with the generation of electron-hole pairs. In general, the conductivity increases with the photo-generated carriers [159, 160] and the resulted conductivity can be expressed as

$$\sigma_{light} = \sigma_{dark} + \Delta\sigma \tag{2.57}$$

where $\Delta\sigma$ is the photo-conductivity contribution to the intrinsic conductivity of the sample,

$$\Delta\sigma = q(\Delta n\mu_e + \Delta p\mu_p) \tag{2.58}$$

with Δn and Δp that describe densities of the generated electrons and holes with the illumination effect, respectively. For the homogeneous material with the assumption of having one-type charge carrier, the conductivity with the photo-excited carriers is given by

$$\sigma_{light} = \mathrm{q}(\mathrm{n} + \Delta\mathrm{n})(\mu + \Delta\mu) \tag{2.59}$$

where Δn and $\Delta\mu$ express the corresponding change concentration and mobility of the material respectively. Therefore, the photo-conductivity effect can be stated as

$$\Delta\sigma = q\Delta n\mu + q(n + \Delta n)\Delta\mu \quad (2.60)$$

When only small changes from the steady state is considered, the change in the carrier concentration, can be considered as being directly related to generation (recombination) rate, or namely the rate of excitation, G, that defines the number of excess electron in unit volume in unit time interval, and lifetime of the charge carriers, τ_n, as in form $\Delta n = G\tau_n$ [126, 161], and therefore the relation in Eq. 2.60 can be re-written as

$$\Delta\sigma = qG\tau_n\mu + qn\Delta\mu \quad (2.61)$$

In this relation, the illumination effect on the conduction of the material can reveal different behaviors under different G-dependence [139]. If the lifetime is not affected by the generation rate, the change in the conductivity can be expressed as,

$$\Delta\sigma = qG\tau_n\mu \quad (2.62)$$

On the other hand, the main approximation on the lifetime τ_n is that it is a function of G, and if this proportionality between the carrier concentration and the generation rate is linear, then the photo-conductivity contribution can be expressed as

$$\Delta\sigma = qG\tau_n(G)\mu_{dark} \quad (2.63)$$

In this specific case, the change in the conductivity is related to order of G, which is greater than one. In addition, when there is a $G^{(\gamma-1)}$ dependence in τ_n, $\Delta\sigma$ varies as G^{γ} with γ where is an integer. In this relation, the value of γ is used to determine the type of model (one-center and two-center models) describing the photo-conductivity process.

There are various models in the evaluation of the change in the carrier lifetime with the rate of excitation, and in addition with the temperature and thermal-equilibrium Fermi-level position. However, it is usually modeled under specific assumptions

[162]. In these two simplest models, the carriers capture is explained by assuming there is a single type of recombination center in one-center phenomena, or two recombination centers with different capture coefficients are considered in the two-center phenomena [126].

2.8 Device Analysis

2.8.1 Heterojunctions

At first, heterojunction concept can be evaluated into two concepts; they are isotype and anisotype heterojunctions. As in the case of isotype heterojunction, the junction is constructed by using two different semiconductors which have the same type of conductivity. On the other hand, if the junction is formed between two different semiconductors with different conductivity types, it is named as anisotype hetero-junctions.

The ideal hetero-junction behavior can be reached only with the two semiconductors having the same lattice constant [131]. If the difference in lattice constants is higher than 10%, there are major mechanical effects observed at the junction interface. Additionally, dislocations and localized interface states can be produced. By changing the ideal behavior, these defects can be dominated the current flow mechanisms in the junction.

The band diagram of a hetero-junction can be constructed by using the abrupt-band model proposed by R.L. Anderson. In this model, the effects of interface states are neglected and the diagram is constructed by considering only of the electron affinity, work function and band gap of the two constituent semiconductor materials. The study on the anisotype semiconductor heterojunctions is analyzed under the abrupt junction approximation where the impurity concentration in a semiconductor varies abruptly from acceptor impurities to donor impurities [39].

2.8.2 Current Transport Processes

The Anderson abrupt-junction model cannot adequately satisfy the details of current flow in hetero-junctions. Band profile, crystalline behavior and defects of the materials are needed include the evaluation of interface states. Under this consideration, current flow through the junction can be discussed by analyzing possible recombination and also tunneling paths. All of these alternative transport mechanisms for forward current flow increase the saturation current in many orders of magnitude larger than that expected from simple diffusion of carriers over the junction barrier. The current transport in a hetero-junction can be also modeled with the current transport mechanisms in metal-semiconductor junctions.

In the diffusion model, the excess carriers in the p-n hetero-junction is assumed to be accumulated locally that can cause a condition of non-uniform carriers and as a result of the gradient of carrier concentration, diffusion can occur by which the carriers migrate from high concentration region through the low concentration region [163]. Then, it can continue until the system reach to the state of uniformity. This transport model was firstly derived by Anderson [165, 166], and then it was developed in addition to the fact that the effect of dipoles and interface states are neglected, the diffusion current is assumed to include only electrons or holes due to the discontinuities in the band edges at the interface [39].

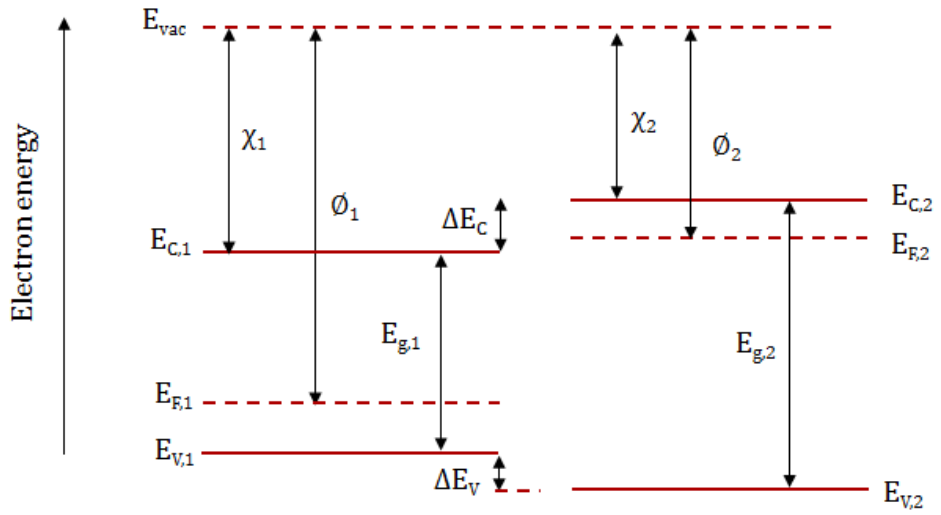

(a)

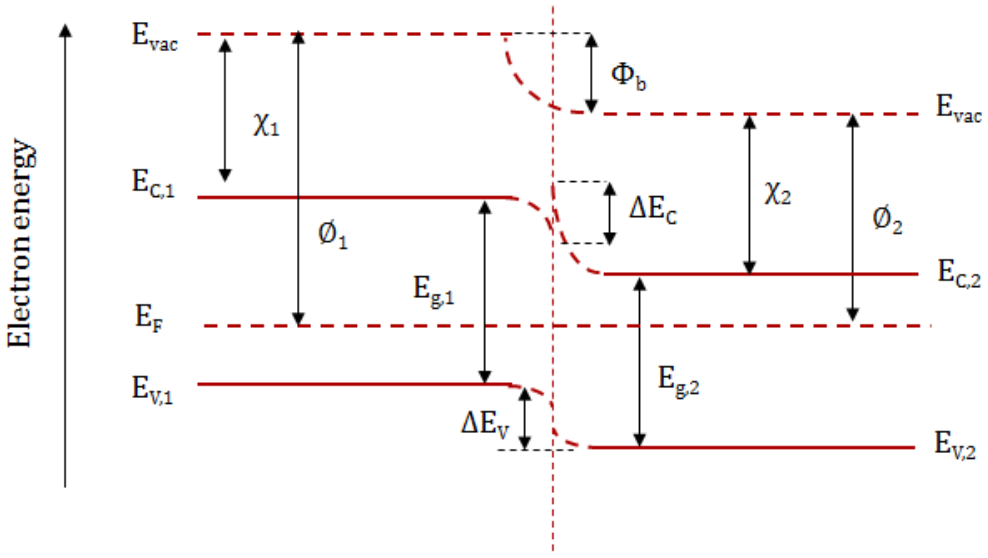

(b)

Figure 2.3: Equilibrium energy band diagrams (a) before and (b) after the formation of an abrupt p-n heterojunction.

In Fig. 2.3 (a) and (b), energy band diagram of the isolated p-type and n-type semiconductors and such hetero-junction structure is shown in the case of thermal equilibrium, respectively [167]. As shown in Fig. 2.3 (b), there is a discontinuity at the conduction band edges of the semiconductors in the equilibrium band profile of

the hetero-junction. This occurs as a result of difference between the natures of the two semiconducting materials in terms of energy band gap, E_g, dielectric constant, ε, electron affinity, χ, and work function, Φ [168]. In a semiconductors, the work function is described as being the energy required to remove an electron from the Fermi level, E_F, to the vacuum level, and similarly the electron affinity is defined as the energy required to remove an electron from the bottom of the conduction band, E_C, to the vacuum level. The case of the difference between the electron affinities as $\chi_1 > \chi_2$, cause the spike and notch formation at the interface shown in Fig. 2.3 (b). Therefore, the conduction band offset, ΔE_C, is

$$\Delta E_C = \Delta\chi = \chi_1 - \chi_2 \tag{2.64}$$

and similar, the valence band discontinuity is

$$\Delta E_V = (E_{g2} - E_{g1}) - (\chi_1 - \chi_2) \tag{2.65}$$

then,

$$\Delta E_V = \Delta E_g - \Delta E_C \tag{2.66}$$

where the sum of the two band discontinuities is equal to the band gap difference between these two layer,

$$\Delta E_g = \Delta E_C + \Delta E_V \tag{2.67}$$

At the thermal equilibrium, the Fermi level of the two different semiconductors coincides on both sides of the p-n junction. In addition, the vacuum levels conserve their parallelism to the each conduction band edges and they are connected by a smooth, continuous curve. Since the dipole layers is neglected by this model, the electrostatic potential difference is observed as the vertical displacement in the vacuum level between two semiconducting layers, and also since the junction

consists of two semiconducting layers having different dielectric constant, the discontinuity at the interface occurs [167].

The depletion layer is expected to be formed in only one side of the junction [165] and because the interface states are neglected by this model, the space charges in each side are predicted to be equal in magnitude. The total built-in potential, V_{bi}, is represented by the difference between the work functions $\Phi_1 > \Phi_2$, and the sum of the built-in voltages on both sides is equal to the total built-in potential,

$$V_{bi} = V_{bi,1} + V_{bi,2} \tag{2.68}$$

In the heterojunction given in Fig. 2.3 (b), the pre-dominant current carriers are electrons because the electrons encounter with the smaller barrier compared to that for holes. With considering the diffusion mechanism by neglecting the generation-recombination contribution, the current flow in the junction can be found as,

$$I = \left(aqXN_{D,1} \left(\frac{D_{n,1}}{\tau_{n,1}} \right)^{1/2} \right) exp\left(-\frac{qV_{bi,2}}{kT} \right) \left[exp\left(-\frac{qV_2}{kT} \right) - exp\left(-\frac{qV_1}{kT} \right) \right] \tag{2.69}$$

where X is the transmission coefficient of the electrons across the interface, a is the junction area, $N_{D,1}$, $D_{n,1}$ and $\tau_{n,1}$ are the equilibrium donor concentration, diffusion coefficient and lifetime of electrons in the p-type region, and also the applied voltage is divided into the two regions as $V=V_1+V_2$ under the forward bias.

In the application of the diffusion model with small transmission coefficient, the effect of the spike in the conduction was taken into consideration with the evaluation of emission current including in the diffusion of the carriers [169]. Again, in the absence of the generation-recombination within the space charge region, the current can be expressed as

$$I = \frac{I_s \left[exp\left(\frac{qV}{kT}\right) - 1 \right]}{\left(1 + \frac{I_s}{I_d}\right)} \tag{2.70}$$

where I_s can be defined as the saturation current as in the case of homo-junction type proposed by Shockley [170],

$$I_s = aqN_{D,1}\left(\frac{D_{n,1}}{\tau_{n,1}}\right)^{1/2} \tag{2.71}$$

and I_d is the emission limited current,

$$I_d = \frac{1}{2} aqX_m N_{D,2} \bar{v}_{xe,2} exp\left[-\frac{q}{kT}(V_F - V)\right] \tag{2.72}$$

In this case, $N_{D,2}$ is the equilibrium donor concentration in n-type region, V_F is the forward barrier as shown in Fig. 2.3, X_m is the transmission coefficient readjusted with the predicted model and $\bar{v}_{xe,2}$ is the *x*-component of the average speed of the electrons in n-type material in the form as

$$\bar{v}_{xe,2} = \left(\frac{2kT}{\pi m_n^*}\right)^{1/2} \tag{2.73}$$

with effective mass of the electron in the corresponding junction layer, m_n^*.

As seen in the denominator of the Eq. 2.70, the current ratio, I_s/I_d, determines the mode of the operation [167]. In fact, the expression given in this equation is approximated to the p-n homo-junction model [194] if $I_d \gg I_s$, however if $I_s \gg I_d$, it turns to the analogous form of the Schottky diode current [171, 172].

In addition, the recombination was included to the assumptions on the carrier transport by the emission-recombination model [169] and the schematic representation of this model is shown in Fig. 2.3. In this model, a thin layer at the

interface with a strongly distributed lattice and an infinitely fast recombination in which the carriers reach the interface by thermionic emission over the respective barriers are proposed [173]. The forward current-voltage characteristics is explained in the expression

$$I = I_s \left[exp\left(\frac{qV}{nkT}\right) - 1 \right] \tag{2.74}$$

with

$$I_s = Bexp\left(-\frac{qV_{bi}}{nkT}\right) \tag{2.75}$$

where *n* depends on the ratio of doping concentrations in the materials and *B* is weakly dependent on the temperature.

On the contrary to the transport model predicted with the influences of the spike in certain voltage regions [169], the tunneling mechanism should be considered in all cases in which emission-recombination model can fail (over the whole voltage range or above a certain voltage). In this model, the electrons are assumed to have low energy to surmount the potential barrier and so that they can tunnel through the barrier in order to flow through the junction [174]. When the tunneling through the barrier is the dominant transport mechanism over the thermal emission, the current-voltage characteristics can be described as

$$I = I_s(T) exp\left(\frac{V}{V_0}\right) \tag{2.76}$$

where V_0 is a constant and $I_s(T)$ increases weakly with temperature [175],

$$I_s(T) = I_{s0} exp\left(\frac{T}{T_0}\right) \tag{2.77}$$

with the constants, I_{s0} and T_0.

The satisfactory explanation for the band-to-band tunneling and thermal emission followed by recombination coupled by the carrier conduction in the junction, tunneling-recombination model is proposed by Riben et. al [176, 177]. In this model, the electrons is considered in a tunneling process from the n-type material the conduction band to the p-type material empty inter-band states and then they are assumed to recombine with holes, or conversely, holes tunnel from p-type material to n-type material occupied states and then they are considered to recombine with electrons. If the tunneling arises from the bottom level of the conduction band or the top level of the valence band, then the corresponding current expression can be expressed as,

$$I = Bexp\left[-\alpha\left(\frac{V_{bi}}{V}\right)\right] \tag{2.78}$$

where B is a weak function of voltage and α depends on the effective mass of the electron in the forbidden region, the dielectric constant, the equilibrium carrier concentration and the shape of the barrier.

2.8.3 Capacitance

The capacitance-voltage characteristics in the hetero-junctions are modeled by applying the abrupt junction approximation on the case of basic p-n junction [166]. The transition widths on both semiconductor layers with respect to the coordinate of the interface, x_0, as shown in Fig. 3.2 (b), can be obtained by applying the Poisson's equation for each of side of the interface with generalizing the solution for homo-junctions [163, 167]. Then, corresponding depletion widths can be found as,

$$W_{d,1} = \left(\frac{2N_{A,1}\varepsilon_1\varepsilon_2 V_{bi}}{qN_{D,1}\left(\varepsilon_1 N_{A,1} + \varepsilon_2 N_{D,2}\right)}\right)^{1/2} \tag{2.79}$$

and

$$W_{d,2} = \left(\frac{2N_{D,2}\varepsilon_1\varepsilon_2 V_{bi}}{qN_{A,1}\left(\varepsilon_1 N_{A,1} + \varepsilon_2 N_{D,2}\right)} \right)^{1/2} \tag{2.80}$$

where $W_{d,1}$ is the depletion region in the p-type material defined by the transition distance, x_1, and $W_{d,2}$ is the depletion region in the n-type material defined by the transition distance, x_2, with respect to x_0. In addition, in these expressions, $N_{A,1}$ and ε_1 denote the acceptor concentration and dielectric constant in the p-type material, and similarly, $N_{D,2}$ and ε_1 denote the donor concentration and dielectric constant in the n-type material, respectively.

Furthermore, the relative built-in voltages $V_{bi,1}$ and $V_{bi,2}$ affected in each semiconducting layers, are evaluated as,

$$\frac{V_{bi,1}}{V_{bi,2}} = \frac{\varepsilon_2 N_{D,2}}{\varepsilon_1 N_{A,1}} \tag{2.81}$$

and the capacitance of the transition region can be found as,

$$C_d = \left(\frac{aqN_{A,1}N_{D,2}\varepsilon_1\varepsilon_2}{2V_{bi}\left(\varepsilon_1 N_{A,1} + \varepsilon_2 N_{D,2}\right)} \right)^{1/2} \tag{2.82}$$

These depletion widths and capacitance expressions can be re-written with dividing also the effect of this applied voltage as $V=V_1+V_2$, when an external voltage, V, is applied across the heterojunction.

2.8.4 Solar Cell Properties

An ideal solar cell can be represented by a diode structure which is sensitive to photovoltaic effect with the creation of electron-hole pairs under illumination. The corresponding ideal current-voltage characteristic is described by the Shockley solar cell equation

$$I = I_{ph} - I_0 \left[exp\left({}^{qV}/_{kT} \right) - 1 \right] \tag{2.83}$$

where k is the Boltzmann constant, T is the absolute temperature, q is the magnitude of the charge of the electron, V is the voltage at the terminals of the solar cell, I_0 is the diode saturation current and I_{ph} is the photo-generated current [178]. In fact, the current-voltage behavior of an ideal solar cell is expressed as a shifting of the diode characteristic in the dark along the current axis by I_{ph} (Fig. 2.4 (a)) [178]. On the other hand, in real case, this relation is modeled due to the power dissipation through the resistance of the contacts and current loss around the sides of the solar cells as,

$$I = I_{ph} - I_0 \left[exp\left({}^{q(V + IR_s)}/_{nkT} \right) - 1 \right] - \left({}^{V + IR_s}/_{R_{sh}} \right) \qquad (2.84)$$

where R_s and R_{sh} are the parasitic resistances in series in parallel (or, named as shunt resistance) with the cell, respectively, and also n is called diode ideality factor that is directly related to these parasitic effects. In fact, this relation is derived from the equivalent circuit of an ideal solar cell as shown in Fig. 2.4 (a) In this schematic illustration, R_s is included in the circuit in series since it arises particularly from resistance of the materials in the solar cell that are the contacts and the bulk material [4]. In addition, R_{sh} is parallel to the circuit in order to represent the leakage current through the solar cell structure that can be observed around the edges of the diode and also between the contacts [4]. The effects of the parasitic resistances on the solar cell current-voltage behavior are also shown in Fig. 2.4 (a) [6, 179].

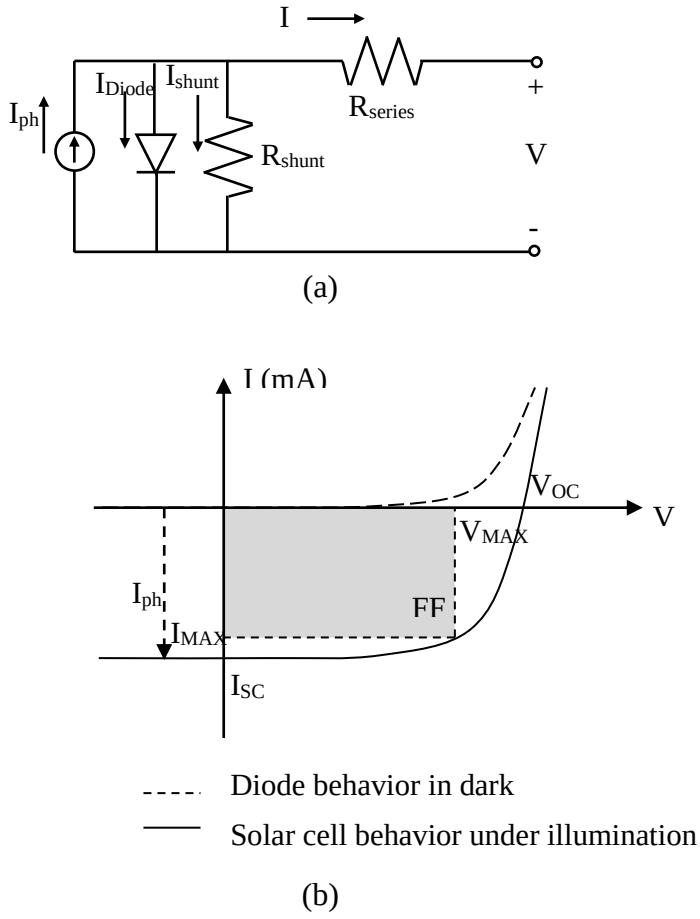

Figure 2.4: a) Equivalent circuit of a solar cell and
b) I-V characteristics of an ideal solar cell

For the short-circuit current, only the photons absorbed within the diffusion length are considered and in ideal case, it is equal to I_{ph} with the absence of the loss mechanisms [180]. However, in the real case from the current-voltage characteristics of the solar cell, it is found as a current value when the voltage across the solar cell is zero.

The potential difference between front and back contact in the solar cell is evaluated with its maximum value called open circuit voltage, V_{OC}. In fact, it is defined as the voltage output of the illuminated solar cell when there is no current flow through the cell. For the ideal solar cell, it is related with the light intensity logarithmically as,

$$V_{OC} = \frac{kT}{q} \ln\left(1 + \frac{I_{ph}}{I_0}\right) \tag{2.85}$$

where to reach the ideal behavior, it is important to obtain small reverse saturation current as possible.

The *FF* is the parameter related to the measure of quality of the solar cell. Since operating region of the solar cells in the current-voltage curve generated under illumination is defined with the I_{SC} and V_{OC} boundaries, the power output of the solar cell at any operating point can be calculated by the area of the rectangle indicated with the corresponding current and voltage values, as *P=IV*. Therefore, the maximum power output can be obtained by the more square-shaped region at the voltage point V_{max} with the corresponding current point I_{max}. Then, *FF* for the cell is defined as the ratio of

$$FF = \frac{I_{max}V_{max}}{I_{SC}V_{OC}} = \frac{P_{max}}{I_{SC}V_{OC}} \tag{2.86}$$

For a reasonable efficiency in solar cell, *FF* should have a value in between 0.7 and 0.85 [206]. Moreover, *FF* of a solar cell in the ideal behavior can be described as a function of V_{OC} and an approximate expression defining the relation between the ideal value of *FF* and normalized voltage v_{OC} is given in the form [181],

$$FF = \frac{v_{OC} - \ln(v_{OC} + 0.72)}{v_{OC} + 1} \tag{2.87}$$

where $v_{OC}=V_{OC}/((kT/q))$.

In addition, the conversion efficiency, η, of the solar cell is defined as the ratio of the maximum power to the incident power with solar irradiation and it can be related to I_{SC} and V_{OC} as,

$$\eta = \frac{I_{SC} V_{OC} FF}{P_{in}} \tag{2.88}$$

CHAPTER 3

EXPERIMENTAL TECHNIQUES

3.1 Introduction

In this chapter, the experimental techniques used in this work are presented. Under this aim, at first thin film deposition process is described with the substrate preparation, thin film deposition, post-annealing treatment and electrical contact deposition steps. Then, structural, optical and electrical characterization measurements in the study of the investigation of material properties of the thin film samples deposited on the glass substrate; device characterization measurements in the study of the investigation of diode parameters of these films deposited on Si-wafer substrate and also photovoltaic properties of their thin film – thin film hetero-structure are introduced.

3.2 The Thin Film Deposition Process

3.2.1 Substrate and Sample Preparation

For different characterization processes, the thin films were deposited on the soda-lime glass, indium tin oxide (ITO) coated glass and silicon wafer. 1 mm thick Marienfeld soda-lime glass substrates were used for the material characterization of the samples. They are optically flat and the refraction index n_s is about 1.53±0.02 at λ~546.07 nm [182]. They were prepared as in different sizes with the requirements of the measurement systems. ITO and Si wafer substrates were used for analysis of their device characteristics. CAIS/Si diode structure was prepared with using n-type and ZIS/Si

diode structure was prepared with using p-type Si wafer substrate where both of them are in (111) mono-crystalline structure with the resistivity value of 1-3 (Ω.cm). Moreover, ITO coated glass substrates were used in CAIS/ZIS heterojunction structure.

In order to produce high quality and pinhole free films, the possible contaminations on the surface of the substrates must be removed before the deposition of the films. Therefore, substrates cleaning were performed in four-step process. As a pre-cleaning step, the surface of the glass slides were hand wiped with dry wiper by using pure acetone, and also they were put into an ultrasonic cleaner by a beaker filled with pure acetone. It is useful step for cleaning process; however, acetone can also leave its own residues on the glass surface. Therefore, the glass substrates were rinsed in hot distilled water which was in about 15 MΩ.cm resistivity. Then, as a second step, after rinsing in hot distilled water, glass substrates were cleaned in a hot detergent solution with using ultrasonic cleaner. This solution provides to remove oils and protein residues on the glass surface. In the next step, after removal of detergent solution with hot distilled water, in order to remove organic contaminations, the 30% hydrogen peroxide solution was used. As a final step, they were rinsed again with hot distilled water to get rid of the possible residues. In addition, ITO coated glass substrates were cleaned in two steps; at first they were hand wiped by using pure acetone and then put into an ultrasonic cleaner with acetone and also isopropanol solutions in a 10-minute period. Both glass and ITO coated glass substrates were kept in methanol solution until the deposition process. Before the deposition process, the surface of the wafers was subjected to a cleaning procedure with 10% dilute hydrofluoric acid (HF) solution in order to remove the native oxide layer and then rinsed in distilled water. In the deposition process, these substrates were dried by pure nitrogen flow.

In order to carry out the electrical and photo-electrical measurements, the glass samples were prepared in a cloverleaf (Maltese-Cross) geometry [183, 184]. These substrates masked in this contact geometry were used because the measurements were easily carried out by simple current-voltage readings without caring of width or distance between contacts.

3.2.2 Growth Process of Thin Films

Under this work, CAIS and ZIS thin films were deposited by stacked layer evaporation technique from the constituent elements of purity 99.999% evaporation sources by using Vaksis PVD/5F Midas thin film coating system (Fig. 3.1). In the deposition of CAIS thin films, Cu, Ag, In_2Se_3 and Se, and in the deposition of ZIS thin films, Zn, In_2Se_3 and Se evaporation sources were used. The layer thickness optimization of all evaporation sources was carried out by conducting several deposition cycles with the same deposition parameters prior to the sequential deposition of thin film samples. In all depositions, the glass substrates were placed at a fixed distance of about 30 cm above the sources and rotated during the deposition, and also the individual layer thicknesses were measured by Inficon XTM/2 deposition monitor. Therefore, each evaporation sources were used to control each elemental ratio in the deposited CAIS and ZIS film structures. Before the deposition process, the evaporation sources were heated up to an optimized temperature and they were treated pre-evaporation for several minutes to get optimized deposition ratio and also to eliminate the potential contaminations introduced during the exposure to atmosphere or source installation stage.

Figure 3.1: PVD system

For CAIS and ZIS film samples, the stacked sequence of the layers were done by depositing Cu and Ag layer between Se and In_2Se_3 layers, and Zn layer between Se and In_2Se_3, respectively. Besides, the thickness of each layer was controlled by deposition monitor. The deposition rates were also measured and monitored as about 1.0 Å/sec during the deposition of Zn, Se and In_2Se_3 layers, and about 0.2 Å/sec during Cu and Ag layers. The Se layers were added in the film deposition steps to adjust Se composition in the structure. The excessive element Se on the top of the film surface was also deposited to get a superior crystalline structure [185].

The PVD system is a typical thermal evaporation system that allows using more than one evaporation sources. In other words, there are four thermal cells that provide to deposit thin films by using four different evaporation sources. Although this system has a rotation stage for substrate holder, the optimization steps were done with caring on the position of the fusion cell used for each sources. In order to vacuum the chamber, automatic procedure is used by the software. In these depositions, pressure value was set at $5x10^{-6}$ Torr. Then, depositions were done with semi-atomic mode at the desired chamber pressure.

3.2.3 Post-Annealing Treatment

In this thesis work, the material characteristics of the thin film samples were investigated in as-grown form without applying any post-growth process. After this analysis step, they were characterized under the effect of post-heat treatment higher than the substrate temperature during the deposition process to observe the variations on the structural, electrical and optical properties of the as-grown thin films. This annealing procedure was applied to the films by horizontal Lindberg type furnace under the continuous nitrogen flow. The temperature range of this annealing treatment was determined 300, 400 and 500 °C with 30-minute time interval where this timing is approximately average of the deposition time. In the annealing process, at first, the temperature of the furnace was set to the desired temperature while the nitrogen gas was given to the quartz tube in the furnace in order to prevent any contaminant from the interior surface. Then, at the annealing temperature, thin

film samples were placed at the centered of the tube via the quartz boat. After that, the annealing process was applied for 30 minutes under the nitrogen gas flow. In order to prevent any harmful effect, such as cracking or oxidation on the film surface, the samples were slowly moved to the end of the tube while cooling down the system to the room temperature.

3.2.4 Electrical Contact Deposition

The front ohmic contact to the CAIS and ZIS thin films, and n- and p-type Si-wafers was deposited by metallic evaporation system. Metal contact production was done with shadow mask suitable for thin film production mask shape and also requirements for the electrical measurements. For the films deposited on the glass substrates, the shadow masks were prepared in geometry appropriate to the van der Pauw geometry; and for device characterization measurements, they were in circular shape with 1mm diameter and also in fringe/grid shape. These Cu-masks used in the metal contact step were illustrated in Fig. 3.2.

Figure 3.2: Thermal evaporation system

The CAIS and ZIS films were coated pure In elemental source and then annealed at 100 °C under the nitrogen atmosphere. The back side of the n-type and p-type Si wafers were thermally coated with Ag and Al metals to form an ohmic contact

region, respectively. After these processes, the wafers were annealed at 450 °C under the constant nitrogen flow to provide the ohmicity of these contacts. The fabricated Si-based and thin film heterojunction diode structures were completed with the thermally evaporated In as a transparent front ohmic contact onthe front surface of the top layer surface. In this case, to get several independent regions for measurements, dot-shaped Cu masks were used during thermal evaporation. As in the case of ohmic contact formation on Si wafers, after this deposition, the samples were annealed at 100 °C under the nitrogen flow to get an ohmic contact behavior.

In the metallic evaporation step, the samples were placed on the substrate holder about 15 cm above the evaporation source. In order to pump the system down to the necessary value, about 10^{-6} Torr, to start the evaporation. This evaporation process was carried out without heating the substrate. Therefore, all In contacts were annealed for 30 minute-time interval by horizontal Lindberg annealing furnace to provide contact diffusion between the ohmic metallic contact and thin film surface.

At the end of the ohmic contact production, the copper wires were attached on the contact surface by using silver paste to complete the sample preparation process for electrical and device characterizations. In electrical measurement, the ohmic behavior of the all deposited metal contacts were checked in terms by applying I-V measurements and it was found that I-V characteristic is independent of applied bias polarity that confirms the ohmic nature of a contact.

3.3 Structural, Compositional and Surface Characterization

3.3.1 Thickness Measurements

Thickness of materials has an important effect on their characteristics and it is used in many characterization methods. Therefore, thickness measurements of studied samples are a critical factor for many optical and electrical measurements and analysis of them. There exist various thickness measurement techniques as contact-type and non-contact-type. Basically, the contact-type devices need a reference

length for the measurements; however non-contact-type devices are based on the some physical relationship, such as capacitance or optical characteristics of the samples. For their easy and quick usage, the thicknesses of the deposited films in as-grown and annealed form were measured electromechanically by Veeco DEKTAK 6M profilometer (Fig. 3.3). It is computer control system with Dektak32 software. In general, it is used in order to measure the vertical profile of samples. During measurement, a diamond stylus with radius of 12.5 μm is moved horizontally into in contact with the reference substrate surface. Then, the stylus is moved to the sample surface and continues its motion on the sample surface for a specified distance and specified contact force. In these measurements, the horizontal resolution in the surface profile of the sample can be controlled by the scan speed and scan length from the Dektak32 program. This device can detect small surface variations in the limit of the properties of the stylus and therefore it is capable of measuring steps below 100 Å [186]. In addition, it can help to get a general view of topographic features on a surface of the samples.

Figure 3.3: Dektak 6M profilometer

3.3.2 X-Ray Diffraction (XRD)

XRD is a very common experimental technique used in the investigation of the crystalline structure of the solid materials because of being a comparatively fast-response and non-destructive analysis technique with a good sensitivity. In the

electromagnetic spectrum, X-rays are located between γ-rays and ultraviolet rays with the corresponding wavelengths of about 0.1-100 Å. However, the most commonly used wavelengths in XRD method range between around 0.5 and 2.5 Å because of having the same order of magnitude as the shortest interatomic distances in solid materials. With the wavelength in this range, X-rays can be used for the structural characterization of the solid material with an interaction of being absorbed, emitted, reflected or transmitted. In XRD method, X-rays sends on the surface of the material and the diffraction pattern of the materials due to the reflections are analyzed. Mainly, when X-rays interact with a solid material, it gives a fingerprint diffraction pattern about its crystalline properties. Therefore, XRD gives a direct evidence for the periodic atomic structure of crystals and allows getting information about crystal structure in terms of lattice planes, d-spacing and Miller indices. In addition, it allows getting initial information about the elemental composition of the samples when comparing the known XRD profiles.

XRD systems, mainly, includes an X-ray source, goniometer and a radiation detector and the XRD analysis depends on constructive interference when the reflection of X-ray sonly occurs. The observation of the XRD pattern of the structure in specific orientations is based on the short range (amorphous) and long range (crystalline) order in the materials. In other words, the specific diffraction peak is the result of reinforcement of reflection of X-rays from the corresponding periodically distributed parallel plane in the structure of a material.

The X-ray diffraction pattern of the deposited films were investigated by Rigaku Miniflex XRD system (Fig. 3.4) equipped with Cu-Kα X-ray source (λ = 1.54 Å) and XRD scans were taken in the range 10–90° with a scanning speed of 2 min^{-1}. It is a bench top and portable system combined with a chiller for cooling X-ray tube. It allows investigating the crystalline structure of the solid materials in crystal wafer, powder or thin film form. The experimental data were analyzed by using computer software licensed by Rigaku. The obtained XRD profile is mainly analyzed by a peak search-and-match process with the help of the program database containing reference patterns. The crystalline structure can also be compared to the literature works and

also International Centre for Diffraction Data (ICDD) in order to get high correlation with the experimental data. Moreover, from these experimental data, the lattice constant, grain size and internal stress properties can be investigated.

Figure 3.4: XRD system

3.3.3 Scanning Electron Microscopy (SEM)

The scanning electron microscope (SEM) is a microscope that uses electrons rather than light to form an image and to examine objects on a very fine scale. In other words, it is a tool used to observe and characterize of the materials up to a nanometer resolution. It also permits the variety in the type of the samples; it can be organic and inorganic materials with three modes of operation. The high vacuum (HV) mode is used for samples in metallic characteristics, in other words, it is suitable for analysis of electrically conducting samples. However, the electrically insulating samples need a conducting coating to analyze in HV mode. Low vacuum (LV) and environmental scanning electron microscope (ESEM) operation modes are preferred for insulating, ceramic or polymeric samples without any coating on the samples. SEM is a common technique to obtain information about topography of the sample surfaces and surface features, their morphology, shapes and sizes. The popularity of the SEM arises from its advantages on the light microscopes and AFM technique in these measurements; such as it can provide better resolution and depth of field than light microscopes, 3D appearance of the sample image as a result of the large depth of field and it is capable of very low magnifications complementing the information

available from the optical image [187]. In addition, SEM images are in high resolution of bulk specimens where it is not needed to make sample thin for transmission electron microscopy (TEM) measurements. SEM can analyze a larger surface area and perform faster scanning compared to AFM. SEM allows compositional analysis of the constituent elements in the samples and gives relative atomic ratios of them when it is equipped with EDAX facility and crystallographic information when it is equipped with electron backscatter diffraction (EBSD) facility. On the other hand, by comparison with optical microscopy and AFM, it is a vacuum-based process. Both the electron source and sample chamber requires being in vacuum with certain pressures.

In this study, the analyses of surface morphology of the samples before and after the annealing processes were carried out by Quanta 400 FEG model SEM system. This system contains secondary electron (SE), backscattered electron (BS), law vacuum, and energy dispersive X-ray spectroscopy (EDS) and EBSD detectors for specific usages. In order to monitor the sample surfaces, Everhart-Thornley detector (ETD) was used to collect SE generated in the sample. In fact, it is a photomultiplier detector designed by Everhart and Thornley. It consists of a Faraday grid, a scintillator, and photomultiplier tube (PMT). In this detector system, Faraday grid is used as a charged collector cage biased from -50 to 250 V to collect the low energetic SEs emitted in all directions from the sample. The part is placed in front of the scintillator and the incident electrons coming from this grid are directed to the scintillator which is a phosphor screen to create a photon corresponding to each coming electron. The outer layer of this part is also positively biased at about 10-15 kV to accelerate SEs to the phosphor screen. The reason in the usage of phosphor is that its response time is fast and it also permits high resolution scanning. Then, PMT amplifies the resulting photon signal and this amplified electrical signal is sent to further electrical amplifier. The electron source is Schottky emitter based field emission gun (FEG) and the electron beam was accelerated at 30 kV in scanning process. Since the SEM image generated by SEs, the interaction depth in the material is about 50 nm. In addition, to monitor an image with high resolution, working distance (WD) and depth of field were calibrated depending on the film properties,

such as thickness, surface features. Samples were also coated with Au/Pd target by sputtering method in order to get an electrically conducting surface required for HV operation mode. During the measurement, the beam in the SEM is moved over the sample to examine the possible surface variations and then appropriate magnifications were chosen to define them.

3.3.4 Energy Dispersive X-Ray Spectroscopy (EDS)

The analyses of chemical composition of the films in as-grown and annealed were carried out by Quanta 400 FEG model SEM equipped with EDAX facility. EDS makes use of the X-ray spectrum emitted by a solid sample bombarded with a focused beam of electrons to obtain a localized chemical analysis. This system detects the X-ray photons emitting from the sample as a result of electron-sample interaction. It is made of Si (Li) crystal which absorbs the X-ray and generates electron-hole pair corresponding to each incident photon with an energy resolution of about 132 eV. Under the bias voltage, this pair is separated and the electrons are detected to get an electronic signal output from the detector. It is used to determine the specific X-rays of different elements into an energy spectrum, and then EDS system software is used to analyze the energy spectrum in order to determine the chemical composition of the materials. With this interval, it cannot distinguish the X-rays having different energy coming from different element.

3.3.5 X-Ray Photoelectron Spectroscopy (XPS)

X-ray photoelectron spectroscopy (XPS) measurements were done to identify the chemical species and chemical bonding states at the surface of the samples by using PHI 5000 VersaProbe system and also to surface composition of the films were analyzed by electron spectroscopy for chemical analysis (ESCA) method. This XPS system is equipped with an MgKα radiation X-ray source of energy value of 1253.6 eV in an ultra-high vacuum system with a chamber pressure below 10^{-7} Pa. The mono-energetic X-ray beam can be focused at a working area between 10-200 μm on the sample surface. In survey measurements, the surface of the samples were scanned

up to 1150 eV to get the general view of the XPS spectra. Then, the elements observed in these spectra were scanned in a specific energy intervals to construct more reliable data. As a result of irradiating the sample surface with X-ray, photoelectrons are emitted from the core levels of surface atoms and also the information can be given from the near-surface layer of the structure. Thus, the electron energy analyzer detects the binding energy and intensity of these photoelectrons. This XPS system also provides depth profiling in order to get information from the bulk by using Ar ion gun in sputtering the film surface. With the dual beam charge neutralization method, it also simplifies the analysis of insulating samples.

3.3.6 Atomic Force Microscopy (AFM)

AFM measurements were used to analyze the surface characteristics of the deposited films, and also to determine the effects of applying annealing and increasing annealing temperature on the surface structure of film samples. Nanomagnetics ambient AFM system (Fig. 3.5) was used.

Figure 3.5: AFM system

As a main concept of AFM, it offers higher resolution imaging capabilities with the method of feeling the surface using mechanical probing. Although SEM and AFM are two common techniques for high resolution surface investigations with a resolution of surface structure at about nanometer scale, AFM can provide 3D

surface analysis where SEM gives a standard in 2D imaging process. Besides, unlike SEM measurements, there is no any requirement on sample preparation before the measurement.

In the AFM measurement, the surface topographical image can be observed by scanning a sharp tip across a sample surface while applying a small constant force. This silicon tip is integrated on the end of a cantilever with a typical end radius in the interval of 2-20 nm, depending on its type. The scanning motion is controlled by a piezoelectric tube scanner that scans the surface of the sample with respect to the tip. The interaction between the end of the tip and the film surface is monitored by reflection of a laser beam from the back side of the cantilever into a split photodiode detector. Then, the AFM image of the sample is obtained by as a change in the photodetector output voltages [188].

3.3.7 Raman Spectroscopy

Raman scattering spectroscopy similar to the XRD method is an effective method in the analysis of chemical structures and physical forms with identifying substances from their characteristic spectral patterns. This technique is mainly based on the inelastic scattering of the monochromatic light after the interaction with the sample. In order to obtain a monochromatic light beam, usually intense laser emission is used. When the photon of the laser light with a frequency ν_0 interacts with the sample, it can be absorbed by the sample and then re-emitted. This interaction causes creation of dipoles where the frequency of them can be in the characteristic of Rayleigh scattering, Stokes frequency or Anti-stokes frequency [189]. In these characteristic frequencies, Rayleigh scattering is the most common, strong one with the same frequency as the incident beam ν_0. With the other absorption cases in Raman-active molecules, frequency of the re-emitted photons is shifted up or down in comparison with the frequency of the incident laser beam. Therefore, Raman spectroscopy deals with these characteristic frequencies which can provide information about vibrational, rotational, and other molecular modes.

In this study, Raman scattering experiments were performed by using Horiba Jobin Yvon iHR550 imaging spectrometer with a three-grating monochromator (Fig. 3.6). This spectrometer provides a scan range of 0-1500 nm in ±0.20 nm wavelength accuracy and 0.025 nm resolution with exit slit and photomultiplier tube (PMT) [190]. The optical Raman microscope is equipped with Euromex fiber optic light source which provides continuous white light by halogen bulb. This focusing process is completed when the sample surface is matched to the focal plane of the light by adjusting the Z position of the objective. In addition, the Raman spectra are obtained with the interaction between the sample and laser beam. Therefore, this system is also equipped with the Ventus532 laser source. It is designed by Laser Quantum with 532 nm green laser beam for the Raman spectroscopy applications. Mpc6000 power supply and controller unit is used to switch on/off the laser beam, monitor the component temperatures in the laser head and control the laser output power.

Figure 3.6: Raman system

3.4 Optical Characterization

3.4.1 Transmission Measurements

For the optical analysis of CAIS and ZIS thin film samples, transmission measurements were done at room temperature condition. Under this purpose, the optical transmittance measurements were carried out by using Perkin-Elmer Lambda

45 spectrophotometer in the 300-900 nm (Fig. 3.7) and also by using Perkin-Elmer LAMBDA 950 UV/Vis/NIR spectrophotometer in the 300-2000 nm wavelength region.

Figure 3.7: Perkin-Elmer Lambda 45 spectrophotometer

In general, spectrophotometer systems are easy to operate without special sample preparation. UV/Vis spectral analysis provides a simple method of measuring the band gap energy value of the samples. In addition, the UV/Vis/NIR systems can offer a detailed analysis of the optical spectra of the samples. Basically, the experimental procedure is that a collimated beam of light is directed on the semiconducting sample and then intensity of transmitted light from the sample is measured as a function of wavelength. Background correction for the glass substrate was performed in each measurement.

3.5 Electrical Characterization

3.5.1 Dark-conductivity Measurements

Temperature dependent dark-conductivity measurements in the temperature interval of 100-420 K with 10 K temperature steps. It was performed inside the Janis cryostat equipped with a cooling system by means of liquid nitrogen and Keithley 2400 sourcemeter was used to apply bias voltage to the sample and to measure the

resultant current (Fig. 3.8). In order to prevent the heat exchange with the environment, all measurements were carried out under about $6x10^{-3}$ Torr. By using Ulvac GVD-200 vacuum pump. In addition, the sample temperature was controlled by LakeShore 331 temperature controller. The sourcemeter can provide precise, low-noise, high stable DC voltage and current source and it can also be used as high-impedance multi-meter that read the voltage and current values in high sensitivity. It supplies source voltage from 5 μV to 210 V; measure voltage from 1 μV to 211 V, and source current from 50 pA to 1.05 A; measure current from 10 pA to 1.055 A, with a 0.012% accuracy [191]. It is a totally computer controlled system.

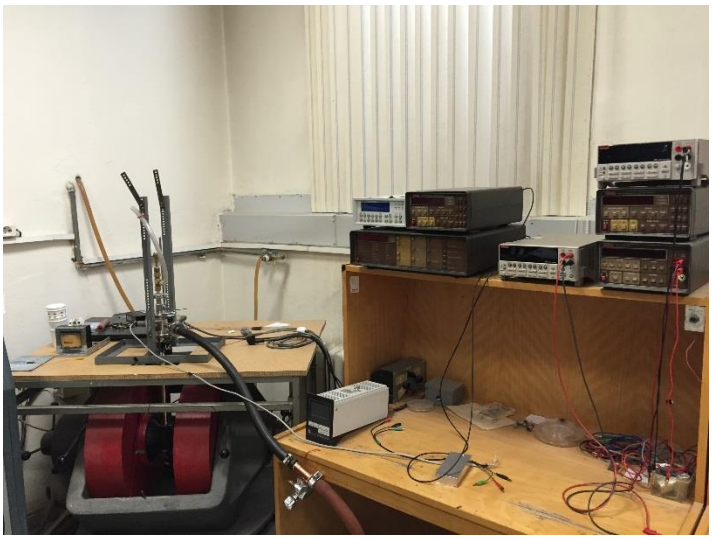

Figure 3.8: Electrical characterization system

From these measurements, the samples were deposited in van der Pauw geometry and also ohmic In-contact formation was done with an appropriate Cu-mask. Then, the dark-conductivity values were measured by using van der Pauw method [192, 193]. It is a standard technique for investigating the electrical conductivity characterization of thin film materials using four point contacts formed on the circumference of the sample arbitrarily. This method is widely used since it decreases the measurement errors which arise in classic characterization techniques due to the possibility of contact resistance and also it gives opportunity to apply it for samples of any shape [194]. In this measurement technique, for each combination of four contacts, resistance value of the sample can be determined at each temperature

point by the ratio of potential difference V_{bias} between two contacts and applied current I_{dark} as,

$$R_{dark} = \frac{V_{bias}}{I_{dark}} \tag{3.1}$$

Therefore, the resistivity value of the sample was found from the following simplified relation [195],

$$\rho_{dark} = f \frac{\pi d}{ln2} R_{dark} \tag{3.2}$$

where d is the thickness of the sample and f is the correction factor. Then, from the average of all contact measurements, the dark conductivity value, $\sigma_{dark}=1/\rho_{dark}$, was determined.

3.5.2 Hot Probe Measurements

Hot probe (or thermoelectric probe) method is the simplest technique to determine the type of the semiconductors. The principal idea of this method is that the carriers move within the semiconductor from the heated (hot) probe to the other (cold) probe. In other words, the thermally excited majority free charge carriers are directed from the hot region to the cold region. In fact, diffusion mechanism affects this carrier motion in the semiconductor structure because the material is uniformly doped by heating from the hot probe contact. Then, the electrical potential can be expressed by the translated majority carriers [196].

For this experiment, Keithley 619 electrometer/multimeter is used. It performs voltage, current, and resistance reading in a programmable range options. In this measurement, while pointing on the surface, positive terminal of the meter was heated while the negative terminal was kept cold. With this arrangement, for the case of n-type semiconductor, the meter reads a positive voltage, in the contrary case, p-type material provides a negative voltage.

3.5.3 Hall Effect Measurements

For this electrical characterization step, room temperature Hall parameters were determined by Hall Effect measurements. In these measurements, the current was applied by Keithley 220 programmable current source, and the voltage values was read from Keithley 619 electrometer/multimeter (Figure 3.8). Walker Magnion Model FFD-4D electromagnet was used to produce magnetic field and applied magnetic field strength was kept stable at around 0.90 T in Hall Effect measurements.

In general, the applicability of this method is taken into consideration when the sample resistance is between 10^3 and 10^9 ohm [136]. For less resistive materials, Hall Effect analysis can be done with the current-voltage measurement from the parallel contacts as shown in the Fig. 3.8. On the other hand, if the semiconductor is high resistive material, it is more appropriate to measure across different pairs of contacts.

From these measurements, the resistivity values were calculated as a result of four I-V measurements presented in Table 3.1.

Table 3.1: Current-voltage contact pairs for resistivity measurements

Applied Current (Keithley 220)	Measured Potential Difference (Keithley 619)
I_{13}	V_{24}
I_{31}	V_{42}
I_{24}	V_{13}
I_{42}	V_{31}

From these I-V measurements, the resistivity of the sample without magnetic field effect was calculated by the following expression,

$$\rho = f\frac{\pi d}{4\ln(2)}(R_{13,24\,(B=0)} + R_{31,42\,(B=0)} + R_{24,13\,(B=0)} + R_{42,31\,(B=0)}) \qquad (3.3)$$

where $R_{13,24\ (B=0)}$ corresponds the resistance value obtained from ratio of the applied current I_{13} with the measured potential difference V_{24}; and f is a function of the potential difference measured called as a correction factor. In our calculations, it was taken as 1 since the contacts are symmetrical [113]. This result gives the same room temperature resistivity value with the dark conductivity measurements. The same experimental and calculation procedures were also applied for the measurements under the applied magnetic field in both forward and reverse directions. For Hall Effect analysis, Hall coefficient R_H was found by using the calculated resistance values with or without magnetic field effect as

$$R_H = \frac{d(\Delta R_+ + \Delta R_-)}{2B} \tag{3.4}$$

where d is the thickness of the sample, and $\Delta R_+ = R_{+B} - R_{(B=0)}$ and $\Delta R_- = R_{-B} - R_{(B=0)}$ with direct (+) and reverse (-) directions. Hence, the sign of R_H also gave the type of the material whether electrons or holes predominate in the conduction process [197]. The conductivity type of all thin films was also checked by the hot probe measurements. Then, the charge carrier concentration was found by the relation:

$$n = {}^{r_n}/_{eR_H} \qquad \text{or} \qquad p = {}^{r_p}/_{eR_H} \tag{3.5}$$

where r (or r_p) is the Hall factor [198] and n (or p) represents the electron (or hole) concentration. From the calculated n value, Hall mobility μ was determined as:

$$\mu = {}^{\sigma}/_{nq} \tag{3.6}$$

3.6 Electro-Optical Characterization

3.6.1 Photo-Conductivity Measurements

Photo-conductivity measurements were performed inside the Janis cryostat, equipped with a liquid nitrogen cooling system (Fig. 3.8) between 100 and 400 K. A perpendicular illumination effect was applied on the film surface by using a 12 Watt

halogen lamp. Therefore, photo-conductivity measurements were carried out under five different illumination intensities between 20 and 115 mW/cm^2. Similar to the dark conductivity experiments, the samples were placed in the cryostat for the temperature dependent measurements. Different than the dark conductivity case, 12-Watt halogen lamp was used as a light source and it was arranged 1 cm above the thin film surface in which the whole surface can be illuminated homogenously. The photo-conductivity measurements are carried out in similar procedure with dark conductivity measurements where under a constant bias voltage, the lateral current flow along the sample is measured by using Keithley 2400 sourcemeter in the temperature interval of 80-420 K with 10 °C temperature steps. Apart from that, the photo-conductivity measurements were done under 5 different illumination intensities. Therefore, lamp current was supplied by Keithley 220 programmable current source and the illumination intensity of the lamp was arranged by changing the current passing through the lamp in the range of 50-90 mA with 10 mA steps. When the halogen lamp is placed at the 1 cm above the center of the sample, the illumination intensities 20, 35, 55, 80 and 115 mW/cm^2 determined by IL Ford 1700 Radiometer corresponding to the currents applied to the lamp. In this experiment, for each temperature step, initial data was taken under dark condition, and then measurement was completed with five different light intensities.

3.6.2 Spectral Photo-response Measurements

In these measurements, photo-responsivity spectra for the illumination at different wavelengths were measured at room temperature giving initial bias voltage to the sample. They were done between the wavelength range of 300 and 1300 nm in order to determine the band gap of the samples.

The photo-response measurements of the fabricated devices were done at room temperature by using Newport Oriel Apex Monochromator Illuminator coupled to Newport Oriel 74125 Monochromator (Fig. 3.9). In this system, the radiated light is generated by illuminator with a halogen lamp light source and 4 optional filters. Then, this generated light beam is directed into a monochromator equipped with 3 diffraction gratings with 600 lines/mm whose ranges are 250-1300 nm/600-2500

nm/900-2500 nm, respectively. In addition, the input F/number of the monochromator is F/3.9 and the resolution is 0.10 nm.

Figure 3.9: Photo-response system

In order to obtain the photo-response spectra as a function of wavelength, the sample is placed on the exit gate of the monochomator with focusing the light beam on the sample. The optical spectra of the samples were obtained under a constant bias voltage. The current-voltage measurements were also carried out by using Keithley 2400 sourcemeter. In this experiment, the bias voltage, illumination time, appropriate grating and wavelength interval can be specified and controlled by a Labview program. Therefore, the electronic shutter in the Monochromator was also controlled for dark and illuminated cases. The net photocurrent was determined as a difference between the current measured in dark and in the presence of illumination. In addition to this, the spectra of the samples were obtained by correcting the net photocurrent values with background elimination caused by the spectral distribution of the light source. The experimental data were used to plot photocurrent versus wavelength graphs, and from the peaks in this graph, activation energies of the sample were calculated.

3.7 Device Characterization

3.7.1 Dark Current-Voltage Measurements

For temperature dependent I-V measurements, CTI-Cryogenics Model 22 refrigerator system combined with Model SC helium compressor provide cooling and heating the sample in the working temperature interval (Fig. 3.10). The design of the sample holder on the sample station of the system limits the working size of the sample as to be at most 2x2 cm^2. The temperature dependent process requires an adequate vacuum integrity for proper system operations. The temperature of the sample was controlled and arranged to the working level by using Lakeshore DRC-91C controller. In a voltage interval determined in terms of the material characteristics, a potential difference was applied between front and back contact of the device and corresponding current flow is measured with Keithley 2401 sourcemeter. This measurement system is controlled by a Labview program where the temperature and voltage range can be specified before the experiment.

Figure 3.10: I-V and C-V measurement system

3.7.2 Capacitance-Voltage Measurements

The frequency dependent capacitance-voltage (C-V) measurements were performed with the computer-controlled measurement set-up and Hewlett Packard 4192A LF model impedance analyzer at room temperature (Fig. 3.10). In this measurements,

the applied voltage range and voltage step, measuring frequency were determined by the help of Labview program, and the all C-V measurements were carried out by impedance analyzer. The voltage interval was selected depending on the electrical properties of the samples, and the built-in frequency can be chosen within the limits of the analyzer which is between 5 Hz and 13 MHz [199]. In addition, the impedance analyzer can perform with oscillation level from 5 mV to 1.1 Vrms and the oscillation level step for this equipment is 1 mV in 5-100 mV regions and 5 mV in 100 mV-1.1 V region. The internal dc bias voltage source range is between -35 V to +35 V with 10 mV step precision.

CHAPTER 4

RESULTS AND DISCUSSIONS-1
($ZnInSe_2$ THIN FILM LAYER)

4.1 Introduction

ZIS structure is a ternary chalcopyrite semiconductor based on the combinations of II-III-VI group of elements [12-14]. The defect in this compound arises from the percentage vacancies of Zn elements in the structure [14] and it is the main factor on the physical characteristics of this film. The crystal structure of this compound belongs to tetragonal system with lattice constants *a=5.7095* Å and *c=11.449* Å [36]. There are many research on ZIS thin films about their crystal and film characteristics; and also applications in solar cell and optoelectronic device applications [10-14, 21, 24, 25, 28-31, 34, 36]. These works demonstrated their applicability of buffer layer as a hetero-junction partner for p-type absorber layers materials. They have an n-type conductivity behavior [14] and can be used as a promising candidate for CdS structure with its environment-friendly characteristics. Moreover, earth-abundant Cu-based chalcogenide semiconductors, Cu_2-II-IV-VI_4 have been the potential materials for solar cell applications with their low cost, abundance in resources and suitable band gap properties [200]. Therefore, ZIS can be a best lattice matched n-layer for this type of photovoltaic absorber compounds. In this part of the thesis work, the material and device properties of Zn-rich ZIS thin films under the effect of post-thermal annealing at different annealing temperatures are reported.

4.2 Structural Characterization of $ZnInSe_2$ Thin Films

ZIS thin films were deposited by sequential layer growth of Zn, In and Se evaporants. The compositions of the films were determined by EDS in order to analyze the elemental content in as-grown film structure. Change in the atomic percentage of these elements in the structure was also evaluated under the effect of post-thermal annealing processes. The atomic ratio of the elements in the as-grown and annealed ZIS films is tabulated in Table 4.1. As given in the Table 4.1, all films are in the Zn-rich characteristics. As the annealing temperature increases, the atomic percentage of Zn increases while that of In and Se decrease. This is usually expected due to the different vapor pressures and sticking coefficients between the constituent elements. The decrease in the atomic percentage of Se with annealing indicates the segregation and/or re-evaporation of Se atoms from the film surface due to the high vapor pressure of selenium before making the bond with the other elements [201].

Table 4.1: EDS results of as-grown and annealed ZIS thin films

Sample	Zn (at %)	In (at %)	Se (at %)
As-grown	22.03	20.80	57.17
Annealed at 300 °C	24.03	19.07	56.90
Annealed at 400 °C	27.49	18.13	54.38
Annealed at 500 °C	28.93	17.51	53.56

The thicknesses of the films were measured electromechanically by a profilometer and the measured film thicknesses were 590, 585, 525 and 505 nm, for the as-grown films, and films annealed at 300, 400 and 500 °C, respectively. According to these results, although the film thicknesses could be evaluated as the same with annealing up to 400 °C, the slight decrease in the thickness values can be taken as the indication of the decrease in the amount of some constituent elements in the structure of the films.

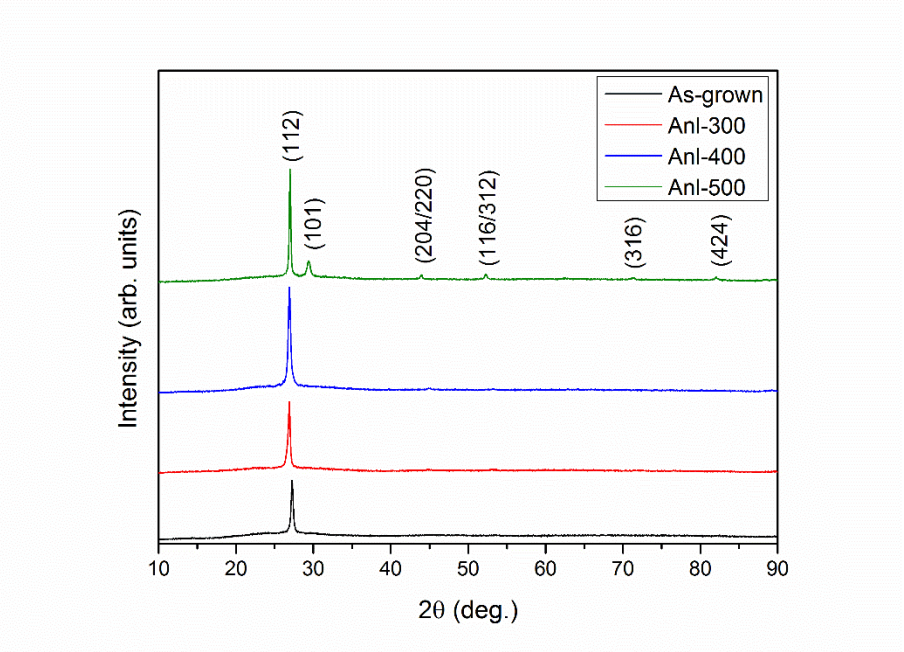

Figure 4.1: The XRD patterns of the as-grown and annealed ZIS thin films at different temperatures.

XRD technique was used to investigate the phases and the orientation of crystalline structure of ZIS thin films. It can be seen from Fig. 4.1 that the films have a tetragonal structure with dominant diffraction peak at (112) direction whose 2θ position is about 26.9° [23, 26, 30]. In fact, these types of structures were reported to have a zinc-blende structure [18]. The XRD patterns of the films are consistent with JCPDS (joint committee on powder diffraction standards) card files 39-0458 [202] and 39-1156 [203]. On the other hand, no remarkable change was observed in the diffraction peak positions in the XRD patterns of the films with annealing (Fig. 4.1) except at the films annealed at 500 °C. In this annealing temperature, ZnSe secondary phase formation was detected in this film structure and it was found to be matched with JCPDS card file 80-0008 [204] which is the most suitable card for this peak. In addition, the peak intensity in the preferred orientation of (112) direction increased appreciably with increasing annealing temperature which gave information about the degree of crystallinity along this direction. The lattice constants of the films were derived by Chekcell software. As a result of the calculations, it was found that the deposited crystalline thin films belong to the space group of *I-42m* and has tetragonal lattice structure. Lattice constants were calculated as, a=*5.6977* Å and

c=11.5095 Å and they are in good agreement with the results given in the literature [3]. In addition to the main crystalline orientation direction, there are additional diffraction peaks in (200), (204/220), (316) and (424) orientations as reported in the previous works [20, 34, 202, 203]. These diffraction peak intensities are very low compared to the main peak, however they became observable with annealing at 500°C. Moreover, the binary ZnSe phase in (101) orientation direction was only observed in this film structure. This formation may be due to the decomposition of this ternary structure or mobile Zn elements on the film surface may promote the probability of the reaction kinetics with Se atoms for the construction of this phase.

The average microcrystalline grain size d was estimated from the XRD pattern using the Scherrer's formula [201, 205] expressed as;

$$d = \frac{k\lambda}{\beta cos\theta} \tag{4.1}$$

where k is the shape factor (Scherrer constant) equal to 0.94 [206], λ is the wavelength of X-rays, β is defined as the diffraction peak width at half height (FWHM), and θ is the diffraction angle. This formula express the relation between peak width, β, and crystallite size, d, and it depends on how the constant of proportionality, k is determined. Therefore, it can give information about the comparison of grain sizes in the as-grown and annealed ZIS films. It was found that the FWHM value decreases and as a result of this grain size of the films increases as in the order of 6.3, 7.3, 8.5 and 12.6 nm depending on increasing annealing temperature. The increase in grain size is a clear indication of improvement in crystallinity following to the annealing process [12, 207]. Accordingly, the strain values, ε, can be approximated by using the following expression [208],

$$\varepsilon = \left(\frac{\lambda}{dcos\theta} - \beta\right)\frac{1}{tan\theta} \tag{4.2}$$

The calculated strain values were found as 6.19, 5.47, 4.70 and 3.14 ($x10^{-2}$) for the as-grown and annealed samples, respectively. This result showed that with increasing

size of the grains, the strain value of the ZIS films were decreased under the annealing processes. This can be related to increase in lattice parameters due to change in the displacement of the atoms with respect to their reference lattice positions [209]. The decreases in ε with increasing annealing temperature may be due to the movement of interstitial Zn atoms from inside the crystallites to the grain boundary, which leads to reduction in the concentration of lattice imperfections [210].

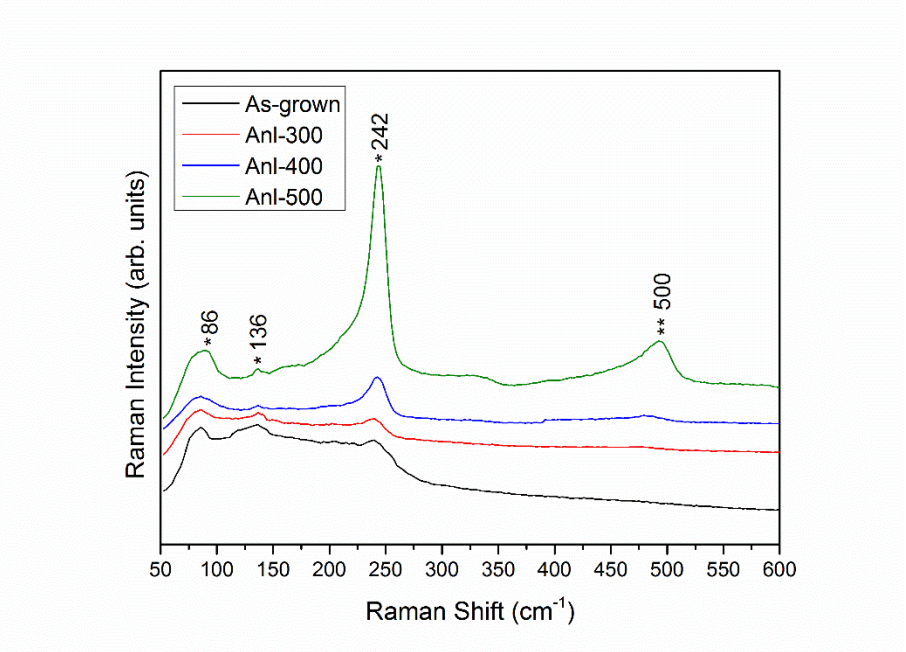

Figure 4.2: Raman spectra of the as-grown and annealed ZIS thin films at different temperatures

Raman analysis was carried out to find out the structure and vibrational modes in the samples. Raman spectra of the ZIS samples are shown in Fig. 4.2. According to these measurements, the observed Raman peak positions common for the all films were 242, 136 and 86 cm^{-1}. However, there were two distinct bands at frequencies around 86 and 242 cm^{-1}, and the other characteristic Raman peak for this structure was rather weak compared to these peaks. The broad and strong band was observed in the wavenumber range about 242 cm^{-1} and it became prominent in the films with annealing processes. This peak is the characteristic peak of the ZIS structure and corresponds to longitudinal optical (LO) phonon mode [15, 35]. In addition, the Raman mode in this highest frequency was reported in ordered-vacancy compounds

in defect zinc-blende structure with only tetrahedrally coordinated cations (thiogallate structure with space group, S_4^2) [35, 211, 212]. The presence of LO mode confirms that the ZIS films have a crystalline structure [34]. In an agreement with the previous works in the literature, there is no additional information about ZIS structures in the wavenumber range above 250 cm^{-1} [35, 213]. On the other hand, as observed in XRD analysis of the films, film annealed at 500 °C has an additional peak at 500 cm^{-1} corresponding to ZnSe structure [79]. The characteristic Raman mode for ZnSe structure observed at about 250 cm^{-1} is very close to the corresponding peak in ZIS structure, and it was also evaluated as a LO phonon mode for ZnSe [79, 214]. In ZnSe Raman spectra, the peak at 500 cm^{-1} corresponds to the LO phonon replica in this structure [79]. When the intensity of the peaks were evaluated, as in the XRD case, this phase was found to be higher than the secondary phases of ZIS structure in the annealed film.

The surface morphology of the ZIS thin films was studied by SEM micrographs technique. The SEM micrographs obtained for the as-grown and annealed films at different annealing temperatures are shown in Fig. 4.3. As seen from Fig. 4.3 (a), before annealing treatment, there are clusters piled up on the surface of the ZIS films and they are distributed irregularly over the film surface. According to the compositional analysis on these features, they were found to be Zn crystallites. As shown in Fig. 4.3 (b), applying first annealing treatment at 300 °C results in increase these crystallites on the film surface. With further annealing processes, these features are disappeared that is probably due to either the diffusing of Zn atoms from surface to bulk or staying under the surface layer consisting of mainly segregated In and Se atoms. It is clearly seen from Fig. 4.3 (c) and (d) that the annealing at 400 and 500 °C cause surface modifications effectively. From corresponding EDS results of these films, there is a considerable decrease in Se ratio in the composition of them. Together with specific EDS analysis, it is found that the relatively dark regions on these film surfaces are the indication of possible segregation of Se atoms and/or re-evaporation from thin film surface due to the high vapor pressure of Se before making the bond to construct the crystalline structure [215].

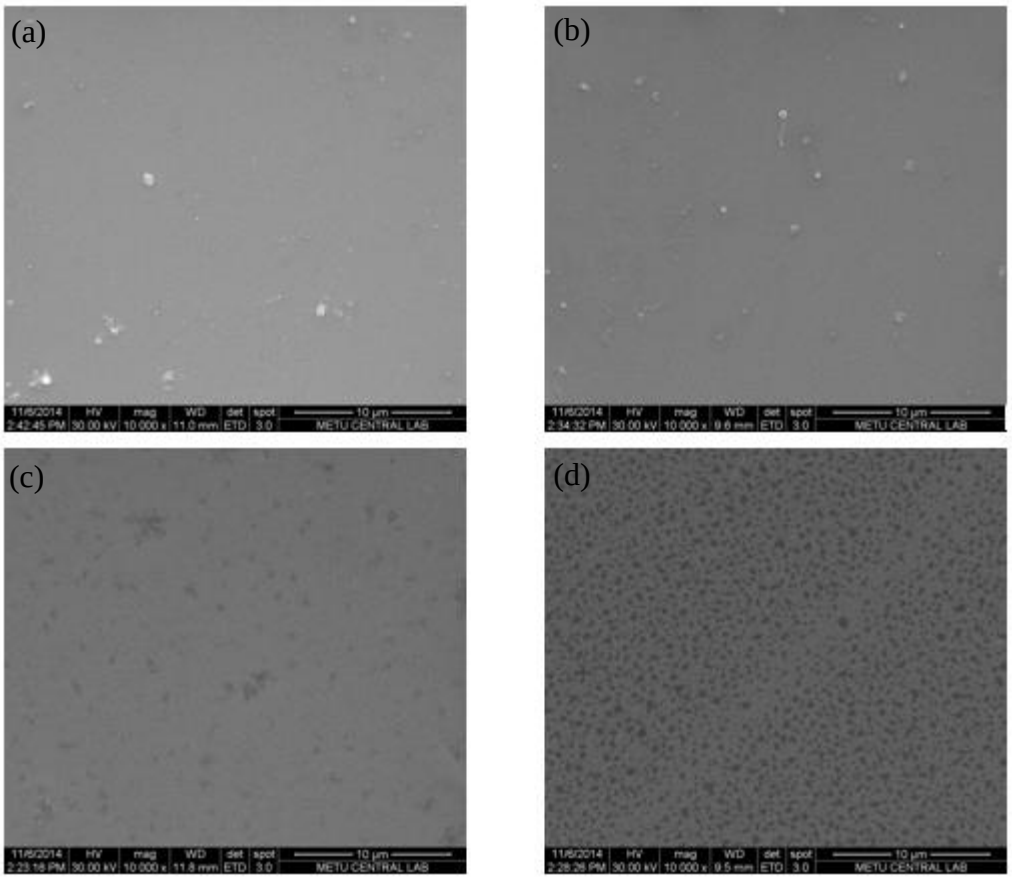

Figure 4.3: The SEM images of a) the as-grown and annealed ZIS thin films at b) 300, c) 400 and d) 500°C

The topographic properties of the as-grown and annealed ZIS thin films were investigated by using AFM measurements. The 3D AFM images of the samples for 5μmx5μm area are shown in Fig. 4.4. As observed in SEM analysis, Fig. 4.4 also shows explicitly the formation of the Zn crystallites on the film surface and the surface modification with increasing annealing temperature. Apart from the Zn formation, the surface of the films is uniform and nearly smooth although the post-thermal annealing processes were applied. The obtained root-mean-square (RMS) surface roughness value was 1.33 nm for as-grown films. By applying annealing process and increasing the annealing temperature, the thin film the surface morphology started to change and the RMS peak to peak distance value became 1.57, 4.69, 3.54 nm for the ZIS films annealed at 300, 400 and 500 °C respectively. By annealing process at 300 °C, the grains were become more close-packed, and at 400

°C their size distribution was decreased. With further annealing process at 500 °C, the grain formation was collapsed and the surface roughness was decreased. This result about the smoothness of the surface could be due to the migration of Se atoms towards the film surface as determined from the EDS and SEM results. On the other hand, the deposited ZIS films could be a well candidate for further film preparation in devices for solar cell with significantly low RMS roughness values [216].

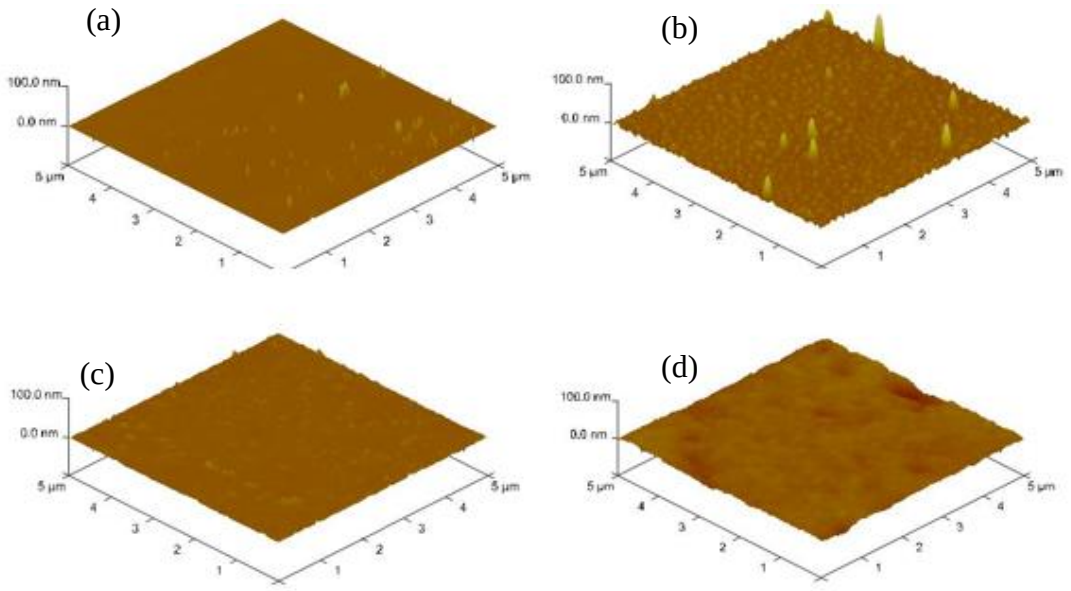

Figure 4.4: The AFM images of a) the as-grown and annealed ZIS thin films at b) 300, c) 400 and d) 500 °C

The surface and near-surface atomic composition and the present chemical environments of the ZIS thin films were analyzed by XPS measurements performed on as-grown and annealed samples. The XPS spectra were obtained using the constant analyzer-energy (CAE) mode with a pass energy of 48 eV. Surface of the films was sputtered two times by using 2 keV Ar+ ions for 5 min duration to reduce the amount of the contaminants due to C and O atoms and to analyze the near-surface composition of films. The corresponding XPS survey spectra of as-grown and annealed films were compared as indicated in Fig. 4.5-4.7. It is clearly observed from the XPS analysis of both as-grown and annealed film, all expected constituent elements, Zn, In and Se, and additionally C and O were appeared on the XPS survey

composition with corresponding photoelectron lines. As shown in these figures, the C 1s and O 1s photoelectron lines were observed in XPS spectrum of the all samples, and this indicated the presence of C and O contamination. The film surfaces may be contaminated with C and O during the characterization of samples. There is a weak increments on background signal on the film surfaces depending on the variations in the peak intensity of these elements with increase in annealing temperature. This indicates that there were in an argon flow in annealing furnace during annealing, but the inert gas was not so pure. Therefore, the samples may be oxidized in these processes accidentally. In XPS spectrum of all film surfaces, there was a decrease in amount of Zn and Se, and an increase in In peak intensities and also oxygen contamination following to post-annealing process. As the annealing temperature was increased, the Se peak intensities become smaller. This situation indicates a Se segregation and/or re-evaporation from the thin film structure with the annealing [216]. In addition to this analysis, high-resolution core level spectra were recorded for the In 3d, Zn 2p, Zn 3d and Se 2p regions in order to investigate binding energies in peak analysis, and to determine the peak decomposition and chemical shift due to a change in the chemical bonding of the elements.

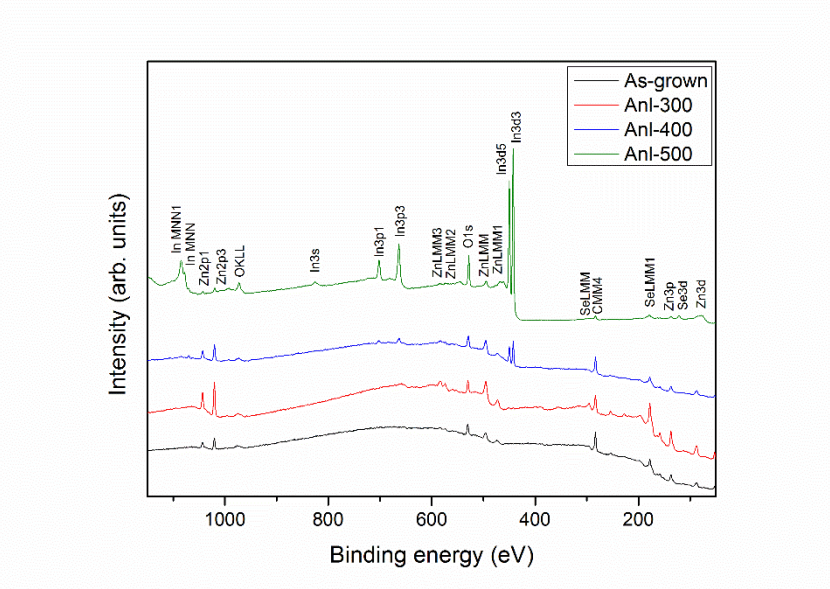

Figure 4.5: The XPS spectra of the as-grown and annealed ZIS thin films at different temperatures before sputtering

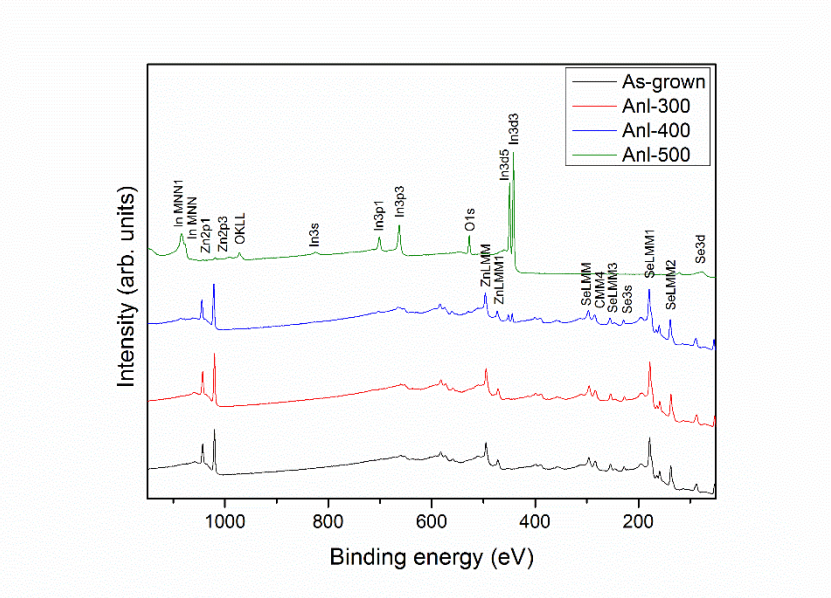

Figure 4.6: The XPS spectra of the as-grown and annealed ZIS thin films at different temperatures after first sputtering

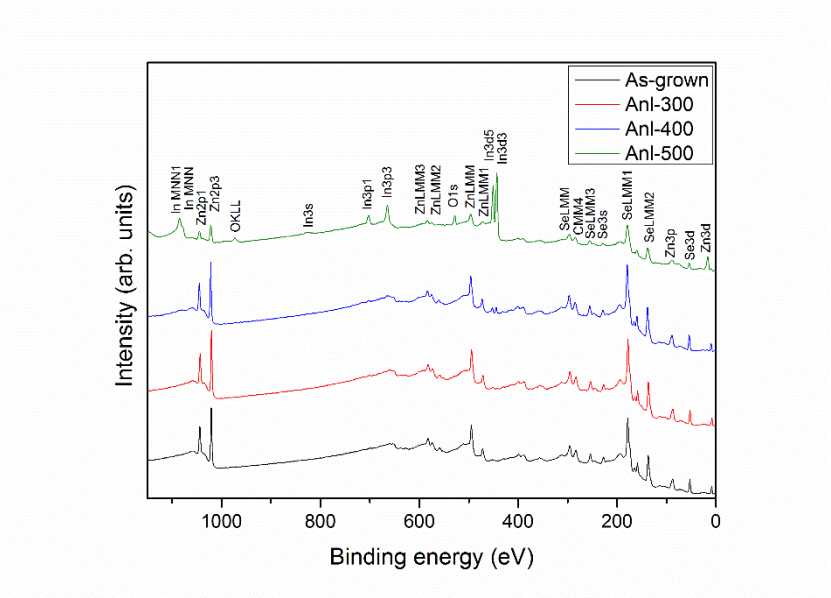

Figure 4.7: The XPS spectra of the as-grown and annealed ZIS thin films at different temperatures after second sputtering

Fig. 4.8 shows the In 3d core level spectrum which exhibit two peaks $3d_{5/2}$ and $3d_{3/2}$. The emissions of photoelectrons from In 3d levels cannot be resolved separately in the as-grown and annealed at 300 °C films (Fig. 4.8 (a) and (b)). In as-grown form, as seen in Fig. 4.8 (a), the In $3d_{3/2}$ peak was decomposed into three contributions

under the effect of all possible bonding with In. The change observed in In photoelectron line obtained from XPS study after annealing is consisted with behavior as found from compositional and morphological studies. The XPS analyses of this peak with fitting parameters were summarized in Table 4.2. The In-Se bonding observed in $3d_{3/2}$ peak analysis for as-grown films is disappeared with annealing because this process can trigger the possible Se segregation and re-evaporation on the film surface [217]. In addition, there is a metallic bonding formation between In and Zn in these two films. This peak was decomposed as In-Zn bond in terms of their electronegativity values. Since Se is more electronegative than Zn, the positive chemical shift may be occurred with In-Zn bonding. The physical fact may be due to the surface characteristics in terms of Zn crystallites. However, the XPS signal of In 3d core level are well separated due to spin-orbit coupling into $3d_{3/2}$ and $3d_{5/2}$ components in the films annealed at higher temperatures, 400 and 500 °C. The binding energy values obtained from In $3d_{5/2}$ peak are also given in Table 4.3 and corresponding energy separation between these two components formed by the spin-orbit coupling are calculated as 5.1, 7.5, 7.8 and 7.6 for the as-grown film and annealed films at 300, 400 and 500°C respectively. These interactions between Zn and Se with In, indicates the very low diffusivity of indium in the films. However, there is a distinct variation on Zn and Se with annealing. This is in agreement with earlier studies of the diffusivity and solubility of indium in ZnSe [218].

Table 4.2: Decomposition parameters of In 3d photoelectron peak with respect to $3d_{3/2}$ line

Sample	Bonding	B.E (eV) (Observed)	B.E (eV) [Ref]
As-grown	In-Se	448.4	451.4 [219]
	In-In	452.1	
	In-Zn	455.5	
Annealed at 300 °C	In-In	450.7	451.4 [219]
	In-Zn	454.9	
Annealed at 400 °C	In-In	452.4	451.4 [219]
Annealed at 500 °C	In-In	451.1	451.4 [219]

Table 4.3: Decomposition parameters of In 3d photoelectron peak with respect to $3d_{5/2}$ line

Sample	B.E (eV) (Observed)	B.E (eV) [Ref]
As-grown	443.3	444.0 [220]
Annealed at 300 °C	443.2	444.0 [220]
Annealed at 400 °C	444.6	444.0 [220]
Annealed at 500 °C	443.5	444.0 [220]

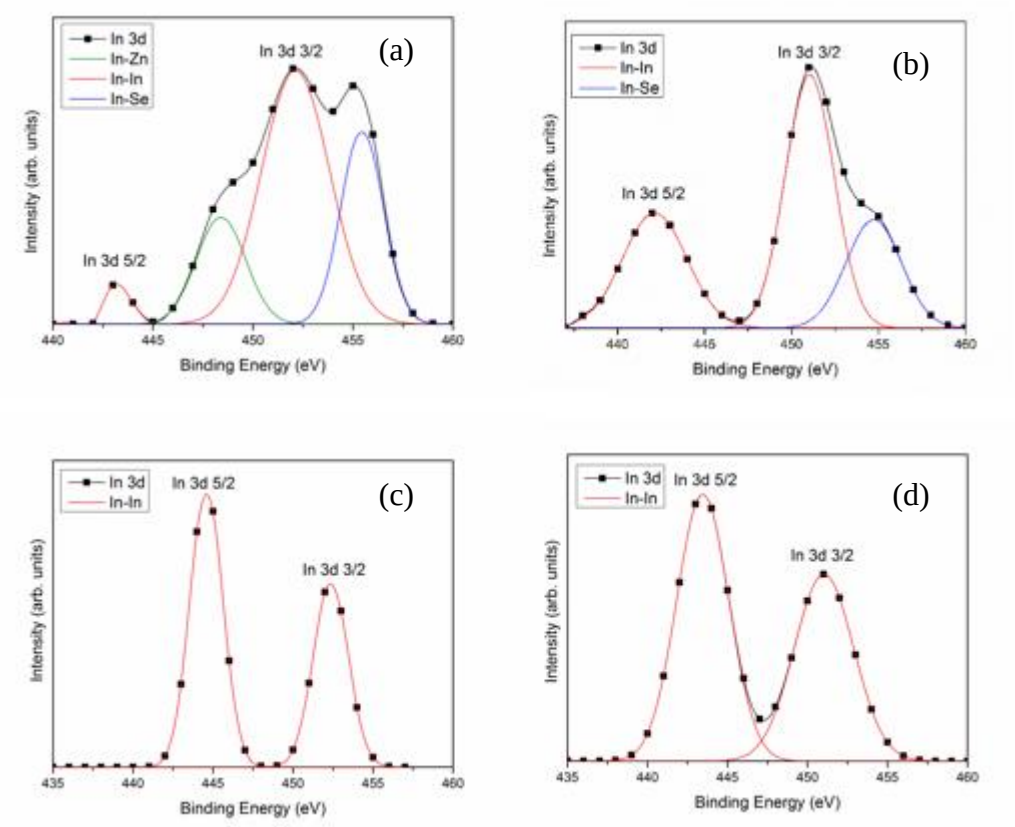

Figure 4.8: In 3d core level XPS spectrum for a) the as-grown and annealed ZIS thin films at b) 300, c) 400 and d) 500°C

The important Zn XPS lines observed in the XPS analysis are 2p and 3d. The corresponding 3d core level spectra are shown in Fig. 4.9. In evaluation Zn 3d peak of our samples, the splitting is not observed and also there is no any bonding contribution to Zn-Zn bond. The binding energy of this peak depending on annealing temperature is given in Table 4.4. Using high resolution analysis, there is only one 2p peak is detected (Fig.4.10). Therefore, the expected decomposition in this peak was

not occurred in our ZIS samples and the Zn 2p peaks obtained between 1020.2-1021.7 eV with changing annealing temperature. The corresponding fitting parameters are listed in Table 4.5. The reference value is used as 1021.8 eV for Zn [221] and this peak was found for ZnSe at 1021.5 eV [218].

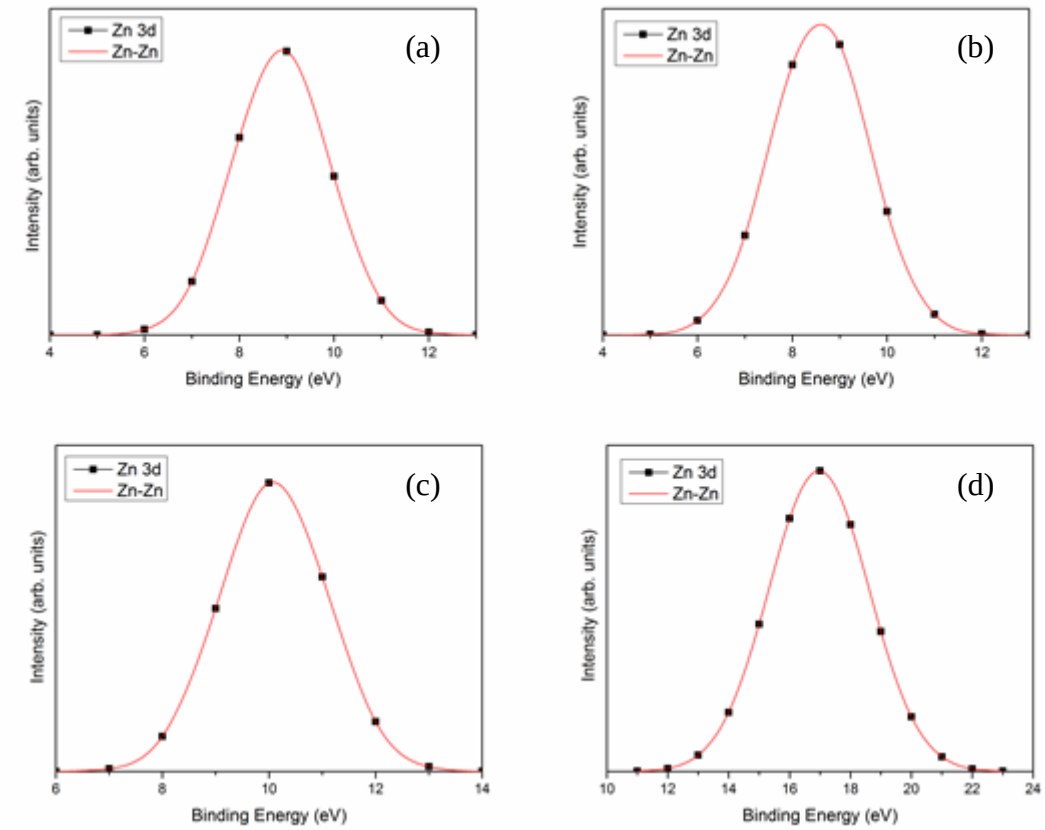

Figure 4.9: Zn 3d core level XPS spectrum for a) the as-grown and annealed ZIS thin films at b) 300, c) 400 and d) 500°C

Table 4.4: Decomposition parameters of Zn 3d photoelectron peak with respect to $3d_{5/2}$ line

Sample	B.E (eV) (Observed)	B.E (eV) [Ref]
As-grown	9.2	10.2 [221]
Annealed at 300 °C	9.2	10.2 [221]
Annealed at 400 °C	10.2	10.2 [221]
Annealed at 500 °C	16.9	10.2 [221]

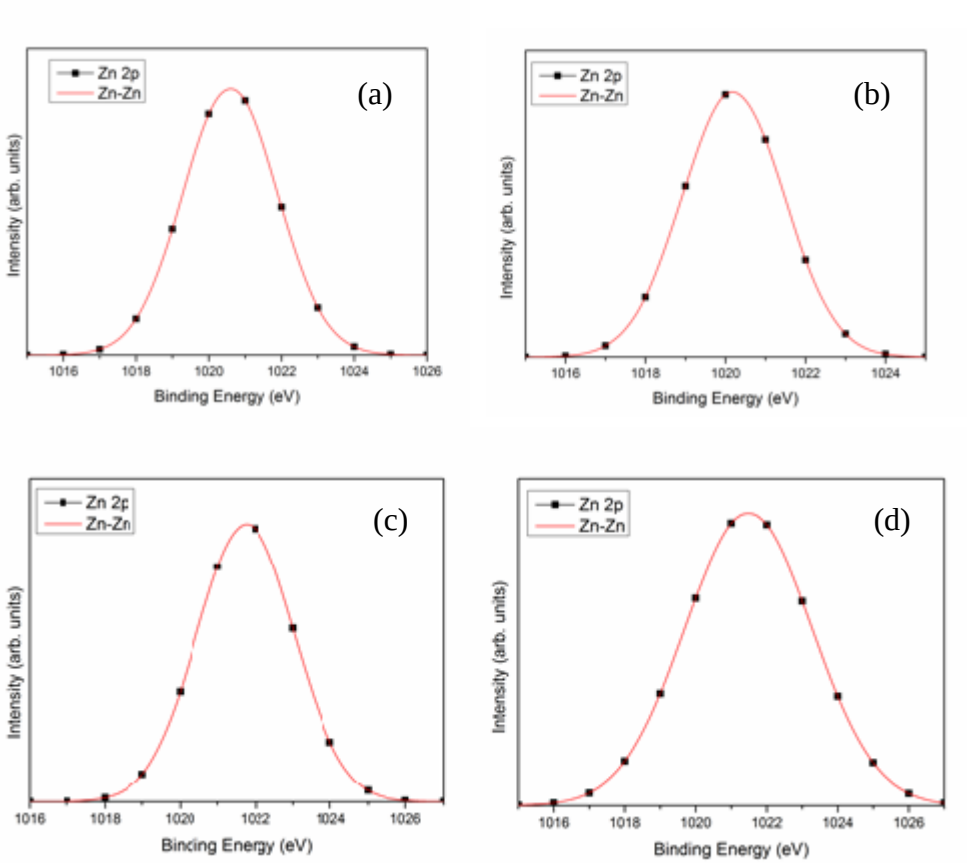

Figure 4.10: Zn 2p core level XPS spectrum for a) the as-grown and annealed ZIS thin films at b) 300, c) 400 and d) 500°C

Table 4.5: Decomposition parameters of Zn 2p photoelectron peak with respect to $2p_{3/2}$ line

Sample	B.E (eV) (Observed)	B.E (eV) [Ref]
As-grown	1020.6	1021.8 [219]
Annealed at 300 °C	1020.2	1021.8 [219]
Annealed at 400 °C	1021.7	1021.8 [219]
Annealed at 500 °C	1021.5	1021.8 [219]

According to peak fitting analysis, for the elemental photoelectron line analysis for Se, any possible contribution due to bonding with constituent elements are not seen within the tolerance of experimental errors. In other words, there is only one chemical bonding detected. The formation of Se 3d peak is given in Fig. 4.11. From the XPS spectra for ZIS film surfaces, the binding energy peak of the Se atoms are

observed between 52.7 and 54.1 eV under the effect of annealing process (Table 4.6). Because Zn and In are less electronegative than Se, the experimental results showed that there is a slight negative chemical shift from the previous works [222]. The change in the surface of the films and also compositional variations depending on the annealing temperature might be responsible to the change in Se photoelectron peaks.

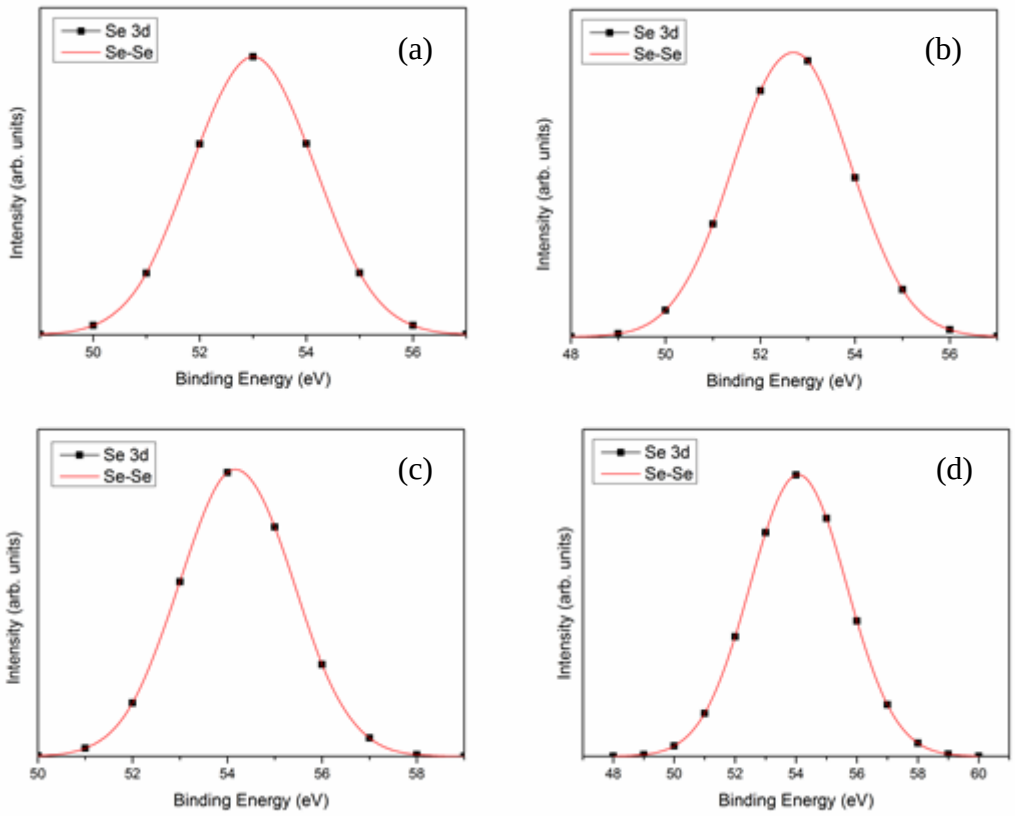

Figure 4.11: Se 3d core level XPS spectrum for a) the as-grown and annealed ZIS thin films at b) 300, c) 400 and d) 500°C

Table 4.6: Decomposition parameters of Se 3d photoelectron peak with respect to $3d_{5/2}$ line

Sample	B.E (eV) (Observed)	B.E (eV) [Ref]
As-grown	53.1	55.5 [222]
Annealed at 300 °C	52.7	55.5 [222]
Annealed at 400 °C	54.2	55.5 [222]
Annealed at 500 °C	54.1	55.5 [222]

4.3 Optical Characterization of $ZnInSe_2$ Thin Films

To describe the physical properties of ZIS thin film structure deposited by PVD technique, the description based on the crystalline structure, composition and surface characteristics in the material were given in the previous section. The results of the structural characterization of these samples were discussed in detail under the effect of annealing temperature. On the other hand, for the aim of the device applications, it is important to get detailed information about their optical properties, such as electronic band structure and optical constants.

In this part, the optical properties of ZIS samples were defined as the interaction between electromagnetic radiation and these semiconducting materials, including transmission, refraction and absorption. The transient nature of the optical properties of semiconductors is important to establish because it gives insight to the various relaxation processes that occur after optical excitation. Therefore, the characterization and optimization the optical properties of the films are important part for device applications, such as solar cell fabrication. In order to analyze the optical characteristics of the samples, transmittance measurements were carried out in between 300-2000 nm at room temperature. The response of the samples in a specific region of interest of the electromagnetic spectrum gives an overview of optical constants, such as, absorption coefficient, refractive index, band gaps, the wavelength dependence of transmittance spectrum was performed. Fig. 4.12 shows the spectral behavior of the transmittance values of the ZIS films in wavelength region of interest with respect to the annealing process. As mentioned in the previous

section, the annealing process was applied by using annealing furnace under the nitrogen atmosphere in the temperature range of 300-500 °C for 30 minutes. As seen from Fig. 4.12, there are interference fringes in the transmittance spectrum of all films with a sharp fall at the band edge in the region 600–2200 nm; whereas the interference effects disappear below this region. A similar interference behavior was reported previously [23, 27, 36, 223] for different deposition techniques and structural formations. Initially, these uniform sequential maxima and minima of the fringes at the transparent wavelength region indicate optical flatness and thickness uniformity of the deposited films even if the annealing processes were applied [23, 26, 224]. Uniformity was also checked together with the homogeneity by SEM and AFM measurements. The optical transmission values of the films were between 80 and 90% in the transparent region. Moreover, both as-grown film and the film annealed at 300 °C showed similar transmittance behavior, in the further annealing process, this optical characteristics was changed and their optical spectra were so close to each other. However, there was a wavelength shift in the transmission spectrum of all samples and a remarkable change in the transmission of the 400 and 500 °C annealed films. The transmittance values were approximately in the same magnitude, as the annealing temperature increases. As the surface of the samples become more reflective due to the morphological changes depending on the compositional changes, the decrease in the transmittance was the expected optical behavior with annealing process [207, 224]. On the other hand, due to the remarkable change in the thickness of the films, this effect can slightly be observed on the optical measurements. As expected, the structural and surface modifications on the films with annealing could trigger this result in transmittance values.

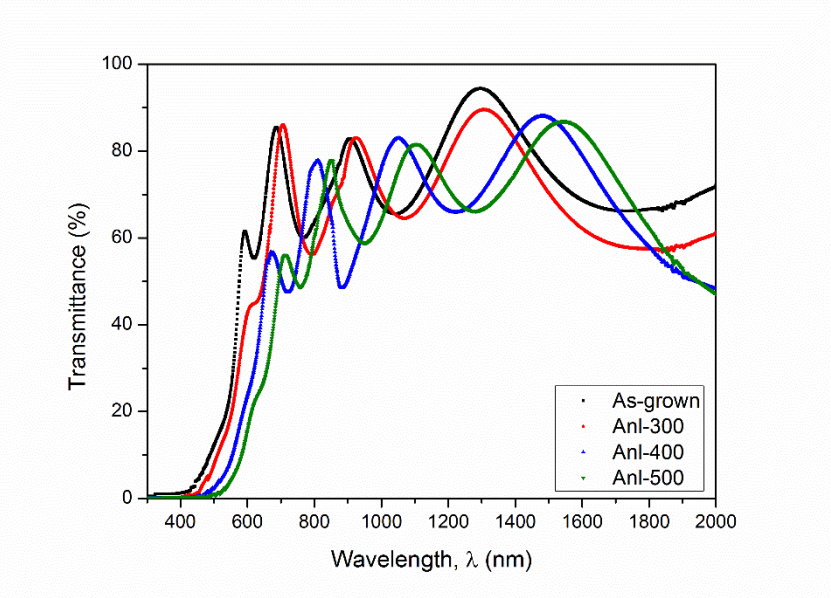

Figure 4.12: The transmittance spectra of the ZIS samples

Because there are interference patterns in the transmission spectra of the films, the envelope model (EM) can be used to determine their refractive indices [223, 225]. With taking care of all possibilities on the reflection and transmission events in the boundaries due to the local fields, the complex refractive index, $\tilde{N}(\lambda)$, can be written as,

$$\tilde{N}(\lambda) = n(\lambda) - i\kappa(\lambda) \tag{4.3}$$

where the real and imaginary part of $\tilde{N}(\lambda)$ is defined as $n(\lambda)$ and $\kappa(\lambda)$. Note that, they are all real and positive numbers. Moreover, $\tilde{N}(\lambda)$ itself and its components n and κ are wavelength dependent [226]. In this analysis, the imaginary part of the refractive index, κ, also called as extinction coefficient or attenuation index, denotes absorption of optical energy by the semiconductor material [227] and n is the ordinary refractive index. The refractive index for each sample was analyzed in the wavelength region 800-2000 nm in the weak and medium absorption regions [81]. This model deals with the interference effects therefore the strong absorption region where the interference fringes are not observed is out of interest for this analysis. In the application of this method, at least two interference fringes in their weak absorption and transparent spectral regions should be determined in order to construct envelope

curves in transmission spectra [223, 225]. Working on EM, the real part of the refractive index, $n(\lambda)$ can be obtained as [225],

$$n = [\mathrm{N} + (N^2 + n_s^2 n_0^2)^{1/2}]^{1/2} \tag{4.4}$$

where

$$N = \frac{n_0^2 + n_s^2}{2} + n_s n_0 \frac{T_M - T_m}{T_M T_m} \tag{4.5}$$

From the Eq. 4.3, $n(\lambda)$ can be determined by using the maxima $T_M(\lambda)$ and minima $T_m(\lambda)$ in the transmission spectra; the refractive index of the substrate, n_s; and the refractive index of the surrounding medium, n_0 at the same wavelength value. In this case, n_0 is the refractive index of the air and approximately equals to 1, and for our soda-lime glass substrate n_s is about 1.53 at λ~547 nm [182]. By optical measurements n_s can also be determined from the substrate's transmission spectra [228] given as;

$$n_s = \frac{1}{T_s} + \left(\frac{1}{T_s^2} - 1\right) \tag{4.6}$$

where T_s is the maximum transmittance of the substrate in the measured spectra. This peak value can be chosen in a region of interest, or at a specific value since there is no any interference effect on the spectra of the glass substrate.

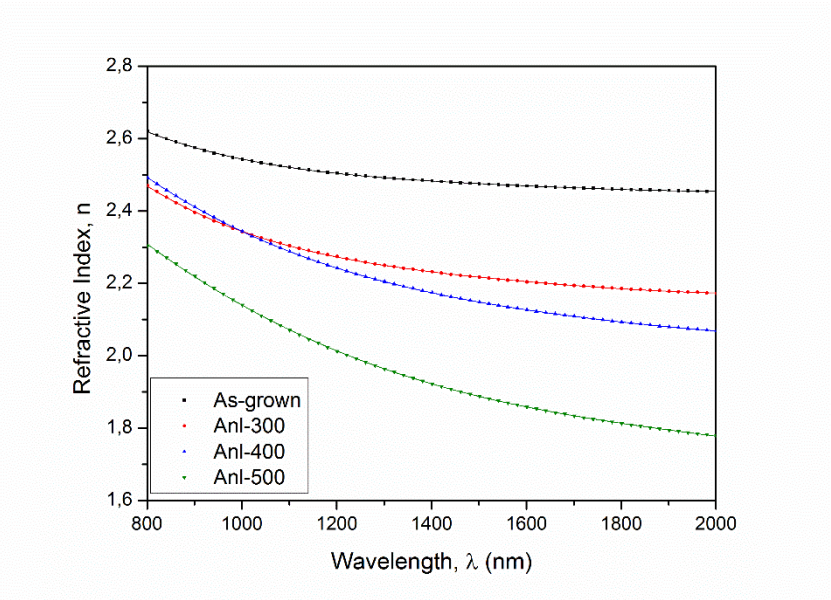

Figure 4.13: The refractive indices of the ZIS samples calculated by EM method (dot) and by three term Cauchy relation (line)

The refractive indices found by EM are shown in Fig. 4.13. As a result of EM, the refractive index values were between 1.8 and 2.6 depending on the annealing temperature and wavelength region. As observed in other ZIS studies, the calculated *n* values decrease in increasing wavelength [27], and also in increasing annealing temperature up to 500 °C [14, 23]. With the annealing process, because of re-evaporation and/or segregation of the elements from the surface of the films and decrease in the thickness of the films, the decrease in the density of the films may be the reason of this type of change in the refractive index values. To get a wavelength dependent relation, these values can also be evaluated by the Cauchy dispersion relation [229];

$$n(\lambda) = \mathrm{A} + \frac{B}{\lambda^2} + \frac{C}{\lambda^4} + \cdots \qquad (4.7)$$

This equation was developed for a substances transparent in visible region and Cauchy parameters, A, B, C, … are all constants in fitting process depend on the optical characteristics of the film. In our case, three-term Cauchy fitting is sufficient

to provide a reasonable fit (Fig. 4.13). The calculated values of the Cauchy parameters were given in Table 4.7 for all samples.

Table 4.7: Three term Cauchy parameters of the ZIS samples

Sample	A	B (nm^2)	C (nm^4)
As-grown	2.43	$9.96x10^4$	$1.57x10^{10}$
300 °C Annealing	2.12	$2.28x10^5$	$5.46x10^6$
400 °C Annealing	1.96	$4.66x10^5$	$-7.88x10^{10}$
500 °C Annealing	1.63	$6.64x10^5$	$-1.45x10^6$

From the refractive indices (n_1 and n_2) of two adjacent maxima or minima (λ_1 and λ_2) in the measured spectra, the thickness approximation of the samples can be done with the following relation [223];

$$d = \frac{\lambda_1 \lambda_2}{2(\lambda_1 n_2 - \lambda_2 n_1)} \tag{4.8}$$

Although this equation is not very sensitive and accurate [221], this can be used to check the correctness of the applied EM [223, 230]. By using Eq. 4.8, the thickness of the films, d were calculated as 584, 577, 550 and 520 nm, for as-grown and annealed films, respectively. The calculated and measured thicknesses of the films were found to be in a good agreement with each other in the corresponding about 10 nm measurement error interval. Since the thickness values are in the estimating error limits with the profilometer, the obtained n values by applying EM, can be accepted with small deviations.

The other optical constant, $\kappa(\lambda)$ can be calculated from the absorption coefficient $\alpha(\lambda)$ as [81];

$$\alpha(\lambda) = \frac{4\pi}{\lambda}\kappa(\lambda) \tag{4.9}$$

where $\alpha(\lambda)$ is related with the transmission values by means of the relation [33];

$$\alpha(\lambda) = \frac{1}{d}\ln\left(\frac{I_0}{I}\right) \tag{4.10}$$

In this relation, I_0 is the incident light perpendicular to the surface of the film, I is the intensity of transmitted light, d is the thickness of the film. In fact, the ratio I/I_0 is the transmittance value of the sample normalized by background signals. The obtained $\kappa(\lambda)$ values are shown in Fig.4.14, and they were found in decreasing behavior with increasing wavelength. Although there is a sharp decrease in $\kappa(\lambda)$ values depending on wavelength and also an observable difference occurred with applying high annealing temperatures (400 and 500 °C), there is no remarkable change in $\kappa(\lambda)$ values for as-grown and annealed at 300 °C.

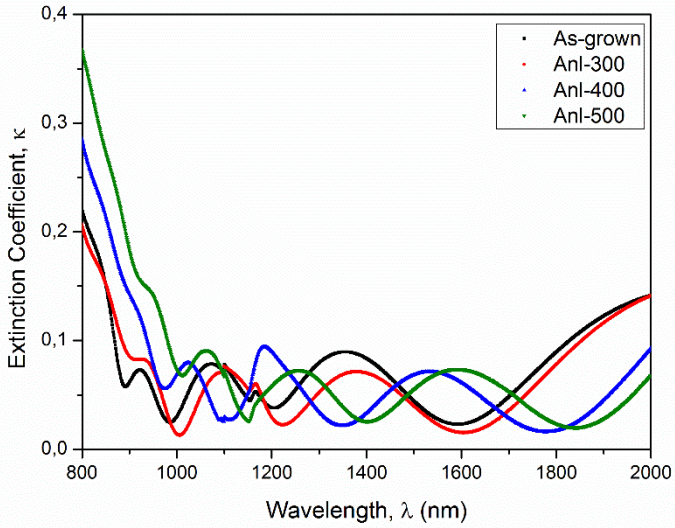

Figure 4.14: Calculated extinction coefficients for the ZIS samples

The complex refractive index of the material is related to complex dielectric function as given below [81, 231];

$$\varepsilon(\lambda) = \left(\tilde{N}(\lambda)\right)^2 \tag{4.11}$$

where $\varepsilon(\lambda)$ is evaluated in terms of its real and imaginary parts as;

$$\varepsilon(\lambda) = \varepsilon_{re}(\lambda) + i\varepsilon_{im}(\lambda) \tag{4.12}$$

Therefore, knowing $n(\lambda)$ and $\kappa(\lambda)$ values, these components of $\varepsilon(\lambda)$ can be obtained from the following relations;

$$\varepsilon_{re}(\lambda) = \mathrm{n}^2(\lambda) - \kappa^2(\lambda) \tag{4.13}$$

and

$$\varepsilon_{im}(\lambda) = 2\mathrm{n}(\lambda)\kappa(\lambda) \tag{4.14}$$

The variations of these optical constants $\varepsilon_{re}(\lambda)$ and $\varepsilon_{im}(\lambda)$ in the wavelength interval of 800-2000 nm, can be evaluated in similar behavior with $n(\lambda)$ and $\kappa(\lambda)$. Note that, in this analysis, the calculated $\kappa(\lambda)$ values should be very small as compared with $n(\lambda)$ values. Fig. 4.15 illustrates the calculated $\varepsilon_{re}(\lambda)$ values in terms of change in wavelength.

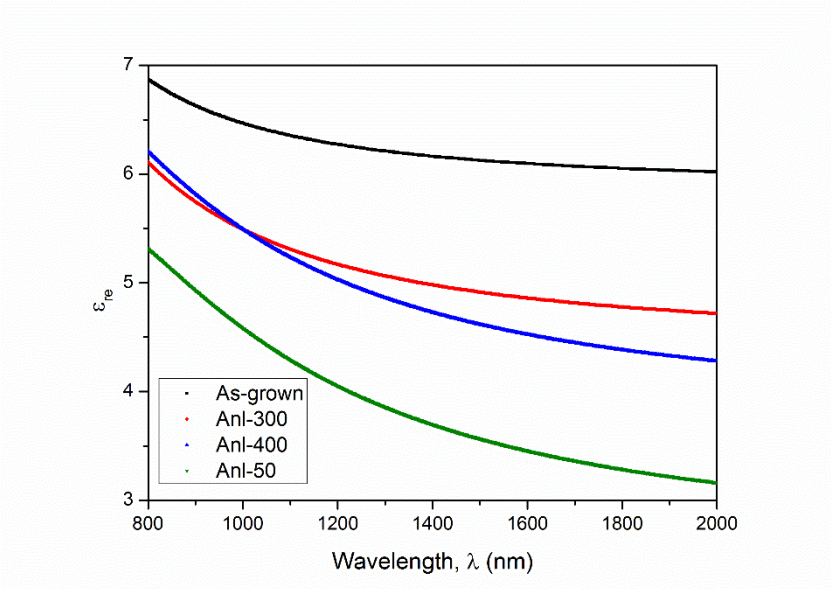

Figure 4.15: Real part of the dielectric constants for the ZIS samples

To get a further knowledge about the refractive index, its dispersion in the semiconducting material can be calculated by a semi-empirical single-effective-oscillator model (SOM) [232, 233]. This model gives reliable results for photon energies below the inter-band absorption edge. It is related to the refractive index of the sample with the inter-band optical transitions and electronic band structure as;

$$n(E)^2 - 1 = \frac{E_p E_d}{E_p^2 - E_d^2} \tag{4.15}$$

where E_d is a parameter that gives a measure of the the inter-band optical transitions strength, E_p relates with the energy gap value and it is also named as the oscillatory energy, and E represents the photon energy *(hv)*. By applying this relation, *n(hv)* values can be fitted to get corresponding SOM parameters (Fig. 4.16) and the results are also listed in Table 4.8. By the analysis of E_d values, it was defined that the strongest optical transition probability is dominant for the as-grown samples and this probability is in decreasing behavior with increasing annealing temperature.

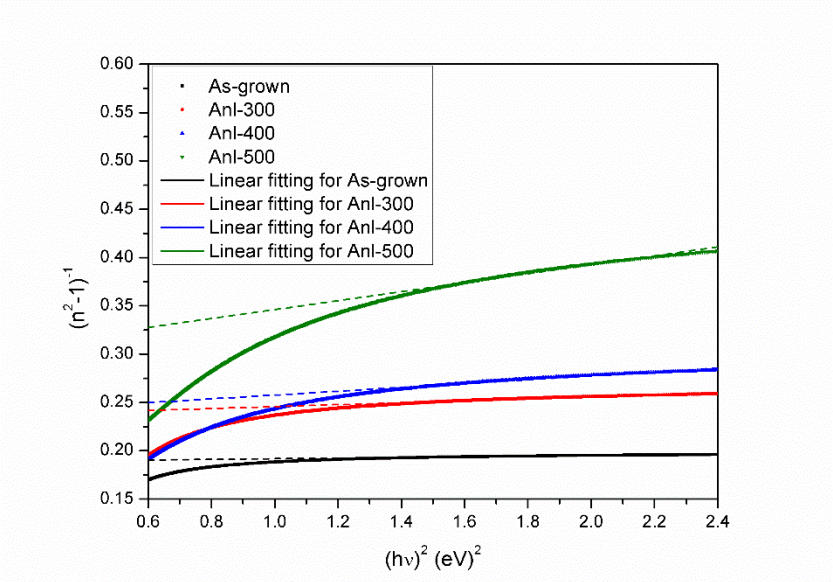

Figure 4.16: Plots of $(n^2 - 1)^{-1}$ vs. $(h\nu)^2$ for ZIS samples

Static and high frequency response of the samples can also be estimated from this dispersion relationship [104]. By extrapolation of the linear part of the plots given in Fig.4.16, the static refractive index *n(0)* and from the corresponding intercept values,

the static dielectric constant $\varepsilon(0)$ can be calculated. Moreover, these values can be found by $n^2(0)=1+ E_d / E_p$ and $\varepsilon(0)=n^2(0)$ [19]. The obtained SOM relations in Fig.4.16 gives a linear behavior between 2.1 and 1.4 eV values, these parameters were calculated from the fitting process in this region. Apart from these low-frequency parameters, the high frequency dielectric constant ε_∞ can be obtained from the $\varepsilon_{re}(\lambda)$ values of the films [225]. This relation can be analyzed from the Spitzer–Fan model [234, 235] as;

$$\varepsilon_{re}(\lambda) = \varepsilon_\infty - \left(\frac{e^2 N}{\pi c^2 m^*}\right)\lambda^2 \tag{4.16}$$

where N is the number of unit cells per unit volume, m^* is the effective mass of the material, e is the electronic charge and c is the speed of light. The real part of the dielectric function asymptotically approaches to $\varepsilon(0)$ below the reststrahlen region, and also it is connected to ε_∞ in the reststrahlen-near-IR range in the optical spectra [81]. These constants are also related to each other with long-wavelength lattice-optical modes by Lyddane-Sachs-Teller relation [236]. This relation gives the information about the amount of the polar characteristics in the chemical bonds of these structures [81]. The results for the deposited ZIS films obtained from the detailed SOM analysis are given in Table 4.8. From SOM analysis ε_∞ was found as 6.69 for as-grown films which is very close to the value reported by Zeyada et al. [14]. Since $\varepsilon(0)\sim\varepsilon_\infty$, as reported in ZnSe structures [236], the hetero-polar character is dominant with respect to homo-polar character in these samples. Moreover, the variation of the obtained optical constants with annealing temperature is in a good agreement with the work reported by El-Nahass et al. [23].

Table 4.8: SOM parameters of the ZIS samples

Sample	E_p (eV)	E_d (eV)	$n(0)$	$\varepsilon(0)$	$\varepsilon(\infty)$
As-grown	3.796	18.546	2.514	6.319	6.701
300 °C Annealing	2.649	9.361	2.293	5.256	5.332
400 °C Annealing	2.140	6.581	2.285	5.219	5.138
500 °C Annealing	1.796	3.622	2.084	4.345	4.292

In the visible and near-visible region, the absorption coefficient of the as-grown and annealed samples was found to be between 10^3 and 10^4, and there is no significant difference in these values in terms of thermal annealing. The wavelength range 400–700 nm determines the transparent region in the optical spectra and this region can be used to evaluate the type of optical transition and the corresponding value of energy gap. Basically two types of optical transition, direct and indirect, can occur at the fundamental edge of crystalline semiconductors. The absorption coefficient $\alpha(\lambda)$ at the optical absorption edge varies with the photon energy $(h\nu)$ according to the expression [227, 237];

$$(\alpha h\nu) = A\left(h\nu - E_g\right)^m \tag{4.17}$$

where A is an energy-independent constant, but it depends on the transition probability, and E_g is the energy gap value. In this relation, the power m is related to the band gap characteristics of the structure; it can be $m=1/2$ or $m=2$ for direct and indirect transition in the band gap respectively. Then, the plot of the optical absorption coefficient $(\alpha h\nu)$ versus photon energy $(h\nu)^m$ for different m values showed principle regions as in the work of Wood and Tauc [237, 238]. In the spectral region where absorption is strongly effective, the absorption coefficient can be analyzed related to the band gap energy. Therefore, the band-gap values of the samples were calculated from transmission data using absorption coefficient and the band gap relation given in Eq. 4.17 above. The data obtained from the absorption analysis of the films showed the existence of allowed direct transitions. In this structure, two absorption mechanisms, direct and indirect transitions, are possibly expected for this material [12, 14, 21, 23, 28, 239]. Based on the band gap analysis, the corresponding figures for direct band gap transition, $(\alpha h\nu)^2$ versus $h\nu$ curves, are shown in Fig. 4.17 (a-d). This type of semiconductors is the structural analogs of II-VI compounds, and therefore direct band gap can be expected in the visible region of the spectrum [240, 241]. In addition, the case of Zn-rich may be accepted as the reason of this type of transition in the deposited film structure [242]. In general, there are contradictions on the nature of the optical absorption in this material. The difference between the reported works was evaluated due to the difficulty in

determination of band gap by optical spectroscopy [242], deposition techniques and variations in the elemental composition [28]. Since there are three linear contributions in the direct band gap transition curves, the effect of spin-orbit and crystal-field perturbations were taken into consideration in the analysis of ZIS structures [230]. However, there is no other work considering the splitting on valence band. The calculated optical band gap values were assigned as the band splitting correspondence of the energy levels. The crystal-field splitting (CF) and the spin-orbit splitting values were determined by the following quasicubic relation [94].

$$E_{1,2} = -\frac{1}{2}(\Delta_{CF} + \Delta_{SO}) \pm \frac{1}{2}\left((\Delta_{CF} + \Delta_{SO})^2 - \frac{8}{3}(\Delta_{CF}\Delta_{SO})\right)^{1/2} \quad (4.18)$$

where $E_{1,2}$ energy differences between the direct transitions obtained from band gap analysis. The results obtained from this absorption process observed in the optical spectra of these films at room temperature are listed in Table 4.9. The band gap values revealed that the energy gap values for all transition levels decreases under the effect of increasing annealing temperature. This may be attributed to the decrease the increase in the crystalline part and decrease in the absorption edge [23].

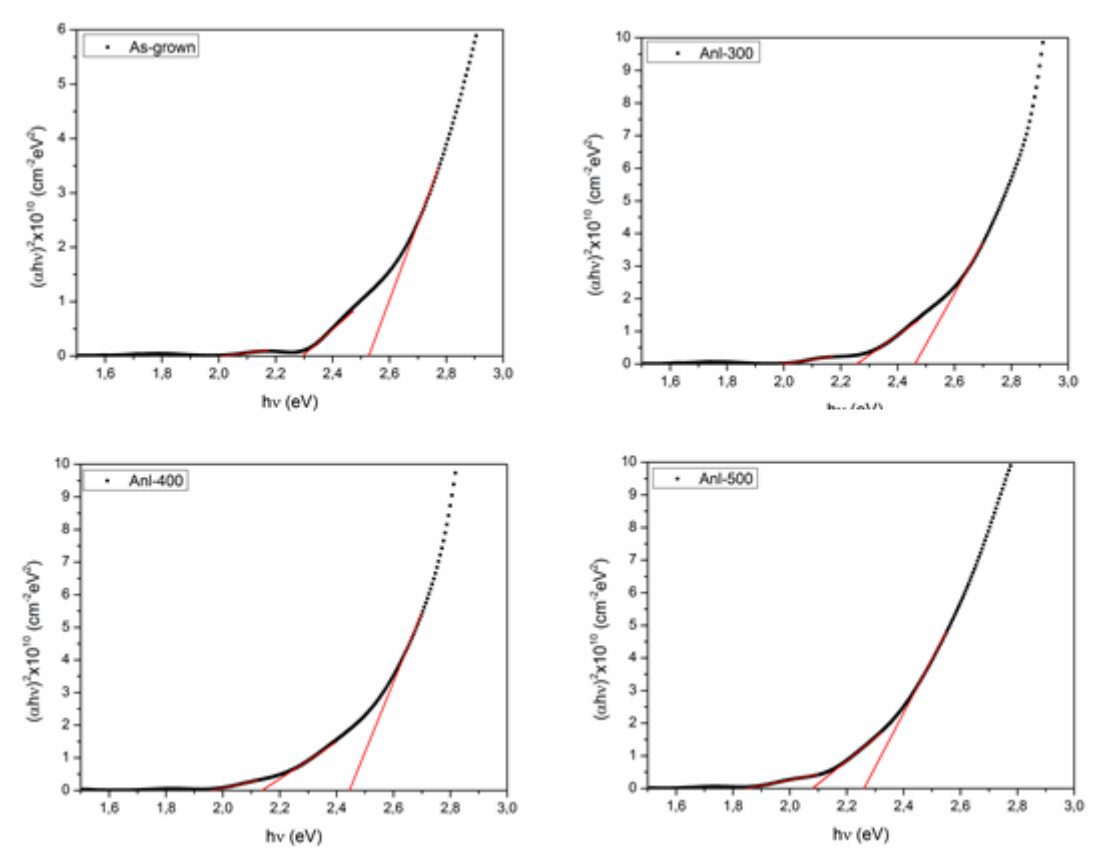

Figure 4.17: The variation of $(\alpha h\nu)^2$ with the photon energy for ZIS samples

The optical absorption coefficient just below the absorption edge was found to vary exponentially with photon energy and this relation is referred as Urbach's tail [243, 244]. In this low energy region, the exponential tail of the absorption coefficient can be written as [81, 243]:

$$\alpha = \alpha_0 exp\left(\frac{h\nu - E_g}{E_U}\right) \tag{4.19}$$

where E_U is the energy correspondence of Urbach's tail, E_g is an energy close to the band gap energy and α_0 is a characteristic parameter for this relation. Urbach energy E_U is an indication of the structural perfection of the materials and it is observed due to the localized states produced by disordered and amorphous structures in band gap region [245]. By using Eq. 4.19, these energy values were calculated from *ln(α)* versus *hν* plots given in Fig. 4.18. Applying linear fitting analysis, the obtained

values were listed in Table 4.9. E_U values were found in decreasing behavior with increasing annealing temperature that may be related to the improvement in the structure.

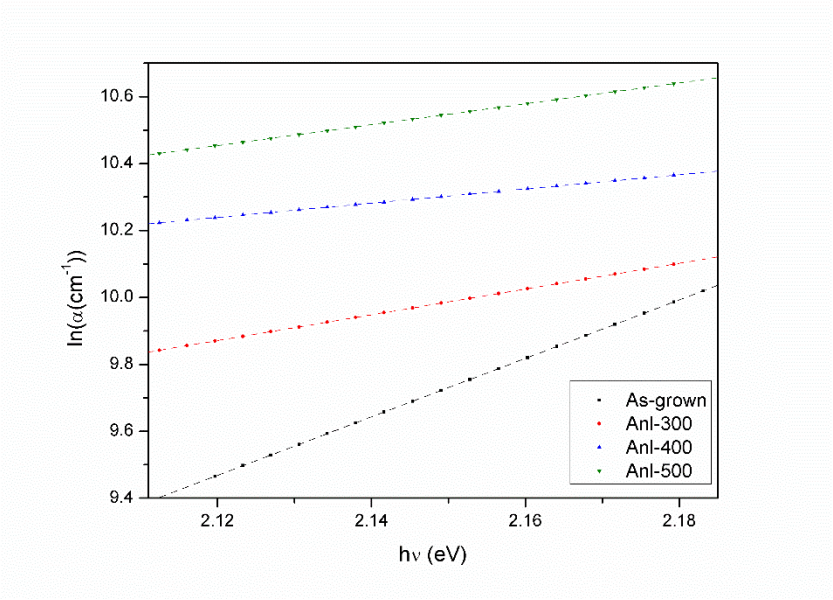

Figure 4.18: Plots of *ln(α)* versus *hν* for ZIS samples

Table 4.9: Band gap and Urbach tail values of the ZIS samples (in terms of eV)

Sample	$E_{d,1}$	$E_{d,2}$	$E_{d,3}$	Δ_{CF}	$-\Delta_{SO}$	E_U
As-grown	2.00	2.29	2.52	0.315	0.185	0.261
300 °C Annealing	1.98	2.26	2.46	0.295	0.388	0.172
400 °C Annealing	1.95	2.14	2.45	0.329	0.365	0.110
500 °C Annealing	1.85	2.09	2.26	0.207	0.163	0.109

4.4. Electrical and Photo-Electrical Characterization of $ZnInSe_2$ Thin Films

The electrical properties of the ZIS thin films were measured by carrying out temperature dependent dark- conductivity and photo-conductivity; and room temperature Hall Effect and photo-response measurements. For this purpose, the samples were prepared in a cloverleaf (Maltese-Cross) contact geometry [183, 184]. Then, the dark-conductivity values were measured by using van der Pauw method [192, 193]. It is a standard technique for investigating the electrical conductivity

characterization of thin film materials using four point contacts formed on the circumference of the sample arbitrarily. This method is widely used since it decreases the measurement errors which arise in classic characterization techniques due to the possibility of contact resistance and also it gives opportunity to apply it for samples of any shape [194]. In this measurement technique, resistance value of the sample can be determined by the ratio of potential difference between two contacts and applied current as $R=\Delta V/I$, and then the resistivity value can be evaluated as [195]:

$$\rho = f\left(\pi d/\ln(2)\right)\left(R_a + R_b + R_c + R_d/4\right) \tag{4.20}$$

where d is the film thickness, f is the correction factor, $R_{a\text{-}d}$ are the resistance values for each combinations of four contacts. Then, from the average of all contact measurements, conductivity values, $\sigma=1/\rho$, can easily be determined from this method. In addition, ZIS structures are in a good ohmic behavior with In contacts [26], therefore the electrical contacts were prepared by thermal deposition of pure In on the films. Fig.4.19 gives the dark-conductivity of the samples, in as-grown form and also annealed at different annealing temperatures, as a function of sample temperature. Since the deposited film was in polycrystalline form with annealing, it conserved this structural characteristic; grain formations and their boundaries are the most effective factor in the electrical conduction processes. In these regions, a reasonably high concentration of active trapping sites exists and they cause capturing of charge carriers at the grain boundaries. In the polycrystalline thin films, they are the most dominant and the least controllable structural formations [246]. As seen in Fig. 4.19, the conductivity values were in increasing behavior with annealing process. This result describes the increase in conductivity with an increase amount of lattice perfections [197]. For as-grown and annealed at 300 ºC films, there was a considerable change in the conductivity behavior with temperature. However, as annealing temperature increases above 300ºC, the conductivity of the sample shows semi-metallic, namely degenerate, behavior. This situation generally explained by segregation and/or re-evaporation of constituent elements from the surface and the compositional change in the film structure [207, 247]. The dark-conductivity values

show an approximately various linear dependences on temperature change in the intervals of studied temperatures. Therefore, the conduction characteristics of these films were analyzed in three different temperature regions by applying all possible conductivity mechanism models. Under this aim, the slope of the straight line regions in conductivity versus temperature plot were calculated and compared with the maximum correlation coefficient (R^2) of the best fits [248]. The samples show similar conduction behaviors in each other except their magnitudes.

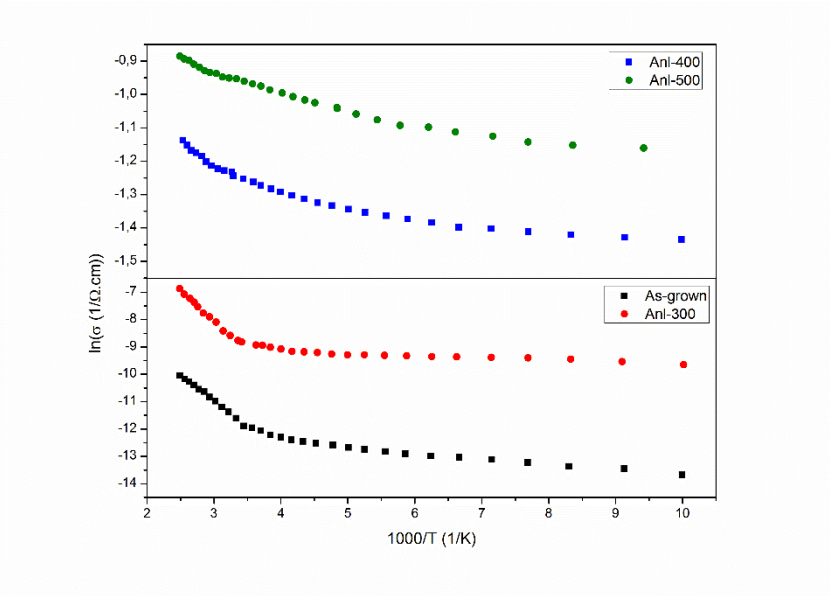

Figure 4.19: Temperature dependent electrical conductivity of as-grown and annealed ZIS films

As seen in Fig.4.19, the conductivity of all samples are in Arrhenius behavior in the high temperature region, above room temperature, and the most possible conduction mechanism in this temperature region is thermionic emission mechanism [133]. This increase is mainly based on the thermal excitation of carriers, from the defect state formations due to the imperfections or across the band gap between top of the valence band and bottom of the conduction band [28]. This conductivity model can be evaluated as;

$$\sigma_{TE} = \sigma_{0TE} T^{1/2} exp\left(-{}^{E_a}/_{k_B T}\right) \tag{4.21}$$

where σ_{0TE} is the pre-exponential term, T is the ambient temperature, k_B is the Boltzmann's constant and E_a is the activation energy for this conduction mechanism. This mechanism is also related to the development of grain boundary potential well inside the structure and therefore increasing in crystalline structure with improvement in grain formations [247]. For this temperature region (see Fig. 4.20), the necessary fitting procedure was applied to the experimental data by using Eq. 4.21 to determine the thermal activation energies. These energy values obtained from this model are 175.4 and 200.2 meV for as-grown and 300 °C annealed samples, respectively. The calculated energy values increases with increasing annealing temperature. This result can be evaluated in the same manner that there was an improvement in the crystallinity of the samples and single valance state formation observed in XPS analysis.

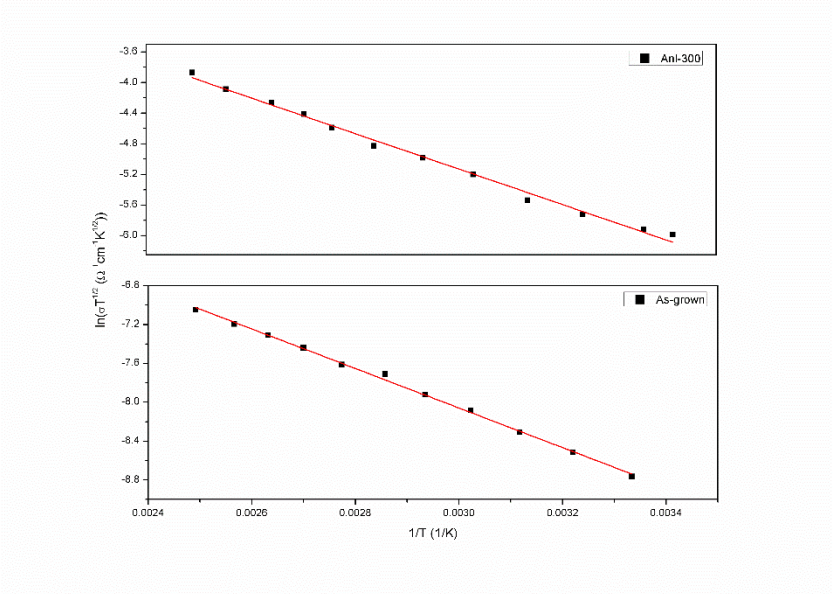

Figure 4.20: Plots of $ln(\sigma T^{1/2})$ versus T^{-1} in the high-temperature region for the ZIS film in as-grown form and annealed at 300 °C. Solid lines are the best fit lines according to Eq. 4.21

At lower temperatures, the hopping carrier transitions between localized states became dominant in the charge transport. Similar observations have been reported previously for ZIS films [14, 28]. In general, the hopping transport mechanism determines the electrical conduction in polycrystalline semiconductors in low temperature regions below the room temperature [142, 249, 250]. In this case, charge

carriers cannot pass over the grain boundary potential well due to the lack of enough thermal activation energy, and then conduction can occur by hopping between localized states near the Fermi energy [142]. In the low temperature region, the conduction mainly occurs by the variable range hopping (VRH). Different from the reported works on this structure [14, 28], the deposited films shows two different linear regions that can be defined by different VRH mechanisms.

The low temperature conductivity data for ZIS samples between 200 and 290 K obeys Mott's relation for the disordered materials [142]. In this region, best fitting parameters were obtained for the conductivity values by this model expressed as [152]:

$$\sigma_M = {\sigma_{0M}}/{T^{1/2}}\, exp\left(\left(-{T_{0M}}/{T}\right)^{1/4}\right) \tag{4.22}$$

where σ_{0M} is the pre-exponential parameter and T_{0M} is the characteristic temperature coefficient. These characteristic values for the samples were estimated from the straight-line nature of $ln(\sigma_M\ T^{-1/2})$ versus $T^{-1/4}$ plot (Fig. 4.21) by Mott's equation (Eq. 4.22). Moreover, σ_{0M} and T_{0M} can be defined as the following relations:

$$\sigma_{0M} = e^2 a_h^2 \nu_{ph} N(E_F) \tag{4.23}$$

and

$$T_{0M} = {\lambda\alpha^3}/{k_B N(E_F)} \tag{4.24}$$

where e is the electronic charge, α_h is the variable hopping distance, ν_{ph} is the phonon frequency, $N(E_F)$ is the density of localized states around Fermi energy level (E_F), λ is the dimensionless constant, α is the localization radius for the wave functions of the localized states around the Fermi level. In this VRH model, T_{0M} is also related to the degree of disorder, T_{0M}/T, in the structure [251]. In addition, ν_{ph} is generally taken $\sim 10^{13}$ Hz [252]. Although the lower limit of λ was reported as to be 16 [207],

its common usage is about 18.1 [252]. The other important parameters in this model is average hopping distance, R_M,

$$R_M = \left({}^{9}/_{8\pi\alpha k_B T N(E_F)}\right)^{1/4} \tag{4.25}$$

and average hopping energy, W_M;

$$W_M = {}^{3}/_{4\pi R_M^3 N(E_F)} \tag{4.26}$$

For as-grown and annealed (at 300 °C) samples, the Mott's parameters calculated through the linear fitting of the conductivity values (Fig. 4.21) are tabulated in Table 4.10. Results in Table 4.10 show that T_{0M} values representing the disorder in the structure decreases with annealing. This is also confirmed by the structural analysis of the samples. The calculated $N(E_F)$ values indicate the trap states near the Fermi level decreases with annealing temperature. These results are found to be in the same order with the work reported by Zeyada et. al [14]. These values for the density of states at the Fermi level and in the band tails are high in the as-grown sample. α decreases and R_M increases by the effect of annealing process, and as a result of this, localization decreases with the annealing process. In addition, a decreasing behavior in the hopping energy values was observed in these samples in this work. In fact, the maximum correlation coefficient of the best fit is not enough for the validity of this model. These parameters can be acceptable within the Mott's requirements of the localized-state model as $\alpha R_M \gg 1$, which is related to the degree of localization, and $W_M \gg k_B T$. As given in Table 4.10, all samples are found to satisfy these requirements for the VRH model.

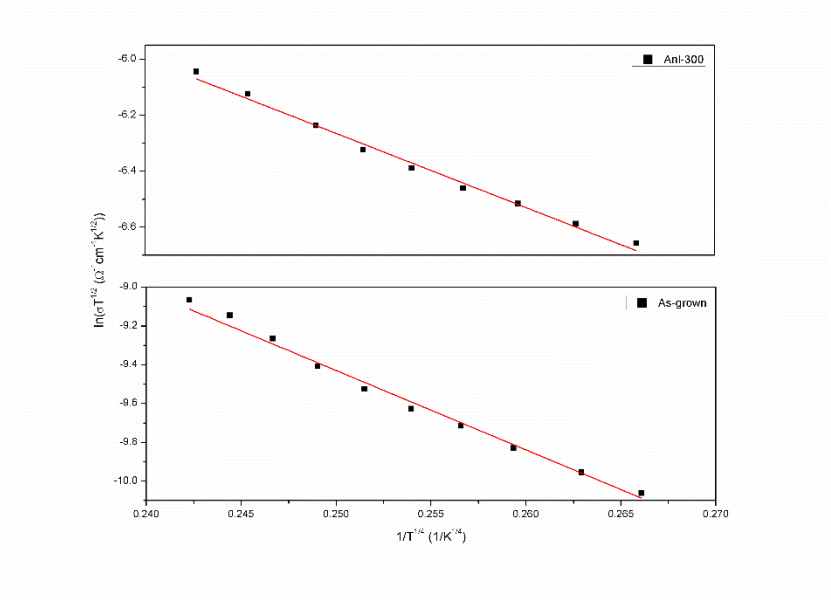

Figure 4.21: Plots of $ln(\sigma T^{1/2})$ versus $T^{-1/4}$ in the low-temperature region for the ZIS film in as-grown form and annealed at 300 °C. Solid lines are the best fit lines according to Eq. 4.22.

Table 4.10: Calculated parameters of Mott VRH model

Sample	T_{0M} (K)	σ_{0M} ($K^{1/2}/\Omega cm$)	α (1/cm)	$N(E_F)$(1/eVcm)
As-grown	2.88×10^{6}	2.22	3.20×10^{6}	3.20×10^{18}
Anl-300	5.16×10^{5}	1.56	1.05×10^{6}	4.70×10^{17}

Sample	R_M (cm)	W_M (meV)	R^2	αR_M	W_M/k_BT
As-grown	1.16×10^{-6}	47.3	0.97	4.12	2.74
Anl-300	2.55×10^{-6}	30.8	0.97	2.68	1.78

In the temperature range of 100–200 K, the validity of the Mott's model was not observed due to the limited temperature range of fit. In this region, Efros-Shklovskii VRH model [156] where Coulomb effect serves as a barrier to the conduction process was the well suited to the electrical conductivity values. As the temperature further decreased, Coulomb effect became important in the conduction mechanism

[253]. In this model, Mott's conduction behavior changes to the following temperature dependence under the effect of Coulomb interaction [153]:

$$\sigma_{ES} = {}^{\sigma_{0ES}}/_{T}\, exp\left(\left(-{}^{T_{0ES}}/_{T}\right)^{1/2}\right) \tag{4.27}$$

where again σ_{0ES} is the pre-exponential term and T_{0ES} is the characteristic temperature for this model. Fig.4.22 shows $ln\ (\sigma_{ES}T)$ versus $T^{-1/2}$ plot and the linear fitting on the conductivity values in the low temperature region, in the interval of 100–200 K. The characteristic temperature in Efros-Shklovskii VRH model becomes,

$$T_{0ES} = {}^{\beta\alpha e^2}\Big/_{4\pi k_B \varepsilon\varepsilon_0} \tag{4.28}$$

where β is a numerical coefficient, α is exponential decay constant defined in Mott's model, ε is the dielectric constant of the material and ε_0 is the free space permittivity. According to Shklovskii, et. al [153], β can be taken as about 2.8. For the Efros-Shklovskii type of conduction, the most probable hopping distance can be defined as:

$$R_{ES} = {}^{1}/_{4\alpha}\left({}^{T_{0ES}}/_{T}\right)^{1/2} \tag{4.29}$$

and also average hopping energy can be calculated from the following relation:

$$W_{ES} = {}^{1}/_{2}\, k_B T \left({}^{T_{0ES}}/_{T}\right)^{1/2} \tag{4.30}$$

According to this model, electron-electron interaction reduces the density of states at the Fermi level and therefore creates Coulomb gap. This gap width, in 3D case, can be expressed as [157]:

$$\Delta_{ES} = {}^{e^3 N(E_F)^{1/2}}\Big/_{(4\pi\varepsilon\varepsilon_0)^{3/2}} \tag{4.31}$$

In this phenomena, the occupied states are separated from empty states by the gap equal to Δ_{ES} [157]. The all hopping parameters related to this conduction model are listed in Table 4.11. Similar to the Mott VRH model, the hopping parameters in Efros-Shklovskii type of VRH conduction model should satisfy the hopping requirement, $W_{ES} \gg k_B T$. This observation supports the possibility of a crossover in VRH mechanism from the Mott type to the Efros-Shklovskii type [249].

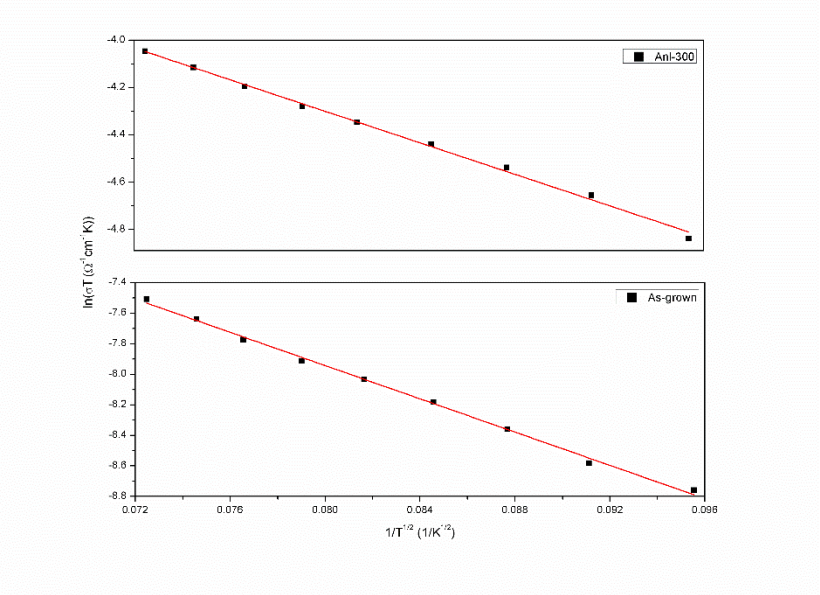

Figure 4.22: Plots of $ln(\sigma T)$ versus $T^{-1/2}$ in the high-temperature region for the ZIS film in as-grown form and annealed at 300 °C. Solid lines are the best fit lines according to Eq. 4.27

Table 4.11: Calculated parameters of Efros-Shklovskii VRH model

Sample	T_{0ES} (K)	σ_{0ES} (K/Ωcm)	R_{ES} (cm)
As-grown	2.96×10^{3}	2.77×10^{-2}	3.51×10^{-7}
Anl-300	1.11×10^{3}	1.96×10^{-1}	7.24×10^{-7}

Sample	W_{ES} (meV)	Δ (meV)	R^2	W_{ES}/k_BT
As-grown	25.7	32.0	0.98	2.48
Anl-300	15.7	21.9	0.98	1.52

As a result of the dark-conductivity analysis as a function of ambient temperature, the total conductivity of the samples can be expressed as a combination of thermionic emission and VRH conduction mechanisms as:

$$\sigma_{dark} = \sigma_{TE} + \sigma_{M} + \sigma_{ES} \tag{4.32}$$

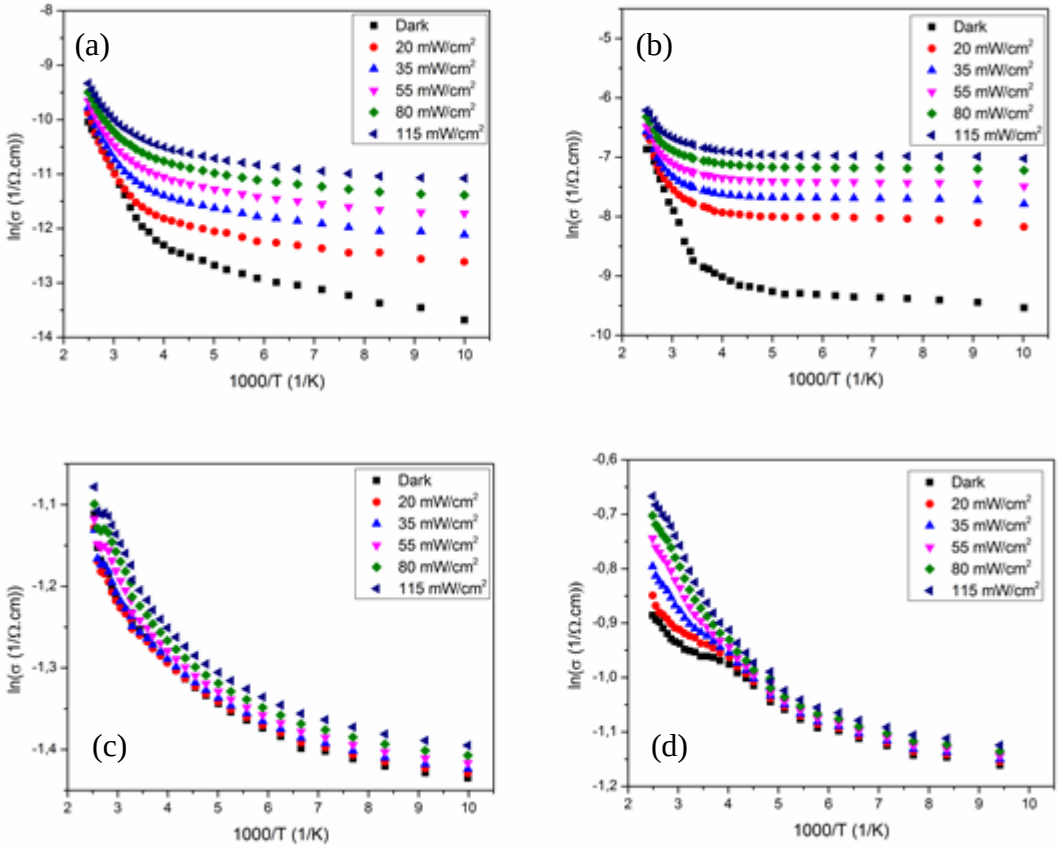

Figure 4.23: The variation of the photo-conductivity with temperature and illumination intensity for ZIS films (a) as-grown, (b) annealed at 300 °C, (c) annealed at 400 °C, (d) annealed at 500 °C.

In order to investigate illumination effect on the electrical behavior of the samples and to characterize the traps in the film structures, the photo-conductivity measurements were carried out under 5 different illumination intensities at the temperature interval between 100 and 420 K. In fact, the annealed films at 400 and 500 °C are shown insensitive to light as compared to as-grown and annealed film at

300 °C because of the low resistivity and semi-metallic surface behavior. The variation of the photo-conductivity with the input light intensity is shown in Fig. 4.23. In general, the conductivity increases with the illumination [126] and the conductivity under illumination, σ_{light}, is given as,

$$\sigma_{light} = \sigma_{dark} + \Delta\sigma \tag{4.33}$$

where $\Delta\sigma$ is the photo-conductivity contribution to the intrinsic conductivity of the sample. As seen in Fig. 4.23, the photo-conductivity values of the samples were found to be greater than the dark conductivity values, because of the contribution of the photo-carriers to the conduction. Moreover, when the illumination intensity increases, the conductivity of the samples increases. For the possibility of photoexcitation under illumination, both charge carrier density and the carrier mobility may change. Since the change in the concentration is related to the direct generation (recombination) rate and lifetime of the charge carriers, $\Delta\sigma$ varies as ϕ^n. In this relation, the lifetime is assumed to be a function of ϕ where *n*, is a distinctive indicator of the non-equilibrium carriers. Therefore, the photocurrent can be related to the photoexcitation intensity as [254];

$$I_{pc} \propto \phi^{\gamma} \tag{4.34}$$

where γ is a power exponent. By using this relation, the possible recombination centers were evaluated by illumination intensity effect on change in conductivity values as shown in Fig. 4.24. This characterization was done by the exponent behavior as given in Eq. 4.34. As shown in Fig.4.24, under illumination, the change in the conductivity values increases with the increasing temperature until a critical temperature. The possible recombination and trap centers in the structure can limit lifetime of the carriers. In this case, the number of carriers in the conduction band can be limited by the recombination processes and therefore, thermal quenching may become dominant factor [126]. In the moderate and low temperature regions, the results indicate that for deposited ZIS films, photocurrent depends on illumination intensity with an order in the range of 0.88-1.78 for as-grown and annealed films. According to relation between photo-conductivity and excitation rate, if γ is lower

than 1, $\gamma<1$, the lifetime decreases with increasing illumination intensity. In this case, it is classified as a sublinear behavior [126]. Otherwise, in the case of $\gamma>1$, the lifetime increases with increasing light intensity; and this behavior is said to be supralinear characteristic [126]. Increasing exponent *n* values with increasing temperature confirms the longer life-time for free carriers and stronger recombination process at the film surface. Although the values of this exponent, between 0.5 and 1, indicates the one recombination center, the results dominantly gives the supralinear characteristic which can be explained by the two-center recombination model having two trap levels dominant at both low and high temperature regions.

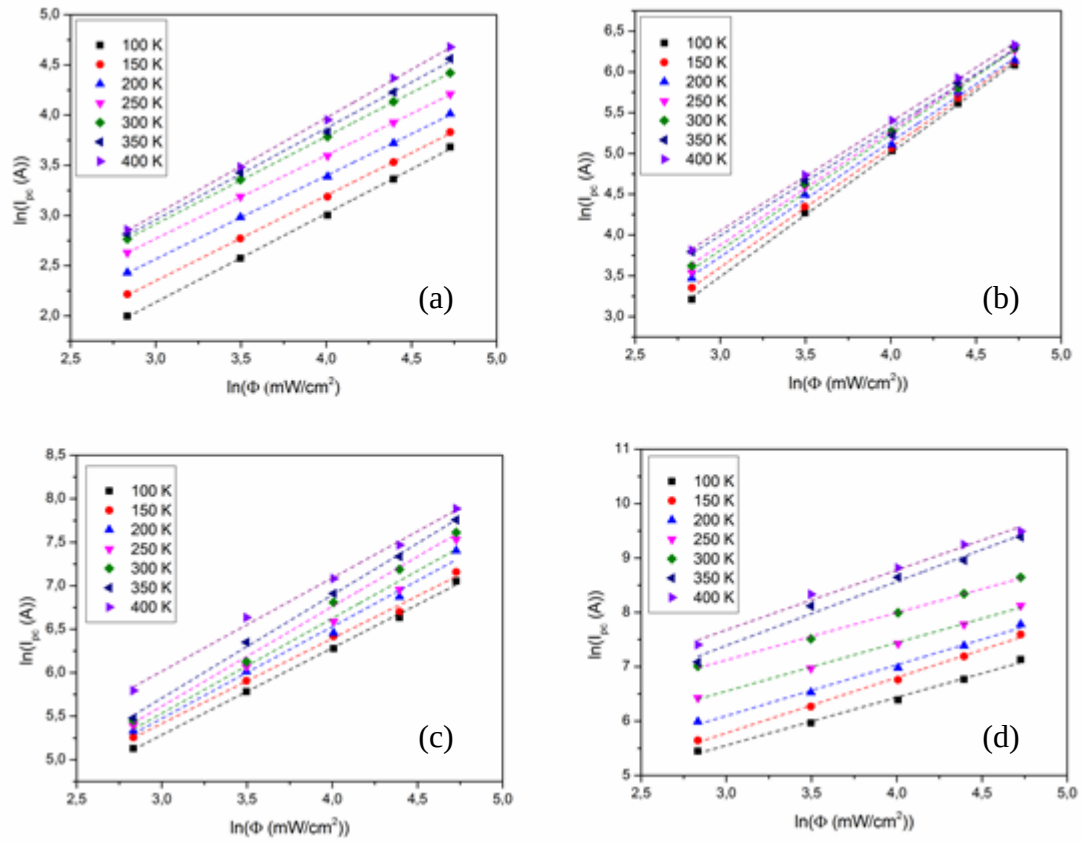

Figure 4.24: The variation of the photocurrent as a function of illumination intensity for ZIS films (a) as-grown, (b) annealed at 300 °C, (c) annealed at 400 °C, (d) annealed at 500 °C.

In the study of the conduction processes, Hall Effect contributes to the detailed analysis on the electrical characteristics of the semiconductors [158]. It is an important experimental technique to determine free carrier density, carrier type, and the mobility of a semiconducting material. In this method, under constant magnetic field, contribution of the charge carriers, affected from the Lorentz force, to the current flow through the sample can be determined. In general, the applicability of this method is taken into consideration when the sample resistance is the range of 10^3-10^9 ohms [136]. For less resistive materials, Hall Effect analysis can be done with the current-voltage measurement from the parallel contacts. On the other hand, if the semiconductor is high resistive material, it is more appropriate to measure across different pairs of contacts. From these measurements, the Hall coefficient R_H can be found using the calculated resistance values with or without magnetic field effect. The sign of R_H determines the type of the material whether electrons or holes predominate in the conduction process [197]. The conductivity type of all ZIS thin films was determined as n-type by calculation of by R_H and also by the hot probe technique [196]. Then, the carrier concentration can be determined by the relation in Eq. 3.5 [198]. From the calculated n value, Hall mobility μ can be determined as in Eq. 3.6. Then, the room temperature Hall mobilities were 3.89, 7.31, 5.97 and 2.77 $cm^2/V.s$ and electron concentrations were $1.69x10^{13}$, $1.32x10^{14}$, $3.01x10^{16}$ and $8.65x10^{16}$ cm^{-3} for as-grown and annealed films, respectively.

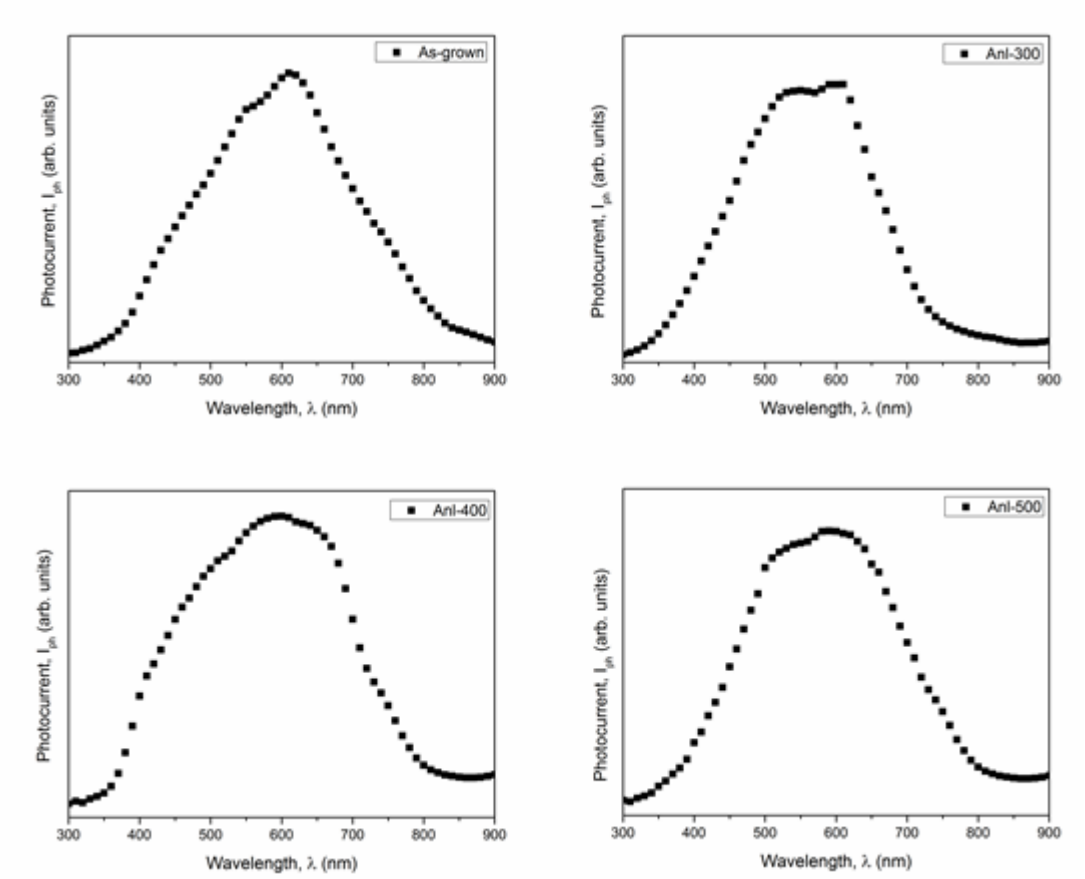

Figure 4.25: The normalized photocurrent response of ZIS films
(a) as-grown, (b) annealed at 300 °C, (c) annealed at 400 °C, (d) annealed at 500 °C.

Spectral dependence of the photocurrent measurements were carried out in order to investigate the energy levels in the film structures [255]. In this characterization step, the photocurrent values are measured as a function of illumination wavelength at room temperature. Fig. 4.25 shows the dependence of the photocurrent in the wavelength range of 300-1100 nm under a fixed incident photon flux. The current rises with wavelength until 620-670 nm for ZIS samples, after it drops abruptly. The other peaks for these samples were observed at 550-600 and 490-540 nm wavelength regions. The main photocurrent peak for as-grown sample corresponds to 2.0 eV at 620 nm, however there are two shoulders at about 490 and 540 nm. The shoulder in the spectral photo-conductivity measurements was correlated with the other possible transitions observed in the optical spectra analysis. These energy levels of as-grown ZIS film were determined from photo-response spectra at about 2.30 and 2.54 eV.

Moreover, the spectral responsivity curve of the annealed films exhibits the main peaks at 1.96, 1.93 and 1.85 eV for ZIS films annealed at 300, 400 and 500 °C, respectively. The other photocurrent maxima for the annealed films were 2.24, 2.15, 2.09 and 2.48, 2.43, 2.25 eV, respectively. It can be seen that the value obtained from photo-response measurements is close to the results of the optical analysis.

4.5. Device Characterization of $ZnInSe_2$ Thin Films

Under this work, the hetero-junction was fabricated by depositing ZIS n-type thin film layer on the p-type Si wafer substrate. The commercial p-type Si wafers were used as a p-type layer to construct this p-n junction. They are about 600 μm thick, one-sided polished, in mono-crystalline phase with (111) orientation and their resistivity values are around 1-3 (Ω.cm) On the other hand, ZIS thin film deposited by using PVD system. Therefore, the basic properties of this structure were analyzed.

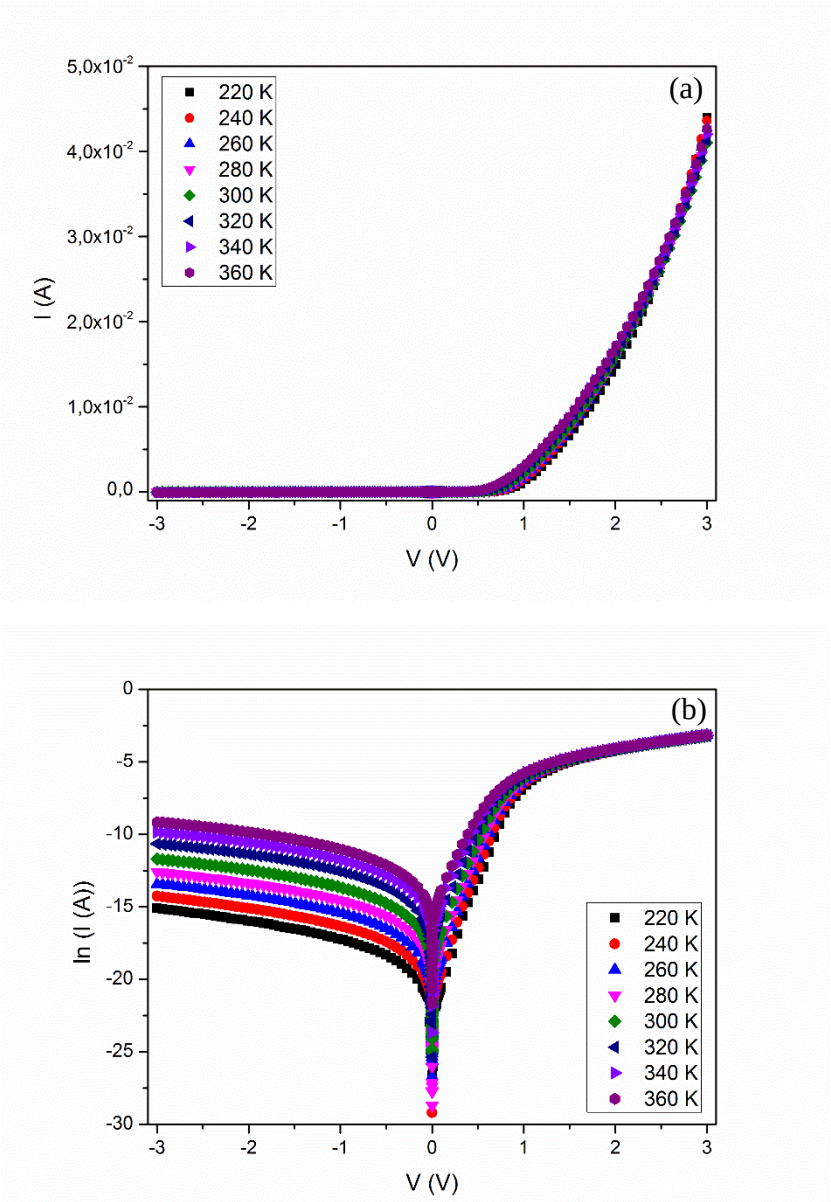

Figure 4.26: (a) Linear and (b) semi-logarithmic I-V plots of n-ZIS/p-Si hetero-junction at different ambient temperatures.

In order to evaluate the device parameters of the fabricated Si based hetero-junction, the temperature dependent dark current-voltage (I-V) characteristics were measured. The typical I–V characteristic of In/n-ZIS/p-Si/Al sandwich structure is shown in Fig. 4.26 (a) and corresponding semi-logarithmic plot of these measurements are given in Fig.4.26 (b). As seen from figure, the rectifying behavior of the deposited hetero-junction structure was observed. [163]. Rectification factor (RF) I_F/I_R, (ratio of forward and reverse currents), was calculated for all voltage and temperature

variations and the maximum RF value was observed on the order of 4 at about 220 K and 0.9 bias voltage. The effect of the sample temperature and bias voltage on the rectification factor was shown in Fig. 4.27. As seen from this figure, the RF values increases with increasing voltage at constant temperature. On the other hand, at each voltage steps, the RF values decreases with increasing ambient temperature. The reaction of RF with temperature and bias voltage variations observed in Fig. 4.27 may be related to the trap levels localized at the interface and inhomogeneous trap distribution in the bulk of hetero-structure [256, 257].

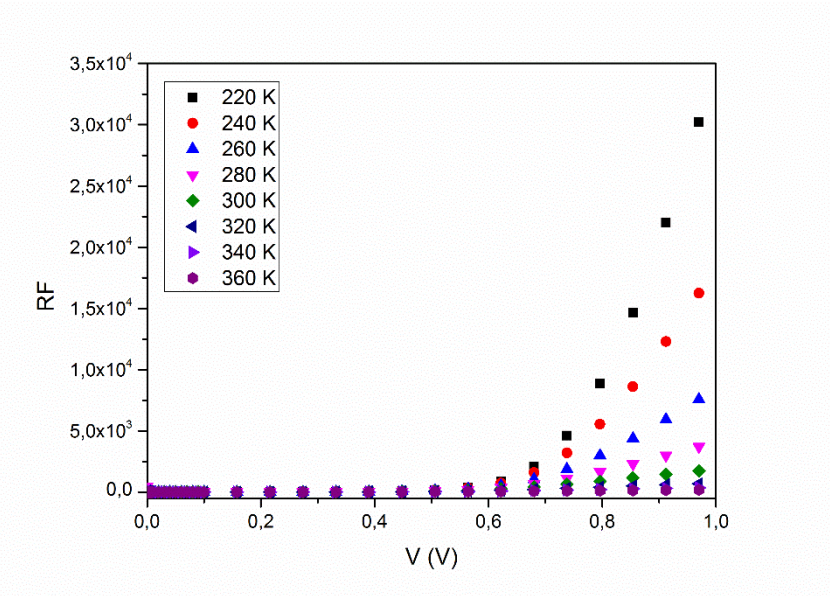

Figure 4.27: Plots of rectification factor (RF) versus V at different ambient temperatures.

Parasitic series and parallel (shunt) resistances are in a significant role in semiconductor devices. These resistance effects manipulate the experimental I-V characteristics of the diode causing saturation effects at the high forward and reverse bias regions. The series resistance (R_S) relates to the resistance effects of both diode structure and contact regions [185]. On the other hand, shunt resistance (R_{Sh}) arises from surface leakage along the edges of the device, defects in crystalline structure [258] and device and the surface inhomogeneities [259]. In Fig. 4.26 (b), from the deviation regions at high forward and reverse voltages, R_S and R_{Sh} values were calculated from the parasitic resistance in the forward and reverse voltage range of 1.5-3.0 V, respectively, and the obtained values were given in Table 4.12. As

observed from the table, the magnitude of both resistance decreases under the effect of increasing temperature. This situation may be related to the increase in the density of the free charge carriers by bond breaking and/or de-trapping mechanism [260, 261].

Table 4.12: The device parameters of the n-ZIS/p-Si hetero-junction by using the parasitic resistance and Schottky diode equations.

T (K)	R_S (Ω)	R_{Sh} (Ω)	n	I_0 (A)	$q\Phi_b$ (eV)
220	$3.95\text{x}10^{1}$	$1.08\text{x}10^{7}$	2.73	$2.41\text{x}10^{-10}$	0.62
240	$3.54\text{x}10^{1}$	$4.60\text{x}10^{6}$	2.65	$5.88\text{x}10^{-10}$	0.66
260	$3.29\text{x}10^{1}$	$1.92\text{x}10^{6}$	2.56	$1.61\text{x}10^{-9}$	0.69
280	$3.03\text{x}10^{1}$	$8.27\text{x}10^{5}$	2.48	$4.25\text{x}10^{-9}$	0.73
300	$2.73\text{x}10^{1}$	$3.35\text{x}10^{5}$	2.45	$1.18\text{x}10^{-9}$	0.76
320	$2.35\text{x}10^{1}$	$1.12\text{x}10^{5}$	2.43	$4.17\text{x}10^{-8}$	0.78
340	$2.10\text{x}10^{1}$	$5.04\text{x}10^{4}$	2.41	$1.03\text{x}10^{-7}$	0.81
360	$1.94\text{x}10^{1}$	$2.45\text{x}10^{4}$	2.40	$2.37\text{x}10^{-7}$	0.84

As shown in Fig. 4.26 (b), at lower voltage region lower than 0.5 V, the forward current follows the applied voltage as in the case of the Schottky barrier diodes. In this part of the I-V plots, forward current changes with applied voltage exponentially and as a result of this, the data were studied under the consideration of the standard diode equation as,

$$I = I_0 \left[exp\left(\frac{qV}{nkT}\right) - 1 \right] \tag{4.35}$$

where q is the electron charge, k is the Boltzmann constant, n is a dimensionless factor representing the diode ideality factor, V is the applied voltage and I_0 is the saturation current given by the expression,

$$I_0 = AA^{*}T^{2} exp\left(-\frac{q\Phi_b}{kT}\right) \tag{4.36}$$

In this equation, Φ_b is the potential barrier, A is the effective diode area of $1.5x10^{-2}$ cm^2, A^* is Richardson constant [113]. The ideality factor and the barrier height were calculated from the semi-logarithmic plot of current-voltage characteristic of the diode. The ideality factor values of the diode at studied temperature region were evaluated from the slope of the Fig. 4.26 (b) by using the relation,

$$\frac{1}{n} = \frac{kT}{q}\frac{d(\ln(I))}{dV} \tag{4.37}$$

The obtained ideality factor and the barrier height values are tabulated in Table 4.12 and showed in Fig. 4.28. In order to determine the dominant current transport mechanism in the junction, the ideality factor *n* can be used. The *n* values were found greater than unity, therefore it reveals that thermal excitation over the barrier is not the dominant transport mechanism. Usually, *n* is expected to be in the range between 1 and 2, however, the calculated *n* values are higher than 2 and it is the indication of the possible transport mechanisms in the conduction [163]. Investigation of transport mechanism on the fabricated diode in studied temperature range was made by assuming that tunneling, interface recombination, recombination-generation in depletion region, and space charge limited current (SCLC) could be a possible conduction mechanisms. Moreover, the activation energy for each transport mechanisms was determined by analyzing the slope of the characteristic I-V relations [262].

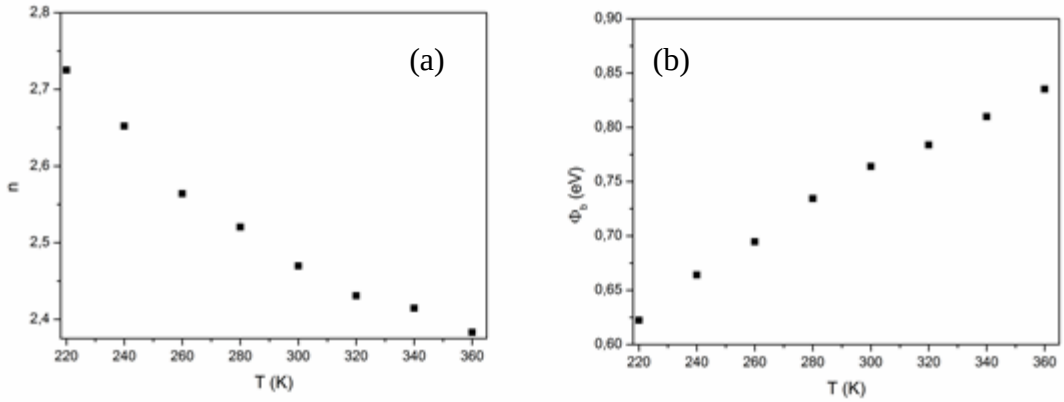

Figure 4.28: The variation of (a) the ideality factor (*n*) and (b) the barrier height (Φ_b) with the sample temperature.

Initially, thermionic emission (TE) mechanism was discussed. In addition to $n=1$, $ln(I_0/T^2)$ versus $1/T$ plot should be linear to satisfy the validity if thermally activated current transport mechanism [263], and the linearity is observed in Fig. 4.29. However, with the 0.29 eV activation energy, the conduction mechanism is not affected from this mechanism. The decrease in Φ_b and increase in the n with decreasing temperatures indicated that tunneling, thermionic field emission (TFE) and/or field emission (FE), may be dominant current transport mechanism [264]. Under these analyses, tunneling may be possible mechanism for the charge carriers having lower energies than the top of the barrier. However, only high concentration about 10^{18}-10^{19} cm^{-3} can provide tunneling in the current flow, and as a result the tunneling become the dominant factor in the junction [264]. Consequently, tunneling may not be the most effective mechanism in this device structure. The requirement for interface recombination (IR) transport mechanism, the activation energy of $ln(I_0)$ versus $1/T$ (Fig. 4.30) should be approximately equal to band gap of ZIS [265]. From the corresponding graphical relation, the activation energy for interface recombination was found about 0.33 eV, and it cannot satisfy the requirement of this transport mechanism model. In order to analyze the suitability of the model based on recombination-generation (RG) in depletion region, the $ln(I_0/T^{-5/2})$ versus $1/T$ is plotted in Fig. 4.31. By this model, the ideality factor value is equal to 2 [163], so that activation energy found from the slope of $ln(I_0\ T^{-5/2})$ versus $1/T$ plot (0.40 eV) should be close to half of the band gap of ZIS [262, 266]. According to these results, there was insufficient evidence for these models to satisfy the dominant transport mechanism.

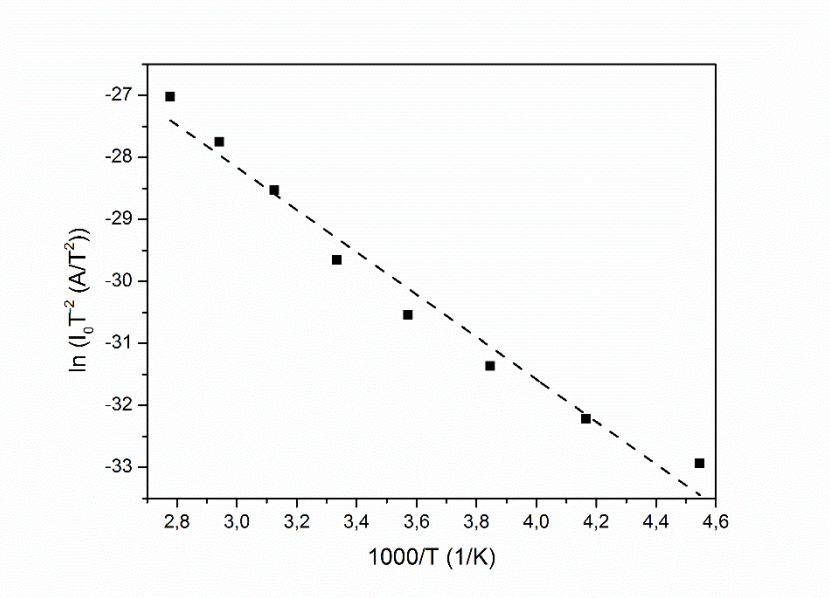

Figure 4.29: Plot of $ln(I_0T^{-2})$ versus $1000/T$ for the n-ZIS/p-Si device.

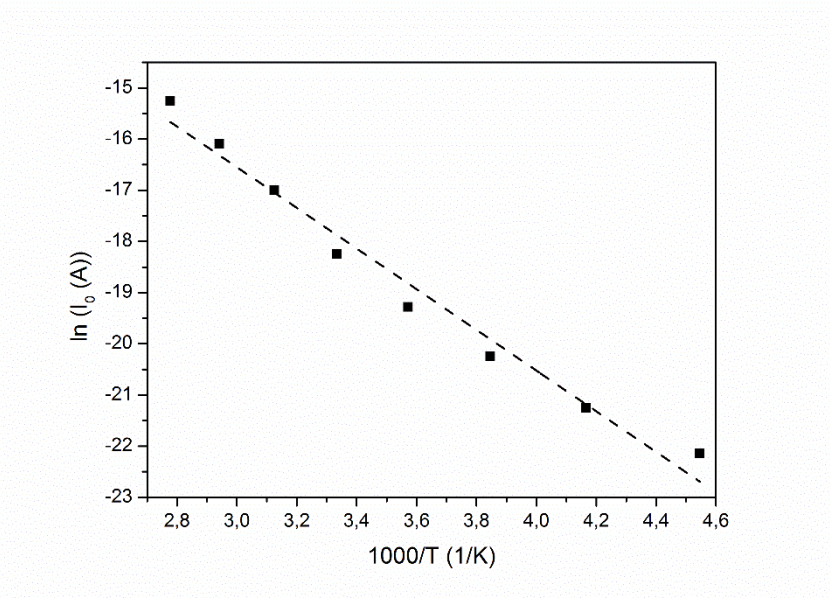

Figure 4.30: Plot of $ln(I_0)$ versus $1000/T$ for the n-ZIS/p-Si device.

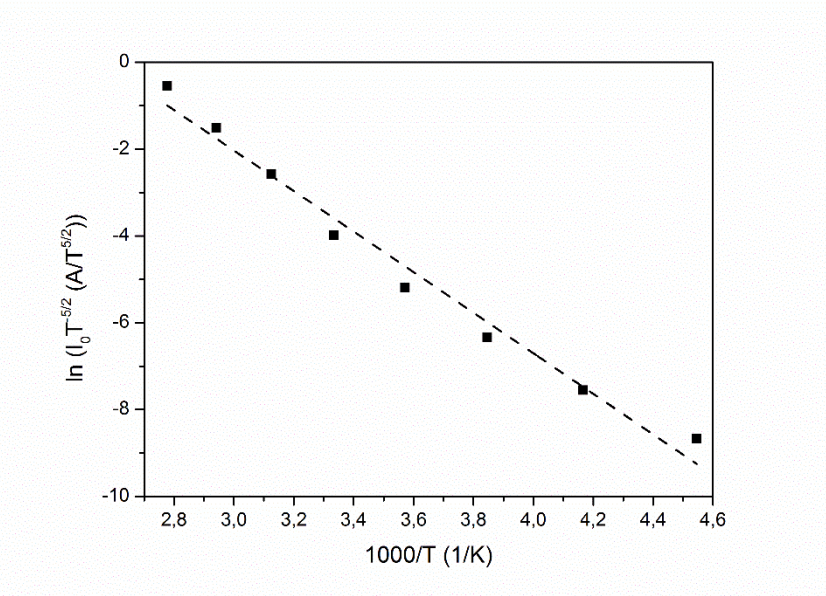

Figure 4.31: Plot of $ln(I_0T^{-5/2})$ versus $1000/T$ for the n-ZIS/p-Si device.

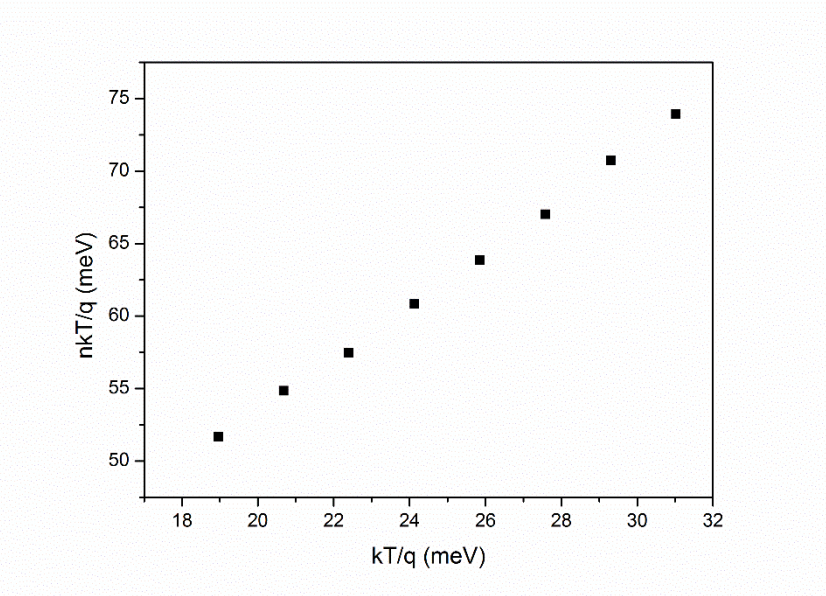

Figure 4.32: Plot of nkT/q versus kT/q for the n-ZIS/p-Si device.

Although, the ideal TE model requires that n should be equal to 1, in the plot of nkT/q as a function of kT/q (Fig. 4.32), there is a linear behavior with the slope closer to unity. Deviation of the T_0 effect is usually accomplished by this type of plot and it indicates that there can be a modified thermionic emission transport model [267]. It shows that the ideality factor is temperature dependent and the observed values need to be modified over the TE. This modification can be expressed as

$$n = \left(1 + \frac{T_0}{T}\right) \tag{4.38}$$

where T_0 is a constant independent of temperature, however dependent of the applied bias voltage [268]. This model is the modification of TE with T_0, and this anomaly is related to the interfacial disorder at or near the junction. From the Fig. 4.33, the relation between *n* and inverse temperature gives T_0 as 211.5 K. This observation further indicates that the conduction mechanism operating in the junction seems most likely T_0 affected current transport mechanism across the junction for this sample in the whole temperature region.

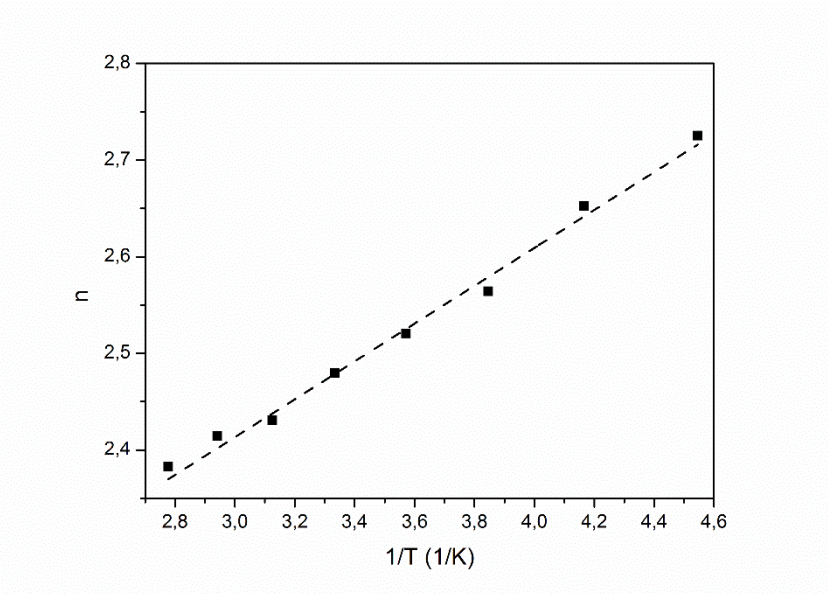

Figure 4.33: Plot of *n* versus *1/T* for the n-ZIS/p-Si device.

However, the predominant current transport mechanism is found to be depend on the other control mechanism. At higher voltages in the range of 0.6 - 0.9 V, current is observed as being proportional to the exponential power of voltage (Fig. 4.34). Therefore, works on SCLC mechanism were concentrated on this region. According to the typical SCLC characteristic, current *I* is proportional to *V* with the following equation,

$$I = \frac{qA\mu N_C}{d^{2l+1}} \left(\frac{\varepsilon\varepsilon_0}{qN_0kT_T}\right)^l V^{l+1} \tag{4.39}$$

where ε is the dielectric constant, ε_0 is the free space permittivity, μ is the mobility of charge carriers, N_C is the effective density of states in the electronic band edge, d is the sample thickness, N_0 is the trap density per unit energy range at the conduction band, l is a power of V given by $l=m\text{-}1=T_T/T$. The figure clearly shows that the applied voltage causes an exponential change in the slopes of curves as expected for exponential distribution of traps by the Eq. 4.39 [269]. According to this equation, calculated m, l and T_T values as a function of temperature are listed in Table 4.13.

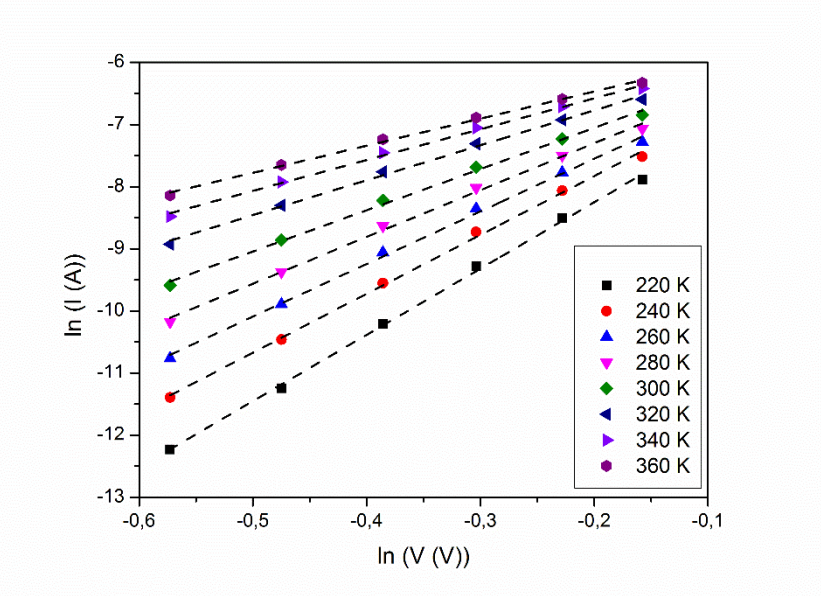

Figure 4.34: Plots of *ln(I)* versus *ln(V)* for the n-ZIS/p-Si device.

By using the Fig. 4.34, the order of voltage relation was found to be greater than 2 that is related to the energy distribution of traps instead of discrete levels (see Table 4.13). This indicates the existence of the SCLCs with the exponential trap distribution [263, 270]. T_T is a parameter depending on temperature and affects the exponential distribution of traps. It can be written as,

$$N(E) = N_0 exp\left(-\frac{E}{kT_T}\right) \tag{4.40}$$

where $N(E)$ is the trap density per unit energy range at an energy E lower than the conduction band edge. The SCLC measurements can present reliable results on the

locations of trapping states and the density of them in the energy gap of the semiconducting materials. The total concentration of traps N_T is given as [271, 272],

$$N_T = N_0 k T_T \tag{4.41}$$

In order to determine both N_T and N_0, ln(I) versus $1/T$ at different bias voltages was plotted in Fig. 4.35. The slope of the figure can be analyzed according to the equation [271]

$$\frac{d\left(ln(I)\right)}{d(1/T)} = T_T ln\left(\frac{\varepsilon\varepsilon_0 V}{q d^2 N_T}\right) \tag{4.42}$$

At high voltage region, the traps are saturated and as a result of this, the current become space charge limited. Therefore, the injected carries directly contribute to the current conduction process and this charge carrier contribution increases the current flow. As given in Table 4.14, the values of N_T and N_0 increases with increasing applied voltage which can due to thermally generated more charges [259]. On the other hand, T_T values show generally decreasing behavior with increasing temperature, which means that the entire distribution of traps lie narrower energy interval in the band gap with increasing temperature.

Table 4.13: The SCLC analysis results of the n-ZIS/p-Si hetero-junction diode.

T (K)	m	l	T_T (K)
220	10.67	9.67	2127.84
240	9.48	8.48	2043.50
260	8.47	7.47	1942.23
280	7.54	6.54	1831.34
300	6.63	5.63	1689.81
320	5.63	4.63	1480.80
340	4.96	3.96	1347.73
360	4.36	3.36	1211.36

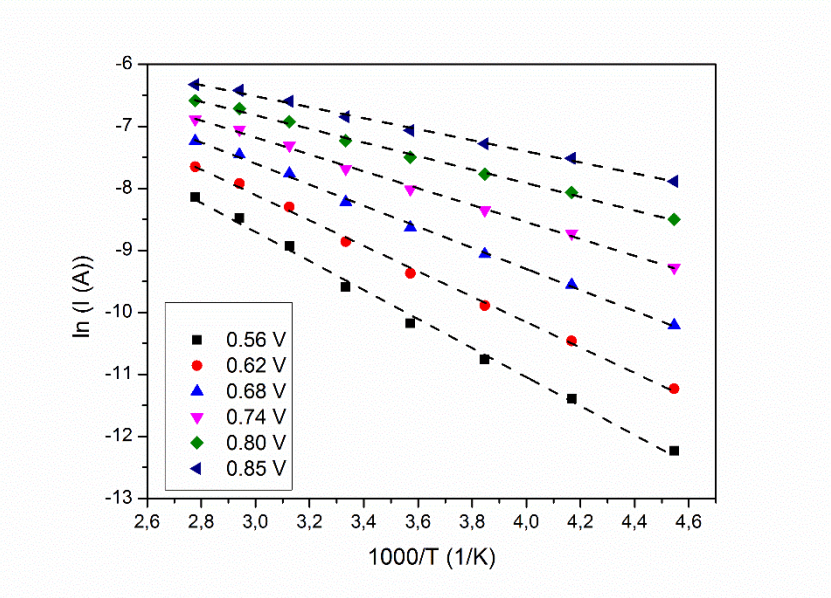

Figure 4.35: Plots of *ln(I)* versus *1000/T* for the n-ZIS/p-Si devices of different bias voltage

Table 4.14: The N_T and N_0 values obtained by using the SCLC analysis with different voltage values in the high bias region at examined temperatures.

T (K)	N_T (x10^{16} m^{-3})					N_0 (x10^{36} m^{-3})
	V=0.5 V	V=0.6 V	V=0.7 V	V=0.8 V	V=0.9 V	V=0.10 V
220	6.65	6.23	4.63	3.03	2.08	2.12
240	6.92	6.48	4.92	3.30	2.31	2.31
260	7.20	6.73	5.23	3.59	2.56	2.51
280	7.55	7.04	5.62	3.97	2.90	2.78
300	8.02	7.47	6.17	4.52	3.40	3.20
320	8.77	8.14	7.08	5.47	4.30	3.98
340	9.38	8.59	7.21	6.17	4.99	4.62
360	9.83	9.09	8.45	6.99	5.81	5.43

The I-V plot for the reverse voltage region can be observed in Fig. 4.27. Current transport characteristic of the diode in the reverse voltage region cannot well described by usual diode characteristic. There is an increasing behavior in the reverse current on temperature as given in $ln(I_R)$ vs. T plot (Fig. 4.36) and this result can be

taken as the indication of tunneling mechanism and modeled as presented in [273]. According to this multistep tunneling model, the I-V relation for the reverse bias region can be expressed as [274],

$$\frac{I_R}{V} exp\left(\gamma(\Phi_b - V)^{-1/2}\right) = ae^2 \frac{N_t}{h} \tag{4.43}$$

where a is the lattice constant and N_t is the traps concentration for tunneling process. Moreover, for the tunneling characteristic, the temperature dependence of I_0 is implicit in Φ_b in this expression [275]. As multi-step tunneling is considered, the number of tunneling steps was found in the order of 10^2 and the trap concentration about 10^6, and these values decreases with increasing sample temperature (Fig.4.36).

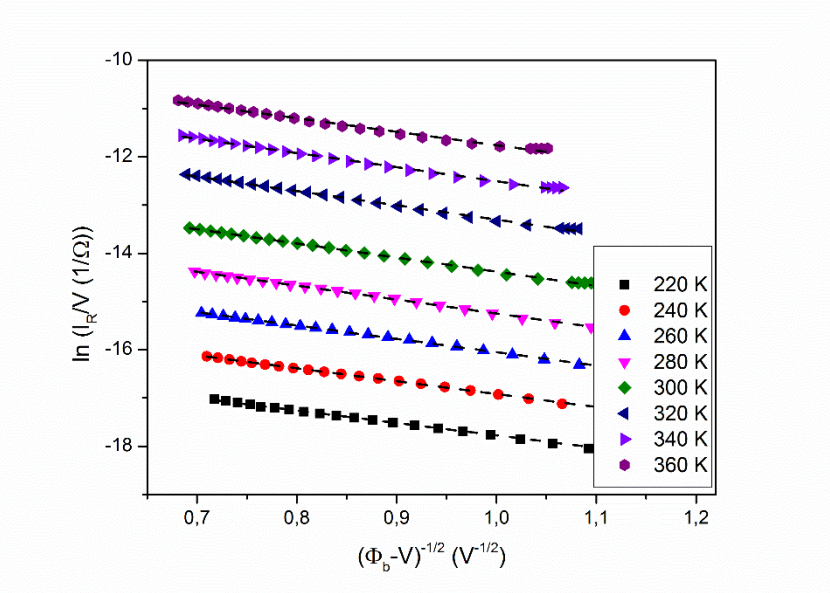

Figure 4.36: Plot of $ln(I_R/V)$ versus $(\Phi_b\text{-}V)^{-1/2}$ for the n-ZIS/p-Si device.

The results of the C-V measurements at room temperature with respect to the variation of the frequency for the n-ZIS/p-Si diode are given in Fig. 4.37. This graph shows that there is no remarkable change in the capacitance values at all voltage region, whereas low capacitance dispersion at high positive voltage region is observed. This is the case that the minority carrier concentration cannot follow the frequency change at the any applied voltage value. Therefore, it may be resulted from the possible traps in the surface and also bulk region [15].

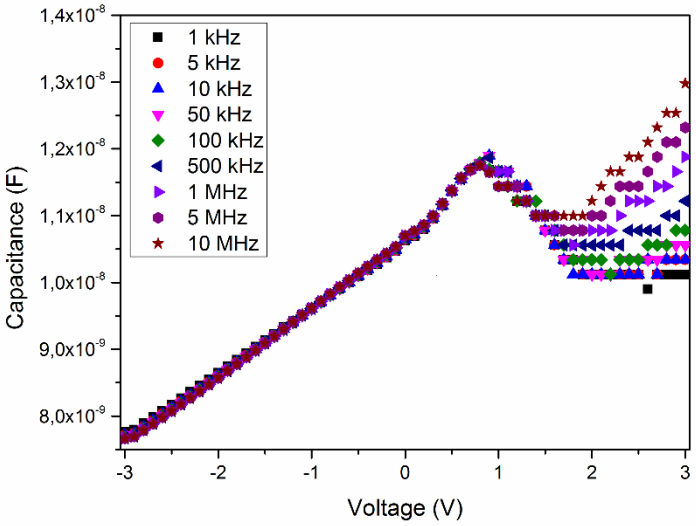

Figure 4.37: Room temperature C-V plots of n-ZIS/p-Si hetero-junction under different frequencies

From the C-V analysis, reverse bias C^{-2} plots of this diode under different frequencies are shown in Fig. 4.38. As seen in this figure, there is an almost linear variation of the C^{-2} values with V. This linear behavior observed in this plot can be attributed to the uniformity in the carrier concentration and also abrupt nature of the junction [6, 276]. Moreover, the p-type Si wafer used in this junction formation has very low resistivity value with compared to the deposited n-ZIS thin film layer, this junction can be assumed acting as one sided abrupt junction, so C–V characteristic can be evaluated as a Schottky diode [276, 277]

$$C^{-2} = 2\left[\frac{\left(V_{bi} - V - {kT}/{q}\right)}{qA^2\varepsilon\varepsilon_0 N_d}\right] \tag{4.44}$$

where V_{bi} is the built-in potential, A is the effective area of the diode and N_d is the donor density of n-ZIS layer. Starting from this relation, the slope of the Fig. 4.38 can be expressed [276] as

$$\frac{dC^{-2}}{dV} = \frac{2}{qA^2\varepsilon\varepsilon_0 N_d} \tag{4.45}$$

which is used to determine the charge density N_d, and the intercept V_0 of this figure at the voltage axis can be attributed to V_{bi} as,

$$V_0 = V_{bi} - {kT}/{q} \tag{4.46}$$

Then, the barrier height of the device can be obtained from this intercept value as

$$\Phi_b = qV_0 + kT + \emptyset \tag{4.47}$$

where $\emptyset$ is the penetration of the Fermi level in the gap of the semiconductor [278]. From this relation, the calculated barrier height values are in a good agreement with the results of the dark I-V analysis. However, these values are around 0.80 eV at the lower frequencies whereas they decrease to about 0.65 eV with increasing the frequency value. In this case, the calculated donor density values are approximately equal to each other with a very small variations and the average value of them is found as 2.78×10^{13} cm^{-3}. This value is also in a good match with the Hall Effect results of the as-grown ZIS film sample.

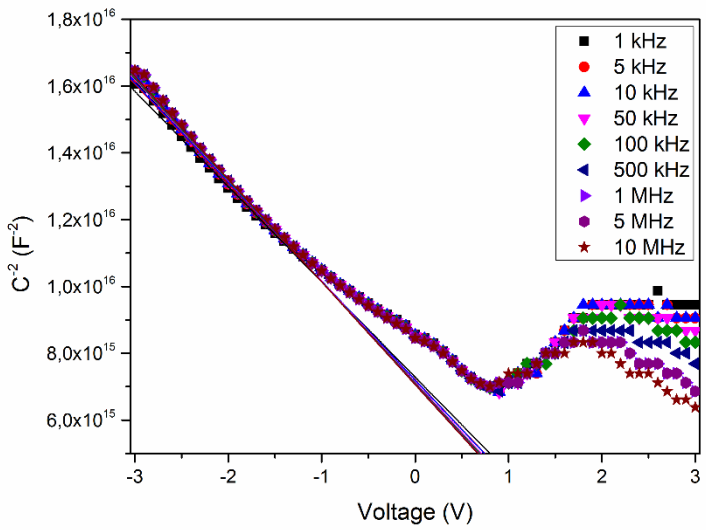

Figure 4.38: The variation of C^{-2} with voltage for the n-ZIS/p-Si device under different frequencies

At low frequencies in the C-V measurements, the measured capacitance values are regarded as being with the effect of states in the depletion and interface regions. On the other hand, the high frequency capacitance values can be resulted only from the states in the depletion region. Under this consideration, capacitance values were plotted with respect to frequency values at zero bias case (Fig. 4.39). Then, the frequency dependence of zero biased capacitance values was observed as being strong at low frequencies compared to the values at high frequencies. Therefore, this indicated that there were some high interface states generating higher capacitance in the junction [278]. Thus, this expression roughly gave the number of total interface states, N_{ss}, by using the equation [278, 279],

$$N_{ss} = \frac{(C_{0,low} - C_{0,high})}{q} \tag{4.48}$$

where $C_{0,low}$ and $C_{0,high}$ are the low and high capacitance values, respectively. At zero bias and room temperature, the number of interface states was calculated from the high and low capacitance values to be 6.87×10^8 $cm^{-2}V^{-1}$ [279, 280].

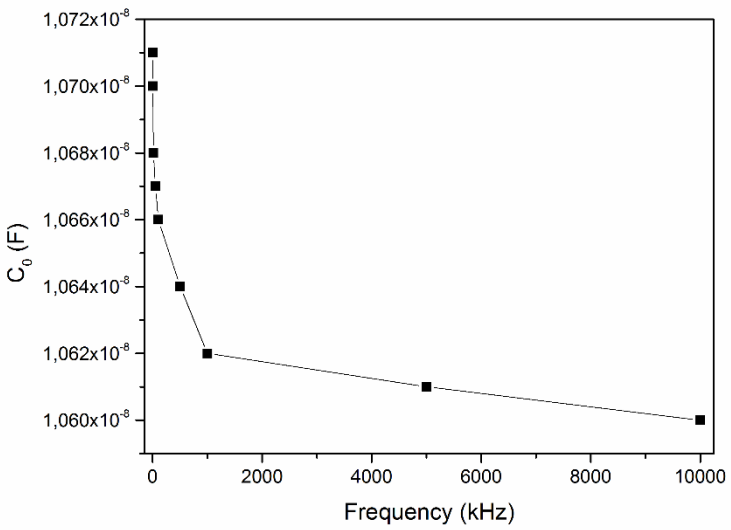

Figure 4.39: The variation of capacitance at zero bias with frequency in the n-ZIS/p-Si device

After these I-V and C-V analysis, the band diagram of the fabricated n-ZIS/p-Si heterojunction was constructed on the basis of Anderson's model (Fig. 4.40) [281]. In this diagram, the electron affinity value was estimated from the ZnSe band structure [282] and also from the results of the optical analysis of ZIS samples; the fundamental band gap value of the as-grown film was used. Then, with the calculated room temperature barrier value, this band diagram was approximated for the ZIS type of structures. In addition, the electron affinity and the band gap of the p-type Si-wafer was accepted as 4.01 eV and 1.1 eV [283]. In this band diagram, as a result of being an abrupt heterojunction, between the conduction and also valence bands of the layers, band offsets were observed. Thus, the conduction and valence band offset values were approximated as to be about 0.86 and 1.73 eV, respectively.

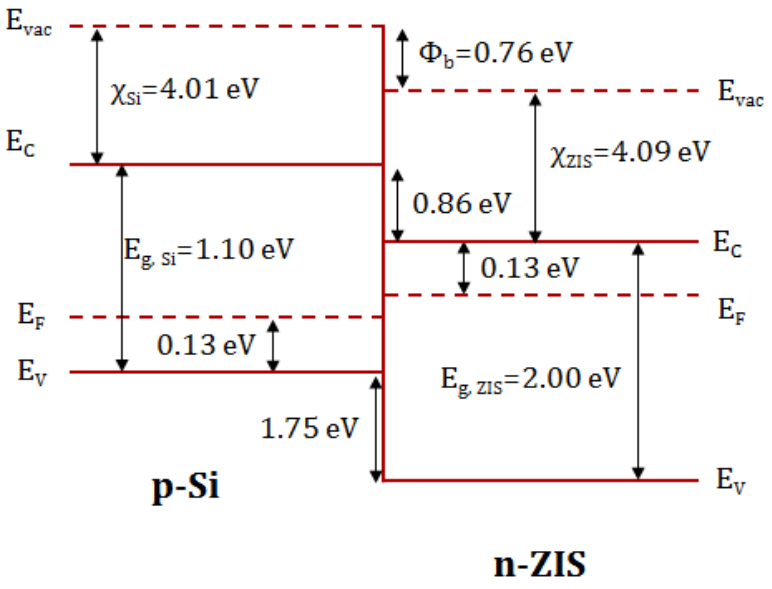

Figure 4.40: The band diagram of the n-ZIS/p-Si device.

The spectral photo-response measurements are based on measuring the photocurrent as a function of the illumination wavelength. In order to determine photo-spectral working range of the junction the wavelength dependent I-V measurements were carried out in the spectral range of 400-1300 nm. This measurement was also performed in order to see the effects and contributions of p-Si and n-ZIS on this device structure. According to the photo-response measurement, the band edges were found to be at 620 nm and 1180 nm (Fig. 4.41). From the ZIS thin film layer, the main photo-current peak corresponds to 2.0 eV. The other peak is originated from the band gap of the Si substrate, which is around 1.1 eV.

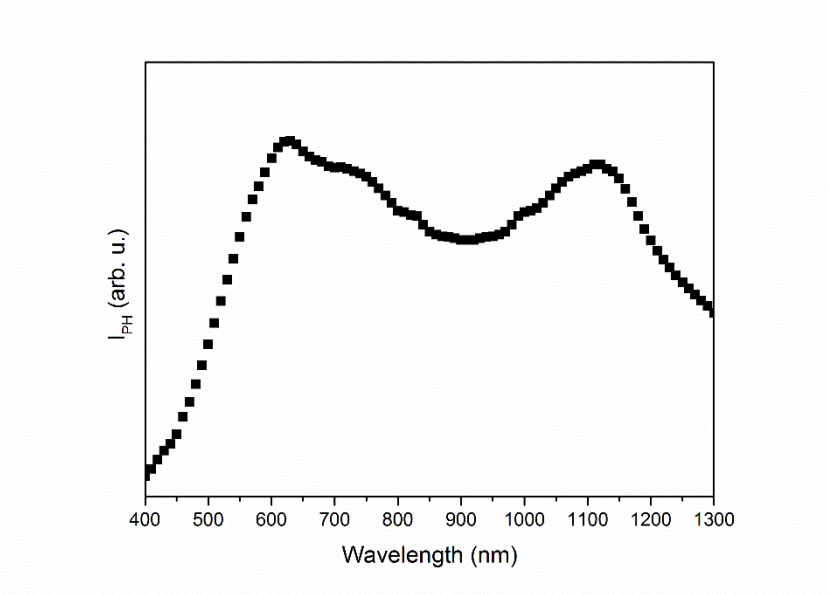

Figure 4.41: Photo-current versus wavelength plot of the n-ZIS/p-Si device.

CHAPTER 5

RESULTS AND DISCUSSIONS-2
($Cu_{0.5}Ag_{0.5}InSe_2$ THIN FILM LAYER)

5.1 Introduction

Polycrystalline thin film solar cells based on CIS and AIS ternary chalcopyrite semiconductor compounds belong to a group of I-III-VI_2 compounds are popular in solar cell applications [2] and non-linear optical devices due to being stable and efficient absorber material [40]. Family of these ternary chalcogenides is isoelectronic with the zincblende II-VI compound semiconductors. By substituting two cations instead of one in a regular zinc-blende type lattice, alternative series of bonds can be obtained which results in differences with respect to the structural, electronic and optical properties. These chalcopyrite semiconductors within the same family have direct band gap, and high absorption coefficients, which make them popular in the device applications [41]. Recently, the quaternary structures have been preferentially studied by different research groups due to the advantage of tailoring suitable values of lattice parameters and energy band gap via the proper choice of composition to reduce the disability of the constituent elements [49]. On this purpose, the maximum solar cell efficiency obtained from the $Cu(In,Ga)Se_2$ quaternary alloy system that achieved through group III isoelectronic substitution of In by Ga. Therefore, the research on group I substitution is based on the similar benefit of these works and Ag is of great interest as a substitute for Cu [56].

Studies on the quaternary compound, $Cu_xAg_{1-x}InSe_2$ (similarly $Cu_{1-x}Ag_xInSe_2$) films as an absorber material for hetero-junction solar cells are a subject of interest since

by changing the composition of the constituent elements in the quaternary alloys, it enables to the tuning of the material properties. Therefore, this quaternary alloy, which is the combination of the ternary chalcopyrite compounds CIS and AIS, can give opportunity to change the structural, optical and electrical characteristics of the material for the requirements on usage. The optical band gap of these compounds for x=0.5 is lying in the range of 1.05 eV - 1.24 eV [42, 43]. As it is known, very little work has been reported on the growth and characterization of CAIS thin film structures. Most of the works are related to structural [42, 48, 49], electrical [45, 49], optical properties [43-46, 49, 52, 53, 56], and device behaviors [47, 50] of CAIS thin film deposited by different deposition methods.

5.2 Structural Characterization of $Cu_{0.5}Ag_{0.5}InSe_2$ Thin Films

The compositions of the films were determined by EDS in order to study the stoichiometric compositions of the deposited thin films. The atomic ratios of the elements relative to each other in the CAIS thin films were tabulated in Table 5.1 with respect to the annealing temperatures.

Table 5.1: EDS results of as-grown and annealed CAIS thin films

Sample Name	Cu (at %)	Ag (at %)	In (at %)	Se (at %)
As-grown	12.11	9.98	24.32	53.60
Anl-300	12.57	10.28	24.33	52.82
Anl-400	12.67	10.98	26.23	50.11
Anl-500	12.87	11.04	26.47	49.61

The films formed at the substrate temperature of 200 °C were found to be nearly stoichiometric. Although there were slight changes in elemental composition of the films with the annealing processes, the films kept its stoichiometric characteristic. In the EDS analysis, all films were found to be deficient in Se and this deficiency was increased by increasing the annealing temperature due to the re-evaporation of weakly bounded Se from the substrate surface during the annealing process because Se is more volatile than the other elements. Since the EDS quantitative analysis is

based on the relative abundance of the constituent elements in the composition, decrease in the Se ratio may result in increase in the ratio of the other elements. However, except Se content in the structure, the deviation of the ratio of constituent elements from as-grown film to annealed film at 500 °C was below the detection limit (~2%) of the measuring system.

The thicknesses of the films were measured electromechanically by a profilometer and they were found about 540, 530, 520 and 500 nm, for the as-grown films, and films annealed at 300, 400 and 500 °C, respectively. According to these thickness measurements, the film thickness of the all films could be accepted as in the same order of magnitude around 500 nm. However, the slight decrease in the thickness values with increasing the annealing temperature can be taken as the indication of the decrease in the amount of some constituent elements in the structure of the films.

XRD analysis was performed to investigate the phase formation and to compare the crystalline size under the effect of annealing temperatures. Besides, these analyses help to observe the possible changes in the film structures depending on the compositional differences and annealing temperatures. The characteristic 2θ values and intensity values of the diffraction peaks corresponding to as-grown and annealed thin films for each deposition were compared with each other with the appropriate XRD data sets from ICDD data base. According to the XRD results, the as-grown CAIS films reveal single phase and polycrystalline nature. In the XRD measurements of the thin films, the high intensity reflection was obtained at the major peak $2\theta \cong 27°$ which indicates the preferred orientation of CAIS films. It is reported as in the (112) phase orientation and giving tetragonal crystalline structure [42]. Actually, the growth CIS usually leads to films with preferred (112) faceting [284] and the same has been found true for the other ternary constituent structure, AIS films [285]. As shown in Fig. 5.1, the peak intensity of the (112) reflection of the CAIS phase dominated all XRD spectra. By increasing annealing temperature, the peak of the preferential orientation (112) becomes more intense; however there is no noticeably change in peak positions of samples annealed at different temperatures. Moreover, the additional phases were observed at 2θ positions of about 36, 43, 54 and 81° with

the corresponding (211), (220/204), (312/116) and (424/228) crystalline orientations, respectively [48]. These XRD profiles are in a good match with the previous works [42, 48, 49, 55, 286, 287]. In addition, there are no any extra diffraction peaks in the XRD pattern of CAIS films from the formation of additional mixture of crystalline phases different than the quaternary structure.

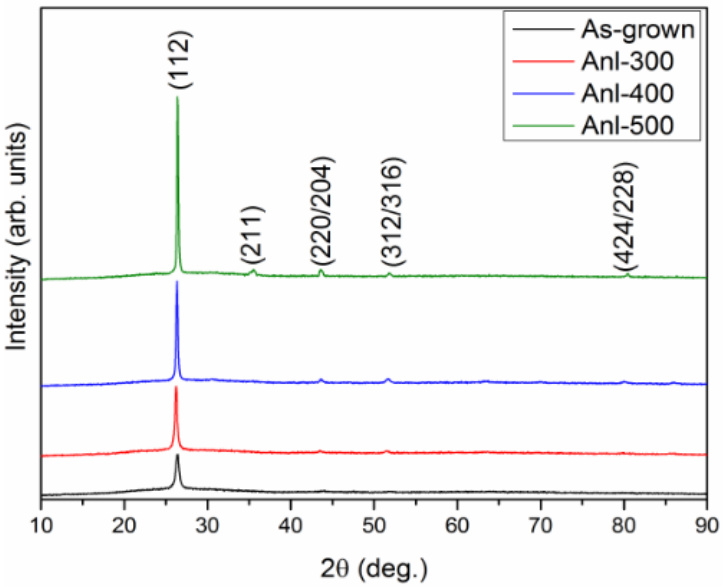

Figure 5.1: The XRD patterns of the as-grown and annealed CAIS thin films at different temperatures

The crystalline sizes in the CAIS thin films were estimated and compared by using Scherer formula [288] where k was taken as 0.94 derived from the simple cubic crystals [289]. The results of this calculation is not related with the strain or composition variations in the structure as a source of peak broadening, so that the grain size values can be underestimated [290]. From this analysis, the grain sizes of the as-grown and annealed films were calculated in the order of 6.5, 7.1, 8.6 and 12.9 nm, respectively. This result can be related to the improvement in the crystalline structure under the annealing process. Ternary analogs, CIS and AIS structures, belongs to the tetragonal crystal system where $c \sim 2a$ [291]. The lattice constants of the CIS and AIS structure were reported as about 5.876 Å [292] and 6.106 Å [293], respectively. Therefore, the lattice constant of this quaternary alloy is expected to be between these values as in increasing behavior from 5.876 Å to 6.106 Å following

Vegard's Law [294]. The structural parameters for the CAIS thin films with the same diffraction spectra were reported as a=0.5937 nm and c=1.1633 nm according to the peak positions of the diffraction phases [42]. Therefore, the tetragonal distortion for these chalcopyrite materials was found approximately as 0.040. From the XRD results of the films and by using Eq. 4.2, the strain values were found as 4.12, 3.79, 3.09 and 2.07 ($x10^{-2}$) for the as-grown and annealed samples, respectively. This result showed that with increasing in grain size, the strain value of the CAIS films decreased with applying thermal annealing and increasing annealing temperature.

This alloy is the quaternary analog of the ternary CIS and AIS semiconductors. Because of the lack of the reported work on Raman spectra of CAIS structure, simple structural relations between these ternary and quaternary compounds were discussed in order to investigate the lattice dynamics of the deposited films. Fig. 5.2 shows the Raman data including three observed peaks. The most intense Raman peak was identified at about 175 cm^{-1} which was positioned between the CIS Raman A_1 mode 177 cm^{-1} and AIS Raman A_1 mode 172 cm^{-1} [295]. In fact, A1 mode which is the strongest mode generally observed in the Raman spectra of I-III-VI_2 chalcopyrite compounds [296]. Therefore, these peaks could indicate the A1 Raman mode of this type of quaternary semiconductor structure. A1 mode appears for all samples in as-grown form and annealed at different temperatures and it was reported that intensity of A1 peak is directly proportional to crystallinity of the sample [297]. This result also verifies the XRD results of the samples. In the Raman spectra of CAIS films, there were two very weak peaks with respect to intensity of the main peak. The peak at 213 cm^{-1} can be attributed to the B2/E1 (LO) mode which corresponds to the 215 and 216 cm^{-1} for CIS and AIS, respectively [295]. The other Raman frequency at 230 cm^{-1} can be assigned to the B2 (LO) mode as observed in CIS structure [295, 298]. These modes reflect the vibration of In–Se atoms in antiphase [296]. In fact, the Raman peaks in B2 and E modes are attributed to the excitation for light polarized parallel and perpendicular to the optic axis, respectively. There is no signal related to any secondary phases or contamination. Since the spectra of CAIS films seem to be reliable and complete with the reported data for CIS and AIS compounds, their structures could be confirmed as to be chalcopyrite. This analysis was based on the

comparison between ternary and quaternary compounds; therefore, further studies are necessary for this compound.

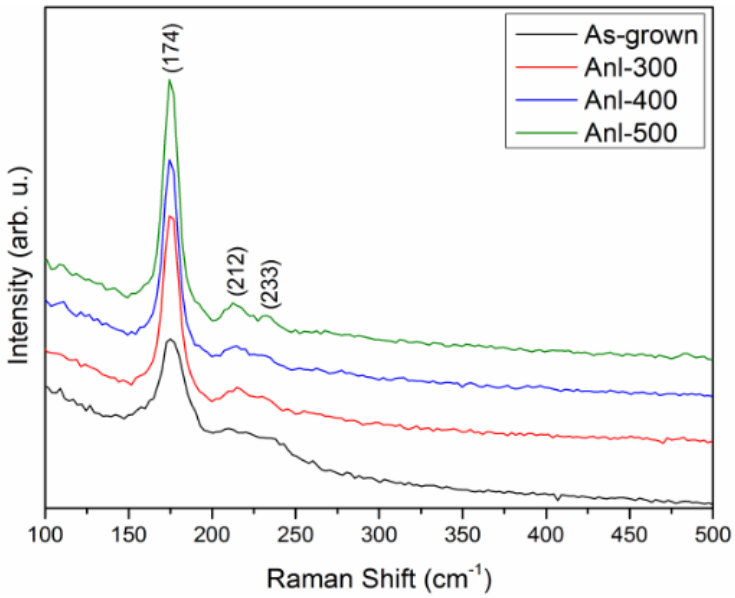

Figure 5.2: Raman spectra of the as-grown and annealed CAIS thin films at different temperatures

In order to study the surface morphology of the samples, SEM measurements were performed and the SEM images of the as-grown and annealed CAIS samples are shown in Fig. 5.3. In general, SEM micrographs clearly show the structure homogeneities and surface uniformity of the films with grain sizes in about tens of nm. As seen in Fig.5.3 (a), surface of the as-grown sample has a smooth, compact, and densely packed morphology. Although the crystal structure of the CAIS samples was considerably improved by annealing, segregation effect was observed on the surface of the annealed samples. According to the EDS analysis of these films, considerably decrease in Se ratio was observed with the effect of annealing. Together with specific EDS analysis, the segregated regions on the surface of the films was found that the relatively dark regions on these film surfaces are the indication of possible segregation of Se atoms and/or re-evaporation from thin film surface due to the high vapor pressure of Se [299]. In addition, there are no any pinholes and voids observed on the plane-view SEM images of films.

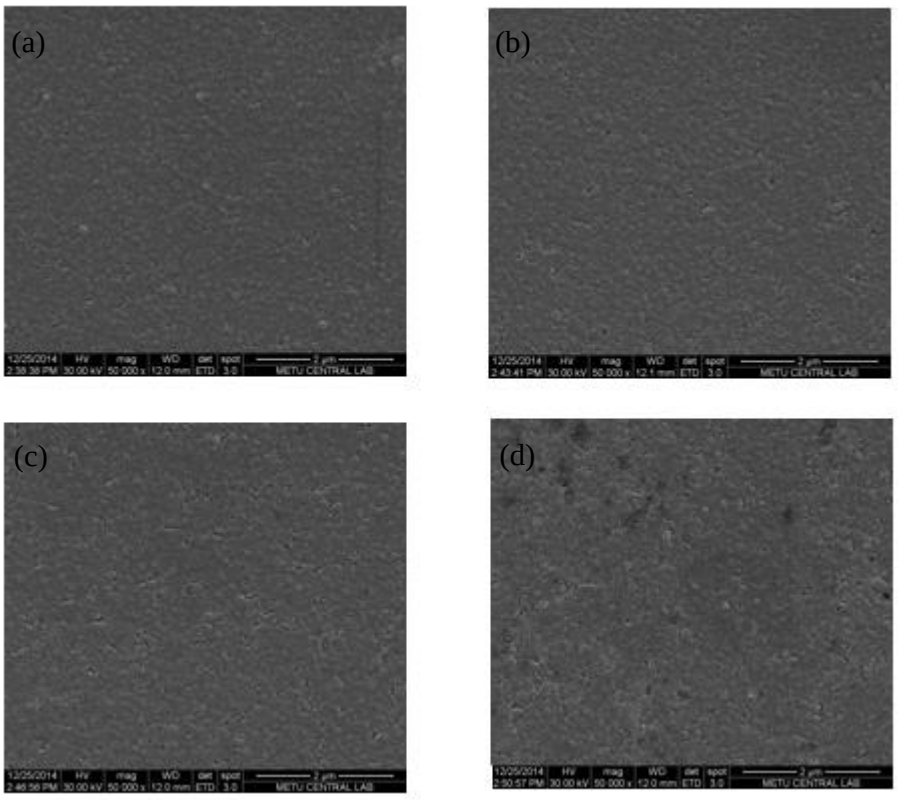

Figure 5.3: The SEM images of a) the as-grown and annealed CAIS thin films at b) 300, c) 400 and d) 500 °C

In addition to the SEM analysis, AFM measurements were carried out to obtain the topography of the films since it is extremely sensitive to surface conditions than SEM imaging. Fig. 5.4 shows the 3D topographic images of the CAIS samples. Although surface morphology of the all CAIS samples seems similar to each other as a result of SEM analysis, the AFM measurements revealed that the formation of crystallites on the as-grown film surface. These bright grains can be evaluated as Se crystallites according to the previous studies [286]. As reported in this work, with annealing process under the nitrogen atmosphere, these Se spots disappeared. This may indicate the possible re-evaporation of Se from the surface of the films by annealing process. The surface morphology from AFM studies shows that the as-grown film samples are smooth with the root-mean-square (RMS) surface roughness of about 10-15 nm except the Se crystallites piled up irregularly on the surface. The roughness values detected from this analysis for the annealed films were 15.5, 6.5, and 8.3 nm, respectively. As a result of this, the surface of the film is observed as

being more close-packed by applying the annealing process at 300 and 400 °C. On the other hand, the further annealing process at 500 °C showed that the grain formation on the surface of the film was collapsed and the surface roughness was decreased. Therefore, this result indicated that the annealing processes with different temperature significantly affected the morphology of the films.

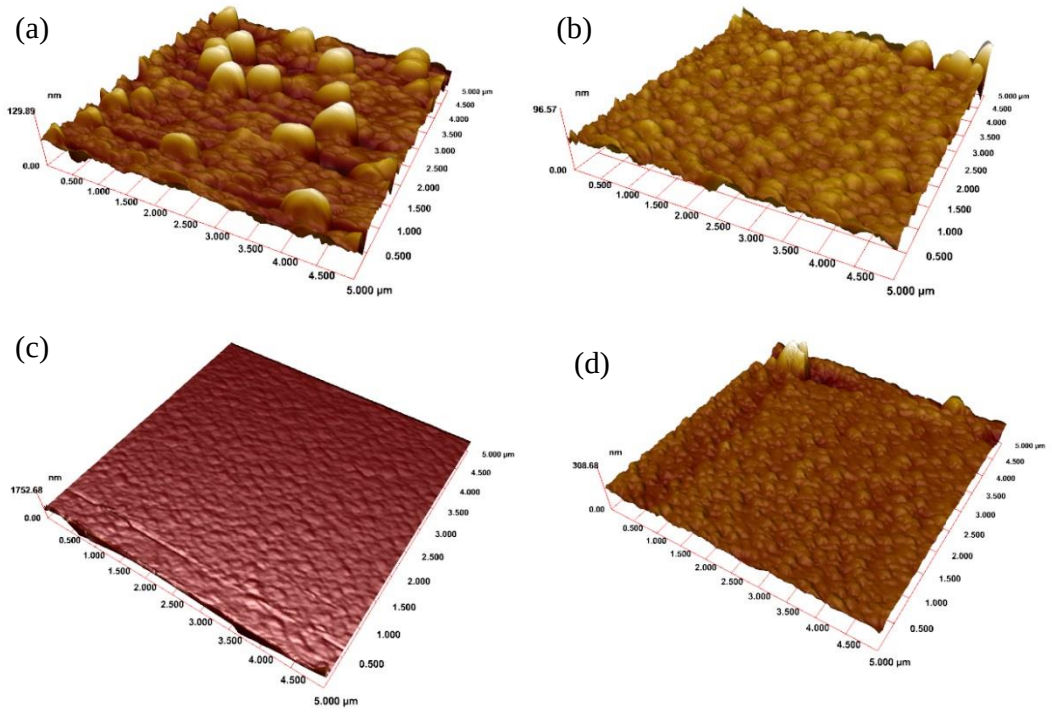

Figure 5.4: The AFM images of a) the as-grown and annealed CAIS thin films at b) 300, c) 400 and d) 500 °C

The detailed XPS peak shape analysis of the core level spectra of the films was carried out to determine the chemical bonding nature of surface and near-surface region of the CAIS samples. Besides, in order to carry out XPS depth profiling, the surface atomic layers were sputtered by using 2 keV Ar+ ions for 5 min in a well-controlled manner. XPS spectra of the CAIS films in as-grown form and annealed at different temperatures before and after sputtering were illustrated in Fig. 5.5 and 5.6, respectively. The existence of C peak in these spectra may be due to the contamination effect of the substrate, evaporation source, deposition system and characterization instruments. In addition, there is O 1s photoelectron peak in the XPS

spectra of the films before sputtering process. The reason of this background signal even it was in the as-grown form indicates the experimental contamination as it was expected for the existence of C peak. This contamination on the surfaces of the films also increased with increasing in annealing temperature. This indicated that although there were in an argon flow in annealing furnace during annealing, the samples may be oxidized in these processes accidentally. The given XPS spectra of the as-grown and annealed CAIS thin films at different temperatures included all constituent elements; Cu, Ag, In and Se. Then, the XPS analysis was done for the identification of the dominant photoelectron peaks of these elements observed in the spectra. Therefore, In 3d, Cu 2p, Ag 3d and Se 3d peaks were analyzed near the surface and local chemical environment by Gaussian fitting analysis.

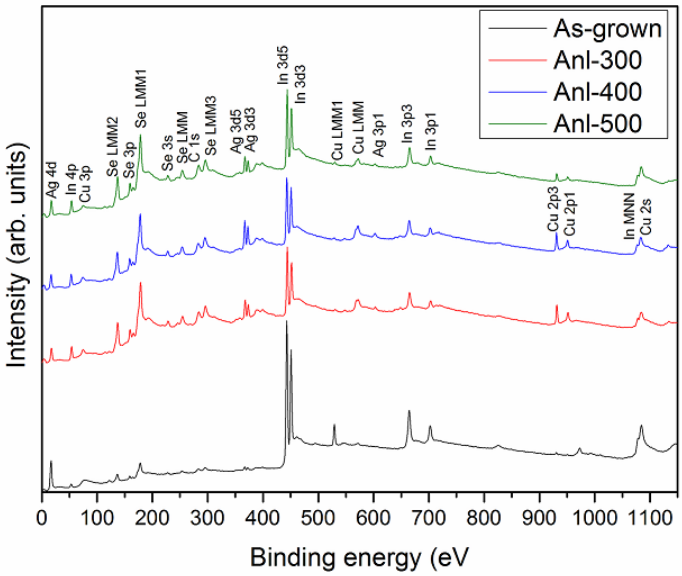

Figure 5.5: The XPS spectra of the as-grown and annealed CAIS thin films at different temperatures before sputtering

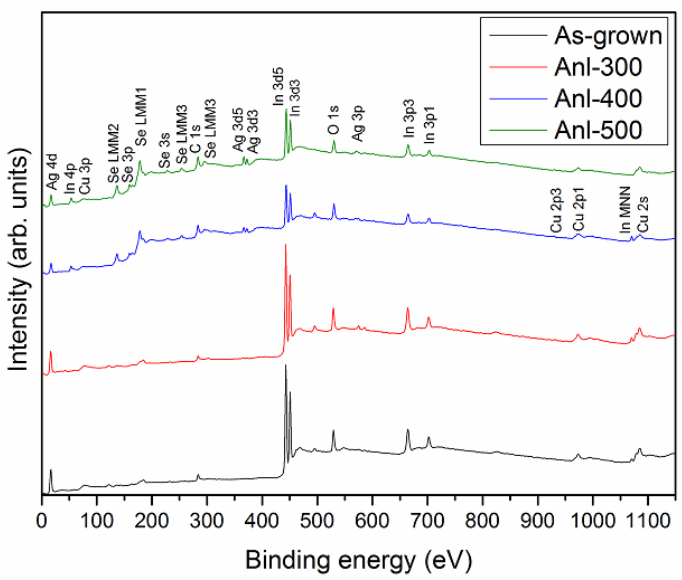

Figure 5.6: The XPS spectra of the as-grown and annealed CAIS thin films at different temperatures after sputtering

Fig. 5.7 shows the valance band electronic structure of In in as-grown and annealed CAIS thin films. From this figure, the corresponding photoelectron peaks were observed as a well-defined spin–orbit doublet with an obvious separation between the 3/2 and 5/2 sublevels. The XPS analysis of In $3d_{3/2}$ peak with fitting parameters were summarized in Table 5.2.The binding energy values obtained from In $3d_{5/2}$ peak are also given in Table 5.3 and corresponding energy separation between these two components formed by the spin-orbit coupling are calculated as 7.8, 7.9, 7.7 and 7.5 for the as-grown film and annealed films at 300, 400 and 500 °C respectively. Although these peak positions are very close to each other, an increase observed in the binding energies may be due to the increase in the oxidation state which causes a decrease in the screening of the bound electron from the ion core [300]. Moreover, local chemical environment on the surface of the films may also cause small shifts in XPS peak positions with respect to the each other.

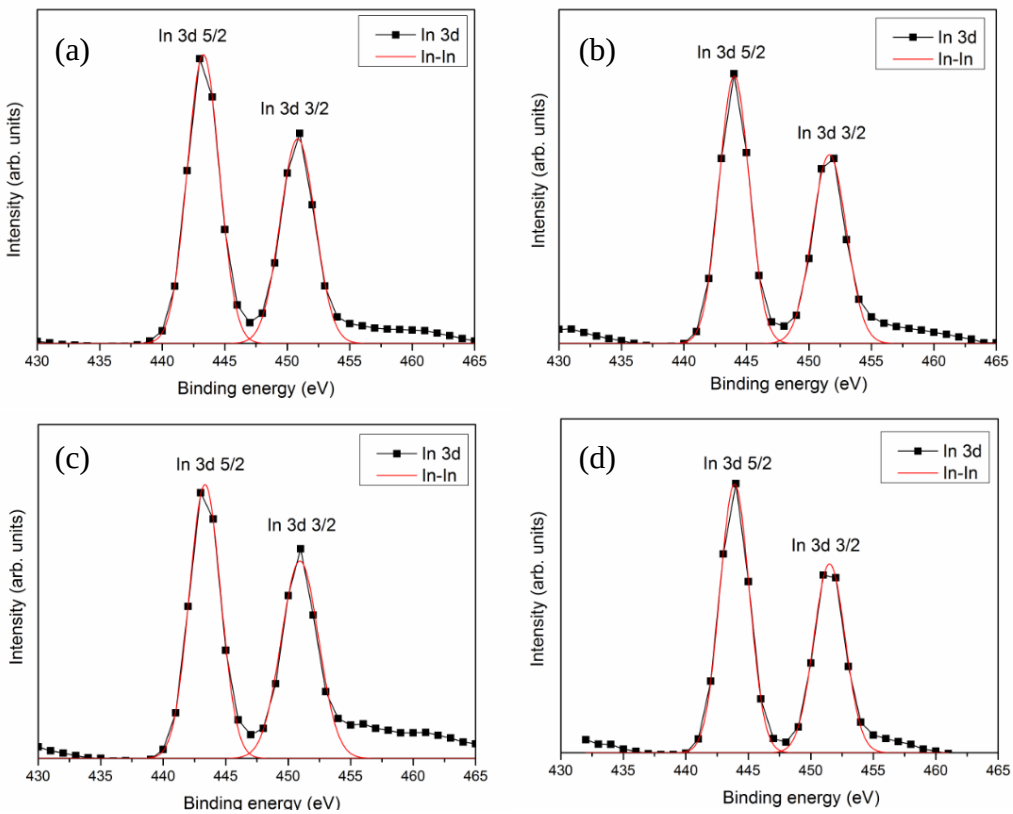

Figure 5.7: In 3d core level XPS spectrum for a) the as-grown and annealed CAIS thin films at b) 300, c) 400 and d) 500 °C

Table 5.2: Decomposition parameters of In 3d photoelectron peak with respect to $3d_{3/2}$ line

Sample	Bonding	B.E (eV) (Observed)	B.E (eV) [Ref]
As-grown	In-In	450.9	451.4 [219]
Annealed at 300 °C	In-In	451.8	451.4 [219]
Annealed at 400 °C	In-In	451.2	451.4 [219]
Annealed at 500 °C	In-In	451.5	451.4 [219]

Table 5.3: Decomposition parameters of In 3d photoelectron peak with respect to 3d5/2 line

Sample	B.E (eV) (Observed)	B.E (eV) [Ref]
As-grown	443.1	444.0 [220]
Annealed at 300 °C	443.8	444.0 [220]
Annealed at 400 °C	443.6	444.0 [220]
Annealed at 500 °C	443.5	444.0 [220]

The core-level spectra of the Cu 2p region are illustrated in Fig. 5.8 for the CAIS films. The corresponding peak intensity increased with annealing temperature which is consisted with behavior as found from compositional analysis. From these photoelectron lines, the spin-orbit doublet of the Cu 2p core level transition at binding energies of about 931 and 951 eV were observed and the corresponding fitting parameters are listed in Table 5.4 and 5.5. In addition, for the as-grown CAIS sample, there is a strong Cu^{2+} satellite positioned at around 942 eV [301]. This satellite feature was related to shake-up transitions by ligand-to-metal 3d charge transfer [302, 303]. However, the spin-orbit splitting seems to be approximately constant for as-grown and annealed CAIS films.

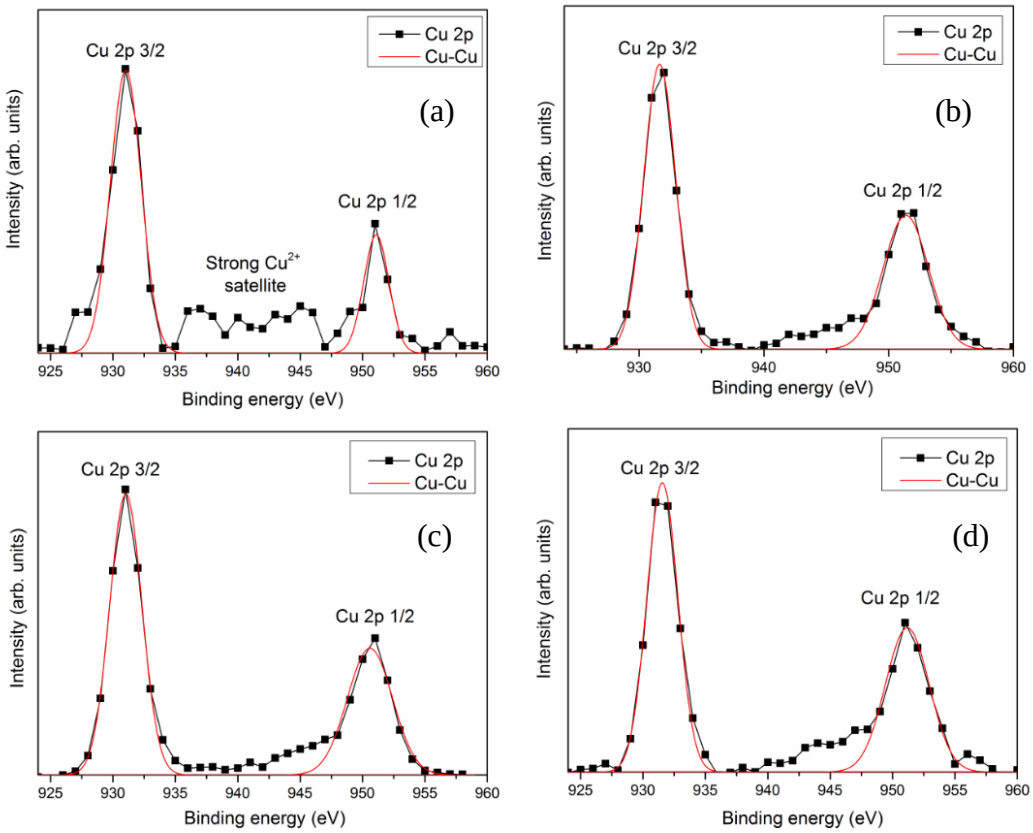

Figure 5.8: Cu 2p core level XPS spectrum for a) the as-grown and annealed CAIS thin films at b) 300, c) 400 and d) 500 °C

Table 5.4: Decomposition parameters of Cu 2p photoelectron peak with respect to $2p_{3/2}$ line

Sample	B.E (eV) (Observed)	B.E (eV) [Ref]
As-grown	951.1	951.6 [304]
Annealed at 300 °C	951.5	951.6 [304]
Annealed at 400 °C	951.2	951.6 [304]
Annealed at 500 °C	950.8	951.6 [304]

Table 5.5: Decomposition parameters of Cu 2p photoelectron peak with respect to $2p_{3/2}$ line

Sample	B.E (eV) (Observed)	B.E (eV) [Ref]
As-grown	931.1	932.7 [305]
Annealed at 300 °C	931.7	932.7 [305]
Annealed at 400 °C	931.6	932.7 [305]
Annealed at 500 °C	931.3	932.7 [305]

Similar to the XPS analysis of In, the intensity of the elemental photoelectron line of Ag 3d core level increased with annealing processes. Then, the detailed peak analysis was illustrated in Fig. 5.9. Due to spin-orbital splitting of Ag 3d core levels, Ag $3d_{5/2}$ and Ag $3d_{3/2}$ sublevels were observed in all XPS spectra of the CAIS films. The Gaussian fitting results were summarized in Table 5.6 and 5.7. Although position of orbitals in atom is sensitive to chemical environment of atom, the peak positions and splitting energies are very close to each other.

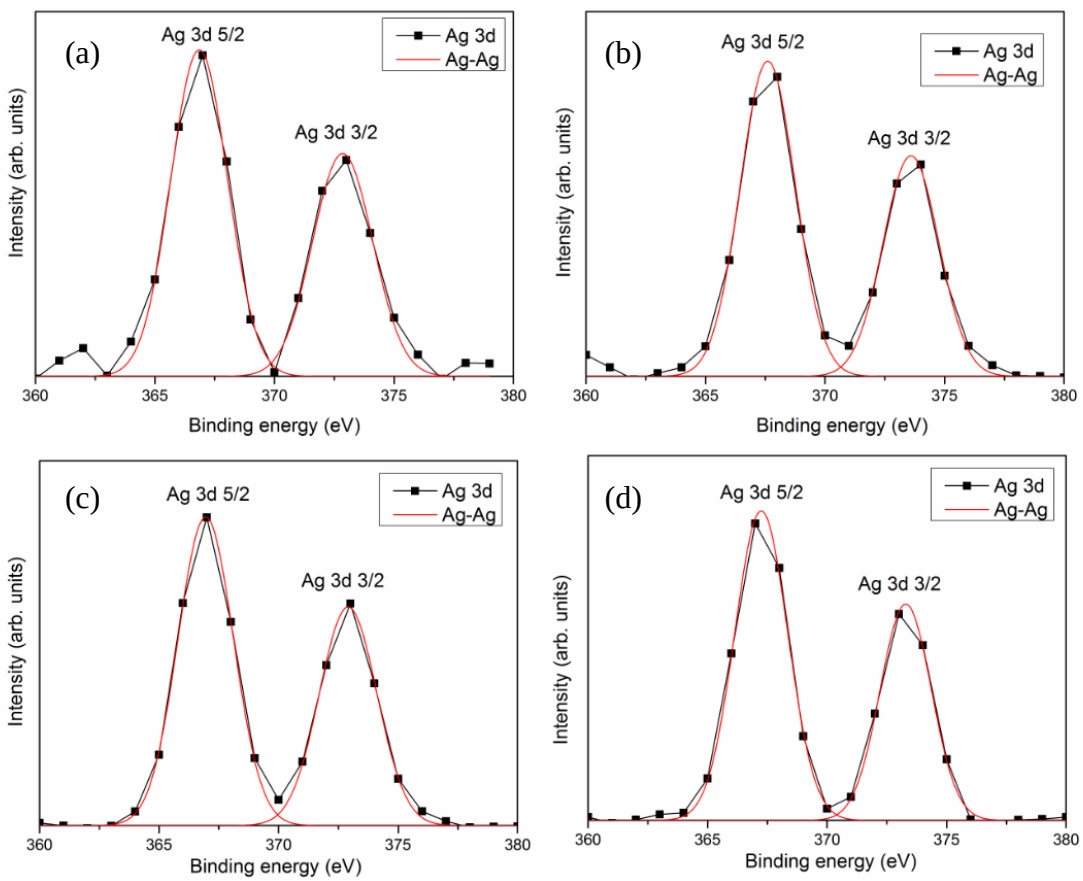

Figure 5.9: Ag 3d5/2 core level XPS spectrum for a) the as-grown and annealed CAIS thin films at b) 300, c) 400 and d) 500°C

Table 5.6: Decomposition parameters of Ag 3d photoelectron peak with respect to $3d_{3/2}$ line

Sample	B.E (eV) (Observed)	B.E (eV) [Ref]
As-grown	372.9	373.4 [306]
Annealed at 300 °C	373.7	373.4 [306]
Annealed at 400 °C	373.0	373.4 [306]
Annealed at 500 °C	373.4	373.4 [306]

Table 5.7: Decomposition parameters of Ag 3d photoelectron peak with respect to $3d_{5/2}$ line

Sample	B.E (eV) (Observed)	B.E (eV) [Ref]
As-grown	366.8	368.1 [307]
Annealed at 300 °C	367.6	368.1 [307]
Annealed at 400 °C	366.9	368.1 [307]
Annealed at 500 °C	367.3	368.1 [307]

Fig. 5.10 shows the XPS spectra of Se 3p core level for as-grown and thin films annealed in the temperature range of 300-500 °C. As seen in this figure, there was no any contribution to the Se 3d peak formation and also the effect of the spin–orbit splitting associated to a 3d core level. The experimental curve fitting results for the Se 3d photoelectron peaks are given in Table 5.8. A low chemical shift in the binding energy may be due to the relative effect of the atomic composition in the film surfaces.

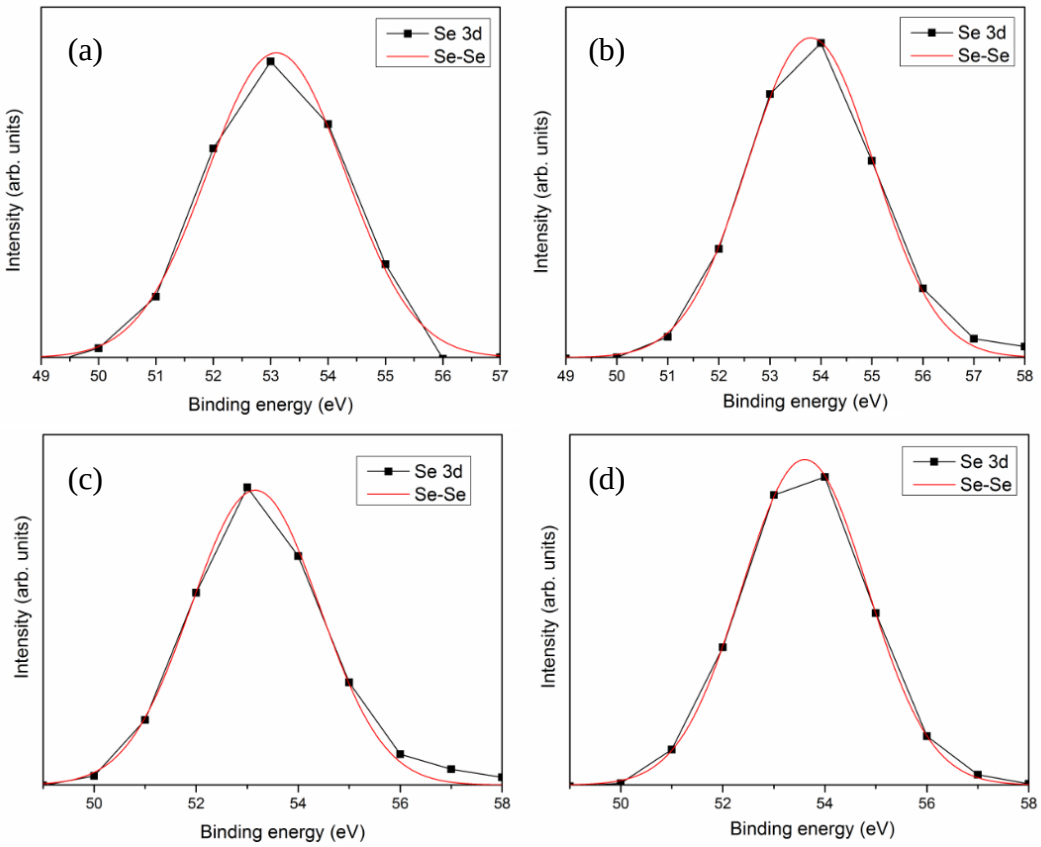

Figure 5.10: Se 3d core level XPS spectrum for a) the as-grown and annealed CAIS thin films at b) 300, c) 400 and d) 500 °C

Table 5.8: Decomposition parameters of Se 3d photoelectron peak with respect to $3d_{5/2}$ line

Sample	B.E (eV) (Observed)	B.E (eV) [Ref]
As-grown	53.9	55.5 [308]
Annealed at 300 °C	53.9	55.5 [308]
Annealed at 400 °C	53.2	55.5 [308]
Annealed at 500 °C	53.8	55.5 [308]

5.3 Optical Characterization of $Cu_{0.5}Ag_{0.5}InSe_2$ Thin Films

The analysis of optical spectra is one of the most useful tools for understanding electronic structure of the semiconductors [81]. The optical properties of the CAIS films was evaluated by transmittance measurements in the wavelength interval from

325 to 1100 nm at room temperature. As seen in Fig. 5.11, an enhancement in the transparency when CAIS thin films were subjected to annealing between 300-500 °C was observed in the optical transmission values of the films with a 40% maximum value. This variation in transmission spectroscopy of the materials might depend on the structural transformations and possible re-ordering on the surface of the thin film with annealing process [286]. In addition, as indicated in EDS analysis, the re-evaporation or segregation of the some constituent elements form the surface of the films may change surface characteristics of the films to metallic behavior.

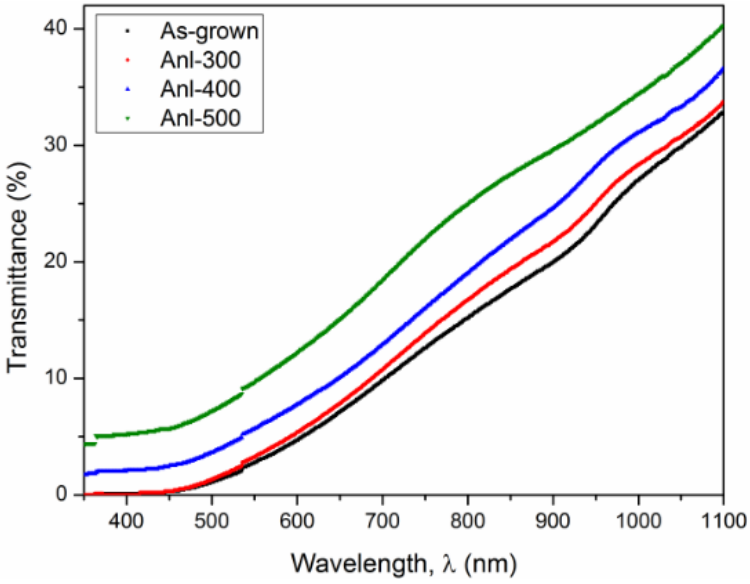

Figure 5.11: The transmittance spectra of the CAIS samples

The absorption coefficient (α) of the samples were calculated using the transmission values by means of the relations given in Eq. 2.9 and Eq. 4.10. where $T(\lambda)$ is the normalized transmittance and d thickness of the thin films. The absorption coefficient of the films was calculated in the visible region and they were found in between 8.5×10^4 and 7.0×10^5 cm^{-1} depending on both the corresponding wavelength value and structural variations with annealing process. The poor transmittance of the films can also be inferred from the high absorption characteristics of the films, since they are evaluated as the absorber layer in device applications [309].

Fig. 5.12 depicts the relation between absorption coefficient and photon energy for the CAIS thin films in the high absorption region reported by Tauc [310] and Davis and Mott [311] from which the optical band gap was determined. As shown from this figure, there is only one direct optical transition that gives band gap energies for the as-grown and annealed films as 1.51, 1.50, 1.48 and 1.44 eV, respectively. Although the calculated bang gap values are different than the results reported by other CAIS works [43, 52-54], they are in a good agreement with results reported by several researchers [311-316]. The differences with the results of the other reported works may be due to the possible morphological variations and also deposition conditions for the films. However, the variation in the band gap values with the annealing processes and temperatures were higher than the substrate temperature so it can be attributed to the observed structural modifications. This change is also evaluated in terms of the increase in the band tailing in the structure under the effect annealing [316]. Therefore, by increasing the annealing temperature, the width of localized states tails may increase and so that it can be explained by increasing of surface dangling bonds around the crystallites [314] and increase in the density of tail states adjacent to the band edge [315]. Although the spin orbit and crystal field splitting behaviors were reported in the literature for this film structure [14, 21, 22, 27], valance band splitting was not observed in the measured optical spectra of the films. Since it is not a general expectation for the chalcopyrite films [207, 317-319], the nature of the single optical transition in both as-grown and annealed CAIS thin films can be related with the strain values in the structures. On the other hand, the variations in the fundamental band gap values between this experimental work and the previous studies on CAIS structure may be due to this non-cubic crystalline field effect [320].

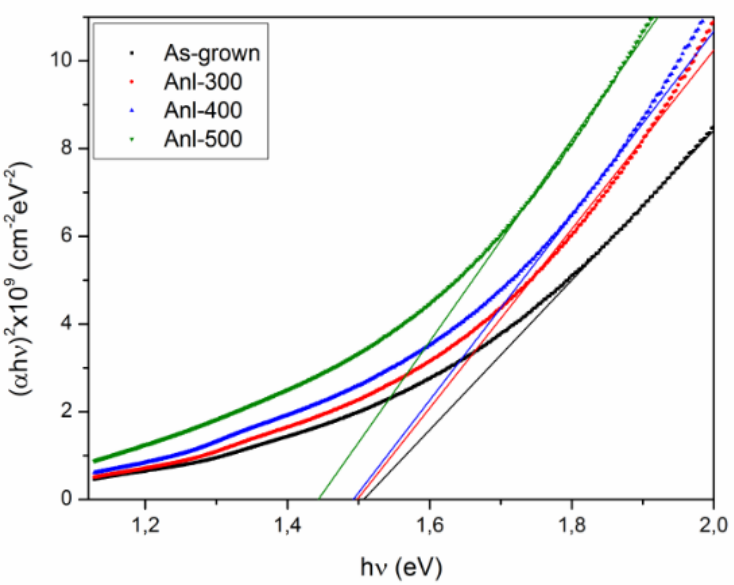

Figure 5.12: The variation of $(\alpha h\nu)^2$ with the photon energy for CAIS samples

5.4 Electrical Characterization of $Cu_{0.5}Ag_{0.5}InSe_2$ Thin Films

The electrical and photo-electrical analysis of the CAIS films were based on temperature dependent conductivity under dark and illuminated situations, Hall Effect measurements at room temperature and wavelength dependent photo-response measurements. These measurements were carried out by the van der Pauw method. Therefore, under this aim, the films deposited with Maltese-Cross geometry. In order to determine the general behavior of the conductivity and the existent current transport mechanisms, the dark conductivity analysis were done against the ambient temperature and the experimental data was illustrated in Fig. 5.13. As shown in this figure, the conductivity of the samples is in an increasing behavior with increasing sample temperature. The variation of dark conductivity as a function of temperature shows different linear regions for samples except film annealed at 500 °C, which can be taken as the indication of existence of different conduction mechanism dominating in a different temperature region with different activation energies. These energies also imply the existence of various defect levels in the forbidden band gap region [312]. On the other hand, at the last annealing step, the variation of the conductivity values was almost temperature insensitive. The semiconductor properties of the film annealed at 500 °C transformed into a degenerate form with the

effect of segregation and/or re-evaporation of Se atoms in the surface structure. As seen from Fig. 5.13, there are three distinct slopes in the curve, two different regions at the low temperature and one at high temperature regions and more than one slope in the conductivity graph indicates different energy levels. Therefore, the expression of the dark conductivity of the samples was determined by considering the all possible conduction mechanism. At first, for the high temperature region where the rate of the electron emission was excessively affected by the change in the temperature, thermionic emission over the barrier was analyzed as a predominant conduction type. Above the room temperature, the calculated activation energies were 264.2, 201.8 and 72.9 eV for as-grown, 300 and 400 °C annealed samples with a good agreement with correlation coefficient, R^2 with a value of 0.99 (Fig. 5.14). Since the conductivity for the sample annealed at 500 °C was almost temperature insensitive, the corresponding activation energy calculated in terms of thermionic emission model in the specific temperature region was found as 28.2 eV.

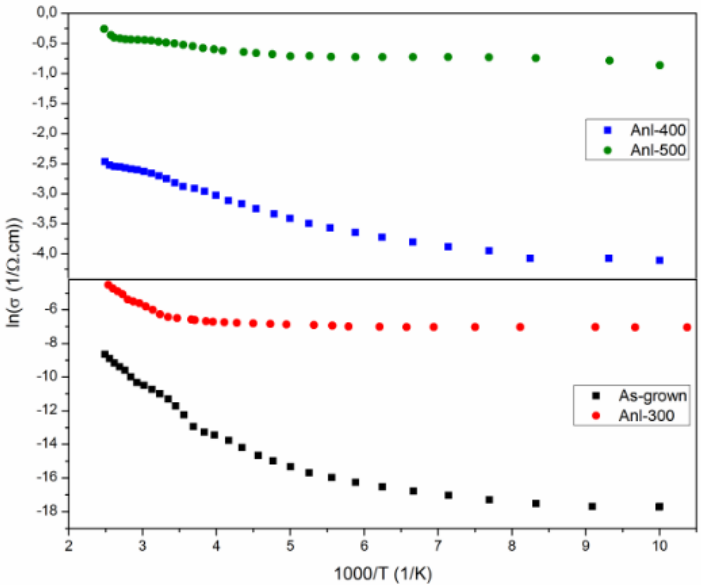

Figure 5.13: Temperature-dependent electrical conductivity of as-grown and annealed CAIS films

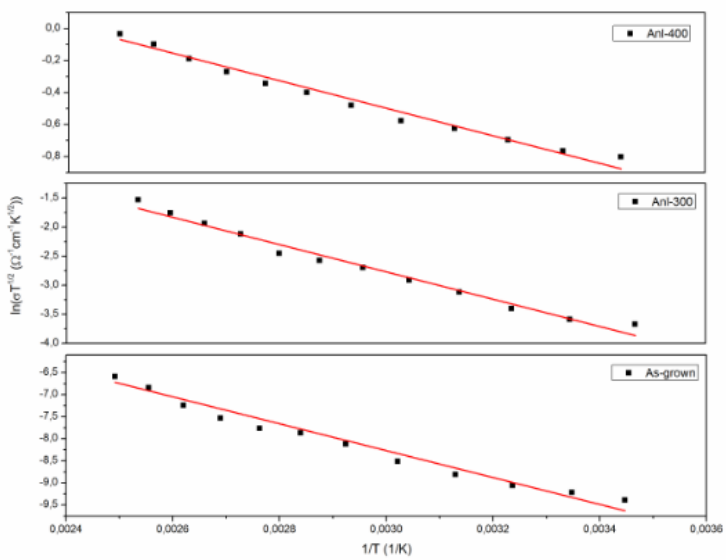

Figure 5.14 Plots of $ln(\sigma T^{1/2})$ versus T^{-1} in the high-temperature region for the CAIS film in as-grown form and annealed at 300 and 400 °C. Solid lines are the best fit lines according to Eq. 4.21

In the low temperature region, 170-270 K, the conductivity increases slowly with temperature which indicates the temperature dependence of the electrical conductivity obeying variable range hopping model. According to this model, the possibility of passing over the grain boundary potential barrier is not taken into consideration for charge carriers because of insufficient thermal activation energy. Therefore, hopping can be agreed as a conduction mechanism between the localized states near the Fermi level [142, 154]. As shown in Fig. 5.15, the conductivity of the films at this specific temperature region obeys 3D Mott VRH model and the parameters related to the Mott-VRH are listed in Table 5.9. In general, annealing process lowers the conductivity by some order of magnitude [252]. In the polycrystalline materials, the value of T_{0M} is a measure of degree of disorder in the structure [321], and it showed the decreasing behavior with increasing annealing temperature. In addition, the VRH results indicated that the calculated density of localized states near the Fermi level decreased with annealing temperature and it may be due to the effects of annealing process on the chemical bonds re-arrangements in the films [322]. Besides, decrease in the conductivity can result in the diminishing hopping states in the structure. The expected value of α and $N(E_F)$ are about 10^8 cm^{-1} and 10^{20} $cm^{-3}.eV^{-1}$, respectively [152, 323, 324] and these parameters listed in Table

5.9 are in a good agreement with these works. The fitting and calculated parameters were reasonable within Mott's requirements of the localized state model as $W>k_BT$ and $\alpha R>1$. In fact, the value of αR indicates the degree of localization of carriers in the trap states [321].

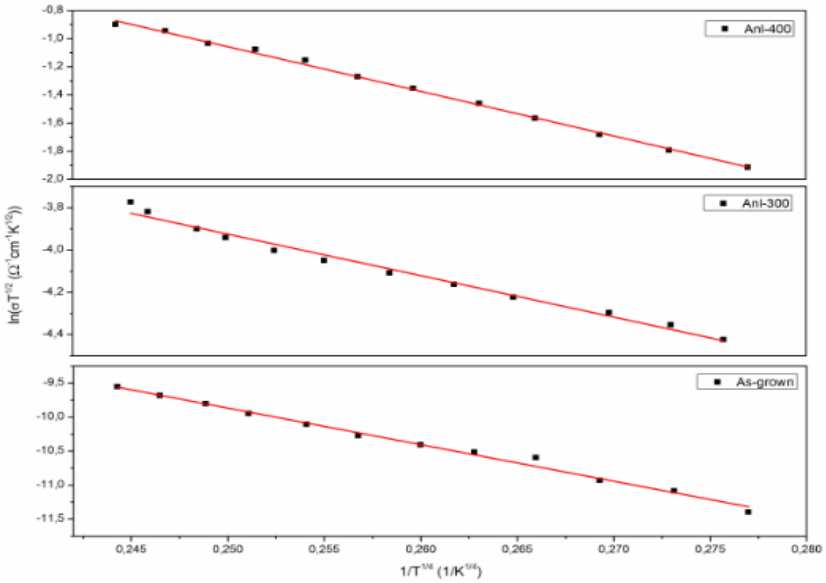

Figure 5.15: Plots of $ln(\sigma T^{1/2})$ versus $T^{-1/4}$ in the low-temperature region for the CAIS film in as-grown form and annealed at 300 and 400 °C. Solid lines are the best fit lines according to Eq. 4.22

Table 5.9: Calculated parameters of Mott VRH model

Sample	T_{0M} (K)	σ_{0M} ($K^{1/2}/\Omega cm$)	α (1/cm)	$N(E_F)$ (1/eVcm)
As-grown	$8.36x10^6$	$3.57x10^2$	$3.32x10^8$	$9.16x10^{23}$
Anl-300	$8.01x10^5$	$9.73x10^1$	$2.37x10^7$	$5.74x10^{21}$
Anl-400	$1.67x10^5$	$1.23x10^1$	$1.62x10^6$	$5.29x10^{18}$

Sample	R_M (cm)	W_M (meV)	R^2	αR_M	W_M/k_BT
As-grown	$1.56x10^{-8}$	68.5	0.98	5.19	3.46
Anl-300	$1.03x10^{-7}$	38.2	0.98	2.89	1.92
Anl-400	$1.21x10^{-6}$	25.8	0.99	1.95	1.30

In the low temperature region, 100-170 K, Efros-Shklovskii $T^{-1/2}$ VRH model, where Coulomb effect serves as a barrier to the conduction process, fits the experimental data with the regression coefficient, R^2 with a value of 0.99 (Fig. 5.16). The obtained values of the VRH parameters were given in Table 5.10. According to these results, there is a good relation between this model and the experimental conductivity values at this temperature interval, and also the calculated values indicated that the gap width Δ is comparable to the hopping energy W_{ES} due to Coulomb effect. The characteristic Efros–Shklovskii parameters varied in a same order as in the Mott parameters. Calculated average hopping distance and average hopping energy values for Efros–Shklovskii model were lower than those for Mott model as observed in [325, 326]. This observation supported the possibility of a crossover in VRH mechanism from the Mott type to the Efros-Shklovskii type [249].

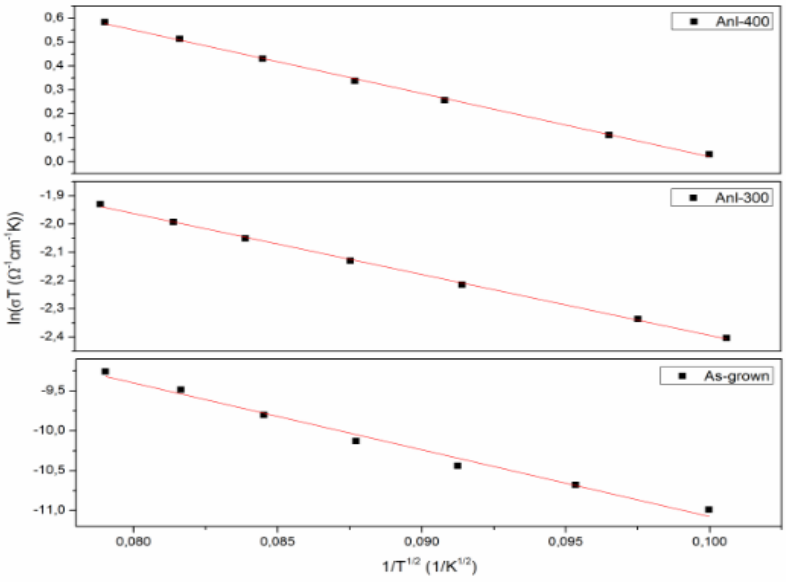

Figure 5.16: Plots of $ln(\sigma T)$ versus $T^{-1/2}$ in the high-temperature region for the CAIS film in as-grown form and annealed at 300 and 400 °C. Solid lines are the best fit lines according to Eq. 4.27

Table 5.10: Calculated parameters of Efros-Shklovskii VRH model

Sample	T_{0ES} (K)	σ_{0ES} (K/Ωcm)	R_{ES} (cm)	W_{ES} (meV)	Δ (meV)	R^2	W_{ES}/k_BT
As-grown	$7.06x10^3$	$7.05x10^{-2}$	$5.77x10^{-9}$	39.7	48.8	0.99	3.84
Anl-300	$5.76x10^2$	$9.54x10^{-1}$	$1.95x10^{-8}$	11.4	6.1	0.99	1.10
Anl-400	$5.58x10^2$	$1.61x10^1$	$3.33x10^{-7}$	11.2	5.7	0.99	1.08

The photo-conductivity characteristics of the samples were also investigated with conductivity measurements under five different illumination intensities. Fig. 5.17 shows the temperature dependence of dark current (I_{dark}) and photocurrent (I_{ph}) in between 100 and 420 K. The graph also shows that conductivity values in all temperature increased with increasing illumination intensity.

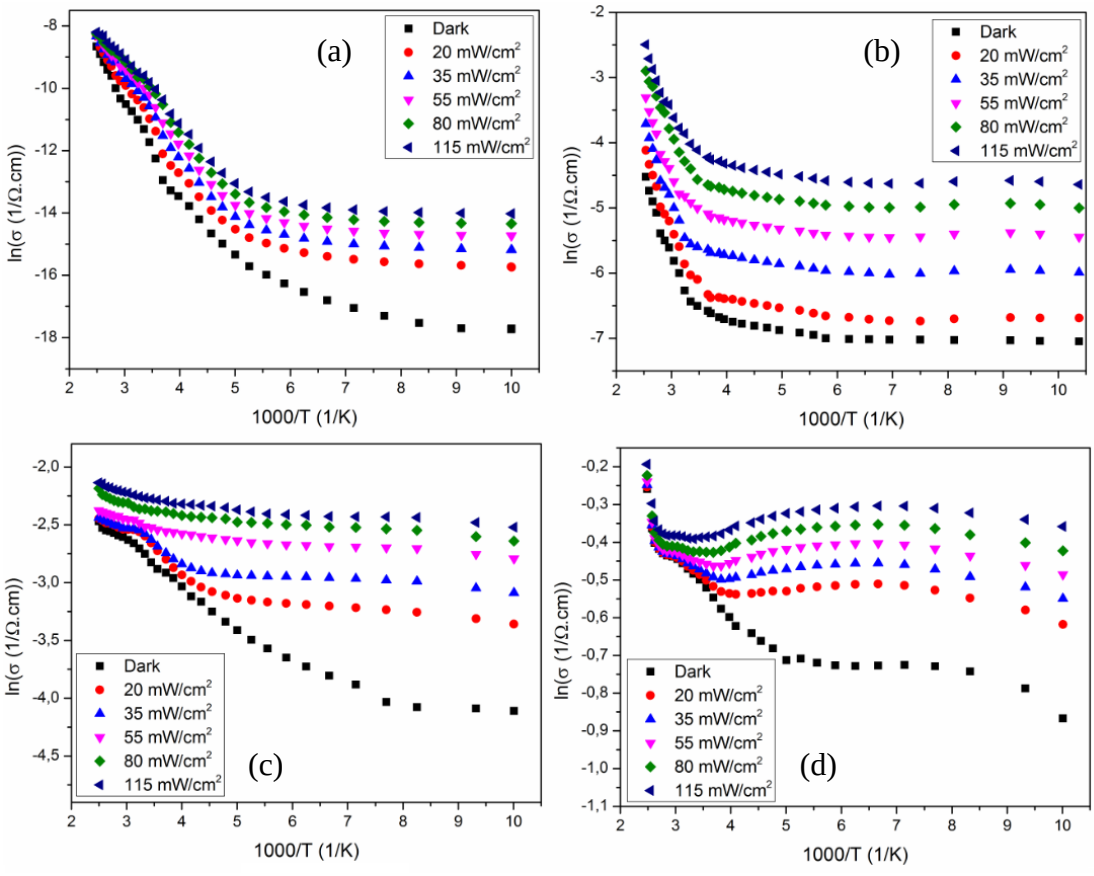

Figure 5.17: The variation of the photo-conductivity with temperature and illumination intensity for CAIS films (a) as-grown, (b) annealed at 300 °C, (c) annealed at 400 °C, (d) annealed at 500 °C.

As seen in Fig. 5.17, the photo-conductivity values are greater than the dark conductivity values, and it can be taken as the contribution of the photo-carriers to the conduction. Moreover, the conductivity of the samples increases with increasing the illumination intensity. The variation of the photo-conductivity values was investigated by photosensitivity calculations in which it was used as a basic parameter for photo-conductive materials [327, 328]. The values of photosensitivity were calculated from total current measured under illumination effect under the reference value out dark current. Then, the photosensitivity analysis of these CAIS films illustrated that there was a decreasing behavior with increasing annealing temperature. On the other hand, the change in the ratio of dark and illuminated currents with the applied voltage increased with the increasing illumination intensity for all samples. In order to study the carrier recombination characteristics in the CAIS films, the relation between the photocurrent and photoexcitation intensity was analyzed. The power exponent coefficient of proportionality for each film at different ambient temperature was calculated. The corresponding analysis for all CAIS films at the absolute temperatures between 100 and 400 K with 50 K increments are shown in Fig. 5.18. The variation with the illumination intensities has the characteristic of $I_{pc} \ \alpha \ \Phi^{\gamma}$ where the exponent, γ, is a distinctive indicator of the non-equilibrium carriers and determines the type of the recombination mechanism [329]. The photo-conductivity dependence of light intensity and temperature was calculated in two-center model [126]. At low temperatures this coefficient was below 0.5 for as-grown films, and around 1.0 for the films annealed at 300 and 400 °C, and it was almost 0.5 for the films annealed at 500°C. Then, the ɣ values increased up to 1.0 for as-grown and to 1.2 for the films annealed at 300 °C. In addition, it reached to about 2.0 for the films annealed at 400 and 500 °C with increasing sample temperature. According to the two-center recombination model; as-grown and 500 °C annealed CAIS thin films change its behavior from sublinear to supralinear with the variation in the sample temperature; however, the other annealed films were found in the supralinear photo-conductivity behavior at all temperatures. This increasing behavior of the exponent γ values with increasing ambient temperature confirmed the longer lifetimes for free carriers and stronger recombination process at the film surface [319].

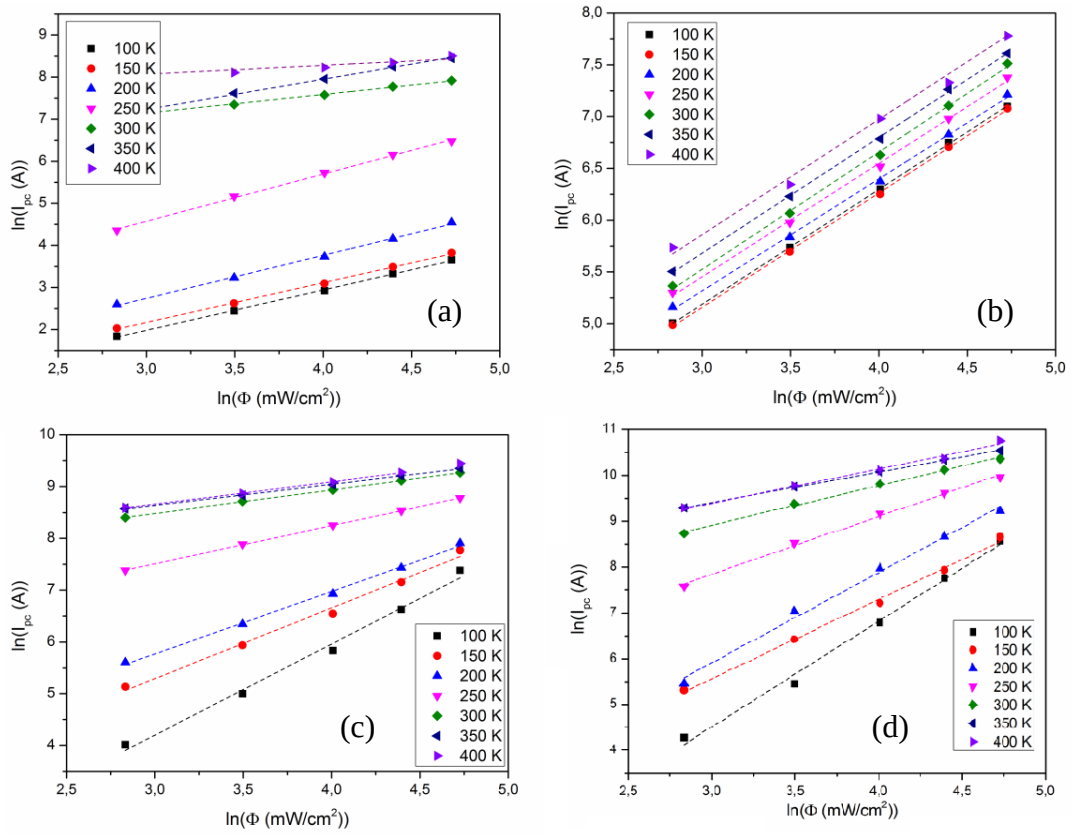

Figure 5.18: The variation of the photocurrent as a function of illumination intensity for CAIS films (a) as-grown, (b) annealed at 300 °C, (c) annealed at 400 °C, (d) annealed at 500 °C.

The standard Hall Effect measurements were performed for all CAIS samples under the constant magnetic field strength of 0.96 T at room temperature. From these measurements, the sign of Hall-voltage showed that all the samples are p-type and their conductivity behaviors were also confirmed by hot probe method. Moreover, the room temperature carrier concentration values of the as-grown film and films annealed at 300, 400 and 500 °C were calculated as, 1.89×10^{16}, 3.47×10^{17}, 1.18×10^{18} and 3.56×10^{18} cm^{-3}; and the Hall mobility values were found as 0.33, 0.75, 1.42 and 3.58 $cm^2/V.s$, respectively.

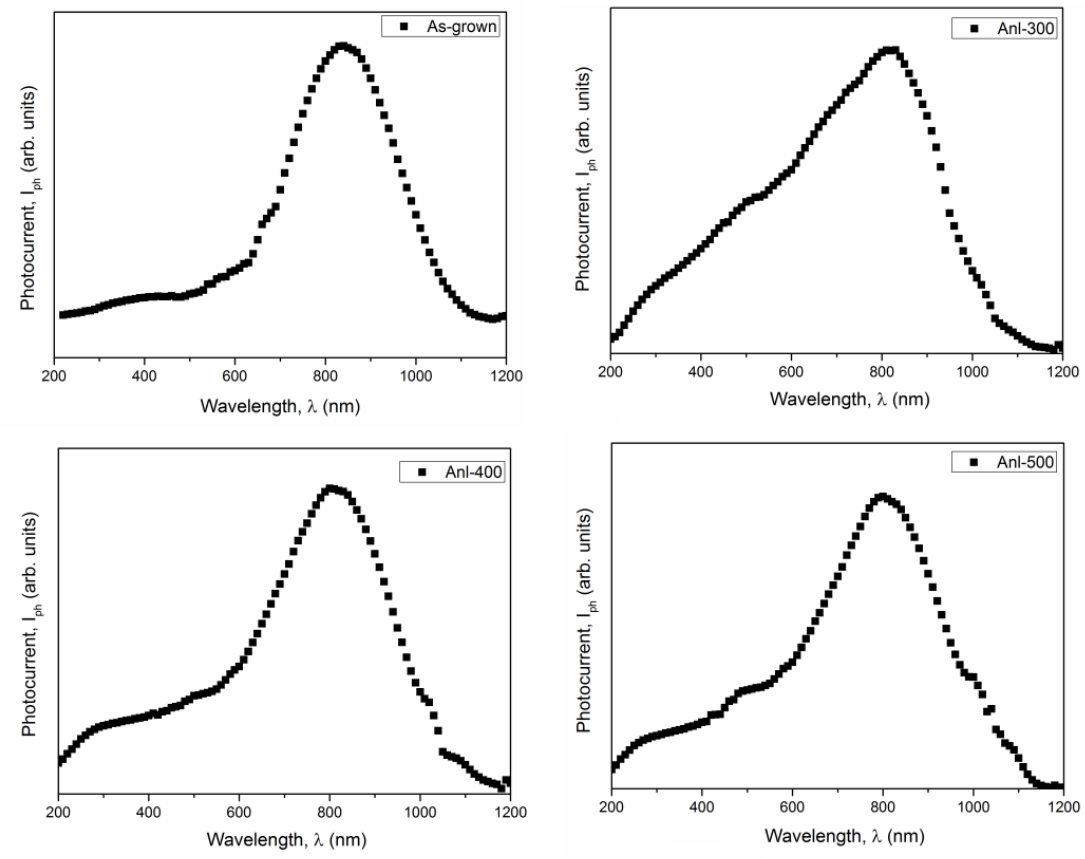

Figure 5.19: The normalized photocurrent response of CAIS films
(a) as-grown, (b) annealed at 300 °C, (c) annealed at 400 °C, (d) annealed at 500 °C.

The spectral photo-response measurements of the CAIS films were carried out to determine the band gap energy of these structures. As illustrated in Fig. 5.19, there was a single peak on each of the spectra that corresponds to only one optical transition in these samples. Calculated energy values of optical transitions from the spectra of the films were very close to the results obtained from the transmission measurements as 1.49, 1.50, 1.52 and 1.54 eV, respectively. These results also indicated the absence of valence band splitting for the deposited CAIS films.

5.5. Device Characterization

In order to determine the device parameters of In/p-CAIS/n-Si/Ag heterojunction, I-V characteristics of the diode at the temperature range of 220-360 K were measured

and plotted in Fig. 5.20. It shows that the rectifying behavior of the deposited heterojunction structure indicated a typical p-n junction diode [163]. The rectification factors, which are formulated as I_F /I_R forward and reverse currents, respectively, were calculated about 10^2 magnitude and the maximum rectification factor (RF) was observed when the temperature was 220 K.

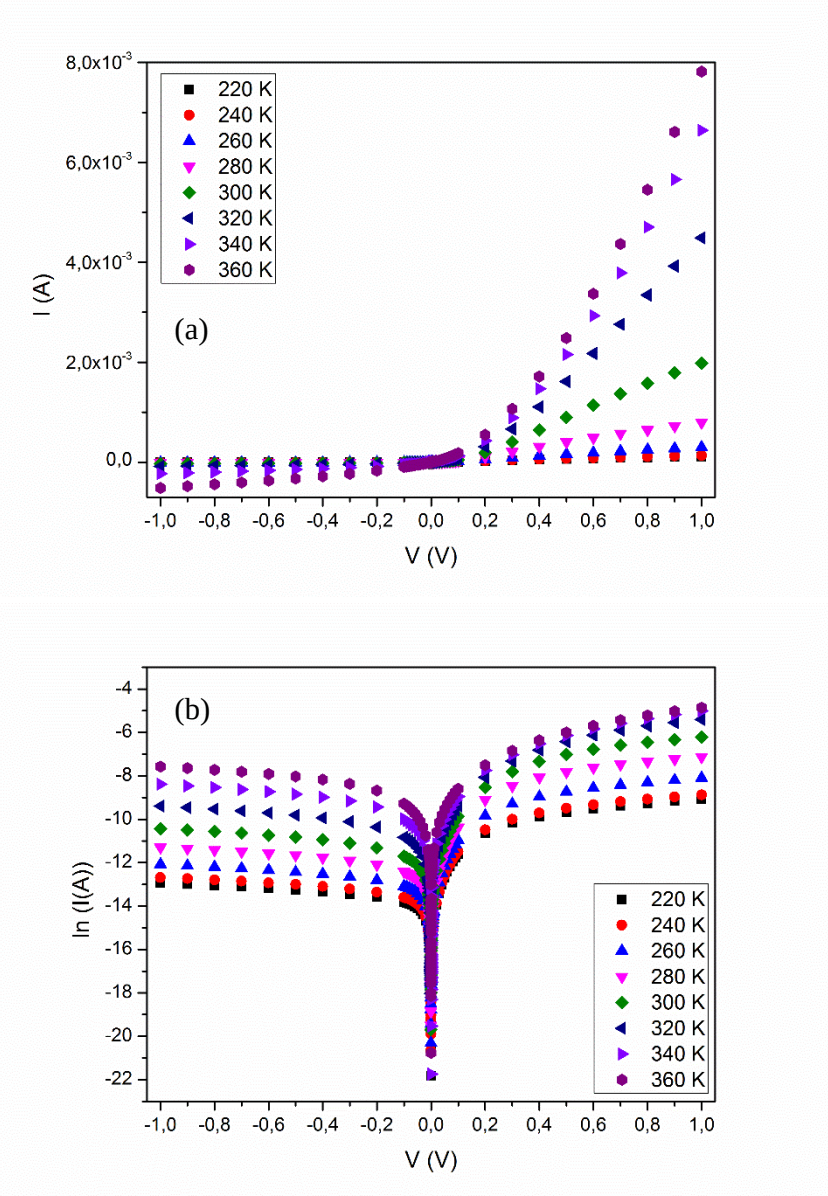

Figure 5.20: (a) Linear and (b) semi-logarithmic I-V plots of p-CAIS/n-Si hetero-junction at different ambient temperatures.

The voltage dependence of rectification factor for studied temperatures was shown in Fig. 5.21. As seen from Fig. 5.21, the RF values increased with increasing voltage at constant temperature. This variation is a natural behavior of a p-n junction. On the other hand, when the voltage was constant, the RF values decreased with increasing ambient temperature.

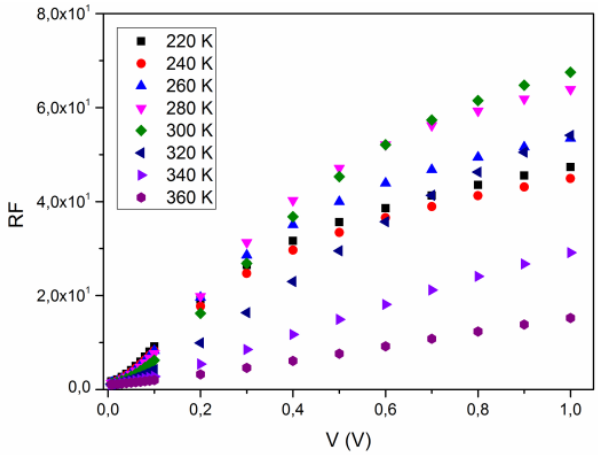

Figure 5.21: Plots of rectification factor (RF) versus V at different ambient temperatures.

In Fig. 5.20, at the forward and reverse bias voltage higher than 0.5 V in magnitude, the currents were linear with bias voltage because of the series and shunt resistances effects [163, 330]. In this study, R_S and R_{Sh} values were calculated from the parasitic resistance ($R_p = \frac{dV}{dI}$) in the forward and reverse bias, respectively, and the obtained values were given in Table 5.11. It was found that the magnitude of both resistances decreased with increasing temperature.

The I-V analysis of In/p-CAIS/n-Si/Al heterojunction diode was analyzed by the diode equation expressed in Eq. 4.35 where, I_0 is the reverse saturation current, V is the bias voltage, n is the ideality factor and k is the Boltzmann constant [113]. The reverse saturation current is given by the following relation Eq. 4.36. In this equation, Φ_b is the potential barrier, A is the device area ($A \cong 15x10^{-3}$ cm^2), A^* is Richardson constant as $A^*=4\pi qm^*k^2/h^3=120(m^*/m)$ (A/(cm^{2}K^2) [113]. The ideality

factor values of the diode at studied temperature were calculated from the slope of the Fig. 5.20 (b) by using the relation, Eq. 4.37.

Other diode parameters I_0 and Φ_b values were determined by the Eq. 4.35 and Eq. 4.36. The obtained parameters were given in Table 5.11. According to these results, Φ_b values increased with increasing temperature (Fig. 5.22 (a)). The ideality factor n can be used to obtain information about transport properties of the junction. Calculated n values were higher than unity (Fig. 5.22 (b)) and it indicated that there can be other transport mechanisms different from the pure thermionic emission mechanism in which $n=1$ [163]. Therefore, the possible transport mechanisms including thermionic emission, interface recombination, recombination-generation and tunneling were discussed to determine the dominant mechanism in the prepared diode structure [262]. Moreover, the activation energy for each transport mechanisms was determined by analyzing the slope of the characteristic I-V relations.

Table 5.11: The device parameters of the p-CAIS/n-Si hetero-junction by using the parasitic resistance and Schottky diode equations.

T (K)	R_S (Ω)	R_{Sh} (Ω)	n	I_0 (A)	$q\Phi_b$ (eV)
220	$6.11\text{x}10^{3}$	$1.56\text{x}10^{6}$	2.78	$3.56\text{x}10^{-7}$	0.48
240	$5.64\text{x}10^{3}$	$1.03\text{x}10^{6}$	2.61	$5.98\text{x}10^{-7}$	0.52
260	$2.39\text{x}10^{3}$	$4.31\text{x}10^{5}$	2.34	$8.10\text{x}10^{-7}$	0.56
280	$8.82\text{x}10^{2}$	$1.58\text{x}10^{5}$	2.12	$1.27\text{x}10^{-6}$	0.60
300	$3.22\text{x}10^{2}$	$5.30\text{x}10^{4}$	2.03	$2.23\text{x}10^{-6}$	0.63
320	$1.37\text{x}10^{2}$	$1.73\text{x}10^{4}$	1.83	$3.58\text{x}10^{-6}$	0.66
340	$8.97\text{x}10^{1}$	$7.02\text{x}10^{3}$	1.80	$6.60\text{x}10^{-6}$	0.59
360	$7.83\text{x}10^{1}$	$3.38\text{x}10^{3}$	1.65	$9.60\text{x}10^{-6}$	0.72

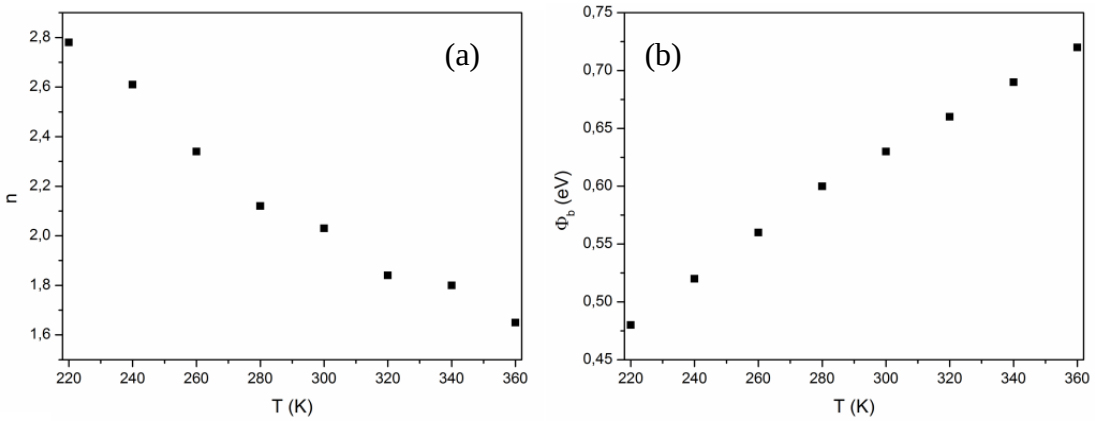

Figure 5.22: The variation of (a) the ideality factor (*n*) and (b) the barrier height (Φ_b) with different sample temperature.

For the thermionic emission (TE) model, the ideality factor values should be unity and also the $ln(I_0/T^2)$ versus $1/T$ plot should be linear [258], and the linearity is observed in Fig. 5.23. If interface recombination (IR) is dominant transport mechanism, the activation energy of $ln(I_0)$ versus $1/T$ (Fig. 5.24) should be approximately equal to band gap of CAIS [163]. To analyze the suitability of the model based on recombination-generation (RG) in depletion region, the $\ln(I_0/T^{-5/2})$ versus $1/T$ was plotted in Fig. 5.25. By this model the ideality factor value is equal to 2 [163], so that the activation energy of $\ln(I_0\ T^{-5/2})$ versus $1/T$ graph should be approximately half of the band gap [266]. The calculated activation energies for these models were about 114.2, 161.1 and 101.1 meV, respectively. According to these results, there was insufficient evidence for these models that they were dominant transport mechanism. In addition to these mechanisms, the I-V relation of this junction cannot provide the requirements of the SCLC mechanism where the order of voltage relation was found to be lower than 2 for all voltage regions.

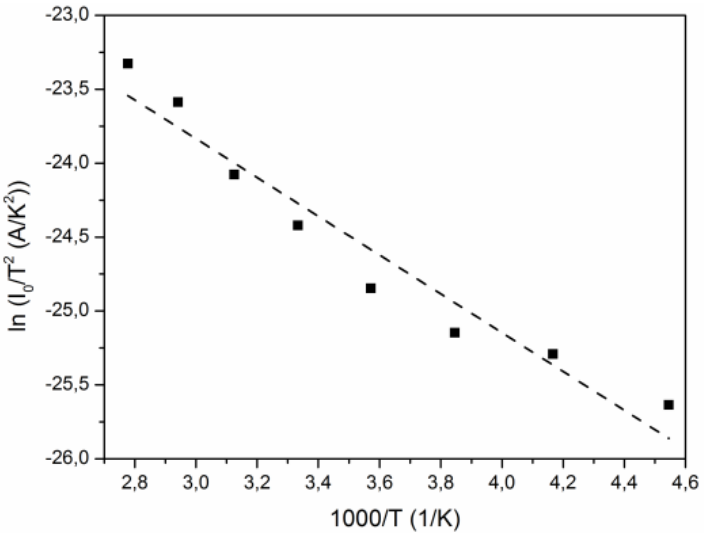

Figure 5.23: Plots of $ln(I_0T^{-2})$ versus $1000/T$ for the p-CAIS/n-Si device.

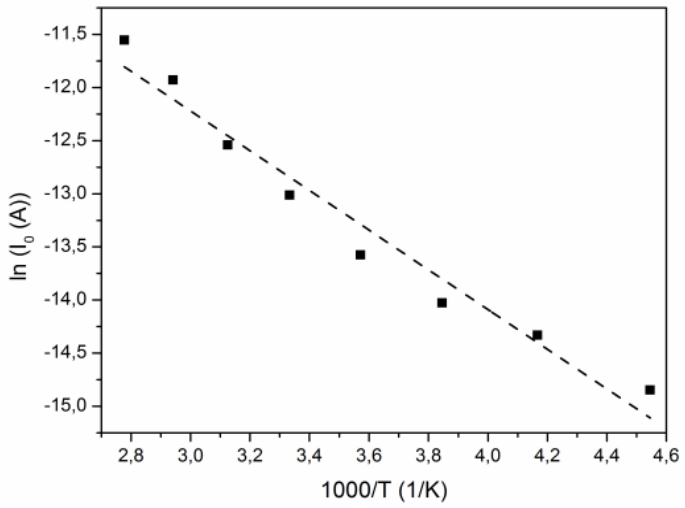

Figure 5.24: Plots of $ln(I_0)$ versus $1000/T$ for the p-CAIS/n-Si device.

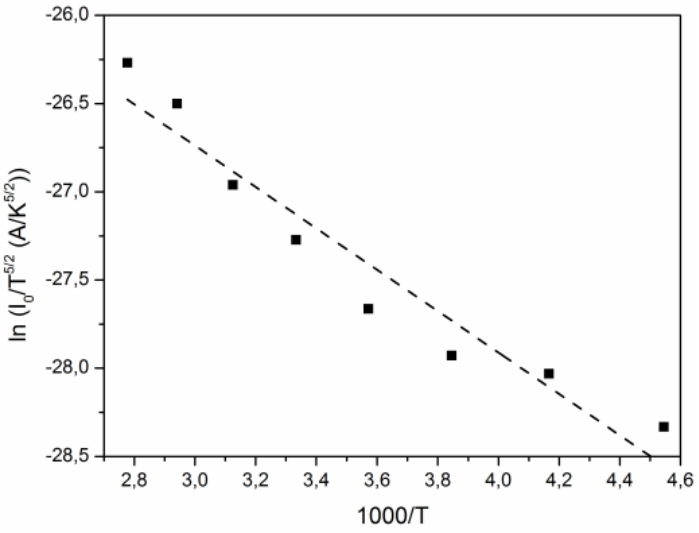

Figure 5.25: Plots of $ln(I_0T^{-5/2})$ versus $1000/T$ for the p-CAIS/n-Si device.

The decrease in Φ_b and increase in the n with decreasing temperatures pointed to the tunneling current mechanisms such as thermionic field emission (TFE) or field emission (FE). If the current transport is controlled by the TFE or FE theory, the relationship between the current and voltage can be expressed as [331]

$$I = I_{tun}\left[exp\left(\frac{qV - IR_s}{E_0}\right) - 1\right] \tag{5.1}$$

with

$$n_{tun} = \frac{E_{00}}{kT}coth\left(\frac{E_{00}}{kT}\right) = \frac{E_0}{kT} \tag{5.2}$$

where E_{00} is the characteristic tunneling energy that is related to the tunnel effect transmission probability

$$E_{00} = \frac{h}{4\pi}\left(\frac{N_A}{m^*\varepsilon_s}\right)^{1/2} \tag{5.3}$$

where m^* is tunneling effective mass. Under this analysis, ideality factor was further analyzed by plotting nkT/q against kT/q in Fig. 5.26. According to Fig. 5.26, it was

observed that the slope was relatively temperature independent. Therefore, the main current transport mechanism of this heterojunction was found tunneling-like transport of the dark diode current with E_{00} =52.4 meV.

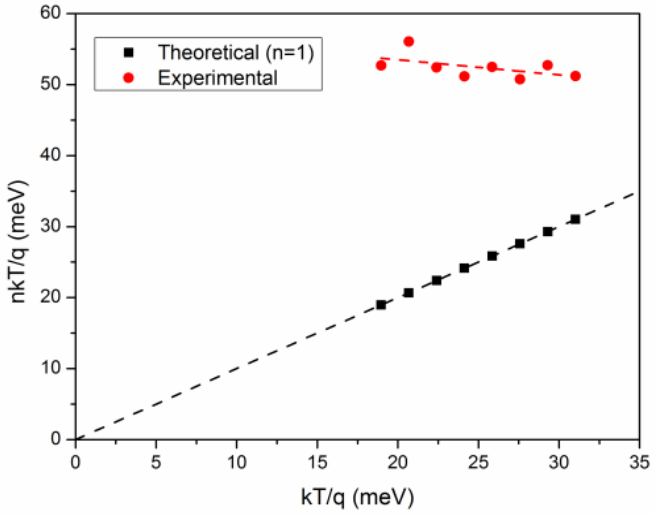

Figure 5.26: Plot of *nkT/q* versus *kT/q* for the p-CAIS/n-Si device.

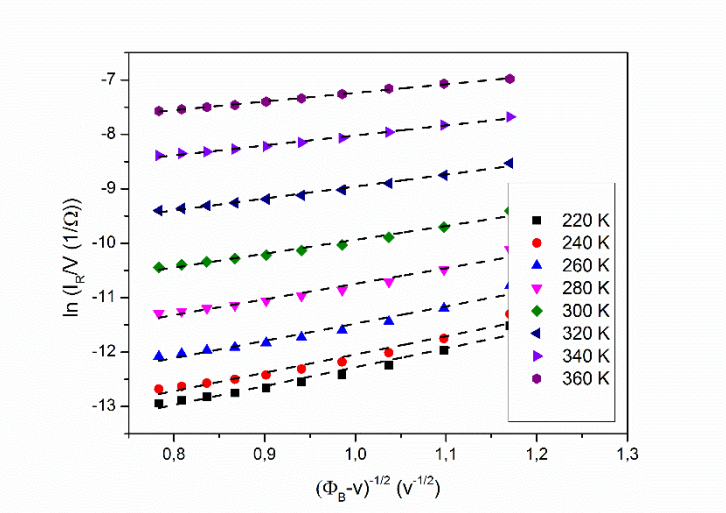

Figure 5.27: Plot of $ln(I_R/V)$ versus $(\Phi_b\text{-}V)^{-1/2}$ for the p-CAIS/n-Si device.

In addition to the forward bias characteristics, the current mechanism in the reverse bias region was investigated to complete the I-V analysis of the p-CAIS/n-Si device. Therefore, the reverse current values were analyzed in terms of the requirements of the possible transport mechanisms. However, as observed in the forward transport behavior, the leakage current characteristics of the junction were found to be approximated by the tunneling mechanism. In fact, the reverse current values showed

an exponential behavior with the voltage variations [332]. Then, the relation between the reverse current and applied voltage was analyzed by using the Eq. 4.42 and the result is shown in Fig. 5.27. The temperature dependence at reverse bias indicates that there were in between 10^1 to 10^2 number of tunneling step and about 10^5 traps act role in the reverse current mechanism across the barrier.

In order to obtain more information about the p-CAIS/n-Si device, C-V measurements were carried out at room temperature under dark condition. The results of the C-V measurements are shown in Fig. 5.28 and also corresponding C^{-2} variations with the voltage values is given in Fig. 5.29. Then, Fig. 5.28 shows that in the forward bias region, the capacitance values decreases with increasing frequencies and also there is a small decreasing behavior with increasing the voltage values when considering on each frequency case. In the reverse bias region, the capacitance values were almost constant value and this can be attributed to the electrical characteristics of the films [328]. In addition, in all voltage regions the C-V dependence was weak at high frequency values.

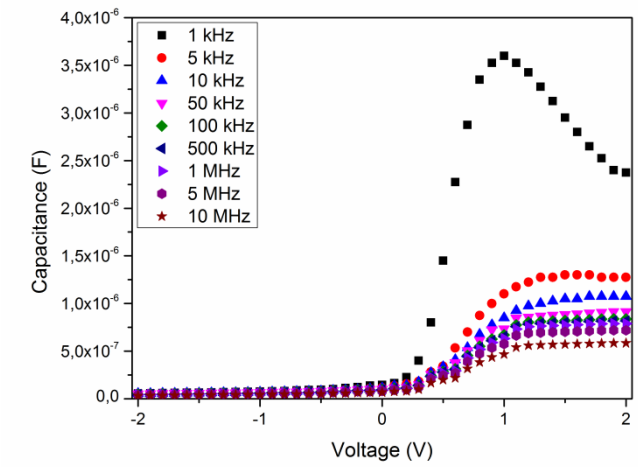

Figure 5.28: Room temperature C-V plots of the p-CAIS/n-Si structure at different frequencies

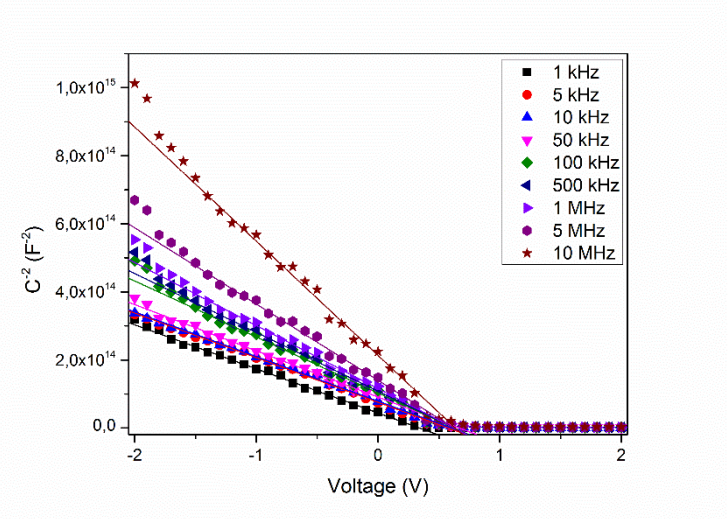

Figure 5.29: The variation of C^{-2} with voltage for the p-CAIS/n-Si device under different frequencies

As seen in Fig. 5.29, there is no remarkable change in the barrier height of the device depending on the variation in the applied frequency values. Therefore, these values are found around 0.70 eV from the intercept values at voltage axis. In addition, in Fig. 5.30 the zero biased capacitance values of the device with respect to the frequency are illustrated and by using these values of capacitance values at low and high frequency, the number of interface states was estimated as in the order of 4.8×10^{10} $cm^{-2}V^{-1}$.

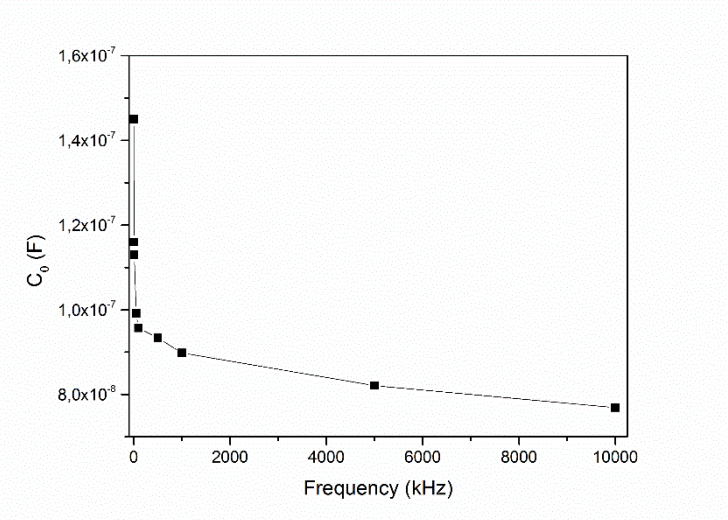

Figure 5.30: The variation of capacitance at zero bias with frequency in the p-CAIS/n-Si device

From these results, the energy band diagram of the p-CAIS/n-Si heterojunction is estimated mainly by Aderson's model in Fig. 5.31 [167]. On the basis of this model, the diagram was constructed with the band gap value found in optical analysis and also barrier height from I-V and C-V measurements. Then, the other values were used from the literature works [94]. On the other hand, the electronegativity of the CAIS structure is approximated from the reported CIS and AIS works [94]. As seen in Fig. 5.31, the discontinuities in the conduction and valence bands were calculated as 0.38 and 0.25 eV, respectively.

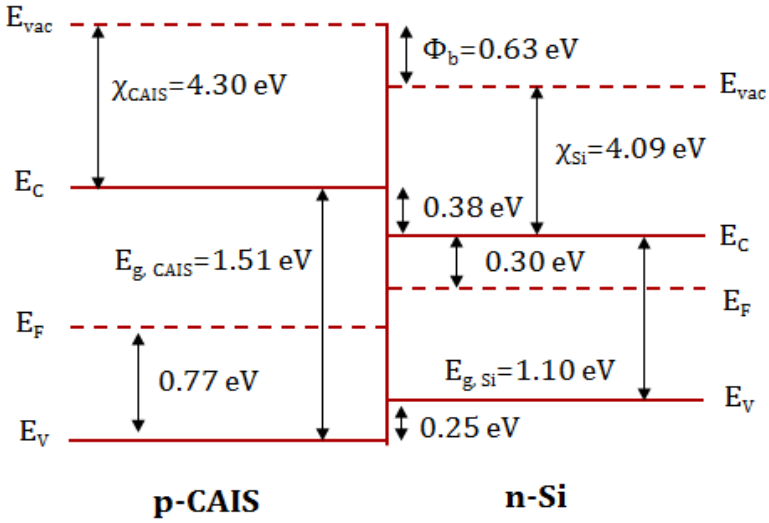

Figure 5.31: The band diagram of the p-CAIS/n-Si device

The spectral photo-response measurement of the p-CAIS/n-Si device was carried out to observe the working range of this structure and also contributions of the layers on this structure. As seen in Fig. 5.32, the photocurrent peak values were found in around 820 and 1050 nm which correspond approximately to 1.50 and 1.18 eV, respectively. The calculated peak values are also found in a good agreement with the results of the optical measurements on the CAIS thin film layer. In addition, according to Fig. 5.32, it can be implied that p-CAIS/n-Si device can cover the optical spectra of 400-1200 nm.

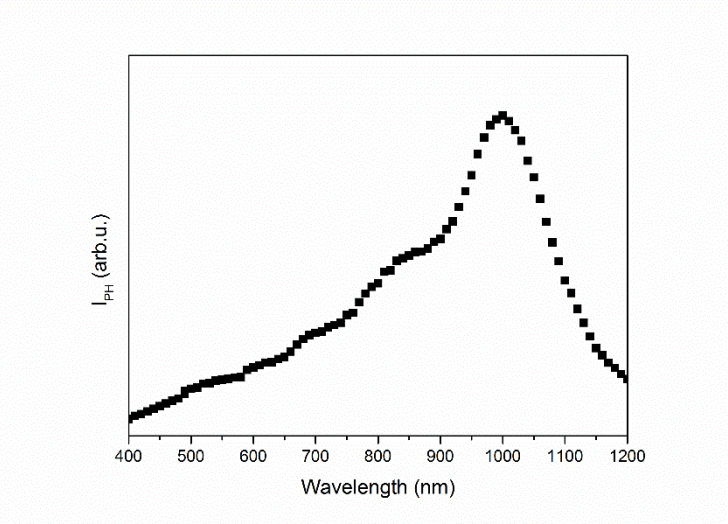

Figure 5.32: Photo-current versus wavelength plot of the p-CAIS/n-Si device

CHAPTER 6

RESULTS AND DISCUSSIONS-3
($ZnInSe_2/Cu_{0.5}Ag_{0.5}InSe_2$ HETEROJUNCTION

6.1 Introduction

Within the scope of the material characterization of the ZIS and CAIS thin films, and also device characterization of these layers from the junction fabricated with the Si-wafer, their thin film heterojunction structure deposited on the ITO substrate was detailed in this section. Although thin film photovoltaic researches are mostly focused CIGS and CIS based solar cells, this work is concentrated on CAIS structures as an absorber layer under the aim of investigation of its tailoring advantages on the CIS structure. In addition, based on the works on the replacement of use of Cd in the n-type layer formation, ZIS structure was discussed as a candidate for the alternative layer. To overcome the resistivity problems and also environmental concerns on the choice of Cd-based structures, as a Cd-free device structure were investigated. As a practical viewpoint, this semiconductor compound contains In and Se elements in the composition which are also present in the absorber layer.

6.2. Device Characterization under Dark

In the temperature range of 220-360 K, Fig. 6.1 (a) and (b) show the current-voltage (I-V) characteristics of the fabricated thin film heterojunction device. As seen in Fig. 6.1, the forward current shows an exponential increase with the applied voltage at low forward bias region, whereas at high forward bias it has a linear behavior. As

shown in Fig. 6.1 (b), the junction exhibits rectifying behavior with approximately 2 rectification factor at 0.8 V, for all sample temperatures. From this dark I-V measurement, RF values at constant bias were found approximately as in the order of 10^3. As given in Fig. 6.2, this calculated value is in decreasing behavior with increasing ambient temperature that may be due to the localized trap levels at the interface and inhomogeneous trap distribution in the structure [333, 334].

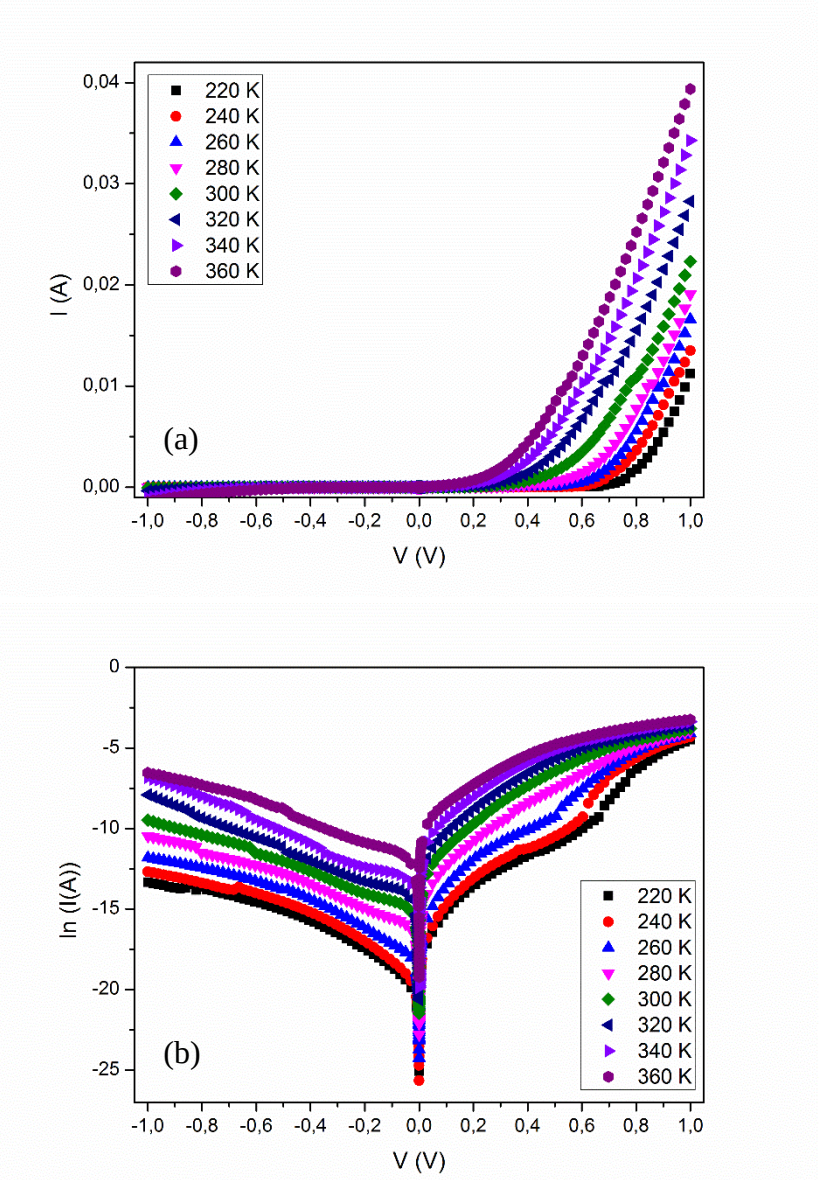

Figure 6.1: (a) Linear and (b) semi-logarithmic I-V plots of n-ZIS/p-CAIS hetero-junction at different ambient temperatures.

The linear behavior in the high forward and reverse bias regions indicates the serial and shunt resistance effects on the junction, respectively. Therefore, the corresponding resistance values were calculated by using the parasitic resistance relation in these applied voltage regions. In addition, since the heterojunctions show the rectifying behavior similar to a typical p–n junction diode, the I-V relation of this junction was described by the standard diode equation. Therefore, the calculated I-V parameters of this diode structure according to the Schottky diode equation are listed in Table 6.1.

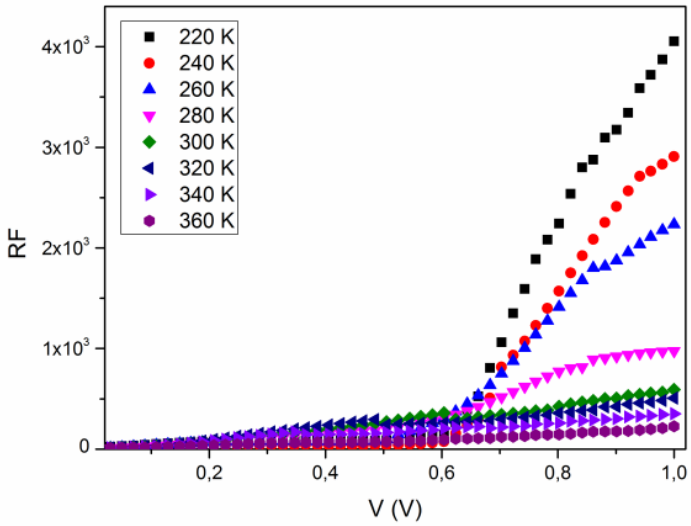

Figure 6.2: Plots of rectification factor (RF) versus V at different ambient temperatures.

Table 6.1: The device parameters of the n-ZIS/p-CAIS hetero-junction by using the parasitic resistance and Schottky diode equation.

T (K)	R_S (Ω)	R_{Sh} (Ω)	n	I_0 (A)	$q\Phi_b$ (eV)
220	$5.68x10^3$	$7.84x10^4$	2.29	$1.87x10^{-8}$	0.64
240	$5.47x10^3$	$6.59x10^4$	2.24	$4.06x10^{-8}$	0.68
260	$4.06x10^3$	$4.51x10^4$	2.19	$1.36x10^{-7}$	0.70
280	$2.41x10^3$	$3.43x10^4$	2.17	$6.27x10^{-7}$	0.71
300	$9.54x10^2$	$1.23x10^4$	2.16	$2.18x10^{-6}$	0.72
320	5.9610^2	$7.03x10^3$	2.13	$5.88x10^{-6}$	0.75
340	$3.89x10^2$	$6.80x10^3$	2.12	$1.63x10^{-6}$	0.76
360	$2.36x10^2$	$4.51x10^3$	2.10	$5.11x10^{-5}$	0.78

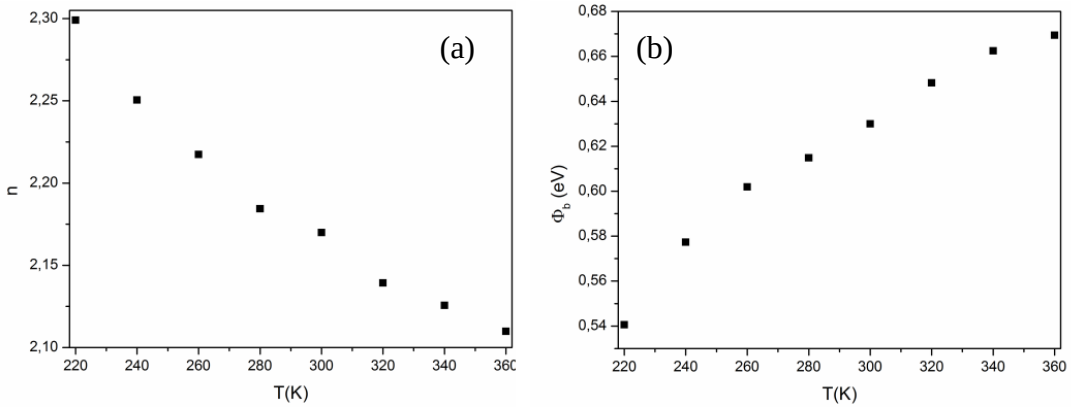

Figure 6.3: The variation of (a) the ideality factor (n) and (b) the barrier height (Φ_b) with different sample temperature.

As given in Table 6.1 and also seen in Fig. 6.3 (a), the ideality factor of this device is found greater than unity at every working temperature, so that it can be the indication of the alternative mechanisms instead of thermal excitation over the barrier. In this case, several transport mechanisms may be operative at the interface of the hetero-junction. Therefore, the requirements of the main models that are the ideal thermal emission, recombination-generation, recombination through interface states at the junction, tunneling were considered in order to determine the possible conduction mechanisms in this diode structure.

ln(I_0/T^2) versus the *1/T* plot (Fig. 6.4) shows a linear behavior as in the case of thermionic emission, from its characteristic plot, the activation energy is obtained as 0.35 eV which does not match with the requirement of this mechanism. Then, the analysis of interface recombination and recombination-generation in the depletion region were given in Fig. 6.5 and 6.6, respectively. From these corresponding graphical representations, the activation energies were calculated as 0.39 and 0.46 eV, respectively. Therefore, these results are found quite different from the expected values.

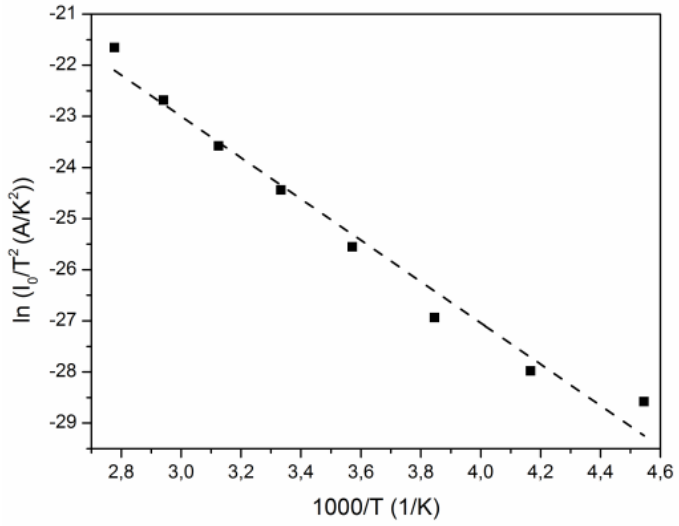

Figure 6.4: Plot of *ln(I_0T^{-2})* versus *1000/T* for the n-ZIS/p-CAIS device.

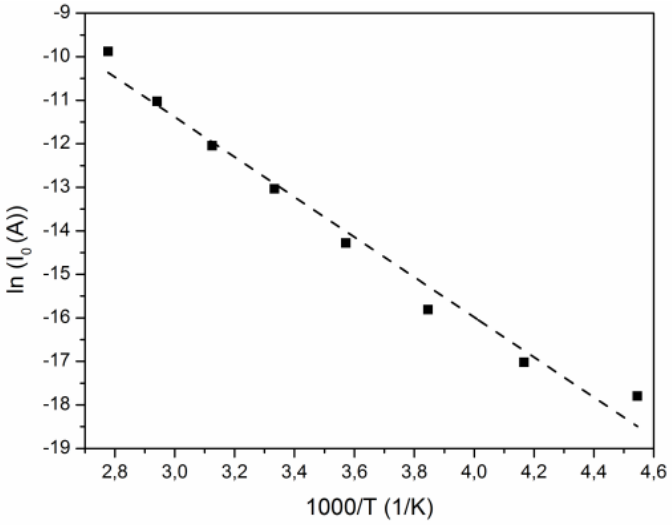

Figure 6.5: Plot of *ln(I_0)* versus *1000/T* for the n-ZIS/p-CAIS device.

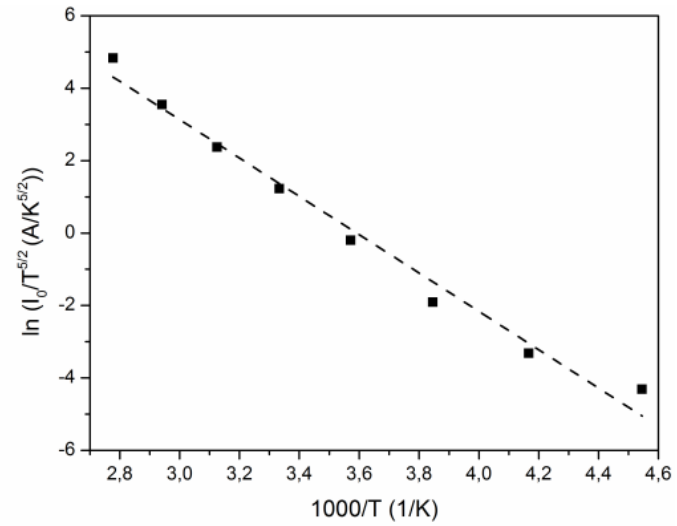

Figure 6.6: Plot of $ln(I_0T^{-5/2})$ versus $1000/T$ for the n-ZIS/p-CAIS device.

As in the case of n-ZIS/p-Si junction, causing from the disorders in the interfacial or near the junction, the T_0 affected current transport mechanism was found to be dominate in n-ZIS/p-CAIS device. As seen in Fig. 6.7, the n values change with temperature under the effect of a constant, T_0, mentioned in Eq. 4.38 [335]. From this modified model analysis, T_0 was calculated as about 102.7 K (Fig. 6.8).

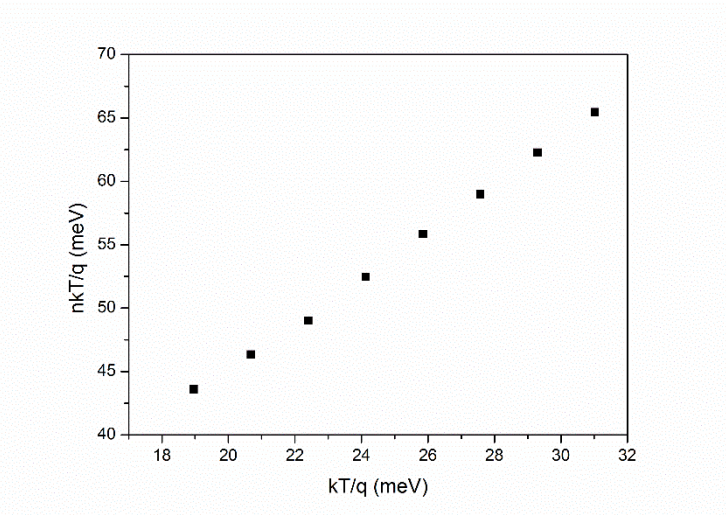

Figure 6.7: Plot of nkT/q versus kT/q for the n-ZIS/p-CAIS device.

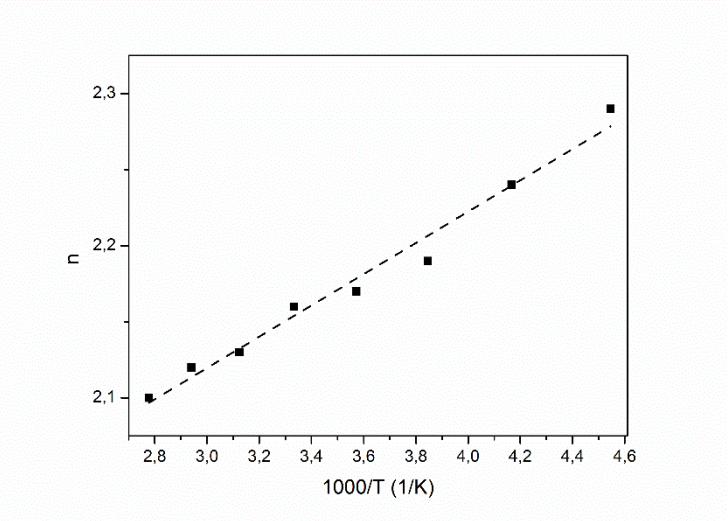

Figure 6.8: Plot of *n* versus *1000/T* for the n-ZIS/p-CAIS device.

In the high voltage region (>0.7 V) the current flow in this n-ZIS/p-CAIS device was observed that there was a power dependence on voltage and this relation could be identified as $I \propto V^m$ dependence (Fig. 6.9) [336]. With the further analysis, the integer *m* is obtained in the value higher than 2 (Table 6.2). Therefore, with the linearity of the Fig.6.8 and the characteristics of the calculated *m* values, this power dependence revealed that the SCLC mechanism was dominant in this diode structure with the exponential trap distribution [337].

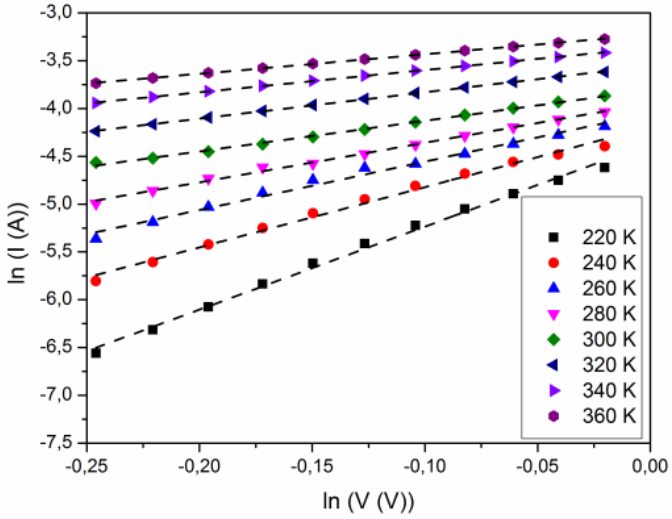

Figure 6.9: Plots of *ln(I)* versus *ln(V)* for the n-ZIS/p-CAIS device.

For the SCLC analysis, the I-V behavior of the device was evaluated using the Eq. 4.39 and the related parameters was deduced from this expression of the exponential trap distribution were tabulated in Table 6.2. In addition, trap density at the conduction band, N_T and the total trap concentration N_0 were calculated from the relation in Fig.6.10.

Table 6.2: The SCLC analysis results of the n-ZIS/p-CAIS hetero-junction diode.

T (K)	m	l	T_T
220	8.69	7.69	1681.69
240	6.30	5.30	1272.14
260	5.06	4.06	1055.83
280	4.14	3.14	878.30
300	3.21	2.21	663.51
320	2.75	1.75	561.06
340	2.33	1.33	451.66
360	2.04	1.04	375.19

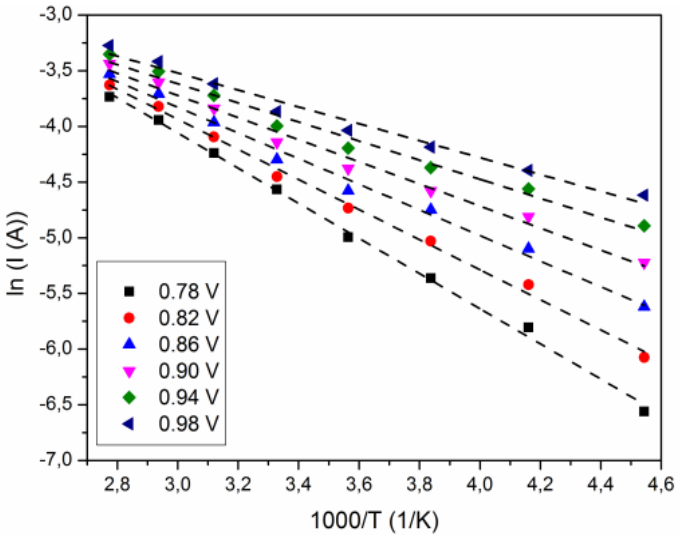

Figure 6.10: Plots of *ln(I)* versus *1000/T* for the n-ZIS/p-CAIS devices of different bias voltage

Table 6.3: The N_T and N_0 values obtained by using the SCLC analysis with different voltage values in the high bias region at the studied temperatures.

T (K)	N_T (10^{17} m^{-3})						N_0 (10^{37} m^{-3})
	V=0.78 V	V=0.82 V	V=0.86 V	V=0.90 V	V=0.94 V	V=0.98 V	V=0.78 V
220	0.71	0.62	0.53	0.49	0.39	0.32	0.31
240	0.93	0.85	0.71	0.70	0.63	0.58	0.53
260	1.06	0.99	0.87	0.85	0.79	0.74	0.73
280	1.19	1.14	1.02	1.01	0.96	0.91	0.98
300	1.36	1.33	1.26	1.25	1.21	1.17	1.49
320	1.45	1.44	1.38	1.37	1.35	1.32	1.88
340	1.57	1.56	1.53	1.50	1.45	1.40	2.50
360	1.68	1.65	1.64	1.62	1.57	1.54	3.16

In order to investigate the reverse current, I_R, in the n-ZIS/p-CAIS device, the I-V behavior in the reverse bias region was analyzed under the possibility of the transport mechanisms. Then, in the low reverse bias region, the reverse current was found to flow under the effect of tunneling mechanism. As discussed in Eq. 4.42, the reverse current was analyzed by the exponential relation with the applied voltage, and this behavior was evaluated in Fig. 6.11. From the consideration of this mechanism, the number of tunneling step effective in the carrier transport was found in the order of 10^2 and the trap concentration involved in this tunneling process was calculated as about 10^6 cm^{-3}.

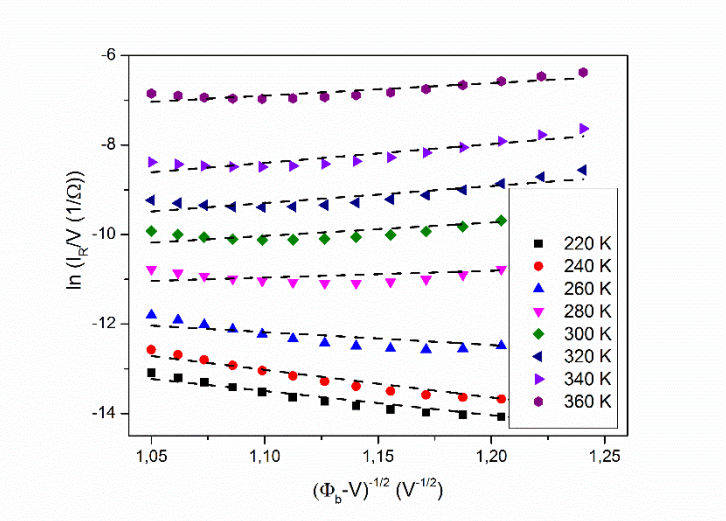

Figure 6.11: Plots of $ln(I_R/V)$ versus $(\Phi_b\text{-}V)^{-1/2}$ for the n-ZIS/p-CAIS device.

In addition, in the high reverse voltage region, Poole-Frenkel emission model was considered as a dominant mechanism where the corresponding plot given in Fig. 6.12 shows a good linearity as a presence of this type of model [338, 339]. In this case, the reverse current can be expressed as

$$I_R \propto Eexp\left(\frac{q}{nkT}\sqrt{\frac{qE}{\pi\varepsilon}}\right) \tag{6.1}$$

where E is the electric field affecting on the device (V/cm) and ε is the relative dielectric permittivity [340]. Furthermore, the coefficient n is the distinction between the Schottky and Poole-Frenkel thermionic emission related from the linear curve of the corresponding plots. Then, the slope of the reverse current plot shown in Fig. 6.12 is found to be close to unity which indicates Poole-Frenkel effect. Although it is a thermionic emission model, it refers to the emission from the trap states [340].

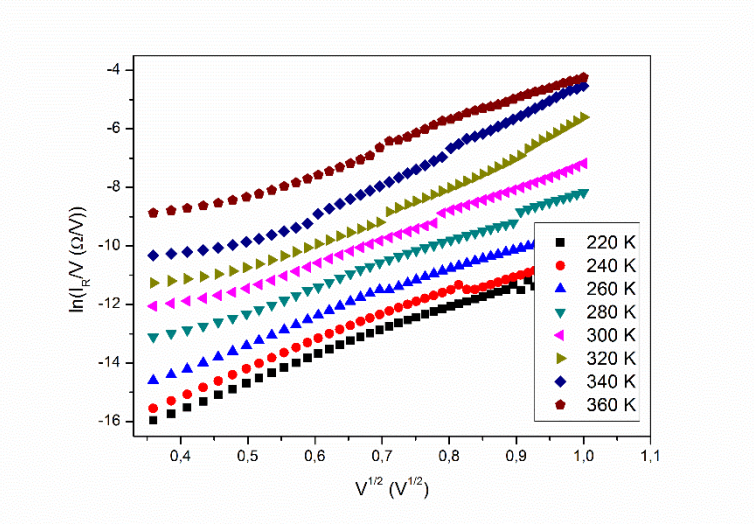

Figure 6.12: Plot of $ln(I_R/V)$ versus $(V)^{1/2}$ for the n-ZIS/p-CAIS device.

The C-V characteristics of n-ZIS/p-CAIS heterojunction device were investigated in order to get information on the barrier height of the junction. As seen Fig. 6.13, the capacitance changes with the applied voltage, whereas the frequency dependence of the capacitance is not clearly observed. That is, the capacitance values remains almost constant under the effect of frequency changes. As shown in Fig. 6.14, the linear behavior of the C^{-2} with respect to the change in voltage reveals the abrupt junction characteristics in this device structure [341]. In addition, the C^{-2}-V plot indicates that the barrier height values vary in between 0.51 and 0.66 eV with respect to the increase in measurement frequency. This variation can be evaluated by the effect of the interface states [278], so that the variation in capacitance is analyzed depending on the applied frequency at zero bias region to compute the number of these states at the interface of the junction. Then, from the relation between zero bias capacitance and applied frequency given in Fig. 6.15, the number of interface states was found to be in the order of 1.6×10^{10} $cm^{-2}V^{-1}$.

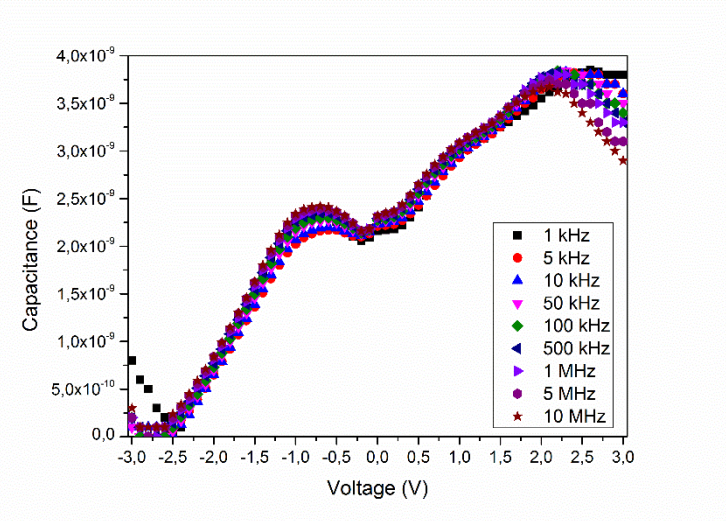

Figure 6.13: Room temperature C-V plots of the n-ZIS/p-CAIS device at different frequencies

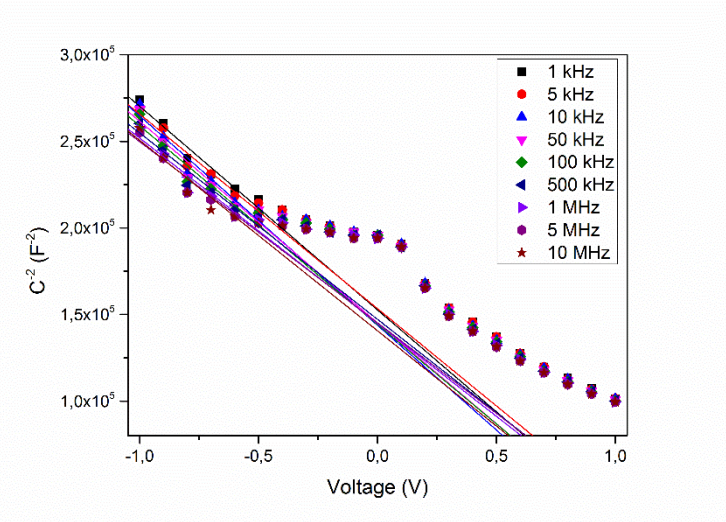

Figure 6.14: The variation of C^{-2} with voltage for the n-ZIS/p-CAIS device at different frequencies

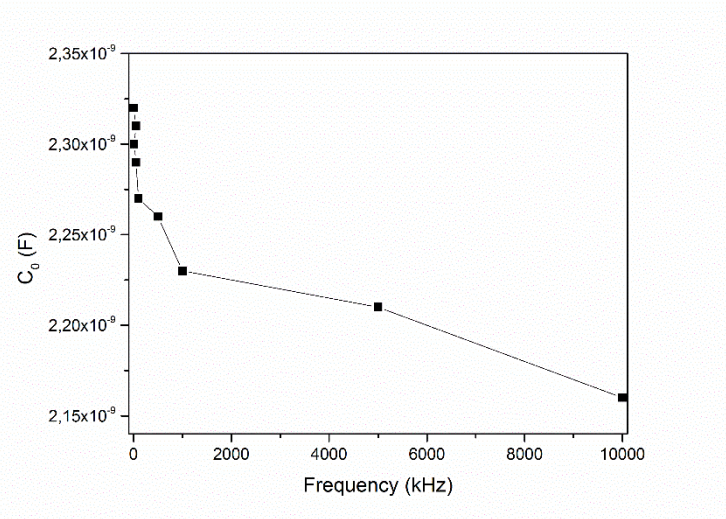

Figure 6.15: The variation of capacitance at zero bias with frequency in the n-ZIS/p-CAIS device

The energy-band diagrams for p-CAIS and n-ZIS layers were constructed by using their device structures. Based on these analyses, in Fig. 6.16 below, the energy-band profile of two semiconductor layers that creates the p-CAIS/n-ZIS heterojunction are shown in the isolated cases. In the band diagram of these layers, energy band gaps (*Eg*) and dielectric constants (ε) were used from the results of the corresponding material analysis, however work functions *(Ø)* and electron affinities (χ) were assumed from the values reported for their binary and ternary analogies in the literature. In the individual band gap profiles, the conduction and valence band edges are illustrated in horizontal direction with considering the space-charge neutrality. The energy difference in the conduction band and valence band edges in these two materials is represented by ΔE_C and ΔE_V, respectively. Then, after the junction is created, by using the Anderson [167] model for the heterojunction, the resulting band profile is constructed as shown in Fig. 6.17.

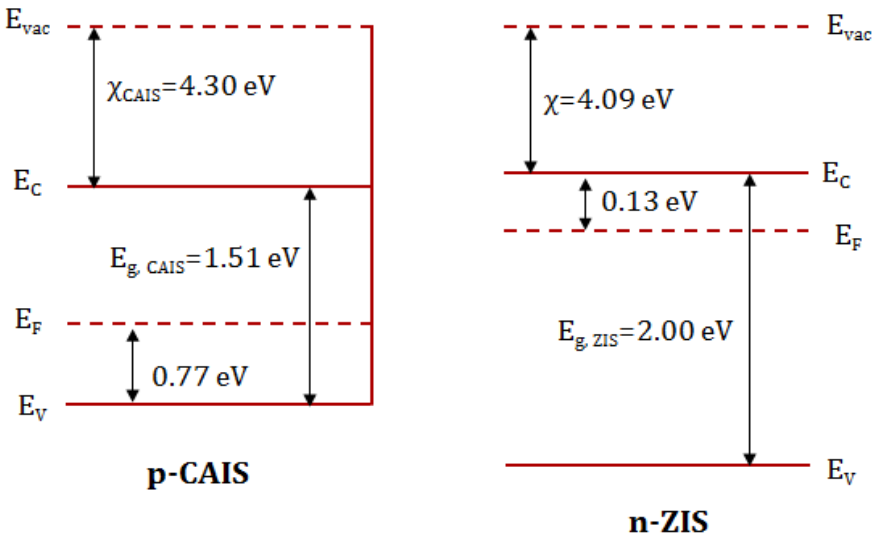

Figure 6.16: Energy-band diagram for two isolated semiconductor layer

The band gap in Fig. 6.17 shows discontinuities in conduction and valence bands of the layers that are found to be 0.41 eV and 0.90 eV, respectively. In addition, the barrier height of the junction is calculated as about 0.62 eV.

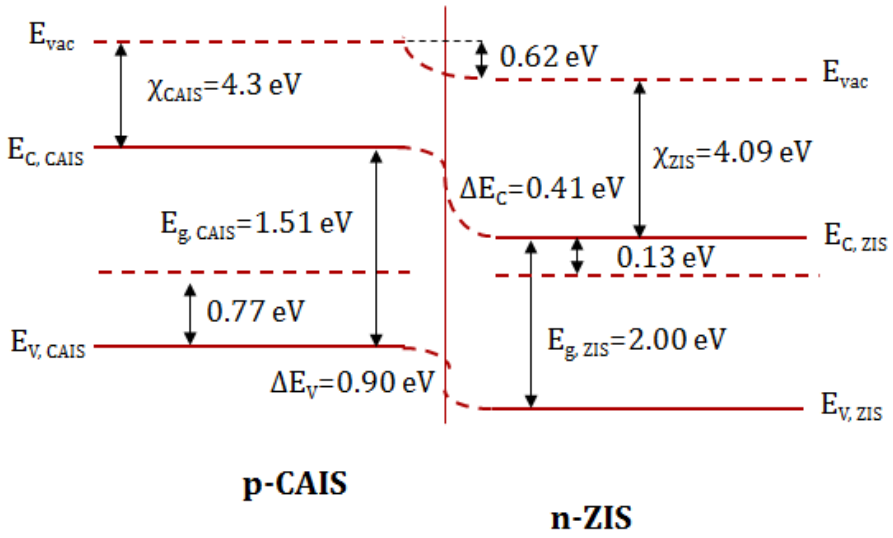

Figure 6.17: The band diagram of the n-ZIS/p-CAIS device

As an optical characterization step, the spectral photo-response measurements were carried out in the spectral range of 300-1300 nm in order to determine the photo-spectral working range of the n-ZIS/p-CAIS junction. This measurement was also performed in order to see the effects and contributions of the each layer on this diode

structure. From the spectral response curve of this device given in Fig. 6.18, the photo-response spectra is found to be quite good agreement with their optical characteristics. In other words, the peak values observed in this spectrum are observed as related to the band gap values of the corresponding thin film layer where they are about 2.10 and 1.53 eV, for ZIS and CAIS layer, respectively. In addition, this spectrum covers a wide wavelength region that can provide a good performance in solar cell applications.

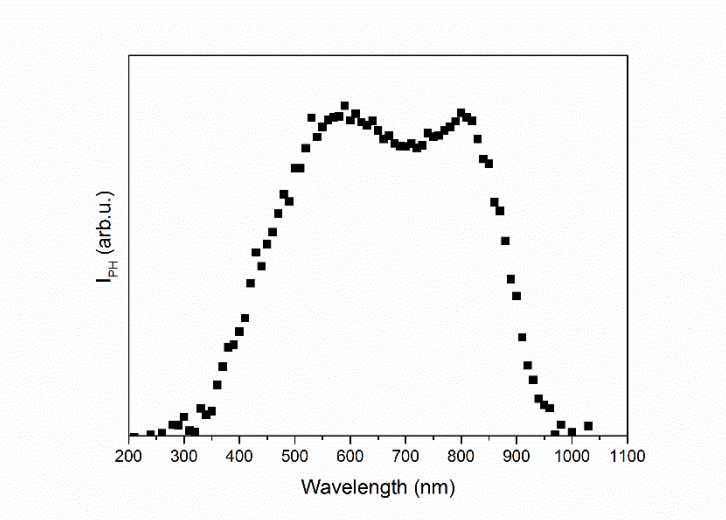

Figure 6.18: Photo-current versus wavelength plot of the n-ZIS/p-CAIS device.

6.3. Device Characterization under Illumination

In addition to the dark condition, I-V measurements were employed in order to get information on the response of this structure under the effect of the different illumination intensities between 20 and 115 mW/cm^2 (Fig. 6.19). Moreover, this measurement was carried out under solar simulator AM 1.5 condition with illumination intensity of 100 mW/cm^2 (Fig. 6.20). Under the description of the photovoltaic characteristics of the n-ZIS/p-CAIS hetero-junction, this I-V behavior was characterized in terms of the short circuit current, I_{SC}, the open circuit voltage, V_{OC}, the fill factor, FF, and the conversion efficiency, η. These parameters were determined with respect to I–V curve obtained at a given intensity and the results were tabulated in Table 6.4.

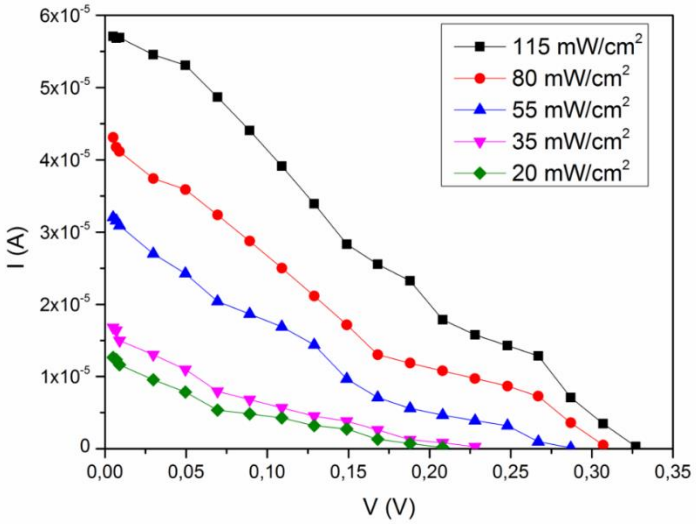

Figure 6.19: I-V characteristic of the n-ZIS/p-CAIS device illuminated under different intensities

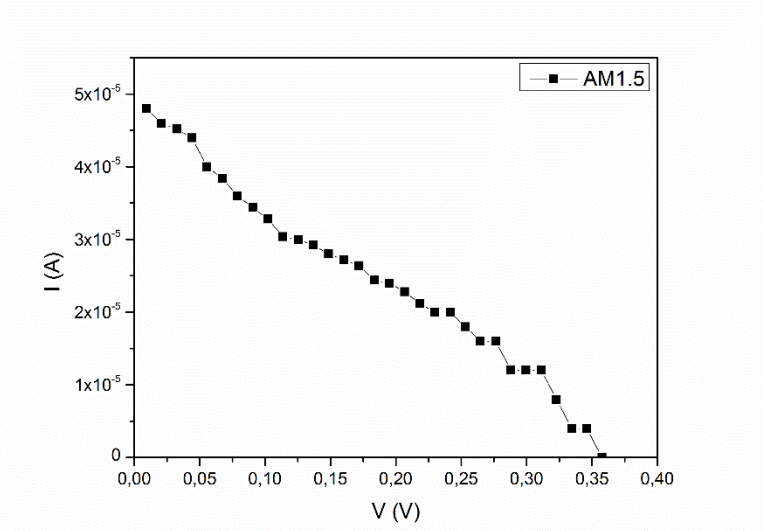

Figure 6.20: I-V characteristic of the n-ZIS/p-CAIS device under AM 1.5 illumination

As seen in Fig. 6.19 and 6.20, there is a high series resistance effects which can be originated from the bulk layer or the contact resistance [6]. In fact, the high behavior of series resistance cause an increase in the photo-generated carriers recombination process which can results in reduction of the carrier collection by the contacts and also affect the solar cell efficiency and fill factor negatively. As given in Table 6.4, the values of the cell parameters, increases with increasing illumination intensity [342, 343] and the efficiency ranges from 0.52 to 0.97% with the intensity chance from 20 to 115 mW/cm^2. They are also found in the AM 1.5 condition as 0.048 mA, 0.36 V, 27.7 and 0.95% corresponds to I_{SC}, V_{OC}, FF, and η, respectively.

Table 6.4: Solar cell parameters of the n-ZIS/p-CAIS device under different illumination intensities

Illumination intensity (mW/cm^2)	I_{SC} (mA)	V_{OC} (V)	*FF*	η (%)
20	0.013	0.23	17.4	0.52
35	0.017	0.27	20.8	0.54
55	0.032	0.28	21.3	0.70
80	0.044	0.31	22.3	0.75
115	0.058	0.33	29.2	0.97

CHAPTER 7

CONCLUSION

The aim of this study was to investigate the material characterization of ZIS and CAIS thin films under the effect of annealing process, and also to analyze their device properties with Si-wafer and with each other. In fact, the starting idea for this work was on the research of the alternative junction strategies [344, 345]. According to these works, there were some works on the use of ZIS layer to fabricate a layer alternative to CdS. Additionally, ZIS can offer a large direct band gap in the order of 2.0 eV appropriate to use in the solar cell applications. Under the aim of material characterization, both of these thin film samples were deposited on chemically cleaned soda lime glass substrates by PVD technique. On the contrary to the reported single crystal sources, the ZIS samples were deposited by the sequentially stacked layer deposition technique. During the deposition process, the substrate temperature was kept at about 200 °C, to eliminate the re-evaporation of the evaporation agents, the sources were heated at different temperatures and the corresponding deposition rates were optimized for the evaporation cycles.

The ZIS thin film samples were deposited by the layer by layer growth process using In_2Se_3, Zn and Se evaporation sources. According to the EDS analysis, they were found to be Zn rich in as-grown form and by annealing process, while the samples preserved this characteristic, Se re-evaporation from the film surface were observed.

In addition, the compositional analysis and the surface analysis of the films were obtained by means of SEM and AFM images. On the as-grown ZIS sample, there were some Zn agglomerations observed on the surface and they were found to be

distributed irregularly on the surface. However, with increasing the annealing temperature, their size distribution was decreased due to either possible diffusion of these atoms from the surface to the bulk or segregation of the other atoms on the surface of the film.

The XPS analyses were mainly concentrated on the decomposition of the core level peaks of the constituent elements. As a remarkable result of this analysis, the photoelectron peak of In core level was decomposed to the peaks corresponding to the In bonding with all constituent elements. After annealing process at 400 °C, the existence of the In-Se and In-Zn was disappeared. All of the samples were found to be in polycrystalline behavior with (112) main crystalline orientation direction without and with annealing process.

The crystallinity of the samples was also checked by Raman measurements. Although there was an improvement in the crystal structure of the samples by applying annealing process, ZnSe secondary phase formation was detected in the (101) orientation direction in the sample annealed at 500 °C.

In the transmission measurements, the interference fringes observed in the optical transmission spectra of the ZIS films were analyzed by EM in order to determine the optical parameters of the samples. These results were also detailed by using the Cauchy dispersion relation. From the Tauc plots, ZIS samples were found to have three distinct direct optical transitions depending on the crystal-field and spin-orbit splitting in the valence band of the structure. The fundamental band gap values were calculated in between 2.00 and 1.85 eV with the increase in the annealing temperature. These values were also observed in the photo-spectral measurements. The analyses of temperature dependent dark conductivity measurements showed that at low temperature region VRH and at high temperature region thermionic emission mechanisms were found to be pre-dominant in the conduction of the carriers. By the photo-conductivity measurements, the samples in as-grown form and annealed at 300 °C showed more response as compared to the annealed films at 400 and 500 °C. The photo-conductivity characteristics of the films were found to be fitted with two-

center recombination model and in the supra-linear conductivity behavior. The results of the room temperature Hall Effect measurements showed that Hall mobility and electron concentration of the ZIS films varied from 3.89 to 2.77 $cm^2/V.s$ and from $1.69x10^{13}$ to $8.65x10^{16}$ cm^{-3} for as-grown and annealed films, respectively. Moreover, as a result of both Hall Effect and hot probe measurements, the conductivity types of the samples were determined as n-type in ZIS samples.

Similarly, Cu, Ag, In_2Se_3 and Se evaporation sources were deposited sequentially on the soda lime glass substrate to fabricate the CAIS thin film samples. EDS works showed that the as-grown samples were nearly stoichiometric as in the case of the ZIS structure, there was a decrease in Se atomic ratios in the composition of the films with increasing annealing temperature due to the high vapor pressure of this element. Based on the SEM and AFM measurements, the surface of the as-grown film was found to have localized Se crystallites on the surface; however by applying post-thermal heating process, they disappeared. Under the XPS analysis, again the chemical bonding natures of surface and near-surface region of the films were investigated. Although the photoelectron peak characteristics of the core level of the elements with annealing temperature were in consisted with behavior as found from compositional analysis, the notable result is the strong Cu^{2+} satellite feature observed in the as-grown CAIS structure. In the XRD measurements of these thin films, the main diffraction was obtained at the major peak $2\theta \cong 27°$ which revealed the (112) preferred orientation of CAIS films. While increasing annealing temperature, the intensity of the main peak increased, the additional phases became more intense. The studies on the optical characteristics of the films revealed that the transmission values of the all films were around 40% and the absorption coefficient of these films were obtained in the order of 10^5 cm^{-1}. In the band structure analysis, the band gap energies were found for the as-grown and annealed films as 1.51, 1.50, 1.48 and 1.44 eV, respectively. The band gap values obtained from the photo-response spectra of the films were very close to these results. The temperature dependent dark conductivity measurements exhibited that the electrical properties of the films were dependent on the same conduction mechanisms even if annealing process was applied. At low temperature region, VRH was found to be main conduction

mechanism; however thermal emission was dominant conduction above the room temperature. Then, by applying five different illumination intensities on the sample, the photo-conductivity characteristics were investigated. With further analysis, photo-conductivity behavior of the films was in a good agreement with the two-center recombination model and so that the supra-linear photo-conductivity was obtained from the relation between the photocurrent and the illumination intensity. From the Hall Effect and hot probe measurements, all of the samples revealed p-type conductivity behavior. As a result of the room temperature Hall Effect measurements, Hall mobility values of the as-grown film and films annealed at 300, 400 and 500 °C were calculated in between 0.33 and 3.58 $cm^2/V.s$ and hole concentration values in the range of $1.89 \times 10^{16} – 3.56 \times 10^{18}$ cm^{-3}, respectively.

For the device characterization of n-ZIS/p-Si hetero-structure, had been studied and about 5 order rectification factor was achieved around 0.9 V. With the temperature dependent dark I-V measurements and rectifying behavior of this heterojunction were analyzed. The diode ideality factor was obtained as higher than 2 in all temperature regions. The series resistance values were calculated around 10^1 Ω, however the shunt resistance values revealed strong variations by changing sample temperature in the interval of 10^4 - 10^7 Ω. As a result of the temperature dependent I-V measurements on the n-ZIS/p-Si heterojunction, current transport in this junction was determined as being dominated by the combination of thermionic emission and SCLC mechanisms. In addition, the multi-step tunneling was observed as a main transport mechanism in the reverse bias region. From both of the I-V and C-V analysis, the barrier height of the junction was calculated as 0.76 eV at room temperature. As in the case of the p-CAIS/n-Si heterojunction, from the I-V measurements carried out at different temperature regions, the diode quality factor were found to be higher than the unity; and the series and shunt resistance values were obtained in the order of 10^2 and 10^4 Ω, respectively. The barrier height of this junction at room temperature was calculated as 0.63 eV. In addition, the main current transport mechanism of p-CAIS/n-Si structure was tunneling with 52.4 meV activation energy. In the reverse bias region, the tunneling process also found as a dominant transport mechanism in the structure.

n-ZIS/p-CAIS hetero-structure produced by using these two layers gave about 2 rectification order at 0.8 V. At low bias region, the most effective transport mechanism in this heterojunction diode was fitted to the T_0 affected current transport mechanism causing from the disorders in the interfacial or near the junction. On the other hand, in the high voltage region (>0.7 V), SCLC mechanism became dominant. Moreover, in the reverse bias region of this structure, the crossover from the Poole-Frenkel emission to the tunneling mechanism was observed by increasing reverse bias voltage. The device analysis of the n-ZIS/p-CAIS structure exhibited about 0.62 eV barrier height obtained from band structure study. The photovoltaic characteristics of this junction were analyzed by I-V measurements under different illumination intensities obtained from halogen lamp and solar simulator. The device parameters were found in the AM 1.5 condition as 0.048 mA, 0.36 V, 27.7 and 0.95% corresponds to I_{SC}, V_{OC}, FF, and η, respectively. As a result of the measurements by using halogen lamp, the efficiency values were found in the range of 0.52-0.97% with the change in the light source intensity from 20 to 115 mW/cm^2.

REFERENCES

[1] S. Willoughby, “Effect of light on selenium during the passage of an electric current”, Nature, vol. 7, p. 303, 1873.

[2] D. M. Chapin, C. S. Fuller, and G. L. Pearson, “A new silicon p-n junction photocell for converting solar radiation into electrical power”, J. Appl. Phys., vol. 25 p. 676, 1954.

[3] D.C. Reynolds, G. Leies, L.L. Antes and R.E. Marburger, “Photovoltaic effects in cadmium sulphide”, Phys. Rev., vol. 96, pp. 533-534, 1954.

[4] J. Nelson, *The physics of solar cells*, Singapore: Imperial College Press, 2007.

[5] M.A. Green, K. Emery, Y. Hishikawa, W. Warta and E. D. Dunlop, “Solar cell efficiency tables (version 44)”, Prog. Photovolt: Res. Appl., vol. 22, pp. 701–710, 2014.

[6] M. Kaleli, “Investigation of electrical and optical properties of Ag-In-Se based devices”, PhD. Thesis in Physics Department of Middle East Technical University, 2010.

[7] J. Poortmans and V. Arkhipov, “Thin film solar cells: fabrication, characterization and applications”, England: John Wiley & Sons, Ltd., 2006.

[8] R. Noufi and K. Zweibel, “High-efficiency CdTe and CIGS thin-film solar cells: highlights and challenges”, IEEE 4th World Conference on Photovoltaic Energy Conversion (WCPEC-4), 2006.

[9] D. Reichelt, “First solar builds the highest efficiency thin film pv cell on record”. Press release on 16 January 2015. Available online: http://www.materialsviews.com/cigs-solar-cells-reach-new-record-efficiency/ (last accessed on 23 July 2015).

[10] First solar builds the highest efficiency thin film PV cell on record. Press release on 5 August 2014. Available online: http://investor.firstsolar.com/releasedetail.cfm?ReleaseID=864426 (last accessed on 19 February 2015).

[11] S. R. Kodigala, "Thin film solar cells from earth abundant materials", USA: Elseiver, 2014.

[12] T.A. Hendia and L.I. Soliman, "Optical absorption behaviour of evaporated $ZnIn_2Se_4$ thin films", Thin Solid Films, vol. 261, pp. 322-327, 1995.

[13] S.H. Choe, "Optical energy gaps of undoped and Co-doped $ZnIn_2Se_4$ single crystals", Curr. Appl. Phys., vol. 9, pp. 1-3, 2009.

[14] H.M. Zeyada, M.S. Aziz and A.S. Behairy, "Structure formation and mechanisms of DC conduction in thermally evaporated nanocrystallite structure $ZnIn_2Se_4$ thin films", Physica B, vol. 404, pp. 3957–3963, 2009.

[15] S. Venkatachalam, D. Mandalaraj and S.K. Narayandass, "Characterization of vacuum-evaporated ZnSe thin films", Physica B, vol. 393, pp. 47-55, 2007.

[16] S. Venkatachalam, D. Mandalaraj, S.K. Narayandass, S. Velumani, P. Schabes-Retchkiman and J.A. Ascencio, "Structural studies on vacuum evaporated ZnSe/p-Si Schottky dioedes" Mater. Chem. Phys., vol. 103, pp. 305-311, 2007.

[17] G.K. Rao, K.V. Bangera and G.K. Shivakumar, "Studies on vacuum deposited p-ZnTe/n-ZnSe heterojunction diodes", Solid-State Electron., vol. 54, pp. 787-790, 2010.

[18] S. Darwish, A.S. Riad and H.S. Soliman, "Electrical conductivity and the effect of temperature on photoconduction of n-ZnSe/p-Si rectifying heterojunction cells", Semicond. Sci. Technol., vol.11, pp. 96-102, 1998.

[19] P.V. Shapkin, A.S. Nasibov, Y.F. Vaksman, Y.A. Nitsuk and Y.N. Purtov, "Indium doping of ZnSe single crystals during vapor phase growth", Inorg. Mater., vol. 42, pp. 845-849, 2006.

[20] K. Lott, S. Shinkarenko, O. Volobujeva, L. Turn, T. Nirk, A. Öpik, R. Nisumaa, U. Kallavus, M. Nöges, V. Mikli, M. Viljus, E. Gorokhova, G. Anan'eva, A. Grebennik and A. Vishnjakov, "High temperature electrical conductivity in ZnSe:In and in CdSe:In under selenium vapor pressure" Phys. Stat. Sol. (b), vol. 244, pp. 1623-1626, 2007.

[21] L.I. Soliman, T.A. Hendia, "Influence of γ-irradiation of the optical and electrical properties of $ZnIn_2Se_4$ films", Radiat. Phys. Chem., vol. 50, pp. 175-177, 1997.

[22] H.M. Zeyada, M.S. Aziz and A.S. Behairy, "Absorption and dispersion studies of thermally evaporated nanocrystallite structure nanocrystallite structure $ZnIn_2Se_4$ thin films", Eur. Phys. J. Appl. Phys., vol. 45, pp. 30601-1-6, 2009.

[23] N.M. El-Nahass, A.A. Attia, G.F. Salem, H.A.M. Ali and M.I. Ismail, "Effect of vacuum annealing and substrate temperature on structural and optical properties of $ZnIn_2Se_4$ thin films", Physica B, vol. 425, pp. 23-30, 2013.

[24] R. Jeyakumar, S.T. Lakshmikumar and A.C. Rastogi, "Preparation of Zn(In)Se films from alloyed precursors", Mater. Res. Bull., vol. 37, pp. 617-629, 2002.

[25] S. Gariazzo and A. Serpi, "Photoconductivity relaxation in $ZnIn_2Se_4$", Phys. Rev. B, vol. 41, pp. 7718-7723, 1990.

[26] E. Fortin and F. Raga, "Low temperature photoconductivity of $ZnIn_2Se_4$ and $CdIn_2Se_4$", Solid State Commun., vol. 14, pp. 847-850, 1974.

[27] G. Gordillo, C. Calderon and F. Rojas, "Determination of optical constants of $Zn_xIn_{1-x}Se$ thin films deposited by evaporation", Rev. Mex. Fis., vol. 49, pp. 329-334, 2003.

[28] S.P. Yadav, P.S. Shinde, K.Y. Rajpure and C.H. Bhosale, "Preparation and properties of spray-deposited $ZnIn_2Se_4$ nanocrystalline thin films", J. Phys. Chem. Solids, vol. 69, pp. 1747–1752, 2008.

[29] S.P. Yadav, P.S. Shinde, K.Y. Rajpure and C.H. Bhosale, "Photoelectrochemical properties of spray deposited n- $ZnIn_2Se_4$ thin films", Sol. Energ. Mater., vol. 92, pp. 453–456, 2008.

[30] K.W. Cheng, Y.H. Cheng and M.S. Fan, "Photoelectrochemical study of $ZnIn_2Se_4$ electrodes, fabricated using selenization of RF magnetron sputtered Zn-In metal precursors", Int. J. Hydrogen Energy., vol. 37, pp. 13763-13769, 2012.

[31] L.I. Soliman, M.H. Wasft and T.A. Hendia, "Thermophysical properties of polycrystalline $ZnIn_2Se_4$", Proc. Indian Acad. Sci. (Chem. Sci.), vol. 110, pp. 193-197, 1998.

[32] L.I. Soliman, M.H. Wasft and T.A. Hendia "Thermal Properties of polycrystalline $ZnIn_2Se_4$", J. Therm. Anal. Calorim., vol. 59, pp. 971-976, 2000.

[33] B.B. Anuradha, B.G. Wagh, N.M. Shinde, S.B. Jambure and C.D. Lokhande, "Crystalline Zinc indium selenide thin film electrosynthesis and its photoelectrochemical studies", Energy Procedia, vol. 54, pp. 549-556, 2014.

[34] X. Sun, Y. He and J. Feng, "Growth and characterization of $ZnIn_2Se_4$ buffer layer on $CuInSe_2$ thin films", J. Cryst. Growth, vol. 312, pp. 48-51, 2009.

[35] V. Riede, H. Neumann, H. Schwer, V. Kramer, I. Gregora and V. Vorlicek, "Infrared and Raman-spectra of $ZnIn_2Se_4$", Cryst. Res. Technol., vol. 28, pp. 641-645, 1993.

[36] H.P. Trah and V. Kramer, "Crystal structure of zinc indium selenide, $ZnIn_2Se_4$", Z. Kristallogr., vol. 173, p. 199, 1985.

[37] G.I. Rusu, M. Diciu, C. Pirghie and E.M. Popa, "Structural characterization and optical properties of ZnSe thin films", Appl. Surf. Sci., vol. 253, pp. 9500-9505, 2007.

[38] A.G. Milnes and D.L. Feucht, *Heterojunction and metal–semiconductor junctions*, New York: Academic, 1972.

[39] K.L. Chopra, K. L. Paulson, and V. Dutta, "Thin-film solar cells: An overview", Prog. Photovolt., vol. 12, pp. 69–92, 2004.

[40] R. Asokamani, R.M. Amirthakumari, R. Rita, and C. Ravi, "Electronic structure calculations and physical properties of ABX_2 (A = Cu, Ag; B = Ga, In; X = S, Se, Te) ternary chalcopyrite systems", Phys. Stat. Sol. (b), vol. 213, pp. 349-363, 1999.

[41] J.L. Shay, B. Tell, H.M. Kasper, and L.M. Schiavone, "Electronic structure of $AgInSe_2$ and $CuInSe_2$", Phys. Rev. B, vol. 7, pp. 4485-4490, 1973.

[42] G.V. Rao, G.H. Chandra, O.M. Hussain, S. Uthana, and B.S. Nadiu, "Characterization of $Cu_{0.5}Ag_{0.5}InSe_2$ thin films", J. Alloys Compd., vol. 325, pp. 12-17, 2001.

[43] G.V. Rao, G.H. Chandra, P.S. Reddy, O.M. Hussain, K.T.R. Reddy, and S. Uthana, "Optical absorption studies on polycrystalline $Cu_{0.5}Ag_{0.5}InSe_2$ thin films", Vacuum, vol. 67, pp. 293-298, 2002.

[44] I.V. Bodnar, V.F. Gremenok, and I.A. Viktorov, "Optical properties of films of $Cu_xAg_{1-x}InSe_2$ solid solutions obtained by laser evaporation", J. Appl. Spectrosc., vol. 69, pp. 413-417, 2002.

[45] J.G. Albornoz, R. Serna, and M.J. León, "Optical properties and electronic structure of polycrystalline $Ag_{1-x}Cu_xInSe_2$ alloys", J. Appl. Phys., vol. 97, pp. 103515-1-7, 2005.

[46] A.A. Lavrentyev, B.V. Gabrelian, I.Y. Nikiforov, J.J. Rehr and A.L. Ankudinov, "Nonlinear energy dependence of the forbidden energy band in the solid solutions $Cu_xAg_{1-x}B^{III}C^{VI}_2$", Phys. Script., vol. T115, pp. 212-–214, 2005.

[47] N.S. McAlpine, P. McConville, and D. Haneman, "Junction sharpness in field-induced transistor structure in $Cu_xAg_{1-x}InSe_2$", J. Appl. Phys., vol. 79, pp. 7370-7372, 1996.

[48] I.V. Bodnar, I.A. Viktorov, and S.L. Sergeev-Nekrasov, "$Cu_xAg_{1-x}InSe_2$ solid solutions", Cryst. Res. Technol., vol. 33, pp. 885-990, 1998.

[49] G.V. Rao, D.H. Chandra, P.S. Reddy, O.M. Hussain, K.T.R. Reddy and S. Uthana, "Influence of substrate temperature on the structural and optical properties of $Cu_{0.5}Ag_{0.5}InSe_2$ films", J. Optoelect. Adv. Mat., vol. 4, pp. 87-392, 2002.

[50] G.V. Rao, G.H. Chandra, O.M. Hussain, S. Uthana and B.S. Naidu, "Characteristics of Al/p- $Cu_{0.5}Ag_{0.5}InSe_2$ polycrystalline thin film Schottky barrier diodes", Cryst. Res. Technol., vol. 36, pp. 571–576, 2001.

[51] V.F. Gremenok, I.V. Bodnar, I. Martil, F.L. Martines, S.L. Segreev-Nekrasov and I.A. Victorov, "Growth and characterization of $Cu_xAg_{1-x}InSe_2$ thin films by pulsed laser deposition", Solid State Phenom., vol. 67-68, pp. 361-366, 1999.

[52] A.R. Aquino, A. Rockett, S.A. Little, and S. Marsillac, "Cryogenic cathodoluminescence from $Cu_xAg_{1-x}InSe_2$ thin films", 35th IEEE Photovoltaic Specialists Conference, pp. 003386-003390, 2010.

[53] A.R. Aquino, S.A. Little, S. Marsillac, R. Collins, and A. Rockett, "Identification of defect levels in $Cu_xAg_{1-x}InSe_2$ thin films via photoluminescence" 37th IEEE Photovoltaic Specialists Conference, pp. 003532-003536, 2011.

[54] T. Begou, S.A. Little, A. Aquino, V. Ranjan, A. Rockett, R.W. Collins and S. Marsillac, "In situ and ex situ characterization of (Ag,Cu)$InSe_2$ thin films", 37th IEEE Photovoltaic Specialists Conference, pp. 000326-000328, 2011.

[55] R. Diaz and F. Rueda, "Formation of a crystalline InSe phase from a quaternary single crystal of the Cu-Ag-In-Se system by massive ion motion", Mater. Chem. Phys., vol. 135, pp. 912-920, 2012.

[56] S.A. Little, V. Ranjan, R.W. Collins and S. Marsillac, "Growth analysis of (Ag,Cu)$InSe_2$ thin films via real time spectroscopic ellipsometry", Appl. Phys. Lett., vol. 101, pp. 231910-1-4, 2012.

[57] R. Diaz, "The n-$Cu_{0.9}Ag_{0.1}In_3Se_5$ chalcopyrite, electronic as well as ionic conductor", J. Phys. D: Appl. Phys., vol. 41, pp. 185102-1-7, 2008.

[58] D.G. Kilday, G. Margaritondo, T.F. Ciszek, S.K. Deb, S.H. Wei and A. Zunger, "Common-anion rule and its limitations: photoemission studies of $CuIn_xGa_{1-x}Se_2$-Ge and $Cu_xAg_{1-x}InSe_2$-Ge interfaces", Phys. Rev. B, vol. 36, pp. 9388-9391, 1987.

[59] K. L. Chopra and S. R. Das, *Thin film solar cells*, New York: Plenum Press, 1983.

[60] K. D. Leaver and B. N. Chapman, *Thin films*, London: Wykehan Publications, 1971.

[61] J. E. Mahan, *Physical vapor deposition of thin films*, Canada: John Wiley & Sons, Inc., 2000.

[62] M. Ohring, *Materials science of thin films: Deposition and structure*, San Diego: Academic Press, 2002.

[63] G. Hass, M.H. Francombe and J.L. Vossen, *Physics of thin films: advances in research and development*, London: Academic Press, Inc., 1982.

[64] A. Dirici, G. Djeteli, G. Tchangbedji, H. Derouiche, K. Jondo, K. Napo, J.C. Bernede, S. Ouro-Djobo and M. Gbagba, "Structured ZnO thin films grown by chemical bath deposition for photovoltaic applications", Phys. Stat. Sol. (a), vol. 201, pp. 1528-1536, 2004.

[65] J. Ouerfelli, M. Regragui M. Morsli, G. Djeteli, K. Jondo, C. Amory, G. Tchangbedji K. Napo and J.C. Bernede, "Properties of ZnO thin films deposited by chemical bath deposition and post annealed", J. Phys. D: Appl. Phys., vol. 39, pp. 1954-1959, 2006.

[66] A. Ennaoui, M. Weber, R. Scheer and H.J. Lewerenz, "Chemical-bath ZnO buffer layer for $CuInS_2$ thin-film solar cells", Sol. Energy Mater. Solar Cells, vol. 54, pp. 277-286, 1998.

[67] T.P. Niesen and M.R. De Guire, "Review: Deposition of ceramic thin films at low temperatures from aqueous solutions", J. Electroceram, vol. 6, pp. 169-207, 2001.

[68] K. Govender, D.S. Boyle, P.B. Kenway, P.J. O'brien, "Understanding the factors that govern the deposition and morphology of thin films of ZnO from aqueous solution", Mater. Chem., vol. 14, pp. 2575-2591, 2004.

[69] K.L. Chopra. "Thin film phenomena", McGraw Hill, New York, 1985

[70] J.F. O'Hanlon, *A user's guide to vacuum technology*, USA: John Wiley & Sons, Inc., 2003.

[71] L.I. Maissel and R. Glang, *Handbook of thin film technology*, New York: McGraw-Hill, 1970.

[72] H. Karaağaç, Electrical, "Structural and optical properties of $AgGaSe_{2-x}S_x$ thin films grown by sintered powder", PhD. Thesis in Physics Department of Middle East Technical University, 2010.

[73] L. I. Maissel and M. H. Francombe, *An introduction to thin films*, New York-London-Paris: Gordon and Breach Science Publishers, 1973.

[74] D. B. Chrisey and G.K. Hubler, *Pulsed laser deposition of thin films*, USA, John Wiley & Sons, Inc., 1994.

[75] M. Jain, *II-VI semiconductor compounds*, Singapore: World Scientific Publishing Co. Pte. Ltd., 1993.

[76] S. Adachi, *Properties of group-IV, III-V and II-VI semiconductors*, England: John Wiley & Sons, Ltd., 2005.

[77] C. Rincón and J. Gonzalez, "Temperature-dependence of the bandgap in $CuInSe_2$", Sol. Cells, vol. 16, p. 357, 1986.

[78] S. Adachi, "Handbook on physical properties of semiconductor Volume 3: II-VI compound semiconductors", USA: Kluwer Academic Publishers, 2004.

[79] T. M. Khan, M. F. Mehmood, A. Mahmood, A. Shah, Q. Raza, A. Iqbal and U. Aziz, "Synthesis of thermally evaporated ZnSe thin film at room temperature", Thin Solid Films, vol. 519, pp. 5971–5977, 2011.

[80] M. Aven, D.T.F. Marple and B. Segall, "Some electrical properties of ZnSe", J. Appl. Phys., vol. 32, p. 2261, 1961.

[81] S. Adachi, *Optical constants of crystalline and amorphous semiconductors: Numerical data and graphical information*, Boston/Drodrecht/London: Kluwer Academic, 1999.

[82] R. Mach and W. Ludwig, "Impact ionization investigations on ZnSe Schottky barrier diodes", Phys. Status Solidi (a), vol. 23, pp. 507-516, 1974.

[83] S. Mora, N. Romeo and L. Tarricone, "Minority carriers diffusion length in ZnSe by SPV method", Solid State Commun., vol. 33, pp. 1147-1149, 1980.

[84] F.J. Gracia, "n-CdS/p-$ZnIn_2Se_4$ thin film solar cell", Thin Solid Films, vol. 69, pp. 137-139, 1980.

[85] J. Fillpowicz, N. Romeo and L. Tarricone, "Photoelectrical memory effect in $ZnIn_2Se_4$", Solid State Commun., vol. 38, pp.619-623, 1980.

[86] H. Yu, X. Quan, Y. Zhang, M. Ning, S. Chen and H. Zhao, "Electrochemically Assisted Photocatalytic Inactivation of Escherichia coli under Visible Light Using a $ZnIn_2S_4$ Film Electrod", Langmuir, vol. 24, pp. 7599-7604, 2008.

[87] S. Gariazzo and A. Serpi, "Photoconductivity relaxation in $ZnIn_2Se_4$", Phys. Rev. B, vol. 41, pp. 7718-7723, 1990.

[88] C. L. Burdick and J. H. Ellis, "The crystal structure of chalcopyrite determined by X-rays", J. Amer. Chem. Soc., vol. 39, pp. 2518 -2525, 1917.

[89] D.S. Su, W. Neumann and M. Giersig, "Structure modifications in chalcopyrite semiconductors", Thin Solid Films, vol. 361-362, pp. 218-222, 2000.

[90] J.E. Jaffe and A. Zunger, "Theory of the band-gap anomaly in ABC_2 chalcopyrite semiconductors", Phys. Rev. B, vol. 29, pp. 1882-1906, 1984.

[91] M. Böhm, G. Huber, A. MacKinnon, A. Scharmann and E.G. Scharmer, *Physics of Ternary Compounds*, Berlin: Springer, 1985.

[92] S. Chen, G. Gong, A. Walsh and S. H. Wei, "Electronic structure and stability of quaternary chalcogenide semiconductors derived from cation cross-substitution of II-VI and I-III-VI_2 compounds", Phys. Rev B, vol. 79, pp. 165211-1-10, 2009.

[93] F. Habashi, *Chalcopyrite: Its chemistry and metallurgy*, USA: McGraw-Hill, 1978.

[94] J. L. Shay and J. H. Wernick, *Ternary Chalcopyrite Semiconductors: Growth, Electronic Properties, and Applications*, Oxford: Pergamon Press, 1975.

[95] S.R. Hall and J. M. Stewart, "The crystal structure refinement of chalcopyrite $CuFeS_2$", Acta Cryst. B, vol. 29, p. 579, 1973.

[96] A. McEvoy, T. Markvart and L. Castaner, *Practical handbook of photovoltaics: fundamentals and applications*, USA: Elseiver, 2012.

[97] C. Rincon and F.J. Ramirez, "Lattice vibrations of $CuInSe_2$ and $CuGaSe_2$ by Raman microspectroscopy", J. Appl. Phys., vol. 72, pp. 4321-4324, 1992.

[98] G.E. Delgado, A.J. Mora, C. Pineda, T. Tinoco, "Simultaneous Rietveld refinement of three phases in the Ag–In–S semiconducting system from X-ray powder diffraction", Mater. Res. Bull., vol. 36, pp. 2507-2517, 2001.

[99] M.L. Fearheiley, K.J. Bachmann, Y.H. Shing, S.A. Vasquez and C.R. Herrington, "The lattice constants of $CuInSe_2$", J. Electronic Materials, vol. 14, pp. 677-683, 1985.

[100] T. Çolakoğlu, "The effects of post-annealing process on the physical properties of Silver-Indium-Selenium ternary semiconductor thin films deposited by electron beam technique", PhD. Thesis in Physics Department of Middle East Technical University, 2009

[101] T.B. Elliot, *Trends in semiconductor research*, New York: Nova Science Publishers, Inc., 2005.

[102] G. Riede, H. Subotta, H. Neumann, and X. N. Hoang, "Temperature dependence of the fundamental absorption edge in $CuGaSe_2$", Solid State Commun., vol. 28, pp. 449-451, 1978.

[103] A.S. Verma, R.K. Singh and S.K. Rathi, "An empirical model for dielectric constant and electronic polarizability of binary (A_NB_{8-N}) and ternary ($A_NB_{2+N}C_{27-N}$) tetrahedral semiconductors", J. Alloy Compd., vol. 486, pp. 795-800, 2009.

[104] H. Sobotta, H. Neumann, V. Riede, G. Kühn, J. Seltmann and D. Oppermann, "Influence of impurities and free carriers on the optical properties of $CuInSe_2$", Phys. Status Solidi (a), vol. 60, pp. 531-537, 1980.

[105] M.C. S. Kumar and B. Pradeep, "Formation and properties of $AgInSe_2$ thin films by co-evaporation", Vacuum, vol. 72, pp. 369–378, 2004.

[106] N. Touafek, M. S. Aida and R. Mahamdi, "$CuInse_2$ Solar Cells Efficiency Optimization", Am. J. Mater. Sci., vol. 2, pp. 160-164, 2012.

[107] P.P. Ramesh, S. Uthanna, S. B. Naidu, and J. P. Reddy, "Characteristics of Ni/n-$AgInSe_2$ polycrystalline thin film Schottky barrier diodes", Thin Solid Films, vol. 292, pp. 290-293, 1997.

[108] B.J. Stanbery, "Copper indium selenides and related materials for photovoltaic devices, Crit. Rev. Sol. Stat. Mater. Sci., vol. 27, pp. 73-117, 2002.

[109] B.D. Cullity, *Elements of X-ray diffraction*, USA: Addison-Wiley Publishing Company, Inc., 1956.

[110] Y. Waseda, E., Matsubara and K., Shinoda, *X-Ray diffraction crystallography*, New York: Springer, 2011.

[111] B.G. Yacobi, *Semiconductor materials: An introduction to basic principles (Microdevices)*, California: Springer, 2003.

[112] S. R. Kodigala, *$Cu(In_{1-x}Ga_x)Se_2$ based thin film solar cells*, USA: Elsevier, Inc., 2010.

[113] D. K. Schroder, *Semiconductor material and device characterization*, New York: John Wiley & Sons Inc., 1998.

[114] J. F. Watts and J. Wolstenholme, "*An introduction to surface analysis by XPS and AES*", England: John Willey and Sons Ltd, 2003.

[115] V. Bellitto, *Atomic force microscopy – imaging, measuring and manipulating surfaces at the atomic scale*, Croatia: InTech, 2012.

[116] G. Binning and H. Rohrer, “Scanning tunneling microscopy”, Helv. Phys. Acta, vol. 55, pp. 726-735, 1982.

[117] G. Binning, C.F. Quate and C. Gerber, “Atomic force microscopy”, Phys. Rev. Lett., vol. 56, pp. 930-933, 1986.

[118] F.J. Giessibl and C.F. Quate, “Exploring the nanoworld with atomic force microscopy”, Phys. Today, vol. 59, pp. 44-50, 2006.

[119] E. Meyer, “Atomic force microscopy”, Prog. Surf. Sci., vol. 41, pp. 3-49, 1992.

[120] A.M. Baro and R.G. Reifenberger *Atomic force microscopy in liquid: Biological applications*, Singapore: Wiley-VCH Verlag & Co., 2012.

[121] J. Golgstein, D.E Newbury, D.C. Joy, P. Echlin, E. Lifshin, L. Sawyer and J.R. Michael, *Scanning electron microscopy and X-ray microanalysis*, New York: Springer, 2003.

[122] S.L. Flegler, J.W. Heckmen and K. L. Klomparens, “*Scanning and transmission electron microscopy: An introduction*, Oxford: Oxford University Press, 1993.

[123] G. Friedbacher and H. Bubert, *Surface and thin film analysis: A compendium of principles, instrumentation, and applications*, Germany: Wiley-VCH Verlag& Co., 2011.

[124] E. Smith and G. Dent, *Modern Raman spectroscopy: A practical approach*, England: John Wiley & Sons, Ltd., 2005.

[125] J.R. Ferraro, K. Nakamoto and C.W. Brown, *Introductory Raman spectroscopy*, USA: Elseiver Science, 2003.

[126] R.H. Bube, *Photoelectronic properties of semiconductors*, Great Britain: Cambridge University Press, 1992.

[127] J.I. Pankove, *Optical processes in semiconductors*, New Jersey: Prentice Hall, 1971.

[128] L. Kazmerski, *Polycrystalline and amorphous thin films and devices*, New York: Academic Press, Inc., 1980.

[129] W. Sritrakool, V. Sa-yakanit and H.R. Glyde, “Band tails in disordered systems”, Phys. Rev. B, vol. 33, pp. 1199-1202, 1986.

[130] L.C. Cohen and R.C. James, *Electronic structure and optical properties of semiconductors*, USA: Springer, 1989.

[131] R.H. Bube, *Electrons in solids: An introductory survey*, San Diego: Academic Press, 1992.

[132] M.V. Garcia-Cuenca, J.L. Morenza and J.M. Codina, "Electrical conductivity in polycrystalline CdS films: I. Theory", J. Phys. D: Appl. Phys., vol. 20, pp. 951-957, 1987.

[133] J.Y.W. Seto, "The electrical properties of polycrystalline silicon films", J. Appl. Phys., vol. 46, pp. 5247-5254, 1975.

[134] B.L. Mattes, *Growth and structure of amorphous and polycrystalline thin films*, London: Academic Press, 1980.

[135] J. Orton, *The story of semiconductors*, New York: Oxford University Press, 2006.

[136] A. Elshabini-Riad and F. D. Barlow, *Thin film technology handbook*, USA: McGraw Hill, 1998.

[137] D.B. Holt and B.G. Yacobi, *Extended defects in semiconductors: Electronic properties, device effects and structures*, New York: Cambridge University Press, 2007.

[138] M. Parlak, "Preparation and electrical, structural, optical characterization of InSe thin films", PhD. Thesis in Physics Department of Middle East Technical University, 1997.

[139] R.L. Petritz, "Theory of Photoconductivity in semiconductor films", Phys. Rev., vol. 10, pp. 1508-1516, 1956.

[140] M.V. Garcia-Cuenca and J.L. Morenza, "On the electrical conductivity of polycrystalline CdS films", J. Phys. D: Appl. Phys., vol. 18, pp. 2081-2086, 1985.

[141] Y. Kajikawa, "Conduction model covering non-degenerate through degenerate polycrystalline semiconductors with non-uniform grain-boundary potential heights based on an energy filtering model", J. Appl. Phys., vol. 112, pp. 123713-1-8, 2012.

[142] N.F. Mott and E.A. Davis, *Electronic processes in non-crystalline materials*, Oxford: Clarendon Press, 1971.

[143] J. Martinez and A. Piqueras, “On the mobility of polycrystalline semiconductors”, Sol. Stat. Elec., vol. 23, pp. 297-303, 1982

[144] C.H. Seager and G.E. Pike, “Electron-tunneling through GaAs grain-boundaries”, J. Appl. Phys. Lett., vol. 40, pp. 471-474, 1982.

[145] M.V. Garcia-Cuence, J.L. Morenza and J. Esteve, “Electron-tunneling in heavily In-doped polycrystalline CdS films”, J. Appl. Phys., vol. 56, pp. 1738-1743, 1984.

[146] J.G. Simmons, “Generalized formula for electric tunnel effect between similar electrodes separated by a thin insulatıng film”, J. Appl. Phys., vol. 34, p. 1793, 1963.

[147] E.M. Conwell, “Impurity band conduction in germanium and silicon”, Phys. Rev., vol. 103, pp. 51-60, 1956.

[148] N. F. Mott, “On the transition to metallic conduction in semiconductors”, Can. J. Phys., vol. 34, pp. 1356-1368, 1956.

[149] D. Pines, “Electron interaction in solids”, Can. J. Phys., vol. 34, pp. 1379-1394, 1956.

[150] N. Apsley and H.P. Hughes, “Temperature- and field-dependence of hopping conduction in disordered systems”, Phil. Mag., vol. 30, pp. 963-972, 1974.

[151] V. Ambegaokar, B.I. Halperin and J.S. Langer, “Hopping conductivity in disordered systems”, Phys. Rev. B, vol. 4, pp. 2612-2620, 1971.

[152] R. Singh, R.P. Tandon, G.S. Singh and S. Chandra, “Evaluation of Mott's parameters BF4- doped polypyrrole films”, Philos. Mag., vol. 66, pp. 285-291, 1992.

[153] B.I. Shklovskii and A.L. Efros, *Electronic properties of doped semiconductors*, Heidelberg: Springers, 1984.

[154] J. Singh, *Electronic and optoelectronic properties of semiconductor structures*, New York: Cambridge University Press, 2003.

[155] M. Pollak, “Effect of carrier-carrier interactions on some transport properties in disordered semiconductors”, Discuss. Faraday Soc., vol. 50, pp. 13-19, 1970.

[156] A.L. Efros and B.I. Shklovskii, “Coulomb gap and low temperature conductivity of disordered systems”, J. Phys. C: Solid State Phys., vol. 8, pp. L49-L51, 1975.

[157] A.L. Efros, “Coulomb gap in disordered systems”, J. Phys. C: Solid State Phys., vol. 9, pp. 2021-2030, 1976.

[158] E.H. Hall, “On a new action of the magnet on electric currents”, Amer. J. Math., vol. 2, pp. 287-292, 1879.

[159] B.R. Pamplin, *Crystal growth*, Oxford: Headington Hill Hall, Pergamon Press Ltd., 1975.

[160] S. Schiller, U. Heisig and S. Panzer, *Electron beam technology*, Berlin: John Wiley & Sons, 1982.

[161] K. W. Böer, *Handbook of the physics of thin-film solar cells*, New York: Springer, 2013.

[162] R. H. Bube, *Electronic properties of crystalline solids: An introduction to fundamentals*, New York: Academic Press, Inc., 1974.

[163] S.M. Sze and K.N. Kwok, *Physics of semiconductor devices*, USA: John Wiley & Sons Inc., 2007.

[164] S. Wolf and R. Tauber, *Silicon processing for the VLSI era*, California: Lattice Press, 1986.

[165] R.L. Anderson, “Germanium-Gallium arsenide heterojunctions”, IBM J. Res. Dev., vol. 4, pp. 283-287, 1960.

[166] R.L. Anderson, “Experiments on Ge-GaAs heterojunctions”, Solid State Electron., vol. 5, pp.341-344, 1962.

[167] B.L. Sharma and R.K. Purohit, “*Semiconductor heterojunctions*, Oxford/New York/Toronto/Sydney: Pergamon Press, 1974.

[168] L.J. van Ruyven, “Germanium-Gallium phosphide heterojunctions”, Thesis, Technische Hogeschool, Eindoven, Netherlands, 1964.

[169] S.S. Perlman and D.L. Feucht, “p-n heterojunction”, Solid State Electron., vol. 7, pp. 911-923, 1964.

[170] W. Shockley, “The theory of p-n junctions in semiconductors and p-n junction transistors”, Bell Syst. Tech. J., vol. 28, pp. 435-489, 1949.

[171] W. Schottky, “Halbleitertheorie der Sperrschicht”, Naturmiss., vol. 26, p. 843, 1938.

[172] C.R. Crowell and S.M. Sze, “Current transport in metal-semiconductor barriers” Solid State Electron., vol. 9, pp. 1035-1048, 1966.

[173] C.J.M. van Opdorp, “Si-Ge isotype heterojunctions”, Thesis, Technische Hogeschool, Eindoven, Netherlands, 1969.

[174] R.H. Rediker, S. Stopek and J.H.R. Ward, “Interface-alloy epitaxial heterojunctions”, Solid State Electron 7 (1964) 621-622

[175] P.C. Newman, “Forward characterstics of heterojunctions”, Electronic Letters, vol. 1, p. 262, 1965.

[176] A.R. Riben and D.L. Feucht, “nGe-pGaAs heterojunctions”, Solid State Electron., vol. 9, pp. 1055-1065, 1966.

[177] A.R. Riben and D.L. Feucht, “Electrical transport in nGe-pGaAs heterojunctions”, Int. J. Electron., vol. 20, p. 583, 1966.

[178] T. Markvart and L. Castaner, *Practical handbook of photovoltaics: Elements and applications*, UK: Elseiver Ltd., 2003.

[179] J.R. Sites and P.H. Mauk, “Diode quality factor determination for thin-film solar cells”, Solar Cells, vol. 27, pp. 411-417, 1989.

[180] P. Würfel, *Physics of solar cells: From principles to new concepts*, Weinheim: Wiley-VCH Verlag GmbH & Co., 2005.

[181] M.A. Green, “Solar cell fill factors: General graph and empirical expressions”, Solid State Electron., vol. 24, pp. 788-789, 1981.

[182] Superior-Marienfeld: Laboratory Glassware, *Instruction manual*, 2007.

[183] H. Bayhan, and Ç. Erçelebi, “Effects of post deposition treatments on vacuum evaporated CdTe thin films and CdS/CdTe heterojunction devices” Tr. J. of Physics, vol. 22, pp. 441-451, 1998.

[184] D.W. Koon, “Effect of contact size and placement, and of resistive inhomogeneities on van der Pauw measurements,” Rev. Sci. Instrum., vol. 60, pp. 271-274, 1989.

[185] M. Kaleli, T. Çolakoğlu and M. Parlak, “Production and characterization of layer by layer sputtered single-phase $AgInSe_2$ thin film by thermal selenization”, Appl. Surf. Sci., vol. 286, pp. 71–176, 2013.

[186] Digital Instruments Veeco Metrology Grou, Dektak 6M Manual, 2002, Available online: http://nano.indiana.edu/Files/Dektak/Dektak%206M%20Manual.pdf (last accessed on 23 July 2015).

[187] J. Golgstein, D.E. Newbury, D.C. Joy, P. Echlin, E. Lifshin, L. Sawyer and J.R. Michael, *Scanning Electron Microscopy and X-ray Microanalysis*, New York: Springer, 2003.

[188] Nanomagnetics Instruments, Ambient AFM manual, 2015, Available online: http://www.nanomagnetics-inst.com/usrfiles/files/Flayers/Ambient-AFM-2015.pdf (last accessed on 23 July 2015).

[189] J.R. Ferraro, K. Nakamoto and C.W. Brown, *Introductory Raman spectroscopy*, USA: Elseiver Science, 2003.

[190] iHR Fully Automated Imaging Spectrometer User Manual. Available online: Available online: https://www.nanocenter.umd.edu/equipment/nanoopticslab/manuals/optics-02/iHR320%20Manual.pdf (last accessed on 23 July 2015).

[191] Keithley Instruments, Inc., 2400 Series SourceMeter User's Manual, 2011.

[192] L.J. van der Pauw, "A method of measuring the resistivity and Hall coefficient on lamellae of arbitrary shape", Philips Tech. Rev., vol. 20, pp. 220-224, 1958.

[193] L.J. van der Pauw, "A method of measuring specific resistivity and Hall Effect of discs of arbitrary shape", Philips Research Reports, vol. 13, pp. 1-9, 1958.

[194] R. Bakish, *Introduction to electron beam technology*, New York: John Wiley & Sons, 1962.

[195] T. Matsumura and Y. Sato, "A theoretical study on van der Pauw measurement values of inhomogeneous compound semiconductor thin films", J. Mod. Phys., vol. 1, pp. 340-347, 2010.

[196] G. Golan, A. Axelevitch, B. Gorenstein and V. Manevych, "Hot-probe method for evaluation of impurities concentration in semiconductors", Microelectronics J., vol. 37, pp. 910–915, 2006.

[197] R.E. Hummel, *Electronic properties of materials*, Berlin: Springer-Verlag, 1993.

[198] F. Szmulowicz, "Calculation of the mobility and the Hall factor for doped p-type silicon", Phys. Rev. B, vol. 34, pp. 4031-4047, 1986.

[199] Hewlett Packard Model 4192A Impedance Analyzer, Operation and Service Manual, Yokogawa-Hewlett-Packard Ltd, Tokyo, 1984.

[200] D.H. Kuo, H.P. Wu, "Preparation and analysis of sputtered $Cu_2ZnSnSe_4$ thin films", Adv. Mat. Res., vol. 463, pp. 602-606, 2012.

[201] A. Roth, *Vacuum technology*, Amsterdam: North Holland, 1980.

[202] Joint Committee on Powder Diffraction Standards (JCPDS) Card no.39-0458.

[203] Joint Committee on Powder Diffraction Standards (JCPDS) Card no.39-1159.

[204] Joint Committee on Powder Diffraction Standards (JCPDS) Card no.80-0008.

[205] E.F. Kaelble, *Handbook of X-rays*, USA: McGraw-Hill Inc., 1967.

[206] J.I. Langford, A.J.C. Willson and A.J. Survey, "Scherer after sixty years: a survey and some new results in the determination of crystallite size", J. Appl. Cryst., vol. 11, p. 102, 1978.

[207] H. Karaagac, M. Kaleli and M. Parlak, "Characterization of $AgGa_{0.5}In_{0.5}Se_2$ thin films deposited by electron-beam technique", J. Phys. D: Appl. Phys., vol. 42, pp. 165413-1-7, 2009.

[208] G.K. Williamson and W.H. Hall, "X-ray line broadening from filed aluminium and wolfram", Acta Metall., vol. 1, pp. 22-31, 1953.

[209] B.G. Jeyaprakash, K. Kesavan, R.A. Kumar, S. Mohan and A. Amalarani, "Temperature dependent grain-size and microstrain of CdO thin films prepared by spray pyrolysis method", Bull. Mater. Sci., vol. 34, pp. 601–605, 2011.

[210] N.J.S. Kissinger, N. Velmurugan and K. Perumal, "Substrate-temperature-dependent structural and optical properties of ZnSe thin films fabricated by using an electron beam evaporation technique", J. Korean Phys. Soc., vol. 55, pp. 1577-1581, 2009.

[211] H. Haeuseler, G. Waschenbach and H.D. Lutz, "Directional dispersion of the phonon modes in optically uniaxial solids, far-infrared reflection spectra, dielectric and optic constants, dynamic effective ionic charges of the defect chalcopyrites $CdGa_2S_4$, $CdGa_2Se_4$, $HgGa_2S_4$, and $HgGa_2Se_4$", Phys. Stat. Sol. (b), vol. 129, pp. 549-558, 1985.

[212] H. Neumann, E. Moise, H. Schwer and V. Kramer, "Infrared lattice vibrations of $CdGa_2Te_4$", Cryst. Res. Technol., vol. 28, pp. 635-639, 1993.

[213] G. Attolini, S. Bini, P.P. Lottici and C. Razzeti, "Effects of group III cation substitution in the Raman spectra of some defective chalcopyrites", Cryst. Res. Technol., vol. 27, p. 685, 1992.

[214] C.M. Lin, D.S. Chuu and T.J. Yang, "Raman spectroscopy study of ZnSe and $Zn_{0.84}Fe_{0.16}Se$ at high pressures", Phys. Rev. B, vol. 5, pp. 13641-13646, 1997.

[215] G.L. Weissler and R.W. Carlson, *Methods of experimental physics - Vacuum physics and technology Volume 14*, New York: Academic Press, 1979.

[216] T. Colakoglu and M. Parlak, "Structural characterization of polycrystalline Ag–In–Se thin films deposited by e-beam technique", Appl. Surf. Sci., vol. 254, pp. 1569–1577, 2008.

[217] B. Canava, J. Vigneron, A. Etcheberry, J.F. Guillemoles and D. Lincot, "High resolution XPS studies of Se chemistry of a $Cu(In, Ga)Se_2$ surface", Appl. Surf. Sci., vol. 202, pp. 8-14, 2002.

[218] S.T. Lakshmikumar and A.C. Rastogi, "Novel two-stage selenization process for the preparation of ZnSe films", Thin Solid Films, vol. 259, pp. 150-153, 1995.

[219] M. Procop, "XPS data for sputter-cleaned $In_{0.53}Ga_{0.47}As$, GaAs, and InAs surfaces", J. Electron Spectrosc. Relat. Phenom., vol. 59, pp. R1-R10, 1992.

[220] R.A. Pollak, S.P. Kowalczyk, L. Ley and D.A. Shirley, "Evolution of core states from energy bands in the 4d5s5p region from Pd to Xe", Phys. Rev. Lett., vol. 29, pp. 274-277, 1972.

[221] M. Cardona and L. Ley, *Photoemission in solids I: General principles*, Berlin: Springer-Verlag, 1978.

[222] T. Ueno and A. Odajima, “X-ray photoelectron spectroscopy of Ag- and Cu-doped amorphous As_2Se_3”, Jpn. J. Appl. Phys., vol. 20, pp. L501-L504, 1981.

[223] R. Swanepoel, “Determination of the thickness and optical constants of amorphous silicon”, J. Phys. E: Sci. Instrum., vol. 16, pp. 1214-1222, 1983.

[224] T. Çolakoğlu, M. Parlak and S. Özder, “Investigation of optical parameters of Ag-In-Se thin films deposited by e-beam technique”, J. Non-Cryst. Solids, vol. 354, pp. 3630–3636, 2008.

[225] J.C. Manifacier, J. Gasiot and J.P. Fillard, “A simple determination for the determination of the optical constants *n*, *k* and the thickness of a weakly absorbing thin film”, J. Phys. E: Sci. Instrum., vol. 9, pp. 1002-1004, 1976.

[226] O.S. Heavens, *Optical properties of thin solid films*, New York: Dover publications, Inc., 1991.

[227] P.M. Amirtharaj and D.G. Seiler, *Optical properties of semiconductors*, in: M. Bass, E.W.V. Stryland, D.R. Williams and W.L. Wolfie, *Handbook of Optics – Volume 2*”, USA: McGraw-Hill Inc, 1978.

[228] G.K.L. Goh, C.P.K. Liew, J. Kim and T.J. White, “Structure and optical properties of solution deposited TiO_2 films”, J. Cryst. Growth, vol. 291, pp. 94-99, 2006.

[229] M. Fox, O*ptical properties of solids*, Londorn: Oxford University Press, 2001.

[230] H.H. Güllü, Ö. Bayraklı, İ. Candan, E. Coşkun and M. Parlak, “Structural and optical properties of Zn-In-Te thin films deposited by thermal evaporation technique”, J. Alloy. Compd., vol. 566, pp. 83-89, 2013.

[231] F.L. Pedrotti and L.S. Pedrotti, *Introduction to optics*, USA: Prentice-Hall, Inc., 1993.

[232] S.H. Wemple and M. DiDomenico, “Behavior of the electronic dielectric constant in covalent and ionic materials”, Phys. Rev. B, vol. 3, pp. 1338-1351, 1971.

[233] J.C. Philips, “Dielectric definition of electronegativity”, Phys. Rev. Letters, vol. 20, pp. 550-553, 1968.

[234] W.G. Spitzer and H.Y. Fan, “Determination of optical constants and carrier effective mass of semiconductors”, Phys. Rev., vol. 106, pp. 882-890, 1997.

[235] N. Khemiri, A. Sinaoui and M. Kanzari, "Determination and analysis of dispersive optical constants of $CuIn_3S_5$ thin films", Physica B, vol. 406, pp. 1778-1783, 2011.

[236] A.J. Sievers and J.B. Page, "Generalized Lyddane-Sachs-Teller relation and disordered solids", Phys. Rev. B, vol. 41, pp. 3455-3459, 1990.

[237] J.C. Philips, *Bonds and Bands in Semiconductors*, London: Academic Press, Inc., 1973.

[238] D.J. Wood and J. Tauc, "Weak absorption tails in amorphous semiconductors", Phys. Rev. B, vol. 5, pp. 3144-3151, 1972.

[239] H.S. Soliman, M.M. El-Nahass and A. Qusto, "Growth and optical properties of $ZnIn_2Se_4$ films", J. Mat. Sci., vol. 26, pp. 1556-1564, 1991.

[240] Y. Rajakarunanayake, R.M. Miles, G.Y. Wu and T.C. McGill, "Band structure of ZnSe-ZnTe superlattices", Phys. Rev. B, vol. 37, pp. 10212-10215, 1988.

[241] H.E. Ruda, *Widegap II–VI Compounds for Opto-Electronic Applications*, London: Chapman & Hall, 1992.

[242] J. Luengo and N.V. Joshi, "Compositional dependence of the energy gap of $Zn_xMn_{1-x}In_2Se_4$ and optical absorption spectroscopy", Mater. Lett., vol. 26, pp. 47-50, 1996.

[243] A.F. Qasrawi, "Temperature dependence of the band gap, refractive index and single-oscillator parameters of amorphous indium selenide thin films", Opt. Mater., vol. 29, pp. 1751-1755, 2007.

[244] F. Urbach, "The long-wavelength edge of photographic sensitivity and of the electronic absorption of solids", Phys. Rev. B, vol. 92, p. 1324, 1953.

[245] S.J. Ikhmayies and R.N. Ahmad-Bitar, "An investigation of the bandgap and Urbach tail of vacuum-evaporated SnO_2 thin films", Renew. Energ., vol. 49, pp.143-146, 2013.

[246] L.L. Kazmerski, *Electrical properties of polycrystalline semiconductor thin films*, London: Academic Press, 1980.

[247] T. Çolakoğlu and M. Parlak, "Electrical and photoelectrical properties of Ag-In-Se thin films evaporated by e-beam technique", J. Phys. D: Appl. Phys., vol. 42, pp. 035416-1-8, 2009.

[248] T. Serin, A. Yıldız, N. Serin, N. Yıldırım, F. Özyurt and M. Kasap, "Electron-Electron Interactions in Sb-Doped SnO_2 Thin Films", J. Electron. Mater., vol. 3, pp. 1152-1158, 2010.

[249] Y.L. Huang, S.P. Chiu, Z.X. Zhu, Z.Q. Li and J.J. Lin, "Variable-range-hopping conduction processes in oxygen deficient polycrystalline ZnO Films", J. Appl. Phys., vol. 107, pp. 063715-1-6, 2010.

[250] L. Pi, L. Zheng and Y. Zhang, "Transport mechanism in polycrystalline $La_{0.825}Sr_{0.175}Mn_{1-x}Cu_xO_3$", Phys. Rev. B, vol. 61, pp. 8917-8921, 2000.

[251] A. Bozkurt, M. Parlak, Ç. Erçelebi and L. Toppare, "Conduction mechanism in H-type polysiloxane-polypyrrole block copolymers", J. Appl. Polym. Sci., vol. 85 pp. 52-56, 2002.

[252] D.K. Paul and S.S. Mitra, "Evaluation of Mott's parameters for hopping conduction in amorphous Ge, Si and Se-Si", Phys. Rev. Lett., vol. 31, pp. 1000-1003, 1973.

[253] S. Lamba and D. Kumar, "Variable-range hopping: Role of Coulomb interactions", Phys. Rev. B, vol. 59, pp. 4752–4765, 1999.

[254] N.V. Joshi, *Photoconductivity, art, science, and technology*, New York/Basel: Marcel Dekker Inc., 1990.

[255] U.N. Roy, Y. Cui, R. Hawrami, A. Burger, L. Orona and J.T. Goldstein, "$AgGaSe_2$: A highly photoconductive material", Solid State Commun., vol. 139, pp. 527-530, 2006.

[256] K. Yilmaz, M. Parlak and Ç. Ercelebi, "Investigation of photovoltaic properties of amorphous InSe thin film based Schottky devices", Semicon. Sci. Technol., 22 (2007), 1268-1271

[257] J. MartinezPastor, A. Segura, J.L. Valdez and A. Chevy, "Electrical and photovoltaic properties of indiumtinoxide/pInSe/Au solar cells", J. Appl. Phys., vol. 62, pp. 1477-1483, (1987.

[258] H.J. Hovel, *Solar cells* in: R.K. Willardson and A.C. Beer, editors. *Semiconductor and semimetal*, vol. 11. New York: Academic Press, 1975.

[259] I.S. Yahia, M. Fadel, G.B. Sakr, F. Yakuphanoglu, S.S. Shenouda and W.A. Farooq, "Analysis of current-voltage characteristics of Al/p-$ZnGa_2Se_4$/n-Si nanocrystalline heterojunction diode", J. Alloy Compd., vol. 509, pp. 4414-4419, 2011.

[260] K.S. Karimov, M.M. Ahmed, S.A. Moiz and M.I. Fedorov, "Temperature-dependent properties of organic-on-inorganic Ag/p-CuPc/n-GaAs/Ag photoelectric cell", Sol. Energ Mat. Sol. C., vol. 87, pp. 61-75, 2005.

[261] H. Uslu, A. Bengi, S.S. Çetin, U. Aydemir, Ş. Altındal, S.T. Aghaliyeva and S. Özçelik, "Temperature and voltage dependent current-transport mechanism in GaAs/AlGaAs single quantum-well lasers", J. Alloy Compd., vol. 507, pp, 190-195, 2010.

[262] A.L. Fahrenbruch and R.H. Bube, *Fundamentals of Solar Cells*, Academic Press: USA, 1983

[263] M.A.M. Seyam, H.T. El-Shair and G.F. Salem, "Electrical properties and transport mechanisms of p-znte/n-si heterojunctions" Eur. Phys. J. Appl. Phys., vol. 41, pp. 221-227, 2008.

[264 M.S. Tyagi, *Metal-Semiconductor Schottky Barrier Junction and Their Applications*, New York: Plenum Press, 1984.

[265] R. Scheer, "Activation energy of heterojunction diode currents in the limit of interface recombination", J. Appl. Phys., vol. 105, pp. 104505-1-104505-6, 2009.

[266] J. Yoo, A.L. Fahrenbruch and R.H. Bube, "Transport mechanisms in ZnO/CdS/$CuInSe_2$ solar cells", J. Appl. Phys., vol. 68, pp. 4694-4699, 1990.

[267] H. Uslu, Ş. Altındal, İ. Polat, H. Bayrak and E. Bacaksız, "On the mechanism of current-transport in Cu/CdS/SnO_2/In-Ga structures", J. Alloys Compd,, vol. 509, pp. 5555-5561, 2011.

[268] R.T. Tung, "Electron transport at metal-semiconductor interfaces: General theory", Phys. Rev. B, vol. 45, pp. 16509-16523, 1992.

[269] R.D. Gould, "The interpretation of space charge limited currents in semiconductors and insulators", J. Appl. Phys., vol. 53, pp. 3353-3355, 1982.

[270] F. Yakuphanoğlu, N. Tuğluoğlu and S. Karadeniz, “Space charge-limited conduction in Ag/p-Si Schottky diode”, Physica B, vol. 392, pp. 188-191, 2007.

[271] A.O. Odour and R.D. Gould, “Space-charge-limited conductivity in evaporated cadmium selenide thin films”, Thin Solid Films, vol. 270, pp. 387-390, 1995.

[272] R.D. Gould and M.S. Rahman, “Power-law currents in some ZnO-Sn composite materials”, J. Phys. D: Appl. Phys, vol. 14, pp. 79-89, 1981.

[273] S.S. Ou, O.M. Stafsudd and B.M. Basol, “Current transport mechanisms of electrochemically deposited CdS/CdTe heterojunction” Solid-State Electron., vol. 27 p. 21, 1984.

[274] S. Vatavu, and P. Gaşin, “The analysis of current flow mechanism in CdS/CdTe heterojunction”, Thin Solid Films, vol. 515, pp. 6179-6183, 2007.

[275] Ç. Ercelebi, A.W. Brinkman, T.S. Furlong and J. Woods, “Current transport mechanisms in epitaxial CdS/CdTe heterojunctions”, J. Cryst. Growth, vol. 101, pp. 162-166, 1990.

[276] G.K. Rao, K.V. Bangera and G.K. Shivakumar, “Fabrication and characterization of thermal evaporated n-Si/p-ZnTe thin film heterojunction diodes”, Cur. Appl. Phys., vol. 13, pp. 298-301, 2013.

[277] V. Janardhanam, H. Lee, K. Shim, H. Hong, S. Lee, K. Ahn and C. Choi, “Temperature dependency and carrier transport mechanisms of Ti/p-type InP Schottky rectifiers”, J. Alloy. Compd., vol. 504, pp. 146-150, 2010.

[278] K. Yılmaz, “Investigation of InSe thin film based devices”, PhD. Thesis in Physics Department of Middle East Technical University, 2004.

[279] H. Mamikoglu, “Investigation of thin film heterojunction devices”, Ph.D. Thesis in Physics Department of Middle East Technical University, 1994.

[280] A. Singh, “Characterization of interface states at Ni/nCdF_2 Schottky barrier type diodes and the effect of CdF_2 surface preparation”, Solid State Electron, vol. 28, pp. 223-232, 1985.

[281] G.K. Rao, K.V. Bangera and G.K. Shivakumar, “Studies on vacuum deposited p-ZnTe/n-ZnSe heterojunction diodes”, Solid-State Electron, vol. 54, pp. 787–790, 2010.

[282] M. Vos, F. Xu, J. H. Weaver, and H. Cheng, “Influence of metal interlayers on Schottky barrier formation for Au/ZnSe (100) and Al/ZnSe (100),” Appl. Phys. Lett., vol. 53, pp. 1530-1532, 1988.

[283] S. Darwish, A.S. Riad and H.S. Soliman, “Electrical conductivity and the effect of temperature on photoconduction of n-ZnSe/p-Si rectifying heterojunction cells", Semicond. Sci. Technol., vol. 11, pp. 96–102, 1996.

[284] D. Liao and A. Rockett, “Epitaxial growth of Cu(In,Ga)Se_2 on GaAs(110)”, J. Appl. Phys., vol. 91, pp. 1978-1984, 2002.

[285] P.P. Ramesh, S. Uthanna, S., B.S. Naidu and P.J. Reddy, “Optical absorption studies on single-phase polycrystalline AglnSe$_2$ thin films”, J. Mater. Sci. Lett., vol. 15, pp. 116-119, 1996.

[286] H.H. Güllü, Investigation of Structural, Electrical and Optical Properties of $Cu_{1-x}Ag_xInSe_2$ Thin Films as a Function of x Content, M.Sc. Thesis in Physics Department of Middle East Technical University, 2010.

[287] H. H. Güllü, E. Coşkun and M. Parlak, Characterization of co-evaporated Cu-Ag-In-Se thin films, Braz. J. Phys., vol. 44, pp. 719-725, 2014.

[288] K. Yılmaz, and H. Karaagaç, “Annealing effects on structural, optical and electrical properties of e-beam evaporated $CuIn_{0.5}Ga_{0.5}Te_2$ thin films”, Appl. Surf. Sci., vol. 256, pp. 6454–6458, 2010.

[289] B.E. Warren, *X-ray diffraction*, USA: Addison-Wesley Pub. Co., 1990.

[290] B.D. Hall, D. Zanchet and D. Ugarte, “Estimating nanoparticle size from diffraction measurements”, J. Appl. Cryst., vol. 33 pp. 1335-1341, 2000.

[291] A. Rockett and R.W. Birkmire, “$CuInSe_2$ for photovoltaic applications”, J. Appl. Phys., vol. 70, pp. R81-R97, 1991.

[292] N.M. Shah, J.R. Ray, K.J. Patel, V.A. Kheraj, M.S. Desai, C.J. Panchal and B. Rehani, “Structural, electrical, and optical properties of copper indium diselenide thin film prepared by thermal evaporation method”, Thin Solid Films, vol. 517, pp. 3639-3644, 2009.

[293] T. Colakoglu and M. Parlak, “Structural characterization of polycrystalline Ag–In–Se thin films deposited by e-beam technique”, Appl. Surf. Sci., vol. 254, pp. 1569–1577, 2008.

[294] T.F. Ciszek, R. Bacewicz, D. Dunlavy, S.K. Deb and J.R. Durrant, "Crystal growth and photoelectrical properties of $Cu_xAg_{1-x}InSe_2$ and $CuIn_xGa_{1-x}Se_2$ solid solutions", 19th IEEE Photovoltaic Specialists Conference, pp. 1448-1453, 1987.

[295] F.W. Ohrendorf and H. Haeuseler, "Lattice dynamics of chalcopyrite type compounds. Part I. Vibrational frequencies", Cryst. Res. Technol., vol. 34, pp. 339-349, 1999.

[296] J. Olejníček, C.A. Kamler, S.A. Darveau, C.L. Exstrom, L.E. Slaymaker, A.R. Vandeventer, N.J. Ianno and R.J. Soukup, "Formation of $CuIn_{1-x}Al_xSe_2$ thin films studied by Raman scattering", Thin Solid Films, vol. 519, pp. 5329–5334, 2011.

[297] D.E. Carlson and C.R. Wronski, "Amorphous silicon solar cell", Appl. Phys. Lett., vol. 28, pp. 671-673, 1976.

[298] K.G. Deepa, K.P. Vijayakumar and C. Sudhakartha, "Lattice vibrations of sequentially evaporated $CuInSe_2$ by Raman microspectrometry, Mater. Sci. Semicond. Process., vol. 15, pp. 120–124, 2012.

[299] L.I. Soliman, M.H. Wasft and T.A. Hendia, "Thermophysical properties of $ZnIn_2Se_4$" Proc. Indian Acad. Sci. (Chem. Sci.), vol. 110, pp. 193-197, 1998.

[300] O. A. Balitskii and W. Jaegermann, "XPS study of InTe and GaTe single crystals oxidation", Mater. Chem. and Phys., vol. 97, pp. 98-101, 2006.

[301] A. Mekki, D. Holland and C.F. McConville, "X-ray photoelectron spectroscopy study of copper sodium silicate glass surfaces", J. Non-Cryst. Solids, vol. 215, pp. 271-282, 1997.

[302] K.S. Kim, "Charge transfer transition accompanying X-ray photoionization in transition-metal compounds", J. Electron Spectr. Rel. Phen., vol. 3, pp. 217-226, 1974.

[303] B. Wallbank, I.G. Main and C.E. Johnson, "2p and 2s shake-up satellites in solid compounds of 3d ions", J. Electron Spectr. Rel. Phenom., vol. 5, pp. 259-266, 1974.

[304] A.N. Mansour, "Copper Mg K_α XPS Spectra from the Physical Electronics Model 5400 Spectrometer", Surf. Sci. Spectra, vol. 3, pp. 202-210, 1994.

[305] M.P. Seah, “Post-1989 calibration energies for X-ray photoelectron spectrometers and the 1990 Josephson constant”, Surf. Interface Anal., vol. 14, p. 488, 1989.

[306] G.B. Hoflund, J.F. Weaver and W.S. Epling, “Ag foil by XPS”, Surf. Sci. Spectra, vol. 3, pp. 151-156, 1994.

[307] G. Schoen, “ESCA Studies of Ag, Ag_2O and AgO”, Acta Chem. Scand., vol. 27, pp. 2623-2633, 1973.

[308] T. Ueno and A. Odajima, “X-ray photoelectron Spectroscopy of Ag- and Cu-doped amorphous As_2Se_3”, Jpn. J. Appl. Phys., vol. 20, pp. L501-L504, 1981.

[309] S. Fonash, *Solar cell device physics*, USA: Elsevier Inc., 2010.

[310] J. Tauc in: F. Abels, editor. *Optical properties of solids*, Amsterdam: North Holland, 1970

[311] E.A. Davis and N.F. Mott, “Conduction in non-crystalline systems V. Conductivity, optical absorption and photoconductivity in amorphous semiconductors”, Phil Mag., vol. 22, pp. 903-922, 1970.

[312] P.J. George, A. Sanchez, P.K. Nair and M.T.S. Nair, “Doping of chemically deposited intrinsic CdS thin films to n type by thermal diffusion of indium”, Appl. Phys. Lett., vol. 66, pp. 3624-3626, 1995.

[313] K.S. Ahn, S.H. Lee, A.C. Dillon, C.E. Tracy and R. Pitts, “The effect of thermal annealing on photoelectrochemical response of WO_3 thin films”, J. Appl. Phys., vol. 101, pp. 093524-1-4, (2007.

[314] A.S. Soltan, “Thermal annealing dependence of the optical and electrical properties of amorphous $Se_{79}Te_{15}Sb_6$ thin films”, Appl. Phys. A, vol. 80, pp. 117-121, 2005.

[315] A.A. Gahamdi, S.A. Khan, S. Al-Heniti, F.A. Al-Agel and M. Zulfequar, “Annealing and laser irradiation effects on optical constants of $Ga_{15}Se_{85}$ and $Ga_{15}Se_{83}In_2$ chalcogenide thin films”, Curr. Appl. Phys., vol. 11, pp. 315-320, 2011.

[316] M.M. Hafiz, A.A. Othman, M.M. El-Nahass and A.T. Al-Motasem, “Composition and thermal-induced effects on the optical constants of $Ge_{20}Se_{80-x}Bi_x$ thin films”, Physica B, vol. 390, pp. 348-355, 2007.

[317] H. Karaagac and M. Parlak, “Investigation of physical properties of quaternary $AgGa_{0.5}In_{0.5}Te_2$ thin films deposited by thermal evaporation” J. Alloy. Compd., vol. 503, pp. 468-473, 2010.

[318] H. Karaagac and M. Parlak, “The investigation of structural, electrical, and optical properties of thermal evaporated $AgGaS_2$ thin films”, Thin Solid Films, vol. 519, pp. 2055-2061, 2011.

[319] H. Karaagac and M. Parlak, Deposition of $AgGaS_2$ thin films by double source thermal evaporation technique” J. Mater. Sci.: Mater. Electron., vol. 22, pp. 1426-1432, 2011.

[320] Y. Wu, G. Chen, S.H. Wei, M. Al-Jassim and Y. Yan, “Unusual nonlinear strain dependence of valence-band splitting in ZnO”, Phys. Rev. B, vol. 86, pp. 155205-1-5, 2012.

[321] A.L. Dawar, K.V. Ferdinand, C. Jagdish, P. Kumar and P.C. Mathur, “Electrical properties of Te-rich, Cd-rich and hydrogen-exposed polycrystalline CdTe thin films”, J. Phys. D: Appl. Phys., vol. 16, pp. 2349-2360, 1983.

[322] M.M.A. Imran, O.A. Lafi and M. Abu-Samak, “Effect of thermal annealing on some electrical properties and optical band gap of vacuum evaporated $Se_{65}Ga_{30}In_5$ thin films”, Vacuum, vol. 86, pp. 1589-1594, 2012.

[323] R.M. Hill, “Hopping conduction in amorphous solid”, Phil. Mag., vol. 24, pp. 1307-1325, 1971.

[324] M. Pollack, “A percolation treatment of DC hopping conduction”, J. Non-cryst. Solids, vol. 8-10, pp. 486-491, 1972.

[325] R. Rosenbaum, “Crossover from Mott to Efros-Shklovskii variable-range-hopping conductivity in In_xO_y films”, Phys. Rev. B, vol. 44, pp. 3599-3603, 1991.

[326] E. Coşkun, H.H. Güllü, M. Parlak and Ç. Erçelebi, “Study on the Structural and Electrical Properties of Sequentially Deposited Ag–Ga–In–Te Thin Films”, J. Low Temp. Phys., vol. 178, pp. 162–173, 2015.

[327] R. Chander and R. Thangaraj, “Photoconductivity studies of Te-substituted Sn-Sb-Se semiconducting films”, Appl. Phys. A, vol. 114, pp. 619–624, 2014.

[328] A. Kumar, S. Goel and S.K. Tripathi, “Steady-state and transient photoconductivity in amorphous thin films of Ge_xSe_{100-x}”, Phys. Rev. B, vol. 38, p. 13432, 1988.

[329] R.H. Bube, *Photoconductivity of Solids*, New York: Interscience, 1960.

[330] A.A.M. Farag, M. Cavas and F. Yakuphanoglu, Mater. “Electrical performance and interface states studies of undoped and Zn-doped CdO/p-Si heterojunction devices”, Chem. Phys., vol. 132, pp. 550-558, 2012.

[331] H. Tecimer, S. Aksu, H. Uslu, Y. Atasoy, E. Bacaksız and Ş. Altındal, “Schottky diode properties of $CuInSe_2$ films prepared by a two-step growth technique”, Sensors Actuator A, vol. 185, pp. 73-81, 2012.

[332] H. Bayhan and M. Bayhan, “An analysis of the effect of illumination to the reverse and forward bias current transport mechanisms in an efficient n-ZnO/n-CdS/p-Cu(In,Ga)Se2 solar cell”, Sol. Energ., vol. 87, pp. 168-175, 2013.

[333] J. MartinezPastor, A. Segura, J.L. Valdez and A. Chevy, “Electrical and photovoltaic properties of indium-tin-oxide/p-InSe/Au solar cells”, J. Appl. Phys., vol. 62, pp. 1477–83, 1987.

[334] K. Yilmaz, M. Parlak and Ç. Ercelebi, “Investigation of photovoltaic properties of amorphous InSe thin film based Schottky devices”, Semicon. Sci. Technol., vol. 22, pp. 1268–71, 2007.

[335] B.L. Sharma, *Metal-semiconductor Schottky Barrier junctions and their applications*, New York: Plenum Press, 1984.

[336] A.S. Riad, “Influence of dioxygen and annealing process on the transport properties of nickel phthalocyanine Schottky-barrier devices”, Physica B, vol. 270, p. 148, 1999.

[337] F. Yakuphanoglu, N. Tugluoglu and S. Karadeniz, “Space charge-limited conduction in Ag/p-Si Schottky diode”, Physica B, vol. 392, pp. 188–91, 2007.

[338] V. Janardhanam, I. Jyothi, K. S. Ahn, and C. J. Choi, “Temperature-dependent current–voltage characteristics of Se Schottky contact to n-type Ge”, Thin Solid Films, vol. 546, pp. 63-68, 2013).

[339] H. D. Lee, “Characterization of shallow silicided junctions for sub-quarter micron ULSI technology. Extraction of silicidation induced Schottky contact area”, IEEE Trans. Electron Devices, vol. 47, pp. 762-767, 2000.

[340] J.Y. Jeong, V. Janardhanam, H.J. Yun, J.H. Lee, J.Y. Kim, K.H. Shim and C.J. Choi, “Carrier transport mechanism of Ni/Ag Schottky contacts to n-type GaN grown on Si(111) substrate”, Jpn. J. Appl. Phys., vol. 53, vol. 08NH01-1-6, 2014.

[341] A.K. Hassan and R.D. Gould, “Asymmetric electrical conductivity in oxygen-doped thin films of copper phthalocyanine, using gold and aluminum electrodes”, Int. J. Electron, vol. 69, pp. 11-17, 1990.

[342] F. Khan, S.N. Singh and M. Husain, “Effect of illumination intensity on cell parameters of a silicon solar cell”, Sol. Energ. Mat. Sol C, vol. 94, pp. 1473–1476, 2010.

[343] M. Chegaar, A. Hamzaoui, A. Namoda, P. Petit, M. Aillerie and A. Herguth, “Effect of illumination intensity on solar cells parameters”, Energy Procedia, vol. 36, pp. 722-729, 2013.

[344] K. Ramanathan, H. Wiesner, S. Asher, D. Niles, R.N. Bhattacharya, J. Keane, M.A. Contreras, and R. Noufi, “High-efficiency Cu(In,Ga)Se_2 thin film solar cells without intermediate buffer layers”, Proc. 2nd World Conf. and Exhibition on Photovoltaic Solar Energy Conversion, 1998.

[345] A.E. Delahoy, J. Bruns, A. Ruppert, M. Akhtar, L. Chen, and Z.J. Kiss “Thin film CIGS photovoltaic technology”, Energy Annual Technical Report, Phase II, Princeton, New Jersey, Photovoltaics, Inc., 2000.

CURRICULUM VITAE

PERSONAL INFORMATION

Surname, Name: Güllü, Hasan Hüseyin
Nationality: Turkish (TC)
Date and Place of Birth: 11 April 1985, Isparta
Marital Status: Married
Phone: +90 312 210 64 38
Fax: +90 312 210 64 25
email: hgullu@metu.edu.tr

EDUCATION

Degree	Institution	Year of Graduation
MS	METU Department of Physics	2010
BS-major	METU Department of Secondary Science and Mathematics Education	2008
BS-minor	METU Department of Mathematics	2008
High School	Isparta Anatolian High School	2003

WORK EXPERIENCE

Year	Place	Enrollment
2016-Present	METU Central Laboratory	Specialist
2009-2016	METU Department of Physics	Research Assistant

FOREIGN LANGUAGE

Advanced English

PUBLICATIOUNS

A. Articles

*1. H. H. Güllü, M. Parlak, "*Structural Characteristics of Thermally Evaporated $Cu_{0.5}Ag_{0.5}InSe_2$ Thin Films"*, Materials Research Express (in press)

*2. H. H. Güllü, E. Coşkun, M. Parlak, "*Investigation of Optical Parameters of Thermally Evaporated ZnSe Thin Films"*, Physica Status Solidi (c), 12 (2015) 1224-1228

*3. H. H. Güllü, İ. Candan, E. Coşkun, M. Parlak, "*Investigation of Structural and Optical Parameters of Cu-Ag-In-Se Thin Films Deposited by Thermal Evaporation Method"*, Optik - International Journal for Light and Electron Optics, 126 (2015) 1578-1583

4. F. Aksoy Akgül, G. Akgül, H. H. Güllü, H. E. Ünalan, R. Turan, "*Enhanced diode performance in cadmium telluride-silicon nanowire* h*eterostructures"*, Journal of Alloys and Compounds, 644 (2015) 131-139

5. F. Aksoy Akgül, G. Akgül, H. H. Güllü, H. E. Ünalan, R. Turan, "*Improved diode properties in zinc telluride thin film-silicon nanowire heterojunctions"*, Philosophical Magazine, 95 (2015) 1164-1183

6. E. Coşkun, H. H. Güllü, İ. Candan, Ö. Bayraklı, M. Parlak, "*Device behavior of an In/p-Ag(Ga,In)Te2/n-Si/Ag heterojunction diode"*, Materials Science in Semiconductor Processing, 34 (2015) 138-145

7. E. Coşkun, H. H. Güllü, M. Parlak, Ç. Erçelebi, "*Study on the structural and electrical properties of sequentially deposited Ag-Ga-In-Te thin films"*, Journal of Low Temperature Physics, 178 (2015) 162-173

8. E. Coşkun, H. H. Güllü, M. Parlak, "*Device application of AgGa0.5In0.5Se2 thin films deposited by thermal sequential stacked layer method"*, Materials Research Express, 1 (2014) 046407

*9. H. H. Güllü, E. Coşkun, M. Parlak, "*Characterization of co-evaporated Cu-Ag-In-Se thin films"*, Brazilian Journal of Physics 44 (2014) 719-725

10. M. Işık, H. H. Güllü, "*Structural and optical properties of thermally evaporated Ga-In-Se thin films"*, Modern Physics Letters B 28 (2014) 1450101

11. H. H. Güllü, Ö. Bayraklı, İ. Candan, E. Coşkun, M. Parlak, "*Structural and optical properties of Zn-In-Te thin films deposited by thermal evaporation technique"*, Journal of Alloys and Compounds 566 (2013) 83–89

12. A. Hosseini, Ç.İçli, H. H. Güllü, "*Preparation and characterization of porous TiO2 thin films by sol-gelmethod for Extremely Thin Absorber-ETA solar cell applications"*, Turkish Journal of Science and Technology 8(2) (2013) 69-79

13. M. M. Metbulut, H. H. Güllü, H. Altan, "*Influence of the Spot Size of the Probe Beam on the Detected THz Power using Electro-optic Detection Method"*, NATO Science for Peace and Security Series B: Physics and Biophysics (2011) 107-111

14. D. Köseoğlu, H. H. Güllü, and H. Altan, "*THz probe studies of MBE grown epitaxial GaAs"*, Journal of Physics: Conference Series 193 (2009), Article number: 012088

15. M. M. Metbulut, H. H. Güllü, H. Altan, "*Influence of the Spot Size of the Probe Beam on the Detected THz Power using Electro-optic Detection Method"*, TERA-MIR 2009, NATO Advanced Research Workshop Terahertz and Mid Infrared Radiation: Basic Research and Practical Applications (2009) 47-48, Article number: 5379634

B. Oral Presentations

1. Ö. Bayraklı, H. H. Güllü, M. Parlak, "*$AgGaxIn_{(1-x)}Te_2$ İnce Filmlerin Üretilmesi ve Aygıt Özelliklerinin Belirlenmesi"*, 21. Yoğun Madde Fiziği Ankara Toplantısı (YMF-21), 2015

2. Ö. Bayraklı, H. H. Güllü, M. Parlak, "*Device Measurements and Analysis of Ag-Ga-In-Te Based Thin Film Heterojunction Diode"*, 3. Turkish Solar Electricity Conference and Exhibition (SolarTR-3), 2015

3. H. H. Güllü, E. Coşkun, Ö. Bayraklı, M. Parlak, "*Material and Device Characterization of $Cu_{0.5}Ag_{0.5}InSe_2$ and $ZnInSe_2$ Thin Films for Photovoltaic Applications"*, Materials Research Society (MRS) Spring Meeting, 2015

4. Ö. Bayraklı, H. H. Güllü, İ. Candan, E. Coşkun, M. Parlak, Ç. Erçelebi, "*Characterization of Ag-Ga-In-Te Thin Film for Solar Cell Applications"*, Science and Applications of Thin Films, Conference and Exhibition, (SATF2014), 2014

C. Poster Presentations

1. H. H. Güllü, Ö. Bayraklı, E. Coşkun, M. Parlak, *"Fabrication and Characterization of p-CuInSe2/n-Si Heterojunction Diodes"*, 31. European Photovoltaic Solar Energy Conference and Exhibition (EU PVSEC 2016), 2016

2. Ö. Bayraklı, H. H. Güllü, E. Coşkun, M. Terlemezoğlu, M. Parlak, "*Characterization of CZTSe Thin Films for Solar Cell*", 31. European Photovoltaic Solar Energy Conference and Exhibition (EU PVSEC 2016), 2016

3. E. Coşkun, H. H. Güllü, Ö. Bayraklı, T. Çolakoğlu, M. Parlak, *"Effect of Nanowire Length on Device Performance of n-ZnSe/p-Si Nanowire Heterojunctions"*, 31. European Photovoltaic Solar Energy Conference and Exhibition (EU PVSEC 2016), 2016

4. M. Terlemezoğlu, H. H. Güllü, Ö. Bayraklı, M. Parlak, *"Effect of Zn Doping on CdS Thin Film Deposited by RF Magnetron Sputtering"*, 31. European Photovoltaic Solar Energy Conference and Exhibition (EU PVSEC 2016), 2016

5. H. H. Güllü, Ö. Bayraklı, İ. Candan, M. Parlak, "*Formation of ZnSnSe2 Thin Films Deposited by Using Sintered Stoichometric Powder*", Materials Research Society (MRS) Spring Meeting, 2016

6. C. Emir, H. H. Güllü, Ö. Bayraklı, M. Parlak, "*Saçtırma Yöntemi ile Üretilen ITO İnce Filmlerinin Farklı Alttaş ve Tavlama Sıcaklıklarına göre İncelenmesi"*, 21. Yoğun Madde Fiziği Ankara Toplantısı (YMF-21), 2015

7. H. H. Güllü, M. Parlak, "*Üretim Sonrası Isıl İşlem Sıcaklığının ZnSe İnce Film Özellikleri Üzerine Etkisi"*, 21. Yoğun Madde Fiziği Ankara Toplantısı (YMF-21), 2015

8. H. Güllü, Ö. Bayraklı, M. Parlak, "*Saçtırma Yöntemiyle Üretilen Ag-Zengin $AgInSe_2$ İnce Filmlerinin Özellikleri"*, 21. Yoğun Madde Fiziği Ankara Toplantısı (YMF-21), 2015

9. H. H. Güllü, Ö. Bayraklı, M. Parlak, "*Investigation of Electrical Properties of Cu-Ag–In–Se Thin Films Deposited by Thermal Evaporation Method"*, 30. European Photovoltaic Solar Energy Conference and Exhibition (EU PVSEC 2015), 2015

10. H. H. Güllü, Ö. Bayraklı, M. Parlak, *"Synthesis and characterization of CuZnSe2 thin film structures"*, 17. International Conferenceon II-VI Compounds and Related Materials, 2015

11. H. H. Güllü, Ö. Bayraklı, M. Parlak, "*Structural Characterization and Optical Properties of $AgInSe_2$ Thin Films"*, 11. Türkiye Nanoscience and Nanotechnology Conference (NanoTR-11), 2015

12. H. H. Güllü, Ö. Bayraklı, M. Parlak, Ç. Erçelebi, **"***Preparation and Characterization of $CuZnSe_2$ Thin Films Deposited by Physical Vapor Deposition Technique"*, 3. Turkish Solar Electricity Conference and Exhibition (SolarTR-3), 2015

13. H. H. Güllü, E. Coşkun, M. Parlak, *"Investigation of Optical Parameters of Thermally Evaporated ZnSe Thin Films"*, 3. Turkish Solar Electricity Conference and Exhibition (SolarTR-3), 2015

14. M. Işık, H. H. Güllü, "*Electrical Properties of Thermally Evaporated Ga-In-Se Thin Films"*, 3. Turkish Solar Electricity Conference and Exhibition (SolarTR-3), 2015

15. A. Hosseini, H. H. Güllü, M. Parlak, R. Turan, Ç. Erçelebi, "*Fabrication and Characterization of TiO_2/CdTe/ZnSnTe ETA Solar Cell"*, 3. Turkish Solar Electricity Conference and Exhibition (SolarTR-3), 2015

16. Ö. Bayraklı, H. H. Güllü, E. Coşkun, M. Parlak, "*Fabrication and Characterization of p-$AgGa_xIn_{1-x}Te_2$/n-$ZnInSe_2$ Heterojuctions for Solar Cell Applications"*, Materials Research Society (MRS) Spring Meeting, 2015

17. H. H. Güllü, Ö. Bayraklı, E. Coşkun, M. Parlak, Çiğdem Erçelebi, "*Cu-Zn-Se İnce Filmlerinin Saçtırmalı Kaplama Tekniğiyle Üretilmesi ve Özelliklerinin Belirlenmesi"*, 20. Yoğun Madde Fiziği Ankara Toplantısı (YMF-20), 2014

18. A. Hosseini, H. H. Güllü, M. Parlak, Ç. Erçelebi, "*Fabrication and Characterization of Sputtered TiO_2 Thin Films"*, Materials Research Society (MRS) Fall Meeting, 2014

19. H. H. Güllü, E. Coşkun, Ö. Bayraklı, M. Parlak, "*Characterization of Zn-In-Se Thin Films for Solar Cell Applications"*, 29. European Photovoltaic Solar Energy Conference and Exhibition (EU PVSEC 2014), 2014

20. H. H. Güllü, A. Hosseini, E. Coşkun, M. Parlak, Ç. Erçelebi, "*Investigation of Si/ZnSnTe Heterojunction Growth and Device Properties"*, Science & Applications of Thin Films, Conference and Exhibition, (SATF2014), 2014

21. A. Hosseini, H. H. Güllü, M. Parlak, Ç. Erçelebi, "*Fabrication and Characterization of Sputtered Zn-Sn-Te Thin Film"*, European Conference on Surface Science (ECOSS30), 2014

22. H. H. Güllü, C. Coşkun, Ö. Bayraklı, İ. Candan, M. Parlak, "*Characterization of Sputtered Cu-Zn-Sn-Te Thin Films for Device Application"s*, European Materials Research Society (EMRS) Spring Meeting, 2014

23. A. Hosseini, H. H. Güllü, E. Coşkun, R. Turan, Ç. Erçelebi, "*Fabrication and Characterization of TiO_2Thin Films for Device Applications"*, European Materials Research Society (EMRS) Spring Meeting, 2014

24. H. H. Güllü, E. Coşkun, M. Parlak, "*Ag/n-Si/p-AGIS/In Heteroeklem Yapısının Aygıt Özellikleri"*, 19. Yoğun Madde Fiziği Ankara Toplantısı (YMF-19), 2013

25. H. H. Güllü, İ. Candan, Ö. Bayraklı, M. Parlak, "*Cu-Zn-Sn-Te İnce Filmlerin Yapısal ve Optik Özelliklerinin İncelenmesi"*, 19. Yoğun Madde Fiziği Ankara Toplantısı (YMF-19), 2013

26. İ. Candan, H. H. Güllü, M. Parlak, Ç. Erçelebi, "*Güneş Pili Uygulamalarında Soğurucu Katman Olarak Kullanılan Cu(In,Ga)Se (CIGS) İnce Filmlerinin Üretimi ve Karakterizasyonu"*, 19. Yoğun Madde Fiziği Ankara Toplantısı (YMF-19), 2013

27. A. Hosseini, İ. Candan, H. H. Güllü, Ç. Erçelebi, "*Saçtırma Yöntemi Kullanılarak Üretilen TiO_2 İnce Filmlerde Üretim Süresinin Yapı ve Optik Özelliklere Etkisi"*, 19. Yoğun Madde Fiziği Ankara Toplantısı (YMF-19), 2013

28. H. H. Güllü, İ. Candan, M. Parlak, "*Characterization of Co-evaporated Cu-Ag-In-Se Thin Film by Physical Vapor Deposition"*, 9. Türkiye Nanoscience and Nanotechnology Conference (NanoTR-9), 2013

29. İ. Candan, H. H. Güllü, Ö. Bayraklı, Ç. Erçelebi, M. Parlak, "*Growth and optimization of ZIT thin films for photovoltaic applications"*, 9. Türkiye Nanoscience and Nanotechnology Conference (NanoTR-9), 2013

30. G. Kılıçerkan, İ. Candan, H. H. Güllü, R. Turan, M. Ertuğrul, "*Structural Characterization of Aluminum Induced Polycrystalline Silicon Films"*, 9. Türkiye Nanoscience and Nanotechnology Conference (NanoTR-9), 2013

31. H. H. Güllü, İ. Candan, Ö. Bayraklı, Ç. Erçelebi, M. Parlak, "*Investigation of The Physical Properties of Cu-In-Zn-Se Thin Films Deposited by Sputtering"*, European Materials Research Society (EMRS) Spring Meeting, 2013

32. İ. Candan, H. H. Güllü, Ö. Bayraklı, Ç. Erçelebi, M. Parlak, "*Growth and Characterization of Ga-rich $CuIn_{1-x}Ga_xSe_2$ (CIGS) Thin Films by Sputtering Technique for Photovoltaic Application"*, European Materials Research Society (EMRS) Spring Meeting, 2013

33. A. Hosseini, İ. Candan, H. H. Güllü, Ç. Erçelebi, "*Device characterization of ITO/TiO_2/CdTe/Au thin film heterojunction"*, 2. Yoğun Madde Fiziği İzmir Toplantısı, 2013

34. İ. Candan, H. H. Güllü, Ö. Bayraklı, M. Parlak, Ç. Erçelebi, "*Effect of In/Ga Ratio on The Properties of Semiconductor $CuIn_{1-x}Ga_xSe_2$ (CIGS) Thin Films"*, 2. Turkish Solar Electricity Conference and Exhibition (SolarTR-2), 2012

35. H. H. Güllü, İ. Candan, M. Parlak, Ç. Erçelebi, "*Saçtırma (Sputtering) Tekniği ile Ag-Zengini Üretilen $Cu_{1-x}Ag_xInSe_2$ İnce Filmlerin Karakterizasyonu"*, 1. Yoğun Madde Fiziği İzmir Toplantısı, 2012

36. İ. Candan, H. H. Güllü, M. Parlak, Ç. Erçelebi, "*CIGS İnce Filmlerde Isıl İşlemin Yarıiletken Özelliklere Olan Etkisi"*, 1. Yoğun Madde Fiziği İzmir Toplantısı, 2012

37. H. H. Güllü, İ. Candan, M. Parlak, Ç. Erçelebi, "*Cu-Zengin CAIS İnce Filmlerinin Yapısal, Elektriksel ve Optiksel Özelliklerinin İncelenmesi"*, 18. Yoğun Madde Fiziği Ankara Toplantısı (YMF-18), 2011

38. İ. Candan, H. H. Güllü, M. Parlak, Ç. Erçelebi, "*Güneş Pili Yapılarında Kullanılan CIGS Yarıiletken İnce Filmlerde Bakır Oranının Yapısal, Elektriksel ve Optik Özelliklere Etkisi",* 18. Yoğun Madde Fiziği Ankara Toplantısı (YMF-18), 2011

39. Ö. Bayraklı, M. Demirtaş, H. H. Güllü, İ. Candan, M. Parlak, "*Elektron Demeti Tekniğiyle Büyütülen $AgGa_xIn_{(1-x)}Te_2$ İnce Filmlerin Yapısal, Optiksel ve Elektriksel Karakterizasyonu",* 18. Yoğun Madde Fiziği Ankara Toplantısı (YMF-18), 2011

40. H. H. Güllü, İ. Candan, M. Parlak, Ç. Erçelebi, *"Investigation of Structural, Electrical and Optical Properties of $Cu_{1-x}Ag_xInSe_2$ Thin Films with Different Cu-Ag Ratios"*, 7. Türkiye Nanoscience and Nanotechnology Conference (NanoTR-7), 2011

41. İ. Candan, M. Parlak, H. H. Güllü, Ç. Erçelebi, "*The Structural and Optical Analyzing of CIGS Thin Films Deposited by Sputtering Technique"*, 7. Türkiye Nanobilim ve Nanoteknoloji Konferansı (NanoTR-7), 2011

42. H. H. Güllü, M. Parlak, Ç. Erçelebi, "*$Cu_{1-x}Ag_xInSe_2$ İnce Filmlerinin Yapısal, Elektriksel ve Optiksel Özelliklerinin x İçeriğine Bağlı Olarak İncelenmesi",* 17. Yoğun Madde Fiziği Ankara Toplantısı (YMF-17), 2010

43. İ. Candan, H. H. Güllü, M. Parlak, Ç. Erçelebi, "*Characterization of CIGS Thin Films Deposited with Double Sources e-beam Evaporation by the Three-stage Process",* European Materials Research Society (EMRS) Spring Meeting, 2009

44. D. Köseoğlu, H. H. Güllü, H. Altan, "*THz probe studies of MBE grown epitaxial GaAs",* 16. International Conference On Electron Dynamics In Semiconductors, Optoelectronics And Nanostructures (EDISON 16), 2009

45. M. M. Metbulut, H. H. Güllü, H. Altan, "*Influence of the Spot Size of the Probe Beam on the Detected THz Power using Electro-optic Detection Method",* Workshop on Terahertz and Mid Infrared Radiation (TERA-MIR), 2009